# Structural and thermodynamic studies of Y based AB2 hydride forming alloys Étude structurale et thermodynamique des alliages hydrurables de type AB2 à base de Y

Hao Shen

THESE

Pour obtenir le grade de

DOCTEUR DE L'UNIVERSITE DE PARIS-EST CRETEIL

*Ecole Doctorale : Sciences, Ingénierie et Environnement*

Par

HAO SHEN

15 December 2022

# Structural and thermodynamic studies of Y based $AB_2$ hydride forming alloys

# Étude structurale et thermodynamique des alliages hydrurables de type $AB_2$ à base de Y

*Devant le Jury:*

| | | |
|---|---|---|
| **Mr X.G. Li** | *Professeur de l'Université de Pékin, Chine* | *Rapporteur* |
| **Mr J-L. Bobet** | *Professeur de l'Université de Bordeaux I* | *Rapporteur* |
| **Mme J.J. Liu** | *Maître de conférences de l'Université de Yangzhou, Chine* | *Examinatrice* |
| **Mme V. Paul-Boncour** | *Directeur de recherche de l'ICMPE, Thiais* | *Examinatrice* |
| **Mr L.J. Jiang** | *Directeur Scientifique de GRINM, Pékin, Chine* | *Directeur de thèse* |
| **Mme J.X. Zhang** | *Ingénieur de recherche CNRS, Thiais* | *Directrice de thèse* |

# Acknowledgement

The work described in this thesis was carried out in ICMPE France and GRINM China under the supervision of Dr. **Junxian ZHANG** and Prof **Lijun JIANG**, I am utterly thankful to have the opportunity to carry out my PhD thesis in such an intellectually stimulating environment.

I would like to express my deepest gratitude to my supervisor **Junxian ZHANG**. Thank you for your guidance, help, encouragement and patience, as well as numerous useful discussions. I could never imagine how my thesis would get done without your professional advice and meticulously redaction. I would like to thank my supervisors in China Prof **Lijun JIANG** and Prof **Ping LI** for their kind guidance on my experimental work.

I am immensely thankful to Dr. **Valérie Paul-Boncour**, Dr. **Michel Latroche** and Dr. **Fermin Cuevas** for the stimulating discussions on all aspects of my work, especially their professional guidance and review on the thesis, academic papers, abstracts, presentations and posters for conferences and meetings. I sincerely admire their professionalism and perseverance. Michel is sadly no longer with us, I will always miss him.

I would like to thank my jury members, Prof. **Xingguo LI**, Prof. **Jean-Louis BOBET**, Dr. **Jingjing LIU**, Dr. **Valérie Paul-Boncour**, Prof. **Lijun JIANG** and Dr. **Junxian ZHANG** for their willingness to read and judge this thesis.

I would like to thank Prof. **Michel Latroche**, Dr. **Junxian ZHANG** and Dr. **Nicolas Emery** for their help on the analysis of Neutron Diffraction data. I am also very thankful to Dr. **Samaneh Sadat Setayandeh** and Prof. **Patrick Burr** for their work on Density Functional Theory Calculation. They all made great contributions to this thesis.

I am thankful to my colleagues at ICMPE for their kindness and help. I would like to thank **Hélène Barrès** and **Gladys Bernari** for their assistance on administration procedure. I would like to express my sincere gratitude to **Hélène Barrès** and **Eric Alleno** for their kind help on the housing problem during the Covid pandemic. Thanks to **Valérie Lalanne**, **Benjamin Villeroy**, **Fabrice Couturas**, **Olivier Rouleau** and **Eric LEROY** for their technical support. I would like to thank **Anis Bouzidi**, **Alejandro Ares Dorado**, **Tuan Minh VU**, **Abou Diack-Rasselio** and **Bruno Hessel Silva** for their company as my colleagues and friends during the two years I passed in ICMPE.

Last, but not least, I would like to thank my dear friends in Paris and Beijing for their kind company and continued support during my PhD. **Wang LIU**, **Liming CHEN**, **Runan XIE**, **Yanlong ZHOU**, **Liqin WANG**, **Guanyu CAI**, **Yingqi BI** and **Jingyi LI**, with you guys I had the best time in Paris. I also thank my wonderful friends in Beijing. **Wenqian LI**, **Weijing WANG**, **Shijie DU**, **Sizhe LIANG**, **Zhouxin WANG**, **Mengzhu LI** and **Ke XU**, thank you for your kind company during my entire PhD.

2019 is a tough year because ravages of COVID-19. I sincerely thank **University of Science and Technology Beijing** (USTB) for the active help in sending me epidemic prevention materials at the beginning of COVID-19 pandemic. I am also very thankful to **Junxian ZHANG** and my friends for their kind concern during the hard time.

I do thank my parents, my sister for their comprehension and support like always.

# Table of Contents

## The structural and thermodynamic studies of Y based $AB_2$ hydride forming alloys

$AB_2$-type alloys ($A$ = rare earth, $B$ = transition metals) show higher theoretical hydrogen absorption capacity than rare earth based $AB_5$ and $AB_n$ ($3 \leq n \leq 4$) alloys, but suffer from hydrogen-induced amorphization (HIA) or hydrogen-induced disproportionation (HID) because of the unstable structure, thus the practical capacities are often low and cycle life is poor. The atomic size ratio $r_R/r_M$ is the most important geometric factor for determining structural stability and HIA occurrence in $RM_2$-type intermetallic compounds with $C15$ structure. Based on $YNi_2$ intermetallic compound, the substitution effects of $A$- and $B$-site elements for Y and Ni were studied in this thesis. The $B$-site substitution, Ni by Al and Mn, is limited by the solubility of these elements in $C15$ structure. It improves the structure stability and hydrogen absorption capacity, but the HIA does not suppressed. It also exhibits various interesting phase occurrence and structural characteristics, such as anti-occupation of Mn in $Y_xNi_{2-y}Mn_y$ compounds. The $A$-site substitution, Y by Mg and Sc, present wider range. The stabilities of $C15b$ (Mg substitution) and $C15$ (Sc substitution) structures were enhanced and HIA was suppressed or eliminated, but they show high plateau pressures and moderate capacities. Further studies of substitution effects on $C15$ structure combining both $A$- and $B$-site elements would be interesting and promising. In this work, compounds with off-stoichiometry show interesting hydrogenation properties: flat plateau, good reversibility and high capacity of 1.7 wt. %.

---

## Étude structurale et thermodynamique d'alliages hydrurables de type $AB_2$ à base de Y

Les alliages de type $AB_2$ ($A$ = terre rare, $B$ = métaux de transition) présentent une capacité théorique d'absorption d'hydrogène supérieure à celle des alliages $AB_5$ et $AB_n$ ($3 \leq n \leq 4$) à base de terres rares, mais souffrent d'amorphisation ou de disproportion induite par l'hydrogénation (HIA ou HID) dû à l'instabilité de la structure. Ainsi, les capacités pratiques sont souvent faibles et la durée de vie est limitée. Le rapport de taille atomique $r_A/r_B$ reste le facteur le plus important pour déterminer la stabilité structurelle et la HIA pour les composés intermétalliques $AB_2$ avec une structure $C15$. En partant du composé intermétallique $YNi_2$, les effets de substitution des éléments $A$ (Y) et $B$ (Ni) ont été étudiés dans cette thèse. Côté $B$, la substitution du Ni par Al et Mn est limitée par la solubilité de ces éléments dans la structure $C15$. La substitution améliore la stabilité de la structure et la capacité d'absorption d'hydrogène, mais le HIA n'est pas supprimé. Des propriétés structurales montrent des caractéristiques intéressantes, telles que l'occupation anti-site d'atomes Mn sur le site de Y dans les composés $Y_xNi_{2-y}Mn_y$. Côté $A$, la substitution du Y par Mg et Sc présente une gamme de composition plus large. Les stabilités des structures $C15b$ (substitution Mg) et $C15$ (substitution Sc) ont été améliorées, et l'HIA a été supprimé. Leur capacité d'absorption est faible sous conditions modérés (température ambiante et 100 bars) car les plateaux de pression sont trop élevés. Finalement des alliages non-stœchiométriques ont montré des propriétés intéressantes pour le stockage de l'hydrogène: un seul plateau, bonne réversibilité et une capacité de 1.7 %m.

# 1 . Introduction of hydrogen and materials for hydrogen storage

This chapter starts with a description of the background of hydrogen storage, hydrogen production and hydrogen storage, especially for solid-state storage system as concerns the use of intermetallic compounds for hydrogen storage. Then, the fundamental principle of solid-state hydrides for hydrogen storage is explained, the comparison of typical hydrides forming intermetallic compounds are surveyed.

## 1.1 Background of hydrogen

### 1.1.1 Hydrogen energy

Humans are on a collision course with the natural world, and the consequences of human activity on the environment lead to exceeding the capacity of eco-systems to guarantee living conditions for humanity [1]. Problems arise from our dependence on combustible fuels, the environmental risks associated with their extraction and the environmental damage caused by the emission of $CO_2$ product of the fossil fuel consummation [2]. Furthermore, continuous growth of the world population and economy, coupled with rapid urbanization has resulted in a monumental increase in energy demand [3,4]. In order to address the consequences of the fossil fuel consummation, developing energy systems which use renewable and sustainable sources is essential for future energy sustainability and global security [5,6].

The idea of hydrogen as an energy carrier was discussed over two centuries ago but was strengthened noticeably after the global energy crises of 1974 [7–9]. Hydrogen is the lightest element with a molecular weight of 2.016, occupying the place of the most abundant element on the Earth, contributing roughly 75% of all normal matter. However, hydrogen does not exist in natural state, most of it store in the water. The energy density of hydrogen is 120 MJ/kg, which is more than three times of the conventional fuels [10]. Combustion of hydrogen releases only water into the environment. The high energy density combining the zero-carbon emission properties of hydrogen make it the most promising energy carrier.

Moreover, in the long term, traditional fossil fuels are non-renewable and will eventually run out, whereas hydrogen exhibits long-term viability due to the recyclable water. The widespread of hydrogen energy can increase the utilization rate of renewable energy and reduce the dependence on fossil energy. Therefore, hydrogen will surely be one important energy carrier for the future economy.

### 1.1.2 Hydrogen production

At present, hydrogen may be produced via two mature pathways: thermochemical way (by processing fossil fuels) and electrochemical way (by electrolysis of water).

Nowadays, we have to say fossil fuels are still the main resource for industrial mass scale hydrogen production, which fact goes against reducing greenhouse gas emissions. The most popular methods that use a fossil fuel feedstock to produce hydrogen are to extract hydrogen

by breaking the bonds between hydrogen and carbon [11]. The feedstock includes coal [12,13], oil [14], biomass [15–17], methanol [18,19] and methane [20–22], *etc.* Specifically, steam methane reforming (SMR) which relies on natural gas as an input is known as the cheapest form of hydrogen production, this method is the most economical with an estimated cost of around 1.8 $/kg and shows high hydrogen yield efficiency of approximately 74% [23]. Indeed, SMR has the largest share of almost 48% in global hydrogen production from fossil fuels [23,24], but it also brings large substantial $CO_2$ emissions, 4 mol of $H_2$ and 1 mol of $CO_2$ will be yielded for each one of methane. Similarly, other common industrial methods to obtain $H_2$ such as partial oxidation and autothermal oxidation of hydrocarbon, coal gasification, *etc*. [25], through various chemical reactions but bring the same issue of being not environmentally friendly.

Although approximately 96% of today's hydrogen is produced via thermochemical conversation of fossil fuels [26], considering that the future energy system needs to be sustainable with low environment impact, carbon-emission-free production of hydrogen with renewable resources start rapidly gaining potential, such as gasification of biomass/biofuels and water splitting by solar, wind or tidal energy [27–29].

The numerous hydrogen production technologies using renewable energy are at an early stage of development. The challenges are to reduce costs and improve the conversion efficiency, coupling with flexible applications by adjusting different renewable energy in different places and times.

### 1.1.3 Hydrogen storage

The hydrogen economy requires good package, storage and transportation from the production site to the users. The hydrogen production using renewable energy is intrinsically intermittent, for customer's use a safe, reliable and cost-effective $H_2$ storage is needed. Hydrogen can be stored in gaseous, liquid and solid states.

$H_2$ with its high diffusivity, light density and low liquefication temperature, traditional storage techniques by compression and liquefaction of gaseous $H_2$ are very inefficient and energetically expensive. Specifically, for gaseous form, hydrogen is stored as compressed gas in highly pressurized tanks up to 700 bar. This requires careful vessels design using strong and lightweight materials. This mode of storage shows still low volumetric density: 17.6g $H_2$/L (2.5 MJ/L) for a 350 bar tank and 26.3g $H_2$/L (5 MJ/L) for a 700 bar tank [30,31], which is close to the 2010 DOE target of 28g $H_2$/L, but far away from the ultimate DOE target of 70g $H_2$/L [32].

For the liquid form storage, hydrogen is stored as liquid in cryogenic tanks which requires cooling the hydrogen to 20 K. This method of physical storage of hydrogen in form of cryogenic liquid requires maintaining very low temperature which consume about 30% of the total energy content [33–35]. Even though the volumetric density of this storage is of 41.8g $H_2$/L [30], which

satisfies the 2015 DOE target of 40g $H_2$/L but will not reach to the ultimate DOE target of 70g $H_2$/L [32].

Hydrogen can also be stored in solid-state materials by physisorption or chemisorption. Physisorption storage is adsorbing molecular hydrogen on surfaces of solids by van der Waals interactions in high specific surface materials, including carbon-based materials, metal-organic frameworks (MOFs), covalent organic frameworks (COFs) [36] or zeolites [37]. Physisorption exhibits the advantages of full reversibility and fast hydrogen uptake and release kinetics, attracting considerable attention. However, physisorption are only applicable at low temperature due to the weak van der Waals forces. According the Chahine's rule [38], for the adsorbents with various carbon structures, the gravimetric hydrogen storage amount is positively associated with available surface area. Moreover, by estimating the hydrogen packing on graphene, they set a maximum hydrogen storage capacity is approximately 1 wt.% at 77 K per 500 $m^2$/g of the adsorbent surface area [38,39]. Indeed, at room temperature, the hydrogen absorption capacities of all known porous materials are below 0.6 - 0.8 wt. % at 100 bar [40]. All reports claiming that they have obtained capacity of more than 1 wt.% at room temperature are erroneous because of the experimental measuring errors [41,42]. On the other hand, the substantive characteristics of physisorption decide that the hydrogen uptakes solemnly depend on the specific surface area. However, a great deal of experimental studies reveal the existence of a volumetric ceiling at ~ 40g $H_2$/L under a pressure varying between 5 bar and 100 bar at 77 K (closer to the compressed liquid hydrogen), and it is hard to enhance volumetric hydrogen storage further by increasing the volumetric surface area [42]. Meanwhile, increasing the gravimetric surface area or optimizing the pore size distributions in MOFs and MOF-derived carbons (MDCs) exhibits the possibility to achieve higher volumetric capacities [42].

Metal hydrides are a category of promising materials where hydrogen is stored via a chemical reaction, exhibiting safety and cost advantages above gaseous and liquid storage systems. Different from the storage methods we mentioned above, hydrogen is stored in metal hydrides in atomic form, which results in a high volumetric hydrogen storage capacity up to 150g $H_2$/L, much higher than the DOE target of 70g $H_2$/L, even they suffer from the disadvantages of we weight [39,43–45].

## 1.2 Solid state storage

Indeed, intermetallic compounds with a variety of compositions are capable of absorbing large quantities of hydrogen in which way hydrogen occupies interstitial tetrahedral or octahedral sites via metallic bond.

The studies of intermetallic compounds starts from the discovery of $LaNi_5$ [46] and TiFe [47] for their outstanding hydrogen absorption properties. In fact, the properties of an intermetallic compound are largely dependent on their crystal structure. Different structures

contain different types and numbers of interstitial sites to accommodate hydrogen, thus various hydrogen sorption behaviors.

### 1.2.1 Hydrogen storage in metal hydrides

Reaction of a $H_2$ molecule with a hydride forming material can be split in 4 steps: a) $H_2$ molecule approaching the metal surface, b) Interaction of the $H_2$ molecule by Van der Waals forces (physisorption state), c) Dissociation of hydrogen molecule to hydrogen atom and chemisorption on the surface of the material (see formula 1.1), d) Occupation of subsurface sites and diffusion into bulk lattice sites. The hydrogen absorption process is exothermic, the released heat is the hydride formation enthalpy $\Delta H$.

$$H_2 \leftrightarrow 2H \tag{1.1}$$

$$M + xH \leftrightarrow MH_x(\alpha) \pm \Delta H \tag{1.2}$$

$$MH_x(\alpha_{max}) + yH \leftrightarrow MH_{x+y}(\beta) \pm \Delta H \tag{1.3}$$

After dissociation on the metal surface, the H atoms have to diffuse into the bulk to form a *M*-H solid solution commonly referred to as α-phase (see equation 1.2). Up to solution limit, the saturated α-phase transforms into ordered hydride β-phase (see equation 1.3), further on all α-phase transformed into β hydride phase, a solid solution branch of hydride β-phase may exist at higher pressure (Figure 1.1). For a determined temperature, this can be illustrated by an isotherm Figure 1.1, corresponding the three regions: the hydrogen concentration in the metal increases with gas pressure, a solid solution phase (α-phase) occurs, second, the plateau region where saturated α-phase transforms into β-phase correspond to the two-phase domain, third, a solid solution branch of hydride β-phase under higher hydrogen pressure.

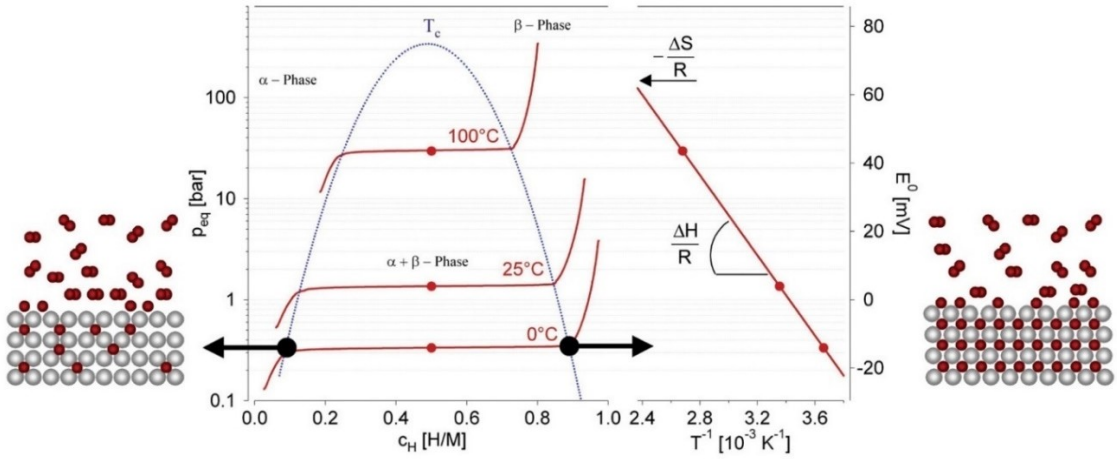


Figure 1.1 Pressure Composition Isotherm (PCI) curve at different temperatures and the deduced Van't Hoff plot, coupled with the formation of α hydride phase (the beginning of the plateau) and β hydride phase (the end of the plateau) in a typical intermetallic compound [48].

For the plateau ( $\alpha + \beta$ phase) region, the system is considered in equilibrium, the thermodynamic properties can be determined by the Van't Hoff plot:

$$lnP_{H_2} = \frac{\Delta H}{RT} - \frac{\Delta S}{R} \tag{1.4}$$

here $\Delta H$ enthalpy and $\Delta S$ entropy during the hydrogenation. The formation enthalpy of hydrides determines the amount of released heat during hydrogen absorption.

Figure 1.2 shows the solid hydride forming elements with their formation enthalpy. The red color stands for very negative enthalpy, which means very stable hydride, high temperature is needed for hydrogen release. Those elements are named *A*-element. The blue color stands for positive enthalpy, means hydride can be formed only under high pressure. Those elements are named *B*-element. By combining the two type elements, intermetallic compounds may show intermediate thermodynamic stability, following the well-known semi-empirical rule of Miedema (see formula 1.5) [49] . For example, the temperature for releasing hydrogen from hydride $TiH_2$ is above 400 ℃ [50], while $TiFeH_2$ can release hydrogen at room temperature [51]. Similarly, in the case of $LaNi_5H_6$, the corresponding values of hydrogen reaction enthalpy for pure metals are -8.8 kJ/mol $H_2$ for Ni-H [52] and -49.6 kJ/mol $H_2$ for La-H [53], whereas the enthalpy is lowered to -30.9 kJ/mol $H_2$ for $LaNi_5H_6$ [54].

$$\Delta H\left(A_nB_mH_{x+y}\right) = \Delta H(A_nH_x) + \Delta H\left(B_mH_y\right) - \Delta H(A_nB_m) \tag{1.5}$$

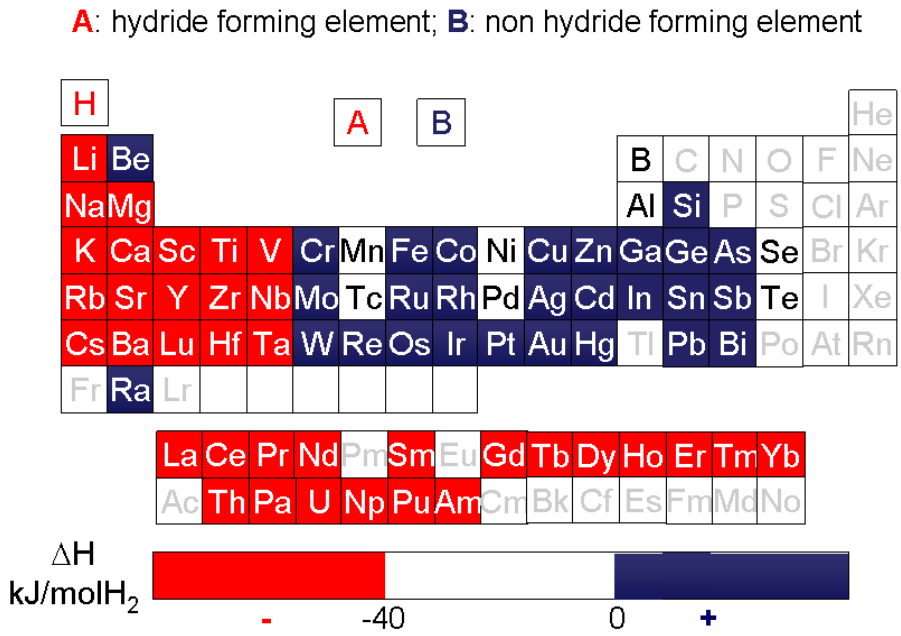


Figure 1.2 Hydride and non-hydride forming elements in the periodic system of the elements [54].

## 1.2.2 Intermetallic compounds for hydrogen storage

Among the various $A_nB_m$ compounds, the most studied materials for hydrogen storage [55] include $AB_5$ ($CaCu_5$-type structure), $AB_{3\text{-}3.8}$ (stacking structure), $AB_2$ (Laves phase), $AB$ (CsCl relative structure), $A_2B$ ($AlB_2$ relative structure), and vanadium-based solid solution alloys.

### 1.2.2.1 $AB_5$-type alloys

$AB_5$-type intermetallic compounds ($A$ here stands for rare earth, $B$ for transition metals) crystallize in $CaCu_5$ type hexagonal crystal structure with space group $P6/mmm$ (191). The representative alloy is $LaNi_5$, which was firstly discovered by Philips company in Netherlands in 1969 [46]. The crystal structure of $LaNi_5$ is represented in Figure 1.3 where La atoms occupy 1$a$ site and Ni atoms occupy 2$c$ and 3$g$ sites respectively. The theoretical hydrogen storage capacity is around 1.4 wt.% with the composition $LaNi_5H_6$. The early neutron diffraction investigation of $LaNi_5D_x$ indicates that α-phase was formed at low deuterium concentrations ($x$ ~ 0.2), with deuterium distributing on positions 3$f$ sites, occupying the octahedral interstices (see the blue octahedron $La_2Ni_2^{2c}Ni_2^{3g}$ in Figure 1.3) [56]. However, the more recent studies suggest that deuterium lie in sites 6$m$ and 12$n$ (see the grey tetrahedrons $La_2Ni_2^{3g}$, $La_1Ni_2^{2c}Ni_1^{3g}$ in Figure 1.3) during the formation of α-phase ($x \sim 0.3$) [57–59]. For the $LaNi_5D_6$ (β-phase), different structure models based on various space groups are found during deuterium atoms-ordering. P. Fischer *et al.* [56] reported a structural distortion based on space group $P31m$ for $LaNi_5D_6$. Latterly, the other authors adopted space group $P6mm$ (a redistribution of the deuterium atoms along the $c$-axis) to describe the symmetry of hexagonal structure for β-phase $LaNi_5D_x$ ($0.4 \leq x \leq 6$), $P63mc$ (doubling of the cell along the $c$-axis due to the rearrangement of deuterium along the $c$-axis) to describe the higher hydride $LaNi_5D_{6.7}$ (solid solution progress: β-phase upon further hydrogenation) [58,60]. The $AB_5$-type intermetallic compounds have been intensively studied as materials used for hydrogen storage and negative electrode of Ni-$M$H batteries, due to their superior hydrogen absorption/desorption properties such as relatively good cyclic ability, low equilibrium pressure and fast kinetic.

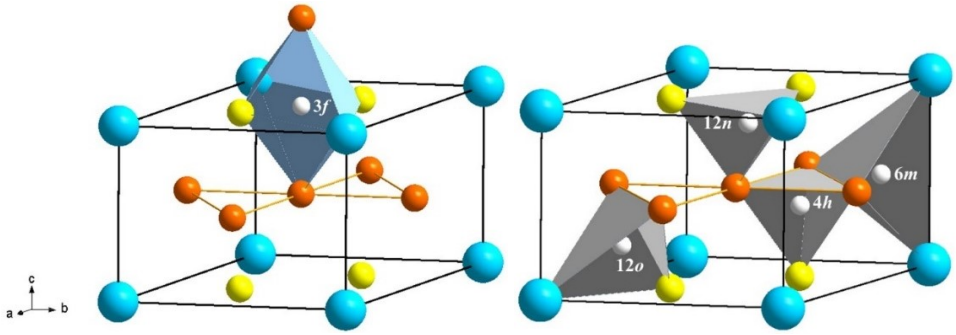


Figure 1.3 Crystal structure of $LaNi_5$: La is in 1$a$ (sky blue balls), Ni is in 2$c$ (yellow balls) and 3$g$ (orange). The white balls represent deuterium atoms which locate at 3$f$ sites in $LaNi_5D_{0.3}$ (octahedral interstices $La_2Ni_2^{2c}Ni_2^{3g}$), 6$m$ and 12$n$, 12$o$ sites (tetrahedral interstices: $La_2Ni_2^{3g}$, $La_1Ni_2^{2c}Ni_1^{3g}$, $La_1Ni_2^{3g}Ni_1^{2c}$) in $LaNi_5D_6$ [59].

However, $LaNi_5$ alloy exhibits a large volumetric change (around 25% for $LaNi_5D_6$) upon hydrogen absorption and desorption. As a result, the hydrogen absorption and desorption cycles lead to the decrepitation of $LaNi_5$ alloy and capacity decay. It is well known that chemical substitution is the most efficient way to turn the properties for application. Therefore, to improve the resistance of $LaNi_5$ to chalking, the substituted $LaNi_5$-related intermetallic compounds were widely studied [61–66]. For example, the studies of Willems *et al.* indicates that partial substitution of Nd for La at *A*-side and Co, Al, Si, *etc*. for Ni at *B*-side significantly reduced the cell volume expansion from ~ 24% to ~ 14% [62]. Especially for Co, in the Co-substituted $LaNi_{5-x}Co_x$ compounds, an intermediate γ-phase is observed between the formation of hydrogen solid-solution α-phase and the fully hydride β-phase. The formation of α- and γ-phase exhibit the same lattice expansion in the basal plane, whereas the transition from γ- to β-phase leads to the expansion along *c*-axis. Therefore, γ-phase offers a buffer effect on cell expansion and relives the internal stress during hydrogen absorption and desorption, the chalking resistance and cycle life were thus significantly improved: $LaNi_{4.5}Co_{0.5}$ exhibits much better cycling properties (stable capacity: ~ 1.33 wt.%, cycling retention: ~ 86%) than parent $LaNi_5$ compound (stable capacity: ~ 1.26 wt.%, cycling retention: ~ 82%) upon 1000 cycles [67,68].

Although $LaNi_5$-type alloys with $CaCu_5$ structure have been well developed and led to the most successful commercial application for metallic hydrides, all built from $CaCu_5$-based structure still shows the limitation of capacity, the gravimetric hydrogen storage capacity is rather low (with a value less than 1.5 wt.%).

#### 1.2.2.2 $AB_2$-type alloys

From a crystallographic point of view, $AB_2$-type intermetallic compounds with Laves phase structure possess more tetrahedral sites than $AB_5$ and $AB_n$ ($3 \leq n \leq 3.8$) ones to accommodate hydrogen atoms, thus higher hydrogen absorption capacity is expected [69–71].

In this section, I will introduce $AB_2$-type intermetallic compounds with Laves phase structure with Ti and Zr as *A* elements and Cr, V and transition metals as *B* elements, crystalizing in the structures of hexagonal *C*14 ($MgZn_2$-type), cubic *C*15 ($MgCu_2$-type) and hexagonal *C*36 ($MgNi_2$-type) [72]. Figure 1.4 shows such three Laves phase structures and the $A_2B_2$ and $AB_3$-type tetrahedral sites which can partly or fully accommodate hydrogen. Among the available tetrahedrons ($A_2B_2$, $AB_3$, $B_4$) for hydrogen occupying in these Laves phase structures, $A_2B_2$-type tetrahedral sites possess the largest size, exhibit the strongest attraction for hydrogen [71].

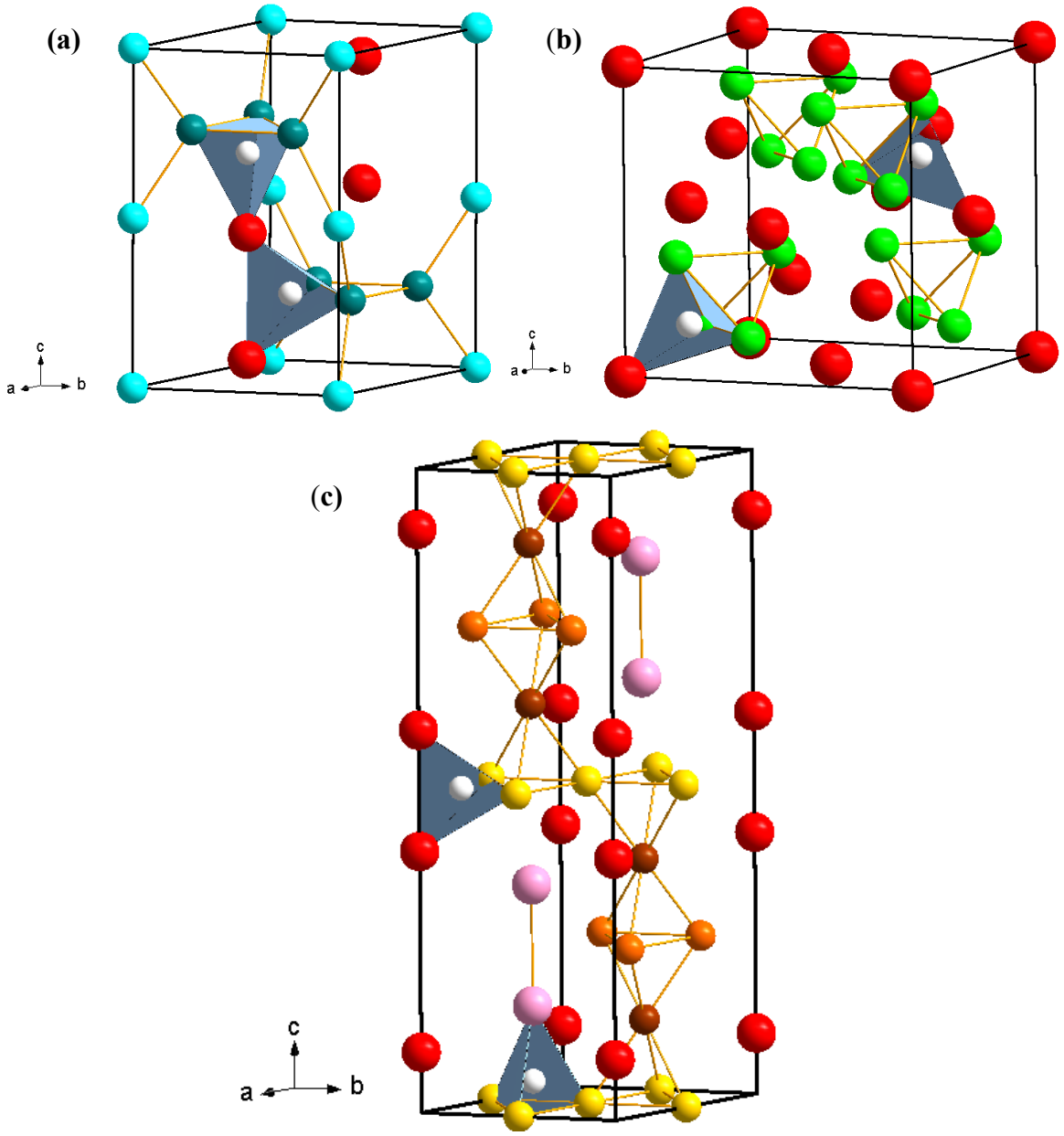


Figure 1.4 Crystal structure of $MgZn_2$ (a): Mg is in 4*f* (red balls) site, Zn is in 2*a* (turquoise balls) site and 6*h* (teal balls) site; $MgCu_2$ (b): Mg is in 8*a* (red balls) site, Cu is in 16*d* (green balls) site; $MgNi_2$ (c): Mg is in 4*e* (red balls) and 4*f* (pink balls) site, Ni is in 4*f* (brown balls), 6*g* (yellow balls) and 6*h* (orange balls) sites. The hydrogen atoms (white balls) may occupy the *A*2*B*2 and *AB*3 type tetrahedral sites.

The maximum hydrogen capacity reaches to H/M = 1.5 (1.9 wt.% for $TiMn_{1.5}$ [73–75]). Similar to $AB_n$ ($3 \leq n \leq 3.8$)-type compounds, $AB_2$-type alloys are also considered for promising hydrogen storage materials and Ni-*M*H batteries due to their higher gravimetric and volumetric energy densities than those of commercial $AB_5$-type alloys.

Although $AB_2$-type alloys are generally less easy activated than $AB_5$ and $AB_n$ ($3 \leq n \leq 3.8$) compounds, but once activated, they exhibit excellent hydrogen absorption and desorption kinetics and a good cycle stability. Usually the interaction of H-$AB_2$ is characterized by a sloping plateau on the pressure-composition isotherms and small hysteresis. The equilibrium

hydrogen desorption pressures for hydrides of $AB_2$-type alloys ranges from ~ 0.003 bar [76] for $ZrV_2$ (227 °C) to > 5000 bar for $TiFe_2$ (room temperature) [77]. Of course, the equilibrium pressure can be modified by multi-element substitution. For example, Mitrokhin *et al*. [78] reported the investigation of $ZrFe_{2-x}M_x$ ($M$ = V, Cr, Mn) alloys, the hydrogen storage capacities of these alloys with V, Cr and Mn substitution (~ 1.8 wt.%) is higher than $ZrFe_2$ (~ 1.7 wt.%) [77]. Meanwhile, the equilibrium desorption pressures decreased dramatically for V-substituted alloys (1.2 MPa at 25 °C) as compared to $ZrFe_2$ one (32.5 MPa at 23 °C) [77]. A dramatic rise in the hydrogen absorption capacities and decrease desorption pressures also occurs for small $x$ values in Al-substituted $Zr(Al_xB_{1-x})_2$ ($B$ = Fe, Co) compounds [79].

Although various attempts have been performed to modify $AB_2$-type alloys, they still suffer from slow activation as compared to rare earth-containing alloys. Meanwhile, they are relatively sensitive to the impurities in $H_2$ [80], which may lead to a serious dilution of their original properties.

Rare earth-Ni based $AB_2$ compounds will be discussed in next Chapter.

### 1.2.2.3 $AB_{3\text{-}3.8}$-type alloys

Currently, the common and commercially available hydrides forming intermetallic are $AB_5$ and $AB_2$ type alloys. In comparison, $AB_5$ alloys suffer from relatively lower gravimetric hydrogen storage capacity, while $AB_2$ alloys are difficult to activate. $AB_n$ class of intermetallic hydrides are of interest due to their roughly intermediate characteristics between $AB_5$ and $AB_2$ alloys, which is the combination of the good features of $AB_5$ and $AB_2$ alloys. Their structure can be descripted by the stacking of the $CaCu_5$-type and Laves phase cubic structures.

As shown in Figure 1.5, these compounds crystallize in unique superlattice structures which show an alternatively stacking of [$AB_5$] subunit and [$A_2B_4$] subunit along $c$-axis in different patterns. Due to the two types of [$A_2B_4$] subunits: $MgZn_2$ and $MgCu_2$ Laves phase structure, the $AB_3$, $A_2B_7$ and $A_5B_{19}$ phases thus form rhombohedral (3$R$-type) lattice ($R\bar{3}m$, 166) and hexagonal (2$H$-type) lattice ($P6_3/mmc$, 194) respectively [81]. For instance, $PuNi_3$ (3$R$-type) and $CeNi_3$ (2$H$-type) structure exhibit the same first layer: one $CaCu_5$-type [$AB_5$] unit is stacked with one $MgZn_2$-type (L1) unit. However, in the second layer, $PuNi_3$ structure adopts the same $MgZn_2$-type unit, whereas $CeNi_3$ structure adopts the $MgCu_2$-type unit (L2). As a result, for sharing $A$ and $B$ atoms in [$A_2B_4$] unit, [$AB_5$] units have to change their positions in the basal plane: in the $CeNi_3$ structure [$AB_5$] unit in the third layer is directly above the first, while in the $PuNi_3$ structure stacking form in the third layer is the same with the second layer (see the dashed box shown in Figure 1.5) [82]. Meanwhile, from characteristics of these two stacking forms along $c$-axis, the correlation of lattice parameters $c$ can be represented by equation: $3c_{hex} = 2c_{rho}$. The $A_2B_7$-type and $A_5B_{19}$-type phases shows the similar stacking patterns [83,84].

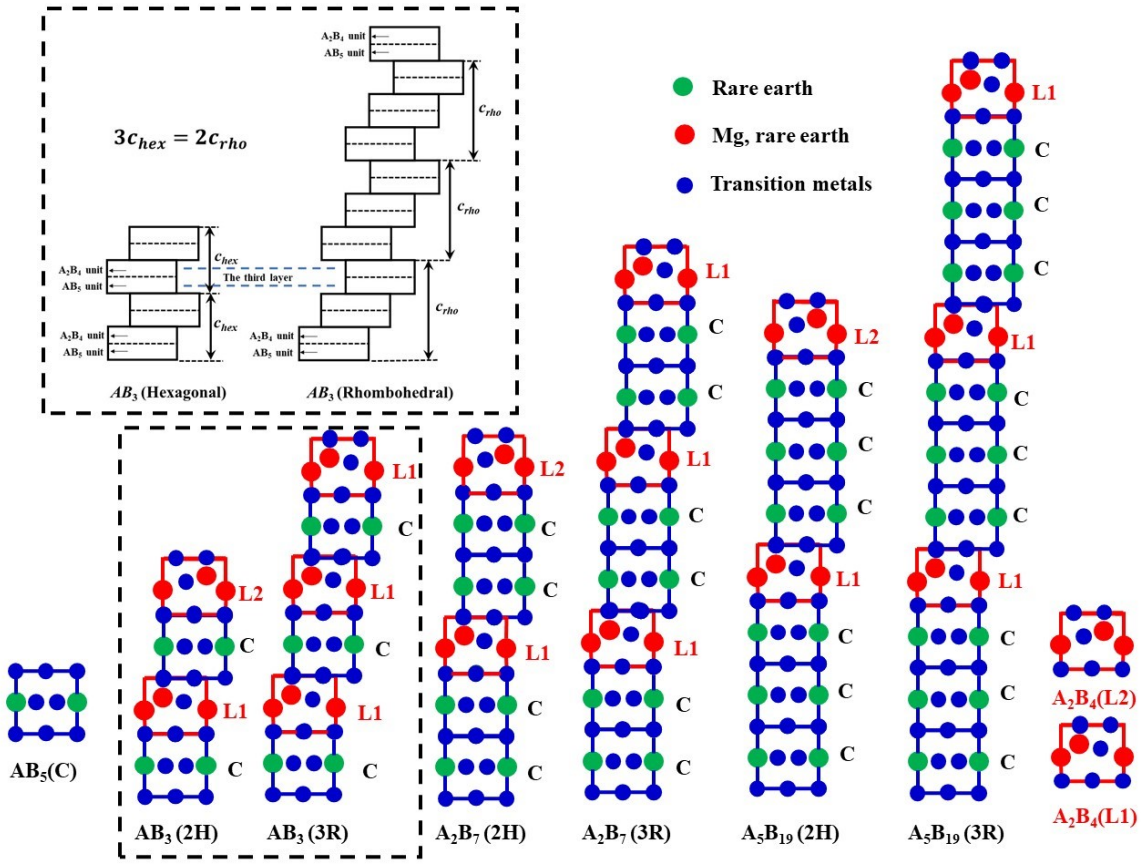


Figure 1.5 Illustration of the stacking forms of rhombohedral and hexagonal $AB_3$-type, $A_2B_7$-type and $A_5B_{19}$-type structures where $A$ is rare earth metals or magnesium and $B$ is transition metals. The schematic drawing in the dashed box is the enlarged stacking forms along $c$-axis of hexagonal- and rhombohedral-type $AB_3$ structures.

For hydrogen sorption properties of binary R-Ni compounds, $LaNi_3$ can react with hydrogen spontaneously but forms an amorphous hydride $LaNi_3H_5$ (1.56 wt.%) [85], which is caused by the mismatch between the [$AB_5$] and [$A_2B_4$] units. Upon hydrogen absorption, anisotropic cell expansion and contraction leads to structural distortion for the stacking structures with large mismatch [86]. The substitution of Mg contributes to stabilize the structure because of the remarkable reduced mismatch, which can be interpreted that Mg atoms occupy only the rare earth sites in [$A_2B_4$] units, leading to its shrink and eliminate the strain generated in [$AB_5$] units [87]. Consequently, both the gravimetric hydrogen storage capacity and structural stability during hydrogen absorption and desorption cycles are enhanced. Upon further multi-element substitution, the hydrogen storage capacities increase from 0.33 wt.% for $LaMg_2Ni_9$ to 1.87 wt.% for $(La_{0.65}Ca_{0.35})Mg_{1.32}Ca_{0.68}Ni_9$ [88], much higher than $AB_5$-type compounds (~ 1.4 wt.%) and binary $LaNi_3$ compound (1.56 wt.%). Subsequently, the cycle life and activation performance were improved by the substitutions of Mn, Co and Al [89–91].

The alloys containing higher contents of $A_2B_7$- or $A_5B_{19}$-type phases are more cyclically stable than $AB_3$ ones [92–94], which can be attributed to the different stacking period of 2:7 and 5:19 compared to 1:3. The presence of one or two additional [$AB_5$] units in $A_2B_7$- and $A_5B_{19}$-

type structures further limit the expansion of the lattice upon hydrogenation, promoting the structural stability and cycling properties [95,96]. However, the increase of stacked [$AB_5$] units also leads to a slight decrease of hydrogen absorption capacity, because the [$A_2B_4$] units exhibit higher capacity than [$AB_5$] units.

### 1.2.2.4 *AB*-type alloy (TiFe, TiNi)

The representative alloy of *AB*-type hydrogen storage materials is TiFe [97]. As described in Figure 1.6, the crystal structure of TiFe, was identified as a cubic lattice (space group $Pm\bar{3}m$) [98], with distinct ordered atoms at the cube vertices, Ti is in 1*a* sites and Fe in 1*b* sites [99,100]. Among the desirable materials TiFe shows light molar mass and high weight capacity, which are capable of absorbing hydrogen reversibly up to 1.9 wt.% at room temperature. However, the Ti-Fe phase diagram exhibits a small homogeneity domain of TiFe phase [101], composition inhomogeneity or deviating stoichiometric ratios will result in the formation of second phase or defect, leading to a significant decrease of hydrogen storage capacity.

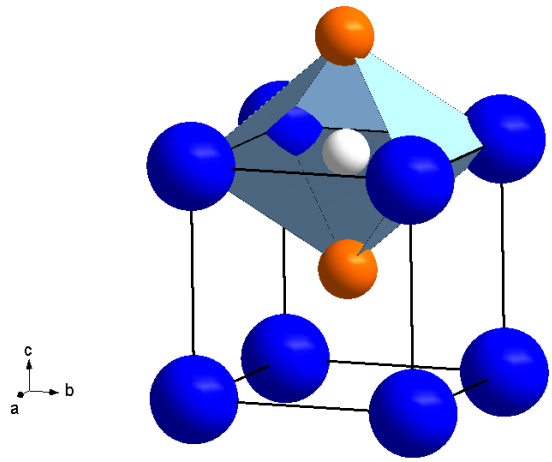


Figure 1.6 Crystal structure of TiFe: Ti is in 1*a* (blue balls), Fe is in 1*b* (orange balls), H is in 3*c* (white balls).

In addition, it is worth noting that TiFe also suffers from the difficult activation, high equilibrium pressure, large hysteresis and the degradation upon hydrogen absorption and desorption cycles. For practical applications, lots of efforts including the substitution of rare earth elements and transition metals for Ti and Fe [102,103], modifying the surface of the alloy, changing melting methods, adopting mechanical alloying method [104–106] as well as severe plastic deformation have been devoted to improve hydrogen sorption properties of TiFe alloy [107,108]. However, except for the low cost and significant capacity, the performance of TiFe-based compounds on activation and kinetics is still inferior to rare earth-containing $AB_n$ ($3 \leq n \leq 5$) intermetallic compounds. So, continuous research effort is needed to overcome these drawbacks.

### 1.2.2.5 $A_2B$-type alloys

One type of $A_2B$ alloys is composed of the Group IVA elements Ti, Zr or Hf ($A$) and transition metals ($B$), typically Ni, crystalizing in a face-centered cubic structure and belonging to the space group $Fd\bar{3}m$. The Ni atoms are in positions 32$e$, for which there are three nearest Ni and nine nearest Ti (16$d$) surrounding it (see Figure 1.7a). Another one is $Mg_2Ni$-based alloys (see Figure 1.7b), crystalizing in hexagonal structure ($P6_222$, 180).

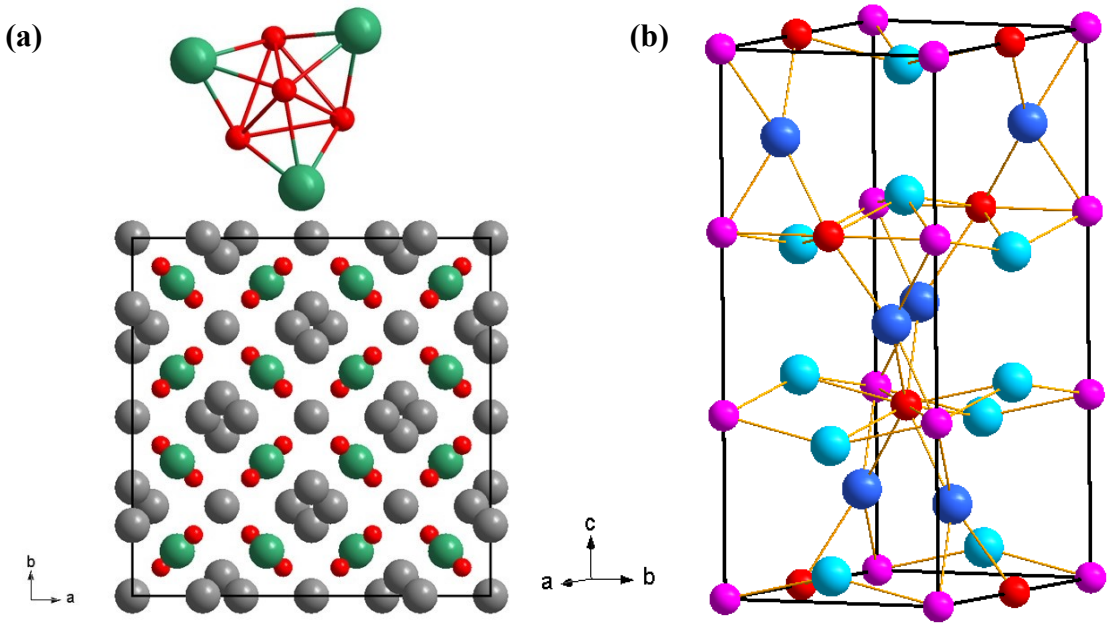


Figure 1.7 Crystal structure of $Ti_2Ni$ (a): Ti in 16$d$ (teal balls) and 48$f$ (grey balls), Ni in 32$e$ (red balls); Crystal structure of $Mg_2Ni$ (b): Mg in 6$j$ (blue balls) and 6$f$ (light blue balls), Ni in 3$c$ (red balls), Ni in 3$a$ (magenta balls).

$Ti_2Ni$ alloy has been attracting much attention owing to its relatively high theoretical capacity. Buchner *et al*. [109] and Mintz *et al*. [110] reported the hydrides $Ti_2NiH_{2.5}$ (1.6 wt.%) and $Ti_2NiH_3$ (1.9 wt.%) respectively. However, although $Ti_2Ni$ is capable to absorb large amount of hydrogen after various activation pre-treatments, the fully hydrogen desorption is hard to realize. Upon heating the hydride $Ti_2NiH_{2.5}$ to 710 °C, there are still small quantities of H stuck in the form of $Ti_2NiH_{0.4}$. Therefore, the unattractive hydrogen sorption properties and harsh conditions for hydrogen absorption and desorption of $Ti_2Ni$ compound limit its further development.

$Mg_2Ni$ intermetallic compound was widely studied among Mg-based materials for its high hydrogen storage capacity of 3.6 wt.%. Moreover, the combination of Mg and transition metals forming intermetallic compounds such as $Mg_2Ni$, $Mg_2Co$ and $Mg_2Fe$, significantly improves the kinetics properties and decreases the temperatures for hydrogen absorption and desorption compared to hydrogen sorption behaviors of α-magnesium dihydride ($MgH_2$) [111,112]. The early studies of Mg-Ni system by J. J Reilly *et al*. [113] turned out that $Mg_2Ni$ alloy can reversibly and rapidly reacted with $H_2$ at ~ 325 °C under ~ 2 MPa. However, their commonly

formed hydrides such as $M_2NiH_4$ (3.6 wt.%), $Mg_2CoH_5$ (4.5 wt.%) and $Mg_2FeH_6$ (5.4 wt.%) belong to the family of complex transition metal hydrides, exhibiting various electron complexes and bonding situation [114].

Whatever, as compared to Mg-free and rare earth-based intermetallic compounds, the Mg-containing $A_2B$-type compounds still show sluggish hydriding/dehydriding kinetics as well as higher thermodynamic stability of their corresponding hydrides, thus hindering their practical application.

## 1.3 Conclusion

As the common formula for intermetallic hydride forming compounds $AB_n$ varying from $AB_5$ to $A_2B$, the proportion of $A$-side hydride forming metals decreases with $n$, thus the hydrogen storage capacity should be supposed to decrease with $n$. However, the fact is, the experimental maximum capacities of $AB_n$ ($0.5 \leq n \leq 3.8$) compounds are not that different from each other, which can be ascribed to various affecting factors such as crystal structures, atomic sizes, electronic structures, *etc.* Among these intermetallic compounds, Ti or Zr-containing $AB_2$-type compounds exhibit the most attractive hydrogen absorption capacities but suffer from sluggish activation and relative slower kinetics comparing to rare earth-containing compounds. That is the main reason we are interested on rare earth based $AB_2$ compounds and dealing to tuning the stability and kinetics by keeping the high storage capacity.

I will emphatically introduce the rare earth-based $RM_2$ compounds in next Chapter, especially for their hydrogen-induced structural stability and substitution effects.

# 2 . Overview of $AB_2$-type rare earth-based materials for hydrogen storage

## 2.1 Introduction

Among the many hydrogen storage systems, intermetallic compounds are attractive for the development of metal hydrides since the crucial safety advantage given by a solid -state storage process under moderate temperature and pressure above gaseous and liquid storage systems [30,45,115]. The current intermetallic hydrogen storage materials can be expressed as the common formula $A_mB_n$, where *A* represents the hydride-forming metals such as rare earth metals, alkaline earth metals or first column of transition metals like Zr or Ti and *B* represents non-hydride-forming metals such as transition elements. The intermetallic hydrides show reduced thermodynamic stability compare to the pure $AH_m$ because of the existence of non-hydride-forming metals *B* at ambient conditions, but low hydrogen storage capacity because of the inherent crystal structure and limited cell volume, relative to pure metals [54]. It has been suggested that the enthalpy of formation for the hydride of an intermetallic compound $AB_x$, can be estimated from

$$\Delta H_{ABxH(m+n)} \approx \Delta H_{AHm} + \Delta H_{BxHn} - \Delta H_{ABx}$$

There are numerous families of intermetallic compounds, including $AB_5$ (*e.g.*, $LaNi_5$), $AB_{3-4}$ (*e.g.*, $PuNi_3$, $Y_2Ni_7$), $AB_2$ (*e.g.*, $ZrV_2$), *AB* (*e.g.*, TiFe, ZrNi), $A_2B$ (*e.g.*, $Ti_2Ni$, $Mg_2Ni$).

Rare earth-based intermetallic compounds have been developed as the most promising materials used for negative materials of nickel-metal hydride (Ni-*M*H) batteries and hydrogen storage, including the widely used and well-explored $RM_5$-type rare earth-based alloys and $RM_{3-3.8}$ type rare earth-magnesium-based alloys. Specifically, hydride forming $LaNi_5$-based $RM_5$-type alloys (*R* = Rare earth, *M* = Transition metals) show excellent performance as chemical reversible storage of hydrogen with capacity ~ 1.5 wt.% [59]. (*R*, Mg)Ni-based $RM_x$ alloys ($3 \leq x \leq 3.8$) with stacking structures have been developed for Ni-*M*H batteries with higher hydrogen absorption capacity ~1.8 wt.% [59]. $RM_2$-type alloys with the *C*15 Laves phase structure possess more tetrahedral sites than $RM_5$ and $RM_x$ ($3 \leq x \leq 3.8$) alloys to accommodate hydrogen atoms, thus higher hydrogen absorption capacity [116].

Even if $RM_2$-type alloys suffer from hydrogen-induced amorphization (HIA) or disproportionation (HID), efforts to explore these systems as candidate for H-storage have been made. In this chapter, the structural and hydrogen sorption properties of rare earth-based $RM_2$-type alloys with *C*15 Laves phase structure will be described. In addition, the studies on the mechanism of HIA, structural stability upon hydrogenation and cycling properties will be reviewed. In the end, pseudo-binary $RM_2$-type compounds are given to discuss the possibility to improve structural stability by partially substituting *A* or *B* site elements using the third element.

## 2.2 Characteristics of rare earth-based $AB_2$-type intermetallic compounds

### 2.2.1 Crystal structure

#### 2.2.1.1 $MgCu_2$-type *C*15 Laves phase structure

Intermetallic compounds $RM_2$ ($R$ = rare earth, $M$ = transition metals), especially for the compounds with $M$ metals of Fe, Co, Ru, Rh, Ir and Pt, often crystallize in $MgCu_2$-type structure (space group: $Fd\bar{3}m$) [117], which can also be described as *C*15 Laves phase structure (Figure 2.1), see Table 2.1.

Table 2.1 Binary $RM_2$ intermetallic compounds with $MgCu_2$-type *C*15 Laves phase structure (All the binary intermetallic compounds are from Inorganic Crystal Structure Database (ICSD): https://icsd.products.fiz-karlsruhe.de/en).

| *R* (rare earth) | *M* (transition metals between group 7 and group 10) | | |
|---|---|---|---|
| | Mn, Fe, Co, Ni (Period 4) | Tc, Ru, Rh, Pd (Period 5) | Re, Os, Ir, Pt (Period 6) |
| La | $LaCo_2$ | $LaRu_2$, $LaRh_2$ | $LaOs_2$, $LaIr_2$, $LaPt_2$ |
| Ce | $CeFe_2$, $CeCo_2$ | $CeRu_2$, $CeRh_2$ | $CeOs_2$, $CeIr_2$, $CePt_2$ |
| Pr | $PrFe_2$, $PrCo_2$ | $PrRu_2$, $PrRh_2$, | $PrOs_2$ (*C*15/*C*14) $PrIr_2$, $PrPt_2$, |
| Nd | $NdFe_2$, $NdCo_2$ | $NdRu_2$, $NdRh_2$ | $NdIr_2$, $NdPt_2$ |
| Sm | $SmMn_2$ (*C*15/*C*14) $SmFe_2$, $SmCo_2$ | $SmRu_2$, $SmRh_2$ | $SmIr_2$, $SmPt_2$ |
| Gd | $GdMn_2$, $GdFe_2$, $GdCo_2$ | $GdRu_2$ (*C*15/*C*14) $GdRh_2$ | $GdIr_2$, $GdPt_2$ |
| Y | $YMn_2$, $YFe_2$, $YCo_2$ | $YRh_2$ | $YIr_2$, $YPt_2$ |
| Tb | $TbMn_2$, $TbFe_2$, $TbCo_2$ | $TbRh_2$ | $TbIr_2$, $TbPt_2$ |
| Dy | $DyMn_2$, $DyFe_2$, $DyCo_2$ | $DyRh_2$ | $DyIr_2$, $DyPt_2$ |
| Ho | $HoMn_2$ (*C*15/*C*14) $HoFe_2$, $HoCo_2$ | $HoRh_2$ | $HoIr_2$, $HoPt_2$ |
| Er | $ErFe_2$, $ErCo_2$ | $ErRh_2$ | $ErIr_2$, $ErPt_2$ |
| Tm | $TmFe_2$, $TmCo_2$ | $TmRh_2$ | $TmIr_2$, $TmPt_2$ |
| Yb | $YbCo_2$ | $YbRh_2$ | $YbIr_2$, $YbPt_2$ |
| Lu | $LuFe_2$ (*C*15/*C*14/*C*36) $LuCo_2$ | $LuRh_2$ | $LuIr_2$ |
| Sc | $ScFe_2$ (*C*15/*C*14/*C*36) $ScCo_2$, $ScNi_2$ | $ScRh_2$ | $ScIr_2$ |

$AB_2$ *C*15 Laves phase belongs to the class of Frank-Kasper phases showing topologically tetrahedrally close-packed (*t.c.p.*) structures in which all interstices are exclusively tetrahedral sites [118]. *C*15 Laves phase structure provides highest packing density of 0.710 with the atomic radius ratio $r_A/r_B = (3/2)^{\frac{1}{2}} \approx 1.225$ in the hard spheres model. As shown in Figure 2.1 (a) and (b), each $A$ atom (Wyckoff site 8*b*) lies on a diamond cubic lattice surrounding by 12 $B$

atoms (Wyckoff site 16*c*) at the corners of a polyhedron and 4 *A* atoms at the vertices of a tetrahedron. Each *B* atom lies at the joint point connecting two triangles combined with 3 nearest *B* atoms respectively, surrounding by 6 *A* atoms at the vertices of a nonplanar regular hexagon. There are twelve *A*2*B*2 (Wyckoff site 96*g*), four *A*1*B*3 (Wyckoff site 32*e*) and one *B*4 (Wyckoff site 8*b*) tetrahedral interstices sites per cell could accommodate hydrogen atoms, among which *A*2*B*2 holes have the biggest geometric size and favorite environment (with two *A* atoms) for hydrogen occupation, and then in *A*1*B*3, last in *B*4 sites, which give a hydride $AB_2H_{17}$ in the case all sites fully occupied.

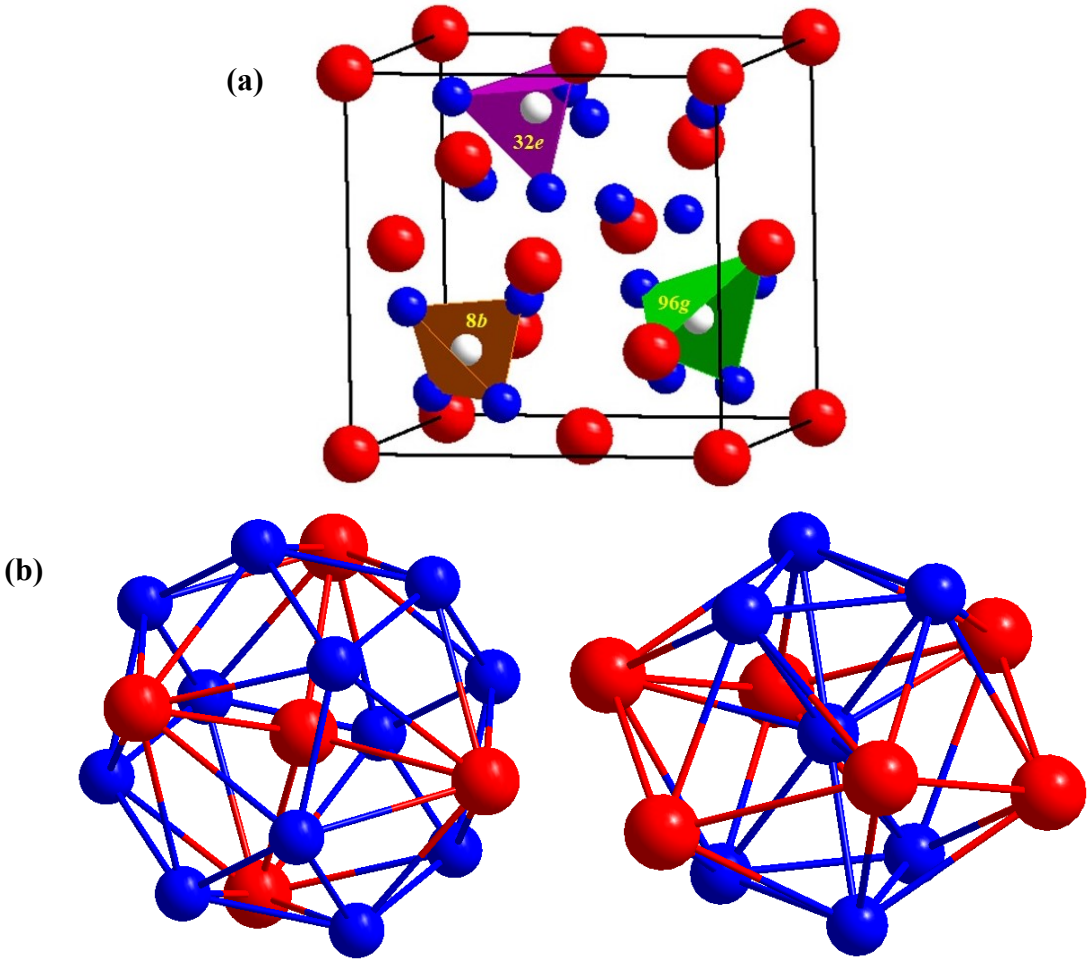


Figure 2.1 The structural model of *C*15 Laves phase structure (a) showing a high dense packing of the hard spheres and all constructed tetrahedra. *A* (red) atom lying on 8*b* site and *B* (blue) atom lying on 16*c* site. Possible site for hydrogen atoms is shown as small white balls which are in the three types tetrahedral interstices: *A*2*B*2 (96*g*, green), *AB*3 (32*e*, magenta) and *B*4 (8*b*, brown). The nearest atoms surrounding each *A* and *B* atom (b).

### 2.2.1.2 $TmNi_2$-type superstructure

$RNi_2$ (*R* = rare earth) belongs to $RM_2$ Laves phase family, recent works show that they do not crystallize in the *C*15 Laves structure but either in a tetragonal $La_7Ni_{16}$-type or cubic $TmNi_2$-type structure, see Table 2.2. Both structures can be described as superstructure of *C*15 with ordered *A*-site vacancies, which allow relaxing the micro strains caused by the large atomic

radius ratio ($r_{La}/r_{Ni} = 1.51, r_{Ce}/r_{Ni} = 1.45$). $La_7Ni_{16}$ can be considered as superstructure of *C*15 by doubling *c* and ordering La-site vacancies [119,120]. Here we are more interested by the cubic $TmNi_2$-type which can be described as a superstructure with *A*:*B* stoichiometry 0.95:2, doubling of the lattice parameter *a* of *C*15, and lower symmetric space group $F\bar{4}3m$. As shown in Figure 2.2, the superstructure is attributed to the formation of ordered *R* vacancies on the 4*a* sites. The type and number of tetrahedral sites in the superstructure can be determined considering *C*15 structure: one 96*g* site in the *C*15 structure leads to eight 48*h* and four 96*i* sites in the superstructure, simultaneously one 32*e* site leads to four 16*e* and four 48*h* sites, one 8*b* site leads to four 4*c* sites, four 4*d* sites and two 16*e* sites.

Table 2.2 Binary rare earth intermetallic compounds $RNi_2$ with superstructure.

| Compounds | Compositions* | Superstructure | Lattice parameter (*Å*)* | Space group |
|---|---|---|---|---|
| $La_{1-x}Ni_2$ | $LaNi_{2.28}$ | Tetragonal $La_7Ni_{16}$-type | *a* = 7.355 (1)<br>*b* = 7.355 (1)<br>*c* = 14.51 (1) | $I\bar{4}2m$ |
| $R_{1-x}Ni_2$ | $Ce_{0.950}Ni_2$ | Cubic | *a* = 14.407 (1) | $F\bar{4}3m$ |
| | $Pr_{0.945}Ni_2$ | $TmNi_2$-type | *a* = 14.574 (1) | |
| | $Nd_{0.947}Ni_2$ | | *a* = 14.532 (1) | |
| | $Gd_{0.946}Ni_2$ | | *a* = 14.399 (1) | |
| | $Y_{0.950}Ni_2$ | | *a* = 14.350 (4) | |
| | $Tb_{0.956}Ni_2$ | | *a* = 14.342 (1) | |
| | $Dy_{0.957}Ni_2$ | | *a* = 14.282 (1) | |
| | $Ho_{0.963}Ni_2$ | | *a* = 14.259 (1) | |
| | $Er_{0.980}Ni_2$ | | *a* = 14.238 (1) | |
| | $TmNi_2$ | | *a* = 14.156 (6) | |
| | $LuNi_2$ | | *a* = 14.145 (1) | |

* The defect compositions and lattice parameters of $R_{1-x}Ni_2$ compounds are from literatures [119,121–125], the compositions are not fixed but exist a variable range, as well as lattice parameters.

The superstructure was first determined in $TmNi_2$ compound by neutron and X-ray diffraction [121]. Then the superstructure in $YNi_2$ compound was observed by Latroche *et al* [126], they conclude that due to the large atomic radius ratio ($r_Y/r_{Ni} = 1.45$) of the $YNi_2$ the formation of Y vacancies allows stabilization of the structure and leads to the composition $Y_{0.95}Ni_2$. Meanwhile, most of the Y atoms are shifted weakly because of the vacancies (see the superstructure in Figure 2.2), leading to an increase of the average value of the distances between two yttrium from 3.109 Å (*C*15 structure) to 3.230 Å (superstructure) [126]. The subsequent *ab initio* studies of $Y_{1-x}Ni_2$ verified the experimental results [127]. As compare to the distances Y-Y in ideal *C*15-type $YNi_2$, in the superstructure, the distance between the vacancy site (4*a*) and its nearest Y atoms (16*e*) is markedly decreased, and distances Y-Y increase by various extents depending on how far from vacancy site they are. The shifts of all Ni atoms except the nearest Ni neighbors of the vacancy are much smaller than Y. As a result of the formation of vacancies, the symmetry is thus lowered, and the new atomic positions are described in the $F\bar{4}3m$ space group. The further studies of Latroche *et al*. [123] indicates that such superstructure widely exist in $RNi_2$ (*R* = Pr to Lu) compounds. However, with the decrease of the radius of *R* atoms, the quantity of ordered *R* vacancies on the 4*a* site decreases.

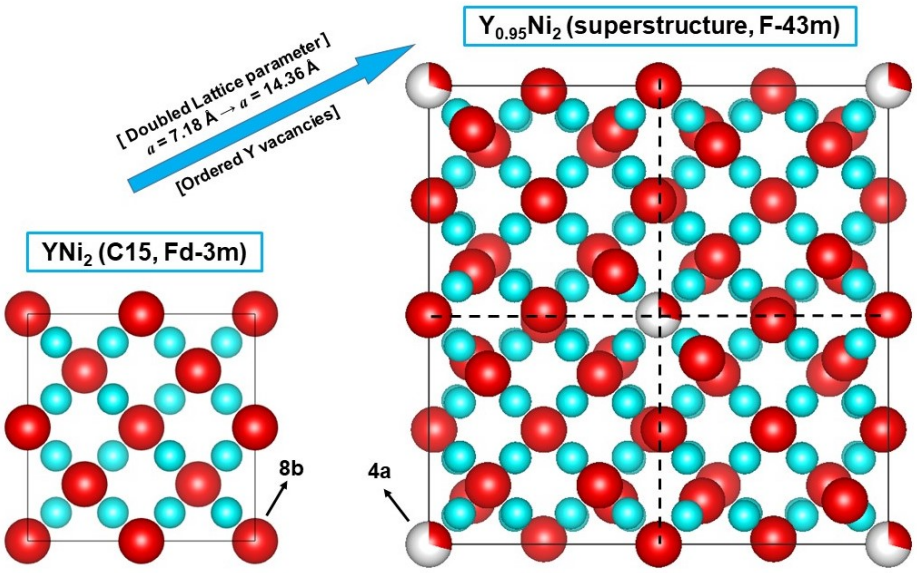


Figure 2.2 The structural models of *C*15 Laves phase structure formed in $YNi_2$ compound and superstructure formed in $Y_{0.95}Ni_2$ compound.

### 2.2.1.3 Other Laves phase structures

Several intermetallic compounds $RM_2$ (*R* = rare earth, *M* = Mn, Fe, Co, Ni) crystallize in $MgZn_2$- or $MgNi_2$-type hexagonal structures (space group: $P6_3/mmc$), which can also be described as *C*14 and *C*36 Laves phase structures respectively. The structural models have been shown in Figure 1.4. We also listed the rare earth and transition metals Mn, Fe, Co, Ni based binary compounds with *C*14 and *C*36 structures in Table 2.3. As compared to the binary compounds $RM_2$ (*R* = rare earth, *M* = Mn, Fe, Co, Ni) with *C*15 structure, the number of *C*14 compounds is limited, this is particular true for *C*36 compounds. Moreover, these compounds all in favor the constituent elements Mn and Fe, forming $RMn_2$ and $RFe_2$ with *C*14 or *C*36 structures.

Table 2.3 Binary $RM_2$ intermetallic compounds with *C*14 and *C*36 Laves phase structures (All the binary intermetallic compounds are from Inorganic Crystal Structure Database (ICSD): https://icsd.products.fiz-karlsruhe.de/en).

| *R* (rare earth) | *M* (Mn, Fe, Co, Ni) |
|---|---|
| Pr | $PrMn_2$ (*C*14) |
| Nd | $NdMn_2$ (*C*14) |
| Sm | $SmMn_2$ (*C*15/*C*14) |
| Ho | $HoMn_2$ (*C*15/*C*14) |
| Er | $ErMn_2$ (*C*14) |
| Tm | $TmMn_2$ (*C*14) |
| Yb | $YbMn_2$ (*C*14) |
| Lu | $LuMn_2$, $LuFe_2$ (*C*15/*C*14/*C*36) |
| Sc | $ScMn_2$, $ScFe_2$ (*C*15/*C*14/*C*36) |

*C*14- and *C*36-type $AB_2$ compounds are same to *C*15 belong to Friauf-Laves phase structures, in which one *A* atom is surrounded by 4 *A* atoms at the vertices of a tetrahedron, and 12 *B* atoms at the corners of a polyhedron [71]. They also belongs to a group of structural types in which all interstices are exclusively tetrahedral sites [118]. Atomic size factor and electron concentration are the two main factors affecting the formation of a particular type Laves phase structure: *C*15, *C*14 or *C*36. Here we compared the effects of atomic radius ratio and valence electron concentration on the formation of *C*14 and *C*15 Laves phase structures of $RMn_2$ (*R* = rare earth, Y, Sc) alloys. As shown in Figure 2.3, the structures change from *C*14 to *C*15 back to *C*14 as atomic sizes decrease from Pr to Sc. This structural changes between *C*14 and *C*15 agrees well with the reported $NbCr_2$-based alloys [128]. In the case of $RMn_2$, at low *e/a* region (*R* = Pr, Nd, Sm), the large $r_R/r_{Mn}$ favors the *C*14 structure formation rather than *C*15. Then, at high *e/a* region (*R* = Ho, Er, Tm, Lu), the large valent electron concentration determines the formation of *C*14 type Laves phase structure.

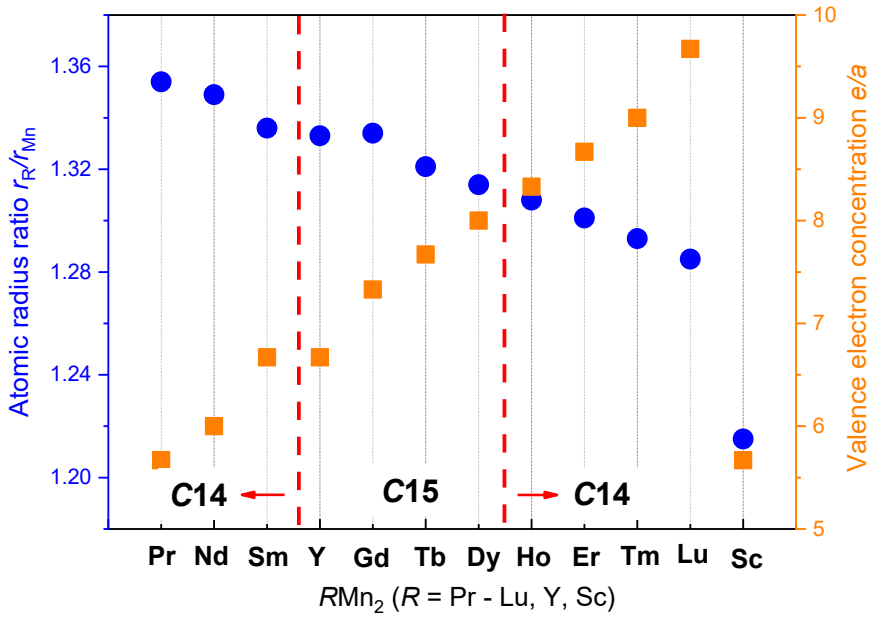


Figure 2.3 Effects of atomic radius ratio $r_R/r_{Mn}$ and valence electron concentration *e/a* on the formation of Laves phase structures in binary $RMn_2$ alloys.

## 2.2.2 Factors controlling structural stability

Considering the subject of $YNi_2$-related alloys in this thesis, I will concentrate on the factors affecting the structural stability of *C*15 type Laves phase structure.

From geometric view, the closest packing density of *C*15 Laves phase $AB_2$ structure is achieved for an ideal atomic radius ratio of $r_A/r_B \approx 1.225$. In reality, a large series alloys can form the *C*15 Laves phase structure with atomic radius ratio varying from 1.05 to 1.68, indicating the other factors such as electronegativity or valence electron concentration are also important [129,130].

#### 2.2.2.1 Indication of stability of the structure

In a multi-component system, the formation of one intermetallic compound means its free energy is lower than that of a mixture of these phases, *i.e.*, the compound is stable. Thus, the enthalpy of formation of intermetallic compounds gives an indication of the structure stability, the higher the enthalpy (more negative) the more stable the structure. Moreover, the enthalpy of formation is related to the bond energies in the compounds. However, for *C*15 $RM_2$ intermetallic compounds, the chemical bond is very complicated, covalent, metallic and ionic bonding may exist simultaneously [131,132], which may further affected by the intrinsic properties of rare earth and transition metals, such as atomic size and electronic structure.

On the contrary, the decomposition temperature reflects the energy required to break the metal-metal bonds, *i.e.*, the stronger the strength of the atomic bonds, the higher decomposition temperature needed, thus more stable the compound. Therefore, the decomposition temperature could be another indication of the structural stability. In the following section, the formation enthalpy, the decomposition temperature is used indicating the structure stability.

#### 2.2.2.2 Atomic size

Among the geometric reasons in affecting the structural stability of *C*15 Laves phase, atomic size ratio of *A* and *B* atoms could be the most important factor for determining the structural stability. For the case of $RM_2$ alloys with rare earth as *A* side atoms and transition metals (Fe, Mn, Co, Ni, Cu) as *B* side atoms, the size ratios are more frequently above 1.225 due to the relative larger *R* atoms. In fact, the atom radii in Laves phase differ from those of pure metals, thus the ability of atoms to contract or expand to approach the idea size ratio is a major factor to control the structure formation and stability. In *C*15-type $RM_2$ compounds, the atomic radius of *R* atoms is contracted while ones of *M* atoms are expanded.

Statistic studies [131,132] have shown that the Laves phases with highest enthalpy of formation have the ideal atom radii ration 1.225, which indicates that most stable (with most negative enthalpy of formation) Laves phase found have the ideal $r_A/r_B$ value. Authors explain it by the fact that as this value left the ideal one, the atomic size adjustment (compression or expansion) is needed for the structure formation, which may introduce the elastic strain energy and reduce the enthalpy of formation.

Another study clearly shows (see Figure 2.4), that for $RM_2$ Laves phases compounds with same *M* element (Fe, Co or Ni), the structural stability increases from La to Lu due to the "lanthanide contraction" caused by atom-radii decrease [133]. These results show that the atomic size is a dominant factor to control the structural stability.

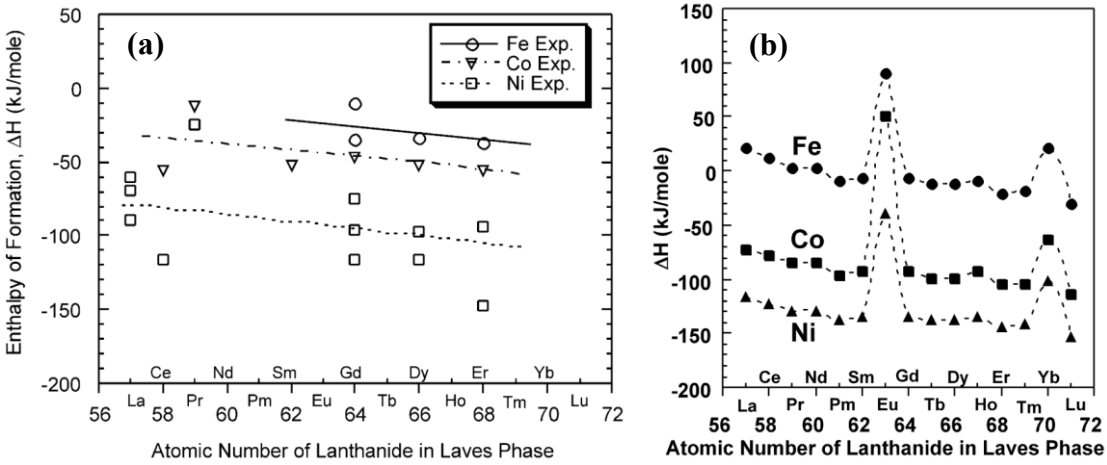


Figure 2.4 The experimental (a) and predicted (b) enthalpy for $RM_2$ intermetallic compounds as a function of lanthanide atomic number [132].

### 2.2.2.3 Electronic concentrations

Besides geometric reasons, the valence electron concentration (VEC) *e/a* (stands for number of valence electron per atom) also plays an important role in determining the structural stability of Laves phases. It was shown that for the same $r_A/r_B$ ration, the structure stability increases with increasing of average electron concentration for $RM_2$ compounds. In the case of same *M* element, the increase of stability from La to Lu was attributed to the geometric effect, as the electronic influence could be neglected. The studies show, for the case of same *R* element (taking Y, for example, see Figure 2.5), the stability of $RM_2$ increases from Mn, Fe, Co to Ni [134], and the geometric effect plays a reverse role. As the atomic radii decrease from Mn to Ni, the $r_A/r_B$ ration increases could decrease the structure stability. In fact, here the electronic influence is more important, the increase of the structure stability from Mn to Ni should be a result of the increased electron concentration from Mn to Ni [131,132].

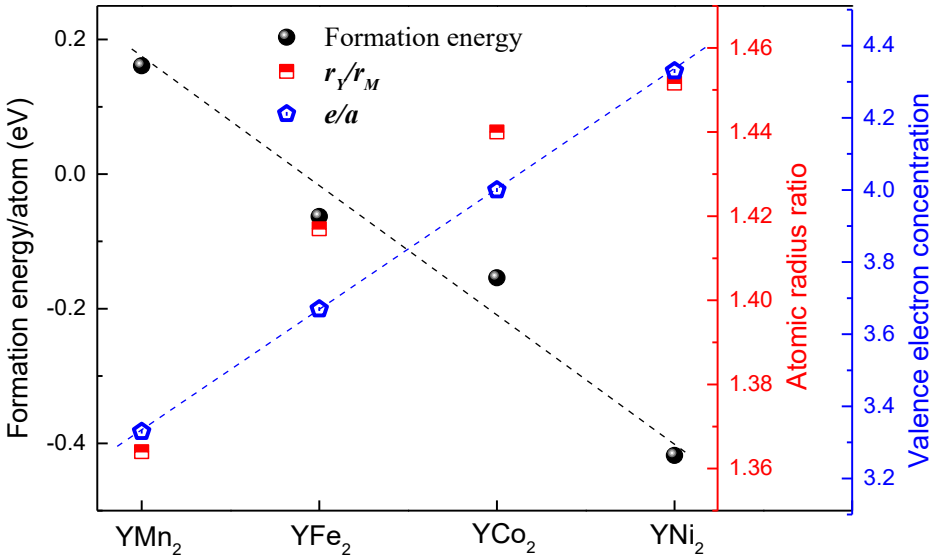


Figure 2.5 The formation energy per atom, atomic radius ratio and valence electron concentration of $YM_2$ (*M* = Mn, Fe, Co, Ni) compounds. The atomic radius of Y, Mn, Fe, Co, Ni are from literature [135,136].

### 2.2.2.4 Vacancy effect on the structural stability

Initial reports on intermetallic binary compounds $RM_2$ indicated that they crystallize in the *C*15 Laves phase structure. It was recently shown that $RNi_2$ compounds (*R* = Y, Ce to Lu) crystalizes in a superstructure with doubling of the cubic lattice parameter and defect composition $R_{0.95}Ni_2$. The formation of such superstructure is attributed to the formation of ordered *R* vacancies on the 4*a* sites in *C*15 Laves phase structure, which can be interpreted in terms of structural relaxation in order to accommodate the large atomic radii of lanthanides. V Paul-Boncour *et al*. [124] reported the correlation between the structural stability of $R_{1-x}Ni_2$ Laves phase and *R* vacancies. The larger atomic radii of the rare earth elements, the more vacancies are needed to release the stress on the *R* atoms, to stabilize the structure. The superstructure is more stable than *C*15 structure because of the *R* vacancies, especially for the light rare earth and Y [125,127]. As shown in the Figure 2.6, the structural transition from superstructure to *C*15 structure containing disordered vacancies requires higher temperatures and pressures for La and Y than for heavier rare earth [137], which further proves the inevitability of the formation of superstructure. But when going from light to heavy rare earth element, the vacancies effect on structural stability becomes weak. Take $Er_{0.98}Ni_2$ and $LuNi_2$, for example, the number of *R* vacancies is very limited [123], their structure is on the verge of superstructure. Indeed, the vacancies effect is largely relied on the atomic size. If we can see that the existence of *R*-vacancies plays a role to stabilize the structure, the mechanism of the vacancy formation remains unknown.

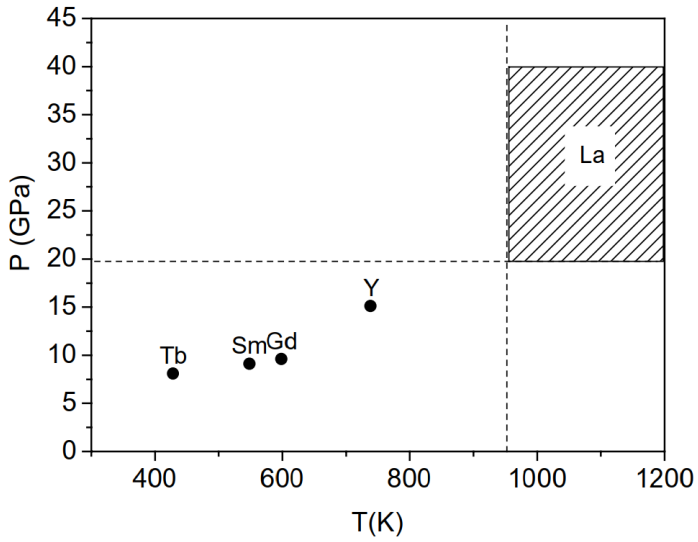


Figure 2.6 The required pressures and temperatures for the structural transition of $R_{1-x}Ni_2$ from superstructure with ordered vacancy to *C*15 structure with disordered vacancy [137,124].

## 2.3 Hydrogenation properties of binary $RM_2$ compounds

### 2.3.1 Hydrogen absorption capacity

$AB_2$-type alloys with $C15$ Laves phase structure possess more tetrahedral sites than $AB_5$ and $AB_n$ ($3 \leq n \leq 3.8$) to accommodate hydrogen atoms, thus higher hydrogen absorption capacity is foreseen [138]. There are 17 tetrahedral sites per formula unit in $C15$ Laves phase structure (12 $A2B2$, 4 $A1B3$ and 1 $B4$ sites), a hydride of $AB_2H_{17}$ could be formed if they are fully occupied [71]. In fact, there is a minimum distance of H-H of 2.1 Å due to their impulsive interaction [139]. For the $AB_2H_x$, the distance between the centers of tetrahedral interstices with a face in common are much shorter (≤ 1.6 Å), so hydrogen can only occupy the tetrahedral interstices without sharing face (≥ 2.0 Å). By doing so, Shoemaker obtained a maximum occupancy of 6 hydrogen atoms per $AB_2$ unit in $C15$ Laves phase [71]. The structure of the maximum deuteride $ZrV_2D_6$ has been refined by neutron diffraction, which crystalizes in a orthorhombic structure (space group *Pnma*) with three D atoms occupying Zr2V2 and three D atoms occupying ZrV3 tetrahedral interstices orderly [140]. However, the capacity approaching 6 hydrogen atoms per formula normally requires low-temperature terms ($ZrV_2D_6$: hydrogenation at pressure of 1 bar in the temperature range 110 K - 210 K), and exhibits various structural evolution. Indeed, under modest conditions, it rarely exceeds 5 hydrogen atoms [72].

#### 2.3.1.1 $R$Mn₂ intermetallic compounds

$R$Mn$_2$ compounds crystallize in the $C15$ $MgCu_2$-type structure ($R$ = Y, Gd, Tb, Dy, Ho) or $C14$ $MgZn_2$-type structure ($R$ = Pr, Nd, Sm, Er, Tm and Lu) [141–144]. These compounds are known for their large hydrogen absorption capacity of around 4.5 H/f.u., as well as various structural changes upon hydrogen absorption and desorption. For example, $YMn_2$-H system exhibits no well-defined plateau region in the pressure-composition isotherms for hydrogen concentration $0 < x < 3.0$ H/f.u. [145]. M. Latroche and V. Paul-Boncour reported the detailed crystallographic information of the hydrides and deuterides of $YMn_2$ [146,147]. The $C15$ cubic structure remains preserved as hydrogen concentration up to 3.5 H/f.u., whereas a rhombohedral distortion (space group $R\bar{3}m$) can be observed for fully charged $YMn_2H_{4.3}$ at room temperature [146]. The neutron diffraction experiments indicate that as deuterium concentration ranging from 1 to 3.4 D/f.u., only $A2B2$-type sites are occupied by deuterium. The minimum $d_{D\text{-}D}$ distance for the formation of cubic $YMn_2D_{3.4}$ should be located in the range 2.11 Å < $d_{D\text{-}D}$ ≤ 2.14 Å, thus for larger deuterium concentration a distorted phase with rhombohedral structure precipitates to satisfy the minimum distance between deuterium atoms [147]. Structural distortions are however observed below room temperature for $x < 1.2$ and can be related to both magnetic and deuterium order [148]. Furthermore, upon heating $YMn_2D_{4.5}$ to 127 °C, the deuteride exhibits a transition from rhombohedral to cubic structure without distinct deuterium desorption [149]. For now, the hydrogen desorption properties and structural evolution of $YMn_2H(D)_x$ are still unclear.

Further, using high deuterium pressure (1.7 kbar) at 200 ℃, V. Paul-Boncour *et al.* [150,151] succeeded to form and study a new complex deuteride $YMn_2D_6$ (3 wt.%), which shows the largest value for such compound [71]. As shown in Figure 2.7, $YMn_2D_6$ crystalizes in a $K_2PtCl_6$-type structure ($Fm\bar{3}m$), where both Y and half of the Mn atoms occupy statistically the 8*c* site, the other Mn atoms are in the 4*a* site with 6 D (24*e*) atoms surrounded. However, as compared to the parent compound $YMn_2$ and metallic hydride $YMn_2H_{4.5}$, the new structure of $YMn_2D_6$ is a complete reorganization of the metallic framework and the Mn-D bands are covalent banding, which is out of the frame of an interstitial metallic hydride.

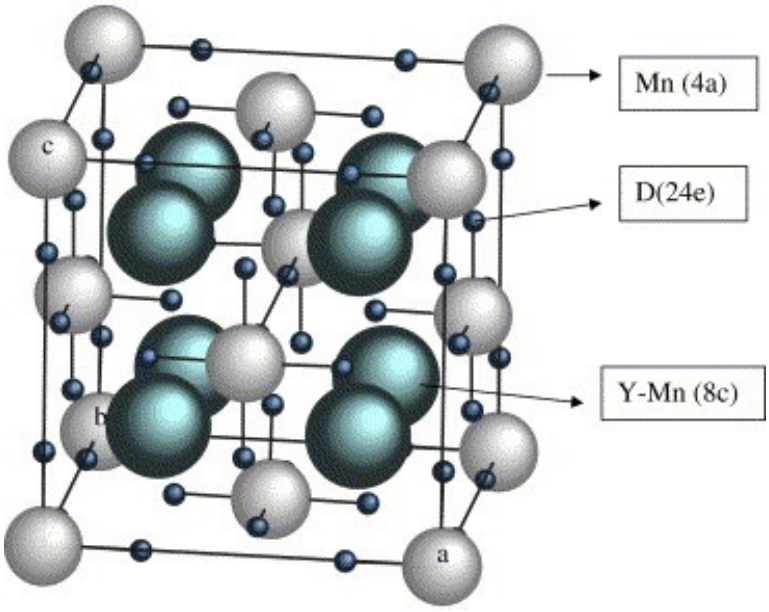


Figure 2.7 The structural model of $YMn_2D_6$ [151].

For the other $RMn_2$ ($R$ = Gd, Dy, Ho, Tb) compounds, similar structural transformation upon hydrogen (deuterium) absorption was observed. The *C*15 cubic structure was preserved at low hydrogen concentration (≤ 3.5 H/f.u.) and 27 ℃ and the same rhombohedral distortion was found for the fully charged $RMn_2H_{4.3\text{-}4.5}$ [152–156]. Complex structural and magnetic phase diagram are observed below RT.

For the $RMn_2$ ($R$ = Pr, Nd, Sm, Er, Tm, Lu) compounds with *C*14 structure, they contain the same *A*2*B*2, *A*1*B*3 and *B*4 tetrahedral sites, showing the similar theoretical maximum hydrogen content ($AB_2H_6$) with *C*15 structure [71]. Taking $ErMn_2$ for example, $ErMn_2D_6$ crystallizes in a $K_2PtCl_6$ type structure [157], which is isostructural to $YMn_2D_6$ and out of the frame of an interstitial metallic hydride [151]. At low hydrogen concentration, as shown in Figure 2.8a, at room temperature $ErMn_2$ absorbs hydrogen by forming two hydrides: $ErMn_2H_{3.4}$ (~ 1.2 wt.%) and $ErMn_2H_{4.8}$ (~ 1.7 wt.%) respectively. $ErMn_2H_{4.8}$ can be reversibly dehydrogenated to $ErMn_2H_{3.4}$ but the latter is irreversible at 25 ℃. Meanwhile, the irreversible hydride retains the hexagonal symmetry of the unit cell (Figure 2.8b) [158].

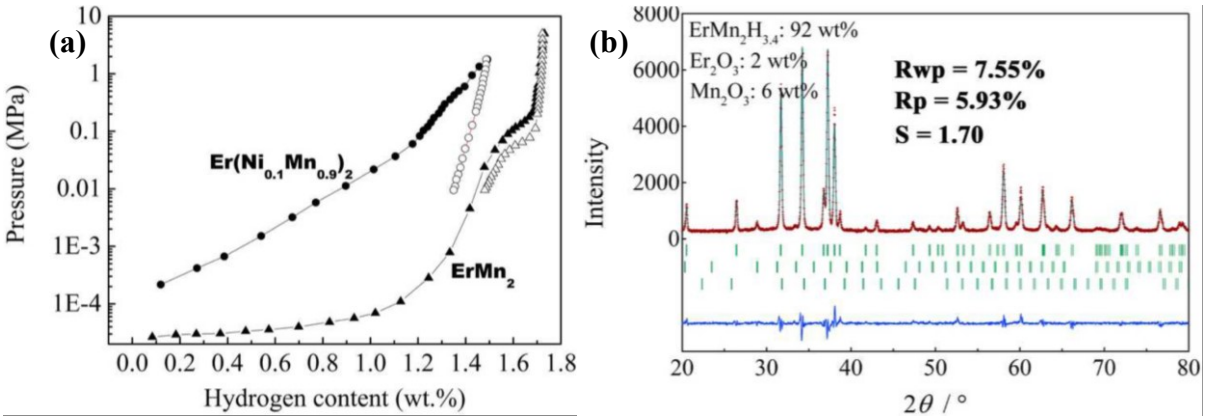


Figure 2.8 PCI curves of $ErMn_2$ upon the first hydrogen absorption and desorption cycle at 25 ℃ (a) and its XRD pattern after the PCI measurement (b) [158].

### 2.3.1.2 *R*Fe$_2$ intermetallic compounds

The study of *R*Fe$_2$ (*R* = Y, Ce, Sm, Gd, Tb, Dy, Ho and Er) intermetallic compounds has raised interest for their ability of forming crystalline hydrides with hydrogen concentrations up to 5 H/f.u.. *R*Fe$_2$ compounds all crystallize in the $MgCu_2$-type *C*15 Laves phase structure, and their hydrides with hydrogen concentrations varying from 1.2 to 5 H/f.u. can be formed without amorphization under appropriate conditions of pressure and temperature. It should be noted that a variety of crystal structures derived from *C*15 one can be observed at different hydrogen concentrations. Amorphization of *R*Fe$_2$ hydrides was also studied generally by DSC [159–162].

Among various *R*Fe$_2$ alloys, the most widely studied alloys are $YFe_2$ and $ErFe_2$, which form several hydrides or deuterides with different crystal structures as hydrogen concentration increases from 1.3 to 5 H(D)/mol [163–168]. As shown in Figure 2.9, the PCI curves measured at 100 ℃, 135 ℃ and 200 ℃ describe the several plateaus, which correspond to the formations of different deuteride phases. For deuterium content below 2 D/mol, the deuterides display various structural distortions from the ideal *C*15 cubic structure with additional superstructure due to long range ordering of H(D) atoms. $YFe_2D_{1.3}$ crystallizes in the tetragonal $I\bar{4}$ space group with $a$ =11.985 Å and $c$ = 7.622 Å, $YFe_2D_{1.75}$ in the cubic $I\bar{4}3m$ space group with $a$ = 15.336 Å and $YFe_2D_{1.9}$ in a tetragonal structure with $a$ = 12.145 Å and $c$ =23.064 Å [164]. As deuterium content varies between 2.5 and 2.9 D/mol, the cubic *C*15 structure can be observed [163,164]. For large deuterium content of 3.3 to 5 D/mol, single phase rhombohedral deuterides can be obtained [165,166].

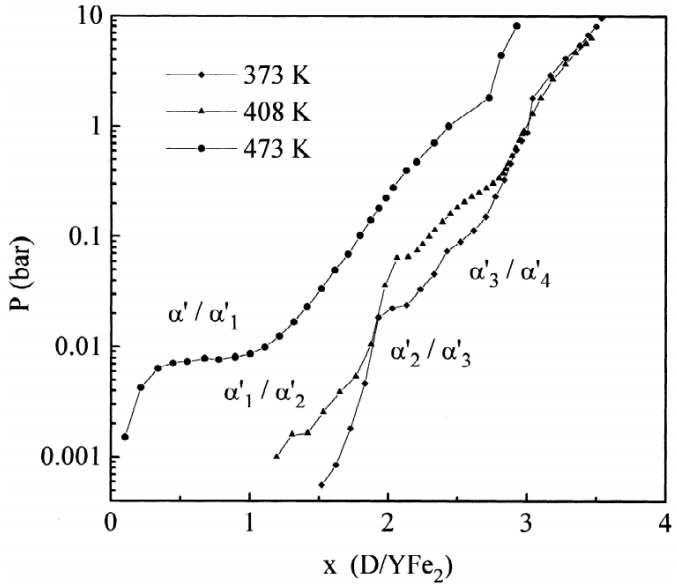


Figure 2.9 Pressure-Composition Isotherms of $YFe_2$ measures at 100 ℃, 135 ℃ and 200 ℃ [163].

Similar structural evolution can also be observed from $ErFe_2$-H(D) system. K. Shashikala *et al* reported the pressure-composition isotherm (PCI) and X-ray diffraction studies of $ErFe_2$-H system [169]. As shown in Figure 2.10, upon hydrogenation at room temperature, $ErFe_2$ exhibits a multi-plateau characteristic, corresponding to the hydrides with various structures formed at different hydrogen concentration. $ErFe_2H_x$ retains the cubic structure of the parent compound as hydrogen concentration $x < 3.2$, then they found the rhombohedral distortion in the range of $3.2 < x < 3.6$, corresponding to the steep slope on the PCI curve. For higher hydrogen concentration $x \geq 4.0$, after a temporary restoration of cubic structure for $x = 4.0$, a new hydride with rhombohedral structure was formed for $x > 4.0$. Indeed, the maximum capacity can reach to 5 H/f.u. for both $YFe_2$ and $ErFe_2$ compounds, and the hydrides crystallize in the same type of orthorhombic structure which was solved by neutron diffraction [170]. The formation of saturated hydrides and distorted structures are mainly attribute to the partial filling of hydrogen in all types of available interstitial sites (*A*2*B*2, *A*1*B*3, *B*4). The filling of *B*4 sites requires a very high hydrogen pressure (hydrogenation at 100 ℃ under 1.5 GPa $H_2$) [166].

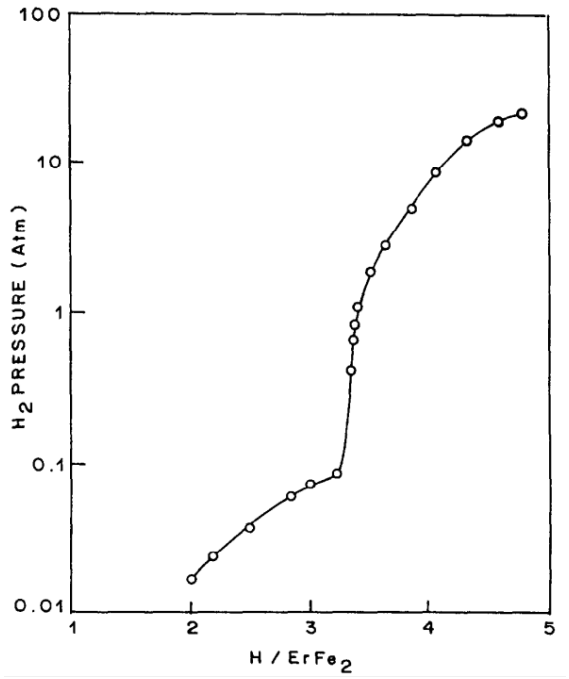


Figure 2.10 Pressure-Composition Isotherms of $ErFe_2$ measured at 25 ℃ [169].

As referred to the reversibility, $YFe_2$ [171] exhibits worse structural stability than $ErFe_2$ [172] upon hydrogen absorption and desorption cycles. $YFe_2$ could absorb 2.9 H/f.u. for the $1^{st}$ hydrogenation at 100 ℃, whereas after the hydrogen desorption for 2 h under vacuum and 300 ℃, only 0.9 H/f.u. can be obtained for the $2^{nd}$ cycle. The prominent capacity decay is attributed to the hydrogen-induced disproportionation (HID), which can be interpreted the formation of $YH_2$ and Fe after hydrogen absorption and desorption [171]. Nevertheless, a thermal desorption study showed that it is possible to desorb fully $YFe_2D_x$ ($x$ = 1.3 to 4.2) down to $YFe_2$ in several steps due to the progressive desorption of all the intermediate hydrides [173]. This indicates, that the amorphization can be avoided, if the desorption conditions are controlled. For $ErFe_2$, the hydrogen absorption capacity decreases gradually with the cycle numbers, from the initial capacity 4.0 H/f.u. to 1.67 H/f.u., upon 50 cycles of hydrogenation at 30 ℃ and dehydriding at 300 ℃ in vacuum, showing a more stable structure than $YFe_2$.

Besides the $R$Fe$_2$ compounds with $C$15 structure, $LuFe_2$ and $ScFe_2$ compounds can also crystallize in the hexagonal $C$14 or $C$36 type Laves phase structures. For no reported hydrogen sorption behaviors of $LuFe_2$ compound, here we concentrate on $ScFe_2$ compound. $ScFe_2$ crystalizes in $MgZn_2$-type ($C$14) structure below 1200 ℃, and in $MgNi_2$-type ($C$36) structure at high temperature [174]. The PCI curve of $C$14 type $ScFe_2$ measured at 20 ℃ is shown in Figure 2.11a, $ScFe_2$ could absorb hydrogen up to 3 H/f.u. and exhibits a plateau extending to 2 H/f.u. at 0.006 MPa [175]. $C$36 type $ScFe_2$ could also rapidly absorb hydrogen at a pressure of 6 MPa and room temperature, forming the hydride $ScFe_2H_3$ [176]. Furthermore, as shown in Figure 2.11b, the almost entirely hydrogen desorption since at 50 ℃ can be observed. However, the hydrogen desorption pressures are very low ($ScFe_2H_{1.4} \rightarrow ScFe_2H_{0.8}$: $1.3 \times 10^5 Pa \rightarrow$

$1.1 \times 10^5 Pa$). Consequently, the hexagonal *C*14 or *C*36 type $ScFe_2$ compounds show a stable structure upon hydrogen absorption and desorption, whereas the hydrogen content is limited and the equilibrium pressures are very low.

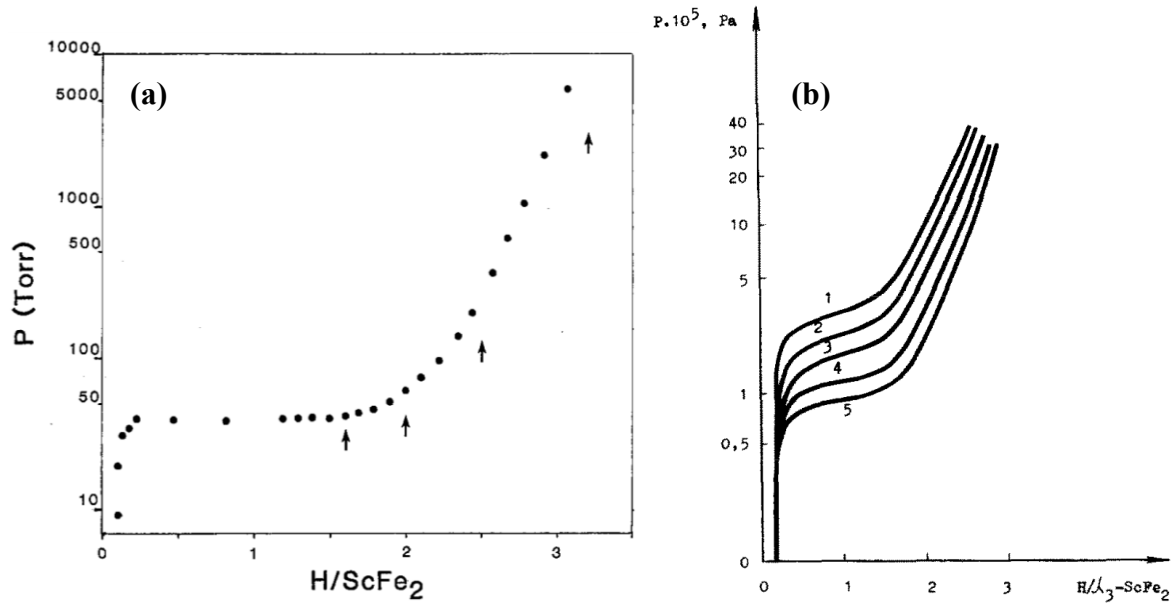


Figure 2.11 PCI curve of $ScFe_2$ (*C*14) measured at 20 ℃ (a) and the desorption isotherms of $ScFe_2$ (*C*36) at 90 ℃ (1), 80 ℃ (2), 70 ℃ (3), 60 ℃ (4), 50 ℃ (5) (b).

### 2.3.1.3 *R*$Co_2$ intermetallic compounds

*R*$Co_2$ (*R* = Y, La, Pr, Nd, Gd, Tb, Ho, Er) intermetallic compounds with $MgCu_2$-type *C*15 structure can absorb hydrogen up to 3.0 and 4.0 H/f.u. [177]. $NdCo_2H_{3.8}$, $HoCo_2H_{3.6}$, $ErCo_2H_{3.5}$ preserved the starting structure with an expanded lattice (29.5%, 23.5%, 23.1%, respectively), whereas the hydrides $YCo_2H_{3.6}$, $PrCo_2H_{4.0}$, $TbCo_2H_{3.3}$ exhibit a primitive cubic structure but with a doubled lattice parameter [177]. Bigger deformation occurs in $LaCo_2H_{3.8}$ and $GdCo_2H_{3.9}$ that an orthorhombic structure was formed. A detailed studies of $YCo_2$ alloy shows that the first hydride can be obtained as hydrogen concentration ranges from 0 to 0.3 H/mol and 1.5 to 3.5 H/mol for the second one [178,179]. In addition, $SmCo_2$ can absorb hydrogen around 4 H/f.u. at 40 ℃ under 0.1 MPa hydrogen pressure, forming a crystalline *C*14-type hydride [180]. If high hydrogen pressure or hydrogenation temperature were imposed on the formed hydrides, amorphous hydrides will appear and replace the crystalline one [181].

### 2.3.1.4 *R*$Ni_2$ intermetallic compounds

Almost all *R*$Ni_2$ (*R* = Y, La, Ce, Pr, Sm, Gd, Tb, Dy, Ho, and Er) compounds show amorphization upon hydrogen absorption [182]. The hydrogenation properties of $YNi_2$ were firstly studied by Van Essen and Buschow [183]. $YNi_2H_{3.6}$ (50 ℃, under 10 MPa $H_2$) crystallizes in *C*15 structure, and a cell volume expansion of 17.7% has been observed. Our recent work [184] about $YNi_2$ alloy shows the similar capacity of 3.8 H/f.u., but exhaustive amorphous hydride was observed upon hydrogenation under 10 MPa at 200 ℃. Further, $ErNi_2$

alloy can absorb hydrogen to form a crystalline hydride $ErNi_2H_3$ at room temperature under 0.12 MPa hydrogen pressure [185]. However, according to the XRD patterns exhibited in the recent studies of $ErNi_2$ hydrides [186], the markedly broadened Bragg peaks of $ErNi_2H_{3.07}$ herald the impending occurrence of formation of amorphous hydrides once hydrogen concentration increases.

For *R* = La and Ce, the intensity of Bragg peaks of $LaNi_{2.18}$ and $CeNi_{2.16}$ (cubic *C*15-type structure with disordered vacancies) decreases regularly as hydrogen concentration increases to 3.5 H/f.u., and beyond this value total amorphization occurs [119]. Similar hydrogen absorption capacity and amorphous hydrides were also observed for $Nd_{0.95}Ni_2$, $Tb_{0.95}Ni_2$ and $Er_{0.98}Ni_2$ compounds. The crystalline hydrides were obtained in a hydrogen concentration of 2.5 H/f.u., once hydrogen concentration increase to 3.35 H/f.u. and 3.23 H/f.u. respectively for $Nd_{0.95}Ni_2$ and $Tb_{0.95}Ni_2$ compounds, the formation of amorphous hydrides occurred [123].

### 2.3.2 HIA and the factors controlling HIA

As a known fact, hydrogenation is usually accompanied by a reduced crystal symmetry of the hydrides. As the hydrogen concentration approach the calculated maximum value gradually, large structural distortion normally occurs. When it comes to $RM_2$ compounds with *C*15 Laves phase structure, amorphous hydrides are often the final products upon hydrogenation. Hydrogen-induced amorphization (HIA) is the transformation from the crystalline to the amorphous state caused by hydrogenation, which has been observed in a variety of *C*15-type $RM_2$ intermetallic compounds.

The amorphization of $RNi_2$ (*R* = La, Ce) intermetallic compounds during hydrogenation process has been adequately studied by Paul-Boncour *et al.* [119,120,187]. The amorphous phase was detected at the beginning of the hydrogen absorption, then the intensity of the Bragg peaks of $La_{1-x}Ni_2$ and $Ce_{1-x}Ni_2$ exhibits a regular decrease without any shift as hydrogen concentration increases. Which indicates that the intermetallic compounds does not form crystalline hydrides and it becomes completely amorphous state as hydrogen concentration up to 4 H/f.u.. For the *C*15 Laves phase $RMn_2$ (*R* = Y, Gd, Dy, Tb, Ho) compounds [188], crystalline hydrides were formed first by heating to 247 °C under 0.2 MPa $H_2$ (hydrogen content up to 1.6 H/f.u., taking $TbMn_2$ for example), upon further heating $RMn_2H_x$ a transformation from the crystalline hydride to the amorphous phase was observed. It is also worth noting that except for $YMn_2$, the amorphization temperature of $RMn_2$ compounds increases with atomic number increasing from Gd to Ho, indicating the atomic size effect on HIA. Similarly, HIA can also be observed in *C*15-type $RFe_2$ [160] and $RCo_2$ [189] compounds.

Summarizing the hydrogen-induced structural evolution and amorphization in *C*15 Laves phase $RM_2$ compounds, some compounds form the crystalline hydrides first before amorphization by increasing hydrogen content, whereas the others go to amorphization directly by absorbing hydrogen. There are different factors controlling the hydrogen induced

amorphization, such as stability of the intermetallic compounds, the mechanic properties of the intermetallic compounds, the hydrogenation conditions and the atomic radius ratio $r_A/r_B$. In following sections, we will discuss them separately.

### 2.3.2.1 Stability of intermetallic compound

As a result of HIA, the metal-metal bond must be broken, thus the occurrence of HIA depends largely on the difficulties in breaking the metal-metal bond of the intermetallic compounds. As mentioned before, the enthalpy of formation or decomposition temperature both indicate the strength of bond energy, as well as the stability of intermetallic compounds. U-In Chung *et al*. [190] compared the HIA behaviors and calculated heat of formation ($\Delta H_f$) and decomposition temperature. As shown in Figure 2.12, the formation of crystalline hydrides was observed before amorphization for Dy$M_2$, Ho$M_2$ and Er$M_2$ ($M$ = Fe, Ni) compounds which exhibit high decomposition temperatures and absolute value of the heat of formation (see Figure 2.4), indicating the higher stability of the compounds the less HIA. Moreover, the absolute value of the heat of formation and decomposition temperature decrease from heavy to light rare earth, which means the structural stability is getting worse with the decreasing atomic number. Clearly, the decreased structural stability is inconsistent with the gradually increased amorphization level from Er to La [123,187], highlighting the effects of stability of intermetallic compounds on HIA.

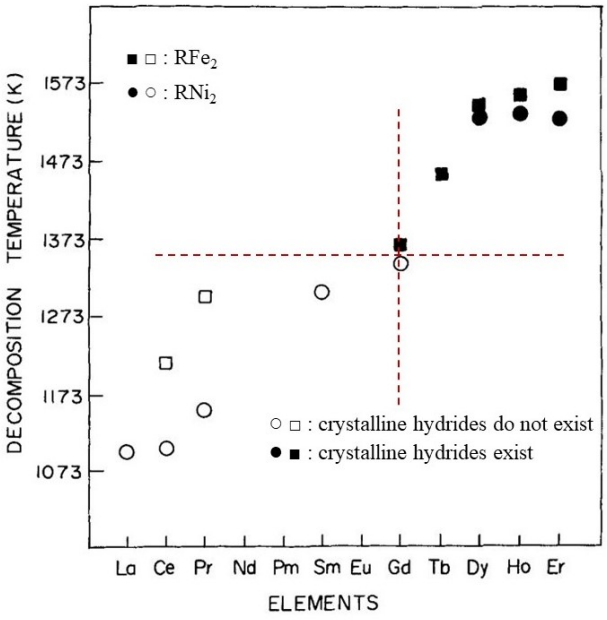


Figure 2.12 Decomposition temperatures of binary $RM_2$ ($M$ = Fe, Ni) compounds [190].

### 2.3.2.2 Hydrogen concentration and hydrogen absorption conditions

We have described two types of HIA, some of the compounds can absorb hydrogen and become amorphous hydrides without the presence of crystalline hydrides, whereas for the others the amorphous hydrides appear with “higher” hydrogen concentration, at different

hydrogenation temperature or pressure. Chung *et al*. [190] adopted the concept of a nucleation barrier for amorphization to explain these two types of amorphization behaviors. The transition from crystalline to amorphous state requires activation energy to overcome the nucleation barrier, which can be supplied by increasing hydrogen concentration, hydrogenation temperature or hydrogen pressure.

Indeed, hydrogen concentration and hydrogenation pressure are the same controlling factor to the occurrence of HIA, for a given temperature the higher hydrogen pressure, the higher hydrogen content could be added to the hydrides. They cause large elastic stress to the lattice and supply the activation energy for breaking the interatomic bonds, and once the energy reach to nucleation barrier for amorphization, HIA occurs. For example, at room temperature, Dy$M_2$ ($M$ = Fe, Co, Ni, Mn) all form crystalline hydrides with hydrogen pressure below 1.3 MPa, whereas the amorphization phase can be observed once the input hydrogen pressure up to 15 MPa [191]. Aoki. *et al*. [181] also reported the pressure dependence of the activation energies for hydrogen absorption and HIA. As shown in Figure 2.13, under higher the hydrogen pressure, lower activation energies are required for the hydrogen absorption and HIA. On the other hand, with the increasing hydrogen pressure, the activation energy for HIA become lower than that of hydrogen absorption, thus easier for the occurrence of HIA than hydrogen absorption.

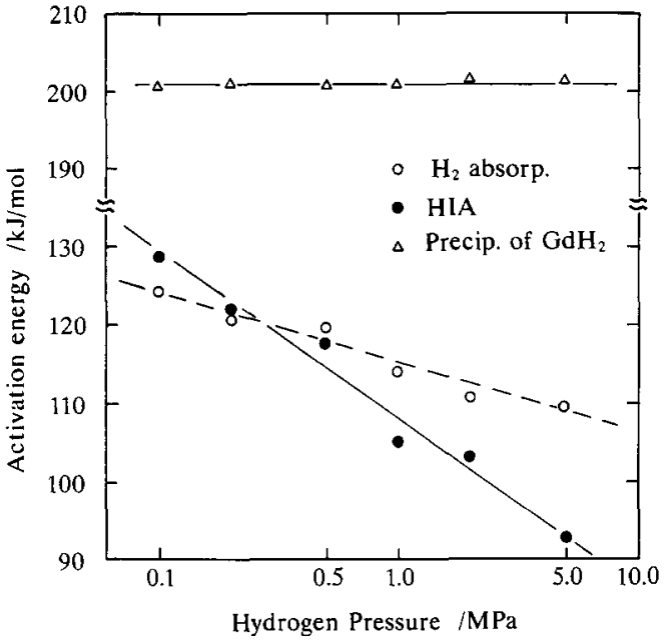


Figure 2.13 Activation energy as function of hydrogen pressure for hydrogen absorption, amorphization and precipitation of $GdH_2$ [181].

Hydrogenation temperature as a controlling factor to the occurrence of HIA can be easily understand on the basis of thermodynamics. Heating materials during hydrogen absorption can be regard as a thermally activated process, the mobility of metal atoms can be dramatically enhanced with increasing of temperature [192]. Therefore, the hydrogen absorption and

amorphization reactions accelerate as the temperature increases. Taking $ErNi_2$ compound [193], for example, as shown in Figure 2.14, under hydrogen pressure of 5 MPa, a mixture of crystalline and amorphous hydrides was observed as temperature below 127 ℃, whereas only amorphous hydrides remain when temperature ranging from 127 ℃ to 227 ℃. However, it is worth noting that for higher temperature (227 ℃ ~ 337 ℃), the mixture even the single crystalline hydrides were obtained. This strange phenomenon can be interpreted that at high temperature the hydrogen concentration is limited in $ErNi_2$ compound, which may manifest that the most important controlling factor for HIA is hydrogen concentration at a particular temperature. Moreover, once the temperatures are higher than 337 ℃, the $ErNi_2$ decomposed into *c*-$ErNi_2H_x$ (low temperature or low hydrogen pressure) or *c*-$ErNi_3$ (high temperature or high hydrogen pressure), accompanying by the formation of $ErH_3$ (low temperature or high hydrogen pressure) and $ErH_2$ (high temperature). Besides crystalline $ErNi_3$ or $ErNi_2H_x$ hydrides, a decomposition into Er hydride and $ErNi_5$ or even elemental Ni can also occur [182,194,195].

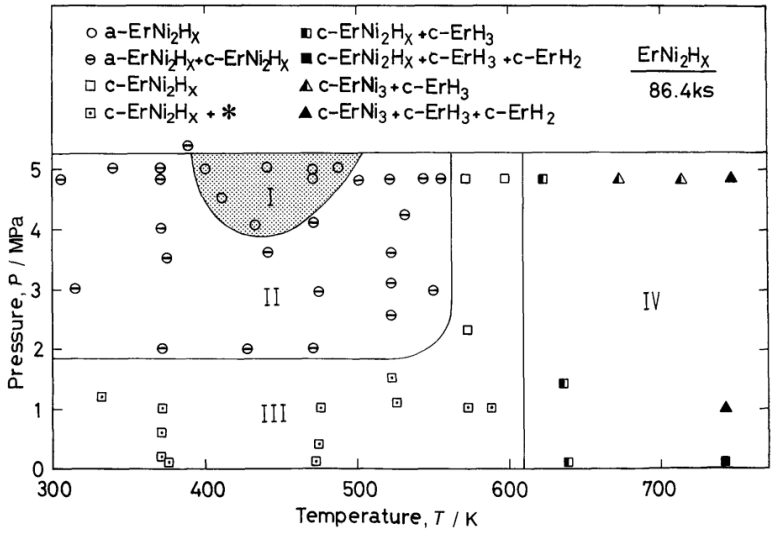


Figure 2.14 The reaction products during hydrogenation of $ErNi_2$ under various pressures and temperatures for 24 h (I: single *a*-$ErNi_2H_x$ phase; II: mixture of *c*-$ErNi_2H_x$ and *a*-$ErNi_2H_x$ phases; III: single *c*-$ErNi_2H_x$ phase; IV: decomposition of $ErNi_2$: $ErNi_2+H_2 \rightarrow$ *c*-$ErNi_2H_x$, $ErNi_3$, *c*-$ErH_3$, *c*-$ErH_2$) [193].

The dependence of hydrogen pressure and temperature for the occurrence of HIA can clearly be seen from Figure 2.15 [196]. The hydrogen pressure and hydrogenation temperatures are closely related. The HIA will not occur within a low hydrogen pressure (0.2 MPa, for example) no matter how high the hydrogenation temperature is, while upon a high pressure for hydrogenation (5 MPa, for example), there will be a temperature boundary of starting HIA. On the other hand, at a low hydrogenation temperature (227 ℃, for example), the occurrence of HIA may requires harsh hydrogen pressure. Once increasing temperature to 327 ℃, increasing hydrogen pressure or temperature could lead to the hydride's decomposition occur.

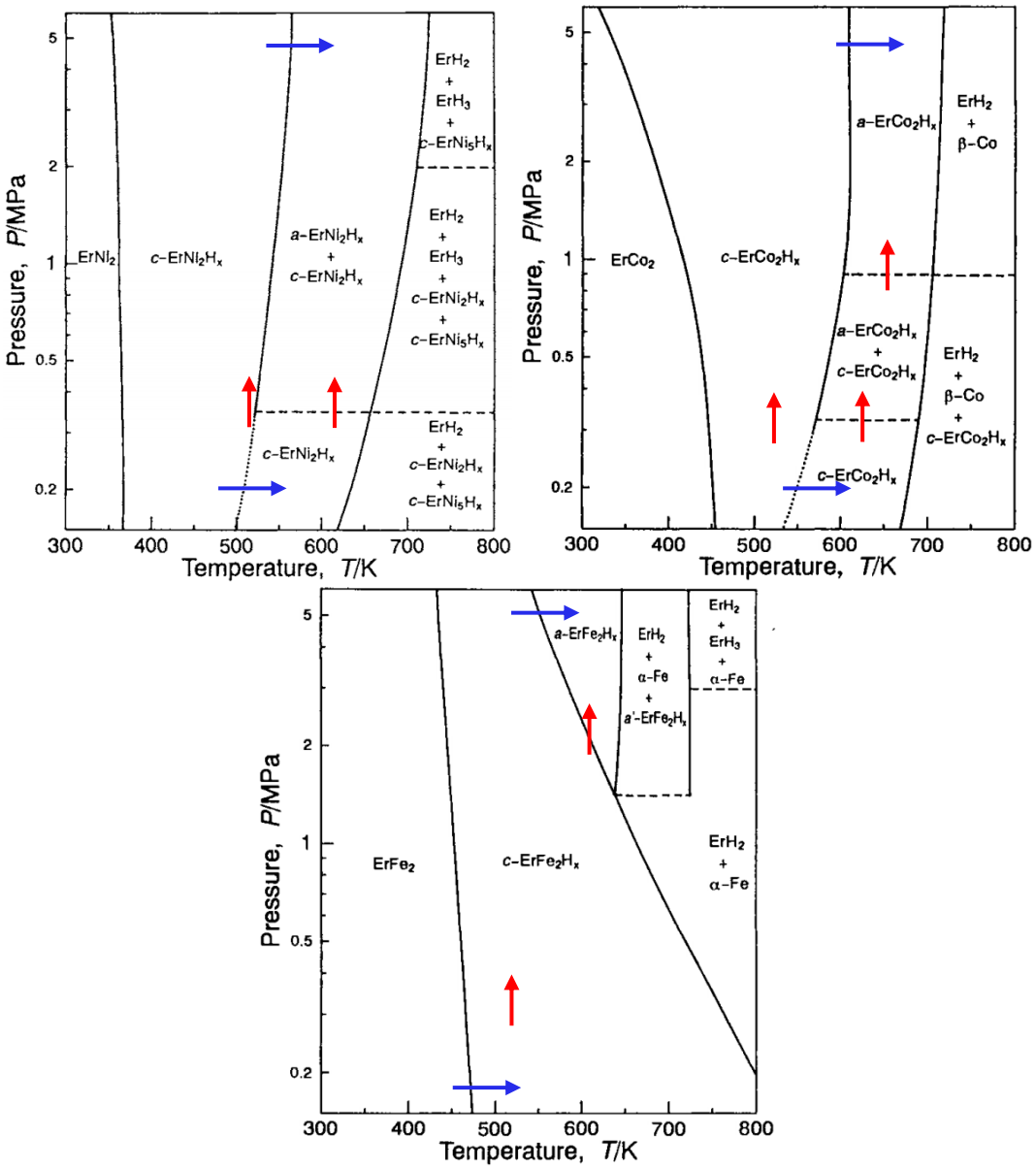


Figure 2.15 The phase occurrence of Er$M_2$ compounds ($M$ = Ni, Co, Fe) heated at 0.2 ~ 5.0 MPa $H_2$ using Differential Thermal Analysis (DTA). The solid and broken lines represent the boundary and critical pressure of each phases, respectively [196].

For the $C14$ type $ErMn_2$ compound, no amorphization phenomenon was observed upon hydrogenation under 5 MPa $H_2$ and 300 ℃ [197]. At higher temperatures, $NdMn_2$ who has the same $C14$ structure, suffers from hydrogen induced amorphization when temperature increases to 327 ℃. Moreover, the higher hydrogenation pressures, the more easily occurrence of amorphous hydrides [198]. Therefore, even for the more stable $C14$ structure than $C15$ one, hydrogen induced amorphization will occur at a high temperature or pressure.

In summary, hydrogen concentration and hydrogenation temperature take two different mechanisms to trigger HIA. Increasing hydrogen concentration contributes to the accumulation of lattice elastic stress to break the interatomic bounds, thus HIA occurs, whereas hydrogenation temperature may decrease the nucleation barrier of HIA and bring its occurrence forward.

Anyhow, these two controlling factors are necessarily based on the inherent properties of the compounds, such as bond energy or structural stability.

#### 2.3.2.3 Mechanical properties: YOUNG's modulus

The elastic constant YOUNG's modulus is one of the important parameters to provide the information of interatomic forces. The interatomic distances change once external force or inner stress is applied on a solid, interatomic forces work to restore the original dimension. Commonly the larger interatomic forces or bond energy, the higher value of YOUNG's modulus, the stronger deformation resistibility capacity.

During hydrogen absorption in the compounds, the lattice expansion and structural distortions have to overcome the interatomic forces. Further, for the occurrence of HIA, the interatomic bond must be broken. Therefore, YOUNG's modulus as an indicator representing the strength of band energy, can be used to predict the occurrence of HIA. U-In Chung *et al.* [190] reported the correlation between YOUNG's modulus and HIA of $RM_2$ compounds ($M$ = Ni, Fe). As shown in Figure 2.16, the compounds with low modulus exhibit earlier occurred HIA than ones with high modulus with the same hydrogen concentration, which illustrates the easily being broken metal-metal bond for the compounds with low YOUNG's modulus For example, $CeRu_2$ has a higher elastic modulus than $CeFe_2$ and $CeNi_2$, thus exhibits perfect structural stability upon hydrogenation at room temperature and 5 MPa hydrogen pressure without HIA [199,200].

On the other hand, it is clearly to see the low values of YOUNG's modulus are often found in light rare earth-containing compounds, which show higher $r_R/r_M$ ratio. As mentioned above, the adjustment of the atomic sizes to the ideal ratio in $RM_2$ leads that $R$ atoms exhibit a size contraction and under compression, whereas $M$ atoms show a reverse trend. Thus, it could be understood easily that the size expansion of $M$ atoms may lead to a lowered interatomic bound and YOUNG's modulus. Moreover, the compressed $R$ atoms produce the elastic strain energies, which will contribute to the lattice expansion induced by H solution. Consequently, it is concluded that YOUNG's modulus is directly dependent on the difference of the sizes between $R$ and $M$ atoms.

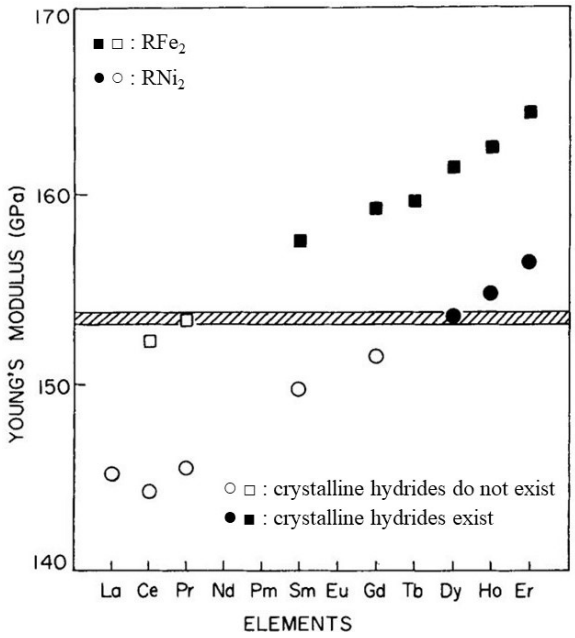


Figure 2.16 YOUNG's modulus of *C*15-type $RNi_2$ and $RFe_2$ intermetallic compounds [190].

### 2.3.2.4 Atomic radius ratio

The above three controlling factors for HIA all exhibit close association with atomic radius ratio in the *C*15 $AB_2$ compounds. The higher $r_A/r_B$ value, substantial mutual atomic adjustments will lead to the larger elastic strain energies, thus smaller YOUNG's modulus and lower structural stability, which result in HIA within a relative lower hydrogen concentration and hydrogenation temperature. Therefore, the dominant controlling factor determining the occurrence of HIA seem to be atomic radius ratio.

K. Aoki *et al.* [201,181] first explicitly proposed the correlation between atomic size and HIA that the $r_A/r_B$ is the most important factor for determining HIA in $AB_2$ compounds with *C*15 structure. Indeed, $AB_2$ compounds with $r_A/r_B > 1.37$ will be subjected to amorphization upon hydrogenation. In the case of $R_{1-x}Ni_2$ compounds, they all exhibit a large $r_A/r_B$ above 1.37 ($ScNi_2$ excepted). Due to the lanthanide contraction the $r_A/r_B$ decreases when the *R* element going from light to heavy rare earths. The compounds with $r_A/r_B$ close to 1.37 could be $Lu_{1-x}Ni_2$ (1.39), $Er_{1-x}Ni_2$ (1.41), which shows excellent structural stability upon hydrogen absorption than $La_{1-x}Ni_2$ (1.51) and $Ce_{1-x}Ni_2$ (1.48) [123].

The structural characteristics differ from other binary rare earth based $AB_2$ compounds is the ordered *R* vacancies in the cubic *C*15 structure as previously described for $R_{1-x}Ni_2$ (*R* = La to Lu) compounds [123,124,202]. The *R* vacancies allow structural constraint relaxation caused by the large atomic radii $r_R/r_M$, but also induce an increased *R*-*R* distances than the one in ideal *C*15 structure, thus leading to the weakness of interatomic bounds. Especially, for light rare earth (*R* = La, Ce and Y), their relative larger $r_R/r_{Ni}$ produces more vacancies and leads to larger interatomic distances, hence the interatomic bounds would be more fragile and easier to

break upon hydrogenation than the heavier rare earths [187]. Therefore, the existence of *R* vacancies favors the occurrence of HIA.

## 2.4 Improvement of *C*15 $RM_2$-type compounds by elemental substitution

As a result of structural instability, most of *C*15 $RM_2$ intermetallic compounds suffer from HIA, and finally decompose into $RH_2$ and another crystalline compounds $RM_3$ or $RM_5$ depending on the hydrogenation conditions and alloy systems. In this case, to improve the structural stability during hydrogen absorption and seek the possibility of application for hydrogen storage, multi-alloying might be the most effective way. As we saw above that the atomic radius ration $r_A/r_B$ is the most important factor for structural stability of intermetallic compounds and the stability against HIA, we focus on Yttrium as *A* element, as is presents multiple advantages: small atom radius for structural stability, high hydrogen affinity and light molar weight for high hydrogen storage capacity.

In the following sections, the influence of the substitution effect on the structural and hydrogenation properties of $YM_2$ compound will be reviewed.

### 2.4.1 Substitution effect on crystal structure and structural stability

The superstructure of $Y_{0.95}Ni_2$ binary compounds is a distortion of $MgCu_2$-type *C*15 Laves phase structure, with doubled lattice parameter and ordered vacancies in the *R* sublattice. The substitution of Ni by small quantities of *M* = Cu and Fe in $Y_{0.95}Ni_{2-x}M_x$ preserve the superstructure of the binary parent compound $Y_{0.95}Ni_2$. But higher content of Cu ($x \geq 0.15$) and Fe ($x \geq 0.10$) led to a phase transition from superstructure to the *C*15 Laves phase structure with a disordered arrangement of Y vacancies [203]. Similar structural evolutions were also observed from our recent study on $YNi_{2-x}Al_x$ system, where the content of Al is limited to $x$ = 0.05 the transition occurred. It is worth noting that Cu (1.28 Å), Fe (1.27 Å) and Al (1.43 Å) all exhibit larger atomic radius than Ni (1.24 Å). Therefore, the substitution of Ni by another element with bigger atomic size than Ni, may stabilize the formation of the *C*15 structure without Y-vacancy ordering compared to the binary $Y_{0.95}Ni_2$. However, the Cu for Ni substitution in $Y_{0.95}Ni_2$ leads to an increase of Y vacancies. Meanwhile, the lattice parameter increases very weakly with the Cu content, deviating from the Vegard's law [204]. This can be interpreted as the effects caused by Y vacancies, which compensates the expected increase of the cell volume and lattice parameter due to Cu substitution. However, further information about the effects of *M*-side substitution on structural and vacancy evolutions in such compounds is scarce, the new studies should be done to compare the substitution effects of Ni by the other transition metals such as Mn, Fe and Co.

For $YMn_2$ compound which crystalizes in the cubic *C*15 structure and exhibit larger $r_Y/r_{Mn}$ than $YNi_2$, upon doping of the third elements, only the cubic *C*15 Laves phase was

detected in $YMn_{2-x}M_x$ ($M$ = Al, Fe, Co) compounds with $x$ varying from 0 to 0.3 [205,206]. As shown in Figure 2.17, the lattice parameters of $YMn_{2-x}Al_x$ shows a large positive deviation from Vegard's law [204], while those of Fe, Co-substituted compounds show small negative deviation, indicating the factors controlling the lattice parameter are not only geometric effects: electronic effects may also play a role. Such rules were further reported by V. Paul-Boncour *et al.*, the evolution of lattice parameters shows a deviation from Vegard's law as $x$ varies from 0 to 2 for $YMn_{2-x}Fe_x$ compounds [207].

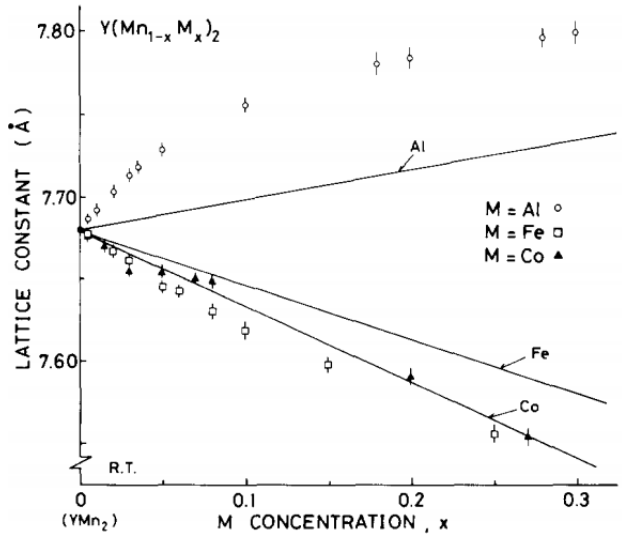


Figure 2.17 Lattice parameters versus $M$ ($M$ = Al, Fe, Co) content for $YMn_{2-x}M_x$ compounds [205].

The substitution of Y by another $R$ element, $R_{0.85}Y_{0.15}Ni_2$ ($R$ = Gd and Er) maintains the parent superstructure [208]. This makes sense, because all $RNi_2$ ($R$ = Lanthanides) compounds crystallize in the superstructure with ordered $R$ vacancies. However, the newest studies of $R$-side substituted $Y_{0.95-x}Sc_xNi_2$ system shows that when the Sc content becomes close to 0.3 the transformation from the superstructure to the $C15$ structure occurred and the number of ordered Y vacancies decreased to almost zero for $Y_{0.65}Sc_{0.3}Ni_2$ [209]. It is interesting to note that the structural evolution and $R$ vacancies are related to the atomic radius ratio $r_R/r_{Ni}$. The Sc element has a smaller atomic radius ($r_{Sc} = 164\,pm$) than Y ($r_Y = 180\,pm$), thus the substitution of Sc for Y leads to a smaller average $R$ atom radius of $r_{Y0.65+Sc0.3} = 175\,pm$ in $Y_{0.65}Sc_{0.3}Ni_2$, closes to $Er_{1-x}Ni_2$ and $Lu_{1-x}Ni_2$ in which it has been supposed to be tiny amount of or none vacancies [123].

By combining the substitution of $R$-side Y by Sc and the $M$ side element Ni, by Fe and Cu with larger radius than Ni, the modified $r_R/r_M$ is close to the idea value of 1.225, a stabilized structure is expected. However, the results show an increased $A$-site vacancies [210] which could be explained by the electronic influence.

Another important element used to improve the structural stability of $YNi_2$ intermetallic compounds is Mg substitution. However, partial substitution of Mg for Y in $Y_{2-x}Mg_xNi_4$ leads

to the formation of *AuBe*$_5$-type *C*15*b* structure (cubic, space group $F\bar{4}3m$, 216) [211,212]. These two *C*15 and *C*15*b* structures differ by the occupation sites of Y and Mg. As there is only one *A*-site (8*b*) in *C*15 structure, if Mg substitutes Y in the solid solution $Y_{2-x}Mg_xNi_4$, Y and Mg should occupy the 8*b* site randomly. But, in *C*15*b* structure, Y and Mg occupation is ordered into 4*a* for Y and 4*c* for Mg [211,213]. However, the subsequent studies of *R*MgNi$_4$ (*R* = La, Ce, Pr, Nd, Y) compounds indicate that there is partial anti-site occupation for 4*a* and 4*c* sites [211]. It seems that, the anti-occupation of *R* and Mg is mainly introduced by non-equilibrium synthesis method; *e.g.* ball-milling [214–216].

### 2.4.2 Substitution effect on suppressing HIA

Regarding the HIA of $RM_2$ (*R* = rare earth, Y, *M* = Mn, Fe, Co, Ni) intermetallic compounds with *C*15 Laves phase structure, the atomic radii ratio $r_R/r_M$ is the most important factor controlling the occurrence of HIA, and the empirical critical value $r_R/r_M = 1.37$ for the occurrence of HIA is generally accepted [201]. Therefore, optimizing the atomic radii ratio nearing 1.37 by substituting *A*- or *B*-side elements shows the possibility to stabilize the *C*15 structure.

Among the *B*-side substitution elements, the atomic sizes of Fe ($r_{Fe} = 1.27$ Å), Co ($r_{Co} = 1.25$ Å), Ni ($r_{Ni} = 1.24$ Å) are close to each other, thus the more suitable elements to significantly decrease $r_R/r_M$ should be Mn ($r_{Mn} = 1.32$ Å) or Al ($r_{Al} = 1.43$ Å).

*C*15-type $RM_2$ (*M* = Mn, Al) compounds exhibit lower atomic radius ratio than 1.37. In the case of $YMn_2$, $r_Y/r_{Mn} = 1.36$, it is difficult to get amorphization upon hydrogenation under modest conditions due to the larger activation energy for HIA compared to hydrogen absorption and decomposition [188]. However, during hydrogen absorption, $YMn_2$ exhibits no well-defined plateau region [145] and various phase transitions [148]. The same goes for $YFe_2$ which displays a multi-plateau behavior and complex $YFe_2$-H diagram [163]. In contrast, $YCo_2$ and $YNi_2$ show a relatively simplified hydriding process, whereas they are vulnerable to HIA. Therefore, the mutual substitution between Mn, Fe, Co and Ni could be attractive for their structural evolutions and effects on HIA. On the other hand, $YAl_2$, with atomic radius ratio $r_Y/r_{Al} = 1.26$ close to the ideal value and crystallizing in the *C*15 structure, do not absorb hydrogen under normal conditions. Nevertheless, as a frequently-used element for substituting *B*-side transition metals, small quantity of Al has succeeded in improving hydrogen sorption properties of $AB_5$ [59] and $AB_n$ ($3 \leq n \leq 3.8$) [217,91] compounds. Thus, the Al-substitution influence on structure and hydrogen sorption properties in $RM_2$ (*M* = Mn, Fe, Co, Ni) compounds is worth studying.

Li *et al*. [171] realized the reversible hydrogen absorption and desorption in $YFe_2$ alloy via partly substitution of Al for Fe, which is directly related to the decrease of $r_Y/r_{Fe+Al}$ from 1.45 ($YFe_2$) to 1.39 ($YFe_{1.7}Al_{0.3}$) and 1.35 ($YFe_{1.5}Al_{0.5}$). This Al substitution eliminates HIA of

$YFe_2$ and realizes reversible hydrogen storage. However, in $RM_2$ compounds, the distinction between geometric size or electronic structures for the third elements and *B*-side elements *M* normally leads to the limited solubility of the third elements, especially for Al which locates at different periods and groups as compare to transition metals. For $YNi_2$, we have not found reports about substitution effects of *B* site on HIA or hydrogen sorption properties. The investigation of $ErNi_{2-x}V_x$ and $ErNi_{2-x}Fe_x$ [138] compounds showed that the hydrogen concentration can be raised upon substitution of V and Fe for Ni. In addition, as the lattice expansion due to H absorption is lowered by substitution, this can also explain the improvement of structural stability upon hydrogenation. Therefore, it can be very interesting to study the influence of Ni substitution in $YNi_2$ compound on its superstructure with large amount of Y vacancies and on its relative high mass hydrogen absorption capacity. MK Benabadji *et al.* [218] tentatively reported the effect of transition metals substitution in $YNi_2$ on the electronic and elastic properties of $YNi_{2-x}M_x$ (*M* = Fe, Co, Zn, Cu). The YOUNG's modulus of $YNi_{1.75}Fe_{0.25}$ and $YNi_{1.625}Fe_{0.375}$ has relative higher values than the pure $YNi_2$ compound, revealing the possible greater deformation resistibility capacity upon hydrogenation.

As we mentioned before, the structural stability of $Y_{0.95}Ni_2$ alloy can also be dramatically improved by Sc alloying [209]. HIA was partially suppressed for $Y_{0.35}Sc_{0.6}Ni_2$ ($r_{Y+Sc}/r_{Ni} = 1.363$) and fully eliminated for $Y_{0.25}Sc_{0.7}Ni_2$ ($r_{Y+Sc}/r_{Ni} = 1.353$). However, as expected, the substitution of Sc also brings significantly reduced hydrogen absorption capacity. Mg exhibits the similar effects on HIA. For example, Aono *et al*. reported the hydriding properties of $YMgNi_4$, showing excellent reversibility during hydrogen absorption and desorption but with a low capacity of 3.6 H/f.u. (1.8 H per $AB_2$ unit) [213]. Its improvement in reversibility and dilution in capacity are caused by the structural distortion from *C*15 to *C*15*b* structure, which brings the change of tetrahedral interstice characteristics and also electronic properties [219,220].

Summarizing the substitution effects on HIA in $RNi_2$ intermetallic compounds, it has been performed by *B*-side substitution with larger atoms as Al, Mn, and smaller atoms to substitute Y as Sc. The hydrogen absorption capacity can be enhanced and the HIA can be suppressed or eliminated.

Summarizing the substitution effects on HIA in $RM_2$ intermetallic compounds, the third elements substituting *R* or M dramatically changes the atomic radius ratio, as well as the crystal structures and electronic structures. The structural stability can be enhanced mildly by *B*-side substitution, whereas the solution of the third elements is limited due to electronic properties. *A*-side substitution by elements with small atomic radius (such as Sc and Mg) is capable of decreasing atomic radius ratio and improving structural stability significantly, HIA can be thus suppressed or eliminated. However, *A*-side substitution also brings the decrease of tetrahedral interstices sizes and changes of atomic environments surrounding H atoms (electronic

properties), which leads to the marked decrease of hydrogen absorption capacity and increase of equilibrium pressure.

## 2.5 Conclusion and perspectives

$RM_2$ intermetallic compounds can easily absorb large amount of hydrogen forming stable hydrides, showing the potential interest as hydrogen storage materials and negative electrode materials for Ni-*M*H batteries. However, HIA hinders the practical application of such materials. Review of the various controlling factors of HIA, like the structural stability, hydrogen concentration, hydrogenation conditions, and mechanical properties show various effects on HIA. Even if the electronic concentration exhibits opposite evolutions on structural stability of hydrides and HIA effect, atomic radii ratio $r_R/r_M$ remains the most important factor controlling the occurrence of HIA.

Multi-element substitution exhibits the effectiveness of suppressing or limiting HIA. Especially for *A*-side elements substitution using smaller atoms, HIA can be fully eliminated. Meanwhile, the vacancies effect also gives us a possible way to increase the amount of solid solution of the substituted elements on the *B* side. Finally, we expect improvement by joint-substitution on both the *A* and *B* sides. In this work, we start with $YNi_2$ for the small size and low molar weight of Y, and we will study the effect on the structure and hydrogen absorption properties of the *B*-side substitution with Al and Mn, *A*-side substitution with Mg and Sc, and both sides simultaneous substitution.

# 3 . Experimental techniques

This chapter presents the used experimental, technical and theoretical supports to complete this PhD thesis. Here, first the synthesis methods then the techniques employed to thoroughly characterize their chemical and structural properties. The measuring and testing techniques used to determine the hydrogen sorption and desorption properties of these intermetallic compounds will be given. Finally, Density Functional Theory (DFT) calculations will be mentioned briefly. This calculation work is performed by the University of New South Wales (UNSW) to ascertain the effect of vacancies on the stability of the *C*15 structure. This thesis is performed partially in GRINM Beijing, partially in ICMPE Thiais, for the reason of clarity, in each chapter the used methods will be mentioned again.

## 3.1 Synthesis of the intermetallic compounds

### 3.1.1 Preparation of metal materials

The high-purity metals used for synthesis of the intermetallic compounds come from Trillion Metals Co., Ltd or Alfa Aesar. The purity of metal materials is listed in Table 3.1. The rare earth metals were pre-melted under vacuum to reduce the impurity content. Subsequently, before weighing the target weights, cleaned metal surface with metallic luster is necessary. The surface of all these piece metals needs to be polished using sandpaper or file in the glovebox. And beyond that, Mn slices are treated using dilute nitric acid to dissolve surface oxides. An appropriate excess (3 wt.% Mn and 20 wt.% Mg) were added to compensate for evaporative loss during induction melting for those Mn and Mg containing compounds.

Table 3.1 Commercial pure metal materials used for alloy synthesis.

| Element | Purity | Provider | Form |
|---|---|---|---|
| Y | >99.9% | Trillion Metals Co., Ltd. (GRINM)<br>Alfa Aesar (ICMPE) | Piece |
| Ni | >99.99% | Trillion Metals Co., Ltd. (GRINM)<br>Alfa Aesar (ICMPE) | Piece |
| Al | >99.99% | Trillion Metals Co., Ltd. | Piece |
| Mn | >99.99% | Alfa Aesar | Slice |
| Mg | >99.9% | Trillion Metals Co., Ltd. | Piece |
| La | >99.9% | Trillion Metals Co., Ltd. | Piece |
| Sc | >99.9% | Trillion Metals Co., Ltd. | Piece |

### 3.1.2 Induction melting

All the as-cast ingots of intermetallic compounds were prepared by induction melting in high purity argon atmosphere (5N) under a pressure of 0.04 MPa in a water-cooled copper crucible. As shown in Figure 3.1 and Figure 3.2, we synthesized samples in both GRINM and ICMPE, where the induction melting equipment exhibit the same principle and preparation

process. Although some detailed equipment information is different, such as the vacuum gauge, the resulting prepared as-cast samples largely identical but with minor differences. The as-cast compounds $YNi_{2-y}Al_y$, $Y_{1-x}Mg_xNi_2$, $Y_{0.7}Mg_{0.3}Ni_{2-y}Al_y$ and $Y_{0.7-x}La_xMg_{0.3}Ni_2$ were prepared in GRINM, $Y_xNi_{2-y}Mn_y$ and $Y_{0.9-x}Sc_xNi_{1.9}Mn_{0.1}$ were prepared in ICMPE.

For the operating process, I will take alloys with nominal composition $YNi_{2-y}Al_y$ ($0 \leq y \leq 1$) for example. We put the well cleaned and weighed pure metals Y, Ni and Al in the crucible and vacuum the chamber (<$10^{-5}$ mbar). Then, we heat the metals until they turn red under vacuum to clean some adsorbed impurities. The melting is performed under argon (~ 0.4 bar) atmosphere to avoid loss due to the evaporation. The ingots were turned over and re-melted three times to ensure homogeneity.

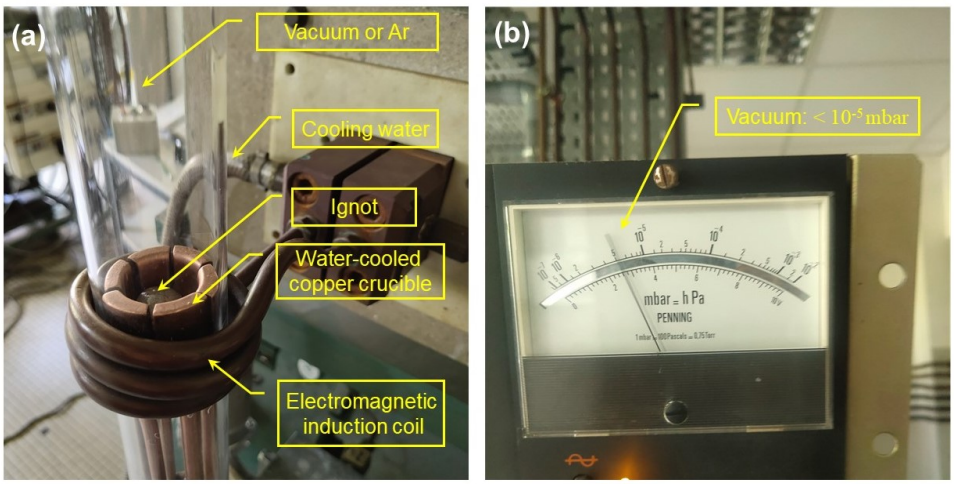


Figure 3.1 The induction furnace (a) and vacuum system (b) in ICMPE.

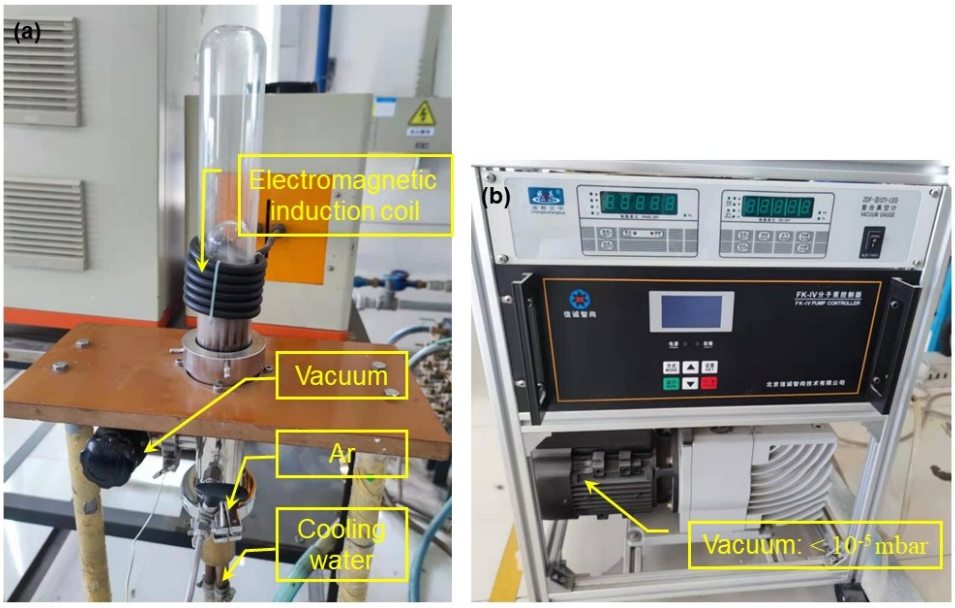


Figure 3.2 The induction furnace (a) and vacuum system (b) in GRINM.

### 3.1.3 Annealing

To get better homogeneity, then the prepared ingots were mechanically crushed and ground into powder (≤ 100 μm) after cleaning the surface using file to remove the oxide. The powder of the alloys was then cold pressed into pellets under 100 MPa in the glovebox. By doing so, we guarantee the chemical homogeneity and help phase formation.

As shown in Figure 3.2, the cold pressured pellets were placed in a cylindrical stainless-steel vessel which will be closed using arc welding in the glovebox (Argon). For the alloys containing magnesium, excess of 9 mg magnesium powder was added in the vessel to compensate for evaporative loss during heat treatment. The alloys were annealed at 850 °C for 3 days, and the prepared alloy pellets were mechanically pulverized into powder, sieved less than or equal to 36 μm, for X-ray diffraction, ranging from 37 μm to 100 μm, for neutron diffraction and hydrogen sorption measurements.

The annealing of as-cast compounds $Y_xNi_{2-y}Mn_y$, $Y_{0.9-x}Sc_xNi_{1.9}Mn_{0.1}$ and $Y_{0.7}Mg_{0.3}Ni_{2-y}Al_y$ were performed in ICMPE.

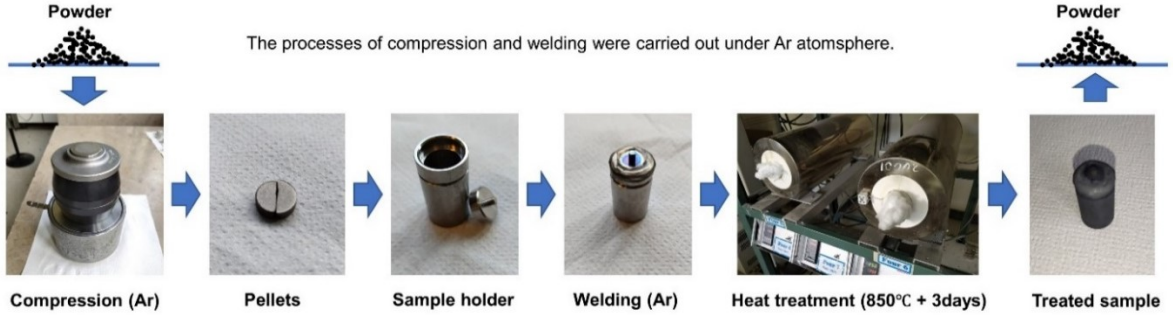


Figure 3.3 The procedure of sample preparation for heat treatment in ICMPE.

The annealing of as-cast $Y_{1-x}Mg_xNi_2$ and $Y_{0.7-x}La_xMg_{0.3}Ni_2$ compounds were performed under various temperatures (700 °C, 800 °C, 900 °C, 1000 °C) in GRINM. As shown in Figure 3.4, after cleaning the surface using file to remove the oxide, the as-cast ingots were covered by tantalum piece and sealed in an argon-filled glass tube (Figure 3.4a). The annealing was performed in a box-type muffle furnace (Figure 3.4b).

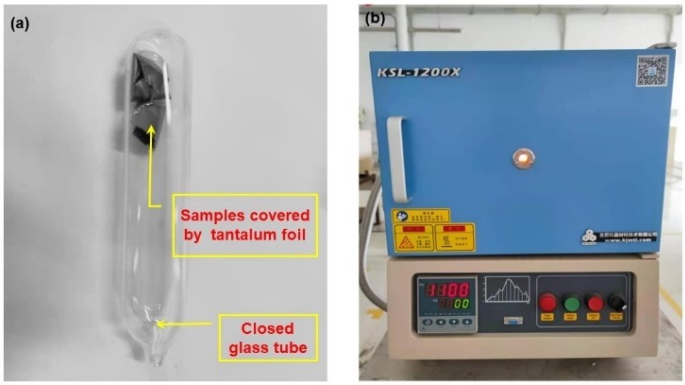


Figure 3.4 The procedure of sample preparation for heat treatment in GRINM.

## 3.2 Chemical characterization

### 3.2.1 Inductively coupled plasma-optical emission spectrometer (ICP-OES)

ICP-OES allows for continuous and rapid multi-element determination with high accuracy and a wide linear range for qualitative and semi-quantitative analysis of samples. As shown in Figure 3.5, the principle of ICP-OES is to use the high temperature produced by the argon plasma to completely decompose the sample to form excited atoms and ions. Due to the instability of excited atoms and ions, the outer electrons will leap from the excited state to lower energy levels, emitting characteristic spectrum. The spectral lines are then collected and analyzed. After light splitting by grating (light-splitting optical system), a detector is used to detect the intensity of the light at a specific wavelength, which is proportional to the concentration of the target element.

The instrument works in three main processes: (1) the evaporation of the sample solution using the energy provided by the plasma light source, forming gaseous atoms, which are further excited to form the light radiation; (2) the light splitting of the polychromatic light using a monochromator, producing spectral lines arranged in wavelength order to form spectrum; (3) the detection of the wavelength and intensity of the spectral lines in the spectrum by a detector to obtain the concentration of each element.

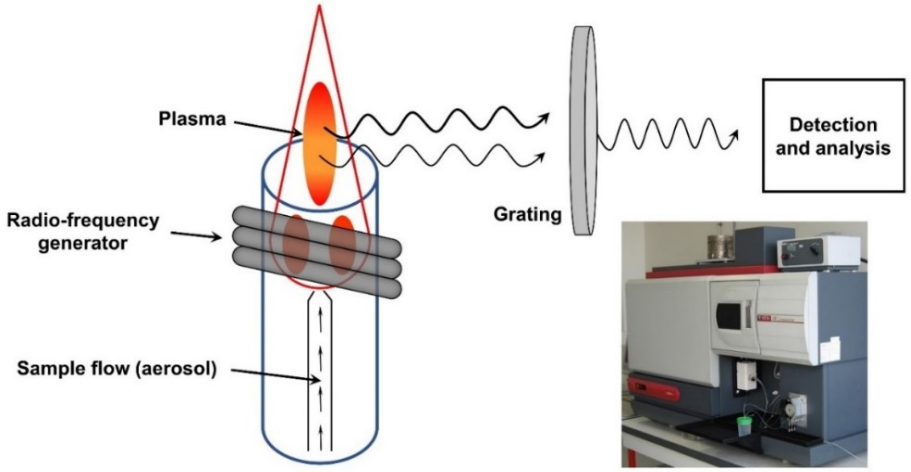


Figure 3.5 General view of how the ICP-OES instrument works.

### 3.2.2 Electron Probe Micro Analysis (EPMA)

#### 3.2.2.1 Basics of EPMA

The Electron Probe (EPMA) is an instrument used for micro-area composition analysis. The principle is that the sample is bombarded with a finely focused electron beam, which excites the characteristic X-rays of the elements contained in the sample, and different elements have different characteristic wavelengths and energies of X-rays. The spectrometer used to

determine the characteristic wavelength of X-rays is called a Wave Dispersive Spectrometer (WDS), which is the main detection method commonly used in EPMA instrument for qualitative and quantitative analysis of micro-areas.

### 3.2.2.2 WDS

The wave spectrometer is the main component of the electron probe used to detect the X-ray signal. X-ray spectroscopy is based on Moselyey's law. For an element, the wavelength λ of characteristic X-ray and the atomic number Z shows a specific correlation: $(\frac{c}{\lambda})^{\frac{1}{2}} = K_1(Z - K_2)$ ($c$ is the speed of X-ray, $\frac{c}{\lambda}$ is the frequency of X-ray, $K_1$ and $K_2$ are constants), which means that the wavelength λ is determined by the atomic number of the element. Therefore, to identify the type of element contained in a sample, it is necessary to detect the wavelength λ of characteristic X-ray wavelength of the element.

As shown in Figure 3.6, a finely focused electron beam bombarding the surface of a sample can excite X-rays in a volume of action on the order of microns from the surface of the sample. Because our sample is composed of multiple elements, the excited X-rays have multiple characteristic wavelengths. After appropriate crystal spectroscopy, only X-rays with characteristic wavelengths λ that are consistent with the Bragg equation $n\lambda = 2dsin\theta$ between the Bragg diffraction angle θ and the crystal plane spacing $d$ will diffract. Thus, various single wavelength characteristic X-rays of different $2\theta$ to the direction of incidence can be separated and analyzed by the detector to obtain the element represented by the characteristic X-rays and the elemental content.

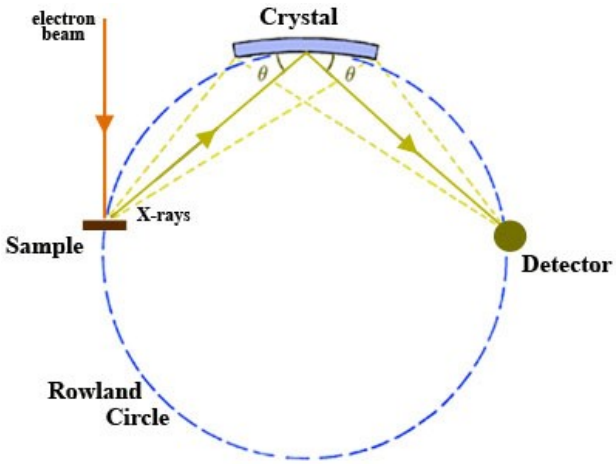


Figure 3.6 Technical drawing (from https://serc.carleton.edu/research_education/geochemsheets/wds.html) of the Wave Dispersive Spectrometer (WDS).

### 3.2.2.3 Structure of EPMA

In this study, the phase composition and microstructure of the alloys were examined in a Cameca SX-100 instrument, which owns tungsten filament electron source, acceleration volage from 1 kV to 30 kV, regulated probe current, secondary and backscattered electron detectors,

four WDS spectrometers equipped with PC1, PC2, PC3, LLiF, LPEF and TAP crystals. A schematic diagram of EPMA instrument is presented in Figure 3.7. The most important part of EPMA is the WDS, which is used to detect the chemical compositions quantificationally.

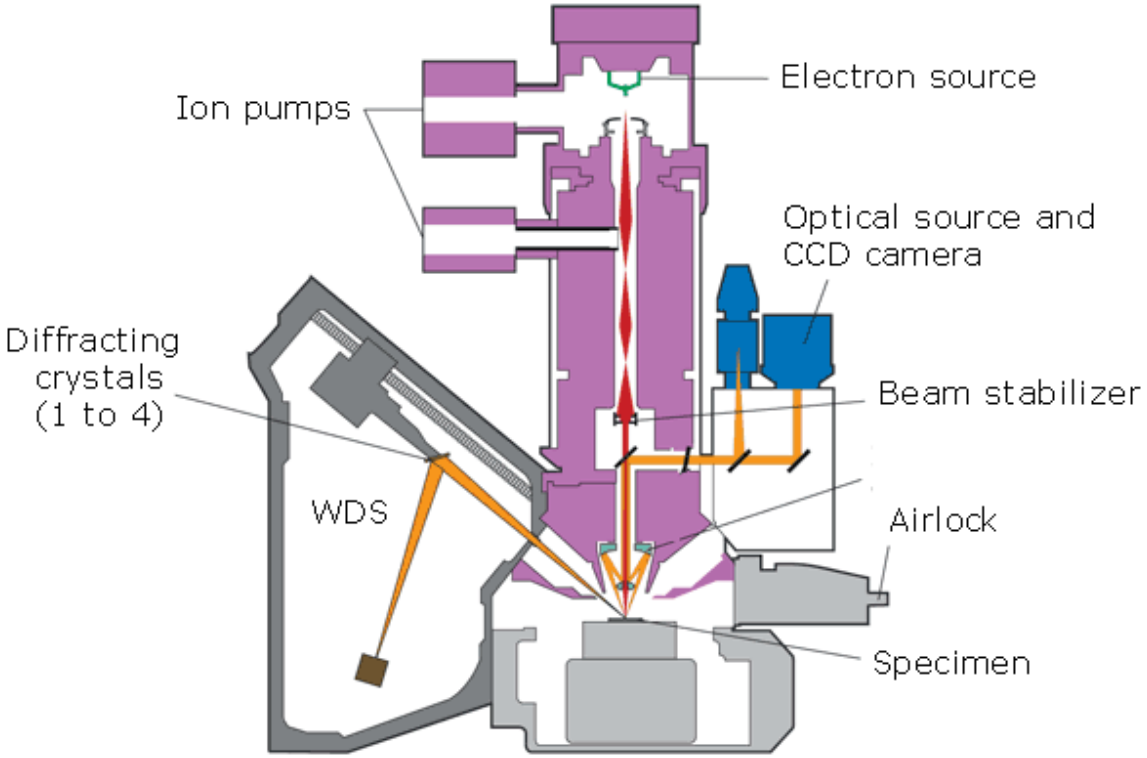


Figure 3.7 Technical drawing (from: https://www.cameca.com/products/epma/technique) of the EPMA instrument.

### 3.2.2.4 Sample preparation

As for EPMA-WDS measurements, a small sample holder shown in Figure 3.8 is used as a device for fixing samples. We choose a small piece of the alloy which has flat face and embed it in a low melting point Wood alloy ($Bi_{50}Pb_{25}Cd_{12.5}Sm_{12.5}$). Then, the sample surface is polished until no visible scratches can be seen in metallographic microscopy.

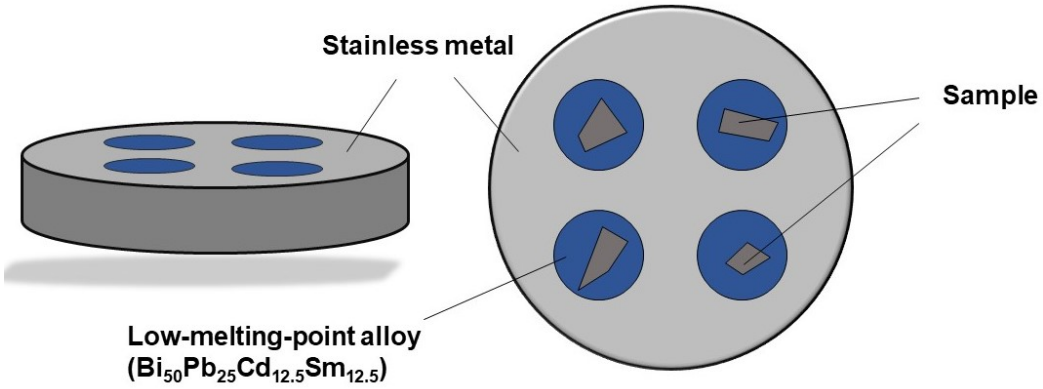


Figure 3.8 The procedure of sample preparation for EPMA measurement.

## 3.3 Structural characterizations (powder diffraction)

Powder diffraction is a scientific technique to determine the structural characteristics of materials using X-ray, neutron or electron diffraction on powder or microcrystalline samples. Such three diffraction forms mean three diffractometers with X-rays, electron or neutron as diffraction sources, performing the powder measurements and various materials characterization. In this thesis, X-ray diffraction is widely used to examine the crystalline or amorphous samples and obtain the crystallographic data. For some special alloy samples with Ni and Mn, Ni to Mn contrast is too low to discriminate them by X-ray diffraction, thus neutron powder diffraction is performed to determine their occupations, as well as the occupations of hydrogen in some selected hydrides.

### 3.3.1 X-ray diffraction

X-rays can be considered as waves of electromagnetic radiation and they are the only kind of energy with the optimal wavelength for their inter-atomic-scale diffraction (1 - 100 Å). In the 110 years since the discovery of diffraction phenomenon in copper sulphate crystals by Max von Laue in 1912 [221], the X-ray diffraction (XRD) has been rapidly developed and already become one of the most basic and important tools for structural characterization.

#### 3.3.1.1 The working principle

In an X-ray diffractometer, X-rays are produced using a high-energy electron beam to bombard a metal target, it has a specific wavelength corresponding to the target material, which is described as characteristic X-rays. The most common target materials include Cr, Fe, Co, Cu and Mo, which will produce characteristic X-rays with different wavelength λ. In this thesis, only X-ray diffractometers with Cu as target ($k_{\alpha 1} = 1.54056$ Å, $k_{\alpha 2} = 1.54439$ Å) are used for structural characterization.

Once the waves reach the sample, part of them will enter the lattice and be diffracted by the regularly arranged atoms present in the sample. When the waves are scattered in a specular fashion (mirror reflection) by the atoms, constructive interference occurs according to Bragg's law. As shown in Figure 3.9, $d$ is the distance between successive layers of atoms, $\theta$ is the glancing angle. The path length of each wave is an integer multiple of the wavelength λ. The path difference between the two waves upon constructive interference can be calculated as $2d \sin\theta$. These parameters can thus be connected by the relation:

$$2d \sin\theta = n\lambda$$

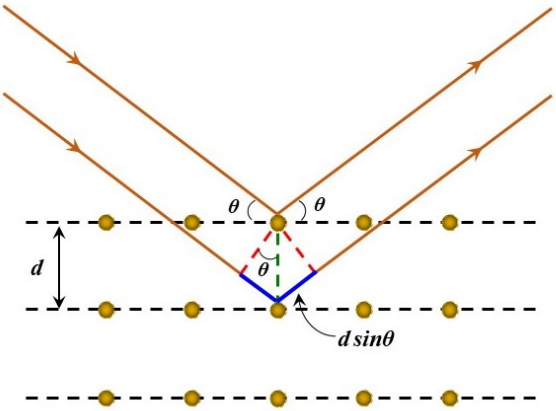


**Bragg's law**

$$2d\sin\theta = n\lambda$$

Figure 3.9 Bragg's law and diffraction, $n$ is the diffraction order (any integer), $\lambda$ is the wavelength of the beam, $d$ is the spacing between diffracting planes, $\theta$ is the incident angle.

### 3.3.1.2 Diffractometers

All the X-ray diffraction characterizations have been performed with a X-Pert-MRD diffractometer from PANalytical (experiments done in GRINM, China) (Figure 3.10a) and a D8 Advance diffractometer from Bruker (experiments done in ICMPE, France) (Figure 3.10b), both in Bragg-Brentano configuration and using Cu Kα radiation. The diffraction patterns are measured in the $2\theta$ range of 10º-90º. The scan patterns or speed depend on the requirements of subsequent structural analysis.

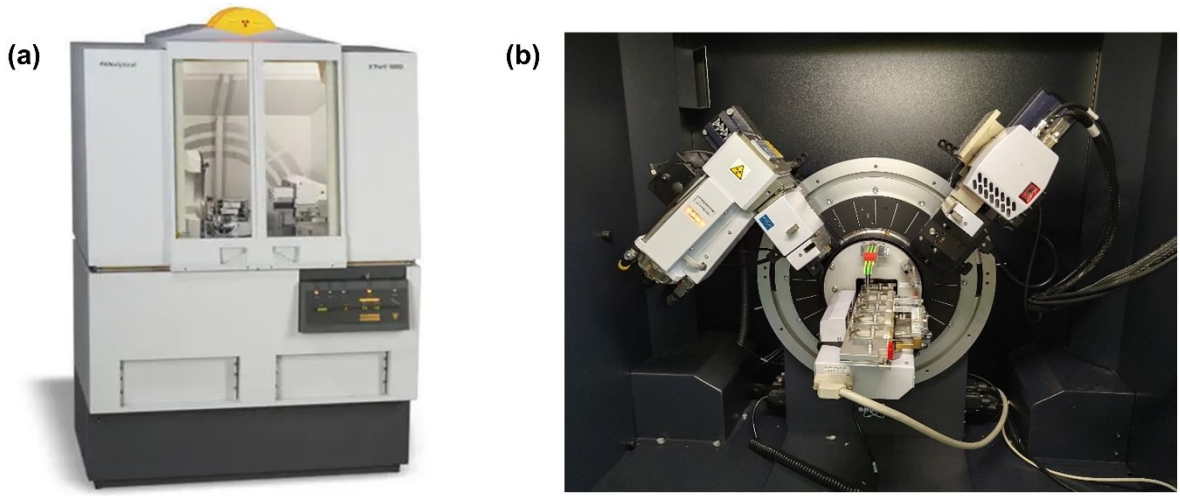


Figure 3.10 X-ray diffractometers: (a) X-Pert-MRD diffractometer from PANalytical; (b) D8 Advance diffractometer from Bruker.

### 3.3.1.3 Sample preparing

In this thesis, the powder samples were filtrated by using a modest sifter, the size of particles normally are lower than 37 μm. For some hydrides and dehydrogenated samples, we selected powders with size lower than 100 μm for the hydrogen absorption or desorption experiments, so the size of prepared samples for X-ray diffraction are lower than 100 μm. As shown in Figure 3.11, the prepared powder was placed on a glass sample holder or a Poly-

methyl-methacrylate plate by using a double slide tape. In the D8 Advance diffractometer, the sample holder rotates to maximize the statistics and get an average powder pattern.

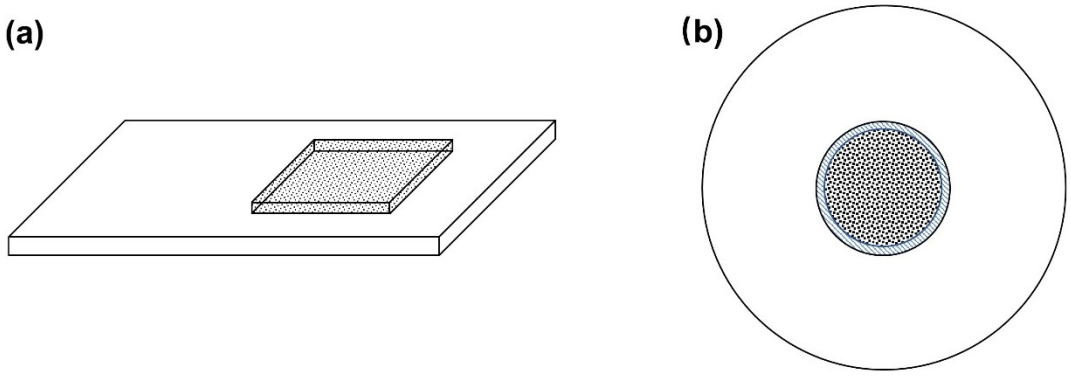


Figure 3.11 Sample holders for X-ray diffraction: (a) for X-Pert-MRD diffractometer from PANalytical; (b) for D8 Advance diffractometer from Bruker.

### 3.3.2 Neutron diffraction

Neutron diffraction refers to the Bragg diffraction occurring when the neutrons with de Broglie wavelength of around 1 Å through crystalline material. Similar to X-ray diffraction, neutron diffraction also follows the Bragg's law and uses a beam of thermal or cold neutrons to obtain a diffraction pattern. Due to their different scattering properties, neutrons and X-rays provide complementary information.

X-rays interact with electrons and thus their scattering intensity on atoms is proportional to the atomic number, whereas neutrons scatter much more readily from the atomic nuclei rather than from the electrons. Therefore, neutron diffraction is very useful for observing the positions of light atoms with few electrons and adjacent elements which cannot be distinguished using X-ray diffraction.

Our experiments were carried out using the General-Purpose Powder Diffractometer (GPPD) in China Spallation Neutron Source (CSNS). GPPD adopts neutron time-of-flight technology, selects the appropriate distance between moderator and sample (30m), and has three detectors with different angles. Low-angle detector (30°) is suitable for measuring the structure of larger crystals; high-angle backscatter detector (150°) owns a resolution of 0.2%, are suitable for material studies which need higher resolution; Medium-angle detector (90°) can effectively avoid the scattering in the sample chamber and is suitable for structural research under special sample environment and experimental conditions.

The size of sample powder used for neutron diffraction is $\leq 100\ \mu m$ with mass of around $3{\sim}5\ g$ in a vanadium sample holder, to keep its homogeneity during experiments as much as possible.

### 3.3.3 Analysis of the diffraction patterns: the Rietveld analysis

The neutron or X-ray diffraction data collected at constant or variable step in scattering angle $2\theta$ in this thesis were analyzed by FullProf program [222], which has been mainly developed for Rietveld analysis.

#### 3.3.3.1 Rietveld method basics

The Rietveld method was first proposed by Hugo Rietveld in 1969 for the diffraction of monochromatic neutrons [223]. It employs the non-linear least squares and adjusts the initial approximation of many free parameters, such as peak scale, peak shape, lattice parameter and atomic coordinates *et al.*, approaching to refine a theoretical line profile until it matches the measured profile. The scattering variable ($2\theta$ angles, times of flight, energies) can be referred as *T*, then the experimental powder diffraction pattern is usually given as two arrays $\{T_i, y_i\}_{i=1,\dots,n}$. During the refinement, the data will be manipulated or normalized, the new data can be expressed as three arrays $\{T_i, y_i, \sigma_i\}_{i=1,\dots,n}$, where $\sigma_i$ is the standard deviation of the profile intensity $y_i$. The profile can be modelled using the calculated counts at the $i^{th}$ step by summing the contribution from neighboring Bragg reflections plus the background:

$$y_{c,i} = \sum_{\phi} S_{\phi} \sum_{h} I_{\phi,\boldsymbol{h}}\, \Omega\left(T_i - T_{\phi,\boldsymbol{h}}\right) + b_i$$

where the subscript *h* labels different Bragg reflection peaks, the subscript $\phi$ labels the number of phases ($\phi \geq 1$). $S_{\phi}$ is the scale factor of the phase $\phi$; $I_{\phi,h}$ is the intensity of a peak of one phase; $\Omega$ is the peak-shape functions that model both instrumental and sample effects; $b_i$ is the background intensity. The whole arrays $\{y_i\}$ and $\{y_{c,i}\}$ are referred as $y_{obs}$ and $y_{calc}$ respectively.

The function upon minimizing the weighted squared difference between the $\{y_i\}_{i=1,\dots,n}$ and $\{y_{c,i}(\boldsymbol{\alpha})\}_{i=1,\dots,n}$ can be expressed as follows:

$$\chi^2 = \sum_{i=1}^{n} w_i \{y_i - y_{c,i}(\boldsymbol{\alpha})\}^2 = \left(\frac{R_{wp}}{R_{exp}}\right)^2$$

where $y_i$ is the observed intensity at a certain $2\theta$, $y_{c,i}$ is the calculated intensity at the same angle, $w_i$ is the weight of the observation, we usually take $w_i = 1/y_i$ $i = 1,2,\dots n$, $\boldsymbol{\alpha} = (\alpha_1, \alpha_2, \alpha_3, \dots, \alpha_p)$ is the parameters to be refined. The $R_{wp}$ and $R_{exp}$ are the weighted profile residual and expected weighted profile residual respectively which will be present next.

To find the best fit between a calculated and experimental pattern, there are a set of conventional factors to characterize the quality of a refinement. The definition of the indices are as follows:

Profile residual:

$$R_p = 100 \times \sum_{i=1,n} |y_i - y_{c,i}| \Big/ \sum_{i=1,n} y_i$$

Weighted profile residual:

$$R_{wp} = 100 \times \left[ \sum_{i=1,n} w_i |y_i - y_{c,i}|^2 \Big/ \sum_{i=1,n} w_i {y_i}^2 \right]^{\frac{1}{2}}$$

Expected weighted profile residual:

$$R_{exp} = 100 \times \left[ (n-p) \Big/ \sum_i w_i {y_i}^2 \right]^{\frac{1}{2}}$$

where $n$ is total number of points in the refinement and $p$ is the number of refined parameters.

Bragg residual:

$$R_{Bragg} = 100 \times \sum_{\boldsymbol{h}} |{}'I_{obs,\boldsymbol{h}}{}' - I_{calc,\boldsymbol{h}}| \Big/ \sum_{\boldsymbol{h}} |{}'I_{obs,\boldsymbol{h}}{}'|$$

$${}'I_{obs,h}{}' = I_{calc,\boldsymbol{h}} \sum_i \left\{ \frac{\Omega(T_i - T_{\boldsymbol{h}})(y_i - b_i)}{(y_{c,i} - b_i)} \right\}$$

### 3.3.3.2 Refinement sets used in this thesis

The background intensity $y_{bi}$ at the $i^{th}$ step is obtained either from a user-supplied table of background intensities or from refinable background functions. In this thesis, we choose some background intensity points manually or adopt a background 6-coefficients polynomial to calculate the background intensity $b_i$ at the $i^{th}$ step:

$$b_i = \sum_{m=0}^{6} B_m \, (2\theta_i)^m$$

where $B_m$ are parameter to be refined.

The peak-shape function used in this thesis is $\Omega_5$:

$$\text{Pseudo} - \text{Voigt: } \Omega_5(x) = pV(x) = \eta L'(x) + (1-\eta)G'(x) \quad 0 \le \eta \le 1$$

with $x$ being the variable $T - T_h$ and $\eta = \eta_0 + X * (2\theta)$ where $\eta_0$ (shape) and $X$ need to be refined. $pV(x)$ function is a linear combination of a Lorentzian ($L'$) and a Gaussian ($G'$) of the

same $FWHM(H)^2$, so two parameters characterize the peak shape: $pV(x) = pV(x, \eta, H)$. The width of the diffraction peaks $FWHM$ is originally represented by:

$$H_k^2 = U \tan^2 \theta_k + V \tan \theta_k + W$$

where *U*, *V* and *W* are the half-width parameters and can be refined during the fit. $H_k$ and $\theta_k$ mean the *FWHM* and position of the $k^{th}$ peak.

#### 3.3.3.3 Evaluation of the Rietveld fit

All the experimental diffraction patterns in this thesis show high quality, satisfying the requirement of Rietveld method. During the refinement, we normally refine the parameters in a sequence of their constringency stability. Such as the first-order parameters zero, scale factor, background, which show better stability, whereas the *U*, *V*, *W* and atomic occupation are easily-divergent. Moreover, we need to prepare a suitable structure model to avoid the huge error at the beginning of refinement. We can define the lattice parameters, scale factor or atomic information manually according to the structural knowledge, and refine them in a minor step. Choosing suitable peak and background functions is also important.

Generally, $R_p$, $R_{wp}$ and $\chi^2$ evaluate how well the entire Rietveld model fits the entire data set, $R_{Bragg}$ evaluates the fit of individual phases. Normally the smaller the values of $R_p$, $R_{wp}$ and $R_{Bragg}$, the higher quality of a Rietveld fit. However, we cannot judge the accuracy of the results obtained from the Rietveld fits depending entirely on the values of these agreement indices. For example, the integrated intensities are related to many parameters like peak-shape, atomic coordinates or preferred orientation *et al*. We may get very low $R_p$, $R_{wp}$ or $\chi^2$ by keeping a wrong value for one parameter, meanwhile, adjusting another one sharply. The final fit looks good but the structural information is not accurate. Therefore, the agreement indices should be used as a reference, it is important to observe the whole refinement process, considering the order of refined parameters and the error ranges for each parameter.

## 3.4 Thermodynamic and kinetic measurements for hydrogen sorption

The hydrogen sorption properties are characterized by Pressure-Composition-Isotherms (PCI), hydrogen absorption kinetics, cycling stability of $H_2$ uptake/release reactions and hydrides with various hydrogen concentrations. All the hydrogen sorption experiments were tested in a homemade Sieverts-type apparatus under various conditions (we will cover the experimental conditions in the main content of this thesis).

### 3.4.1 Sievert's method

The Sieverts technique is a popular method used for determining gas uptake, particularly for hydrogen storage materials. As shown in Figure 3.12, in the Sieverts technique, a calibrated

reference volume $V_{ref}$ is filled with gas to a measured pressure and then opened to the sample chamber, the gas uptake by the sample being calculated from the change in the gas pressure in the system. The Sieverts technique is the most common technique for measuring the uptake of hydrogen into or onto materials owning to its practicability and universally accepted accuracy. In this thesis, all the hydrogen sorption properties are measured in the homemade apparatus based on the Sieverts technique.

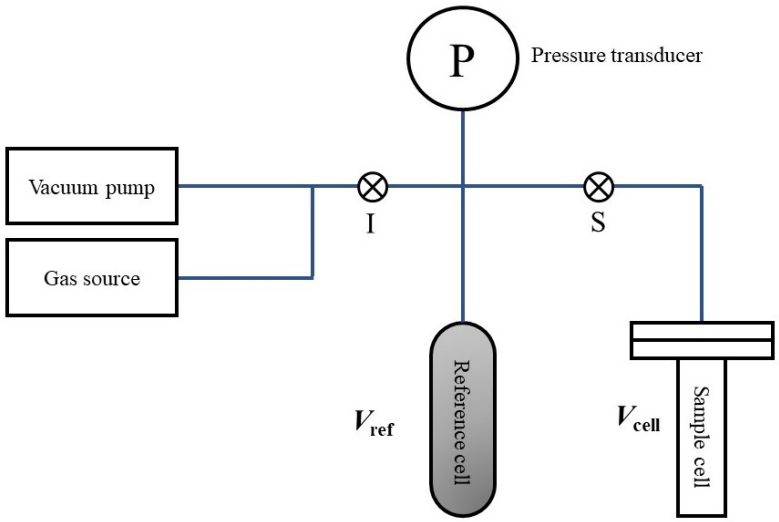


Figure 3.12 Schematic diagram (drawing based on T.P. Blach [224]) showing the working principles of the Sieverts apparatus for determining the uptake of gas atoms or molecules by the sample. Based on the initial pressure or empty volume $V_{cell}$, after opening the value I to boost gas flow to the reference cell and then obtaining a stable pressure, a further measurement of pressure after the value S has been opened.

## 3.4.2 Sieverts-type apparatus

There are two apparatus measuring the hydrogen uptake in this thesis. The measurements of Y(Ni, Al)$_2$ and Y$_x$(Ni, Mn)$_2$ ternary systems presented in Chapter 4, Y$_{0.7}$Mg$_{0.3}$(Ni, Al)$_2$ and (Y, Sc)$_{0.9}$Ni$_{1.9}$Mn$_{0.1}$ quaternary systems presented in Chapter 6 were executed at ICMPE, whose apparatus is shown in Figure 3.13. The system temperature can be controlled by the thermostatic water bath. Thermodynamic and kinetic for hydrogen sorption The kinetic curves of Y(Ni, Al)$_2$ ternary system and the hydrogen sorption properties of YNi$_2$-based Mg-containing compounds were executed at GRINM. The schematic diagram of the sieverts-type apparatus in GRINM is shown in Figure 3.14, it adds the inert gases sources (Ar or He) for the clean of the air in the chambers and sample volume calibration.

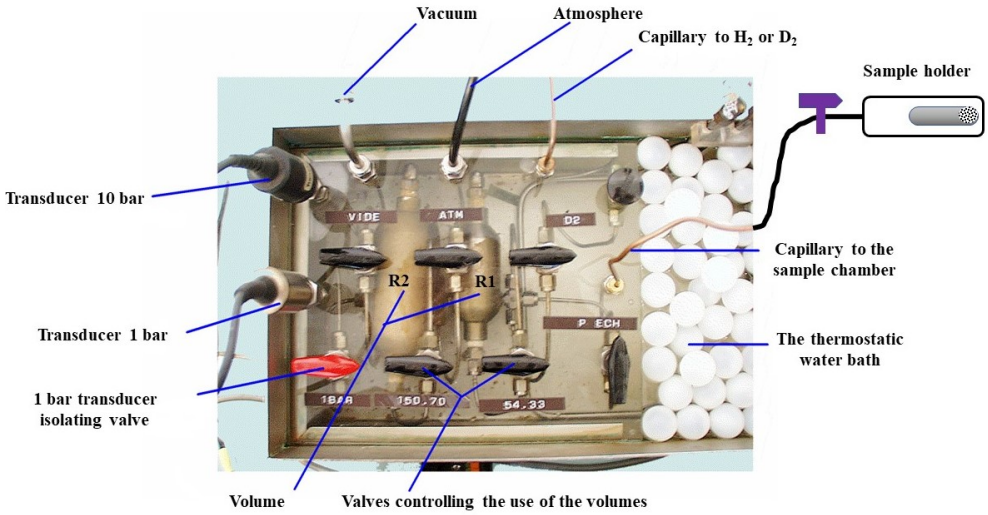


Figure 3.13 The Sieverts-type apparatus measuring the hydrogen uptake in ICMPE.

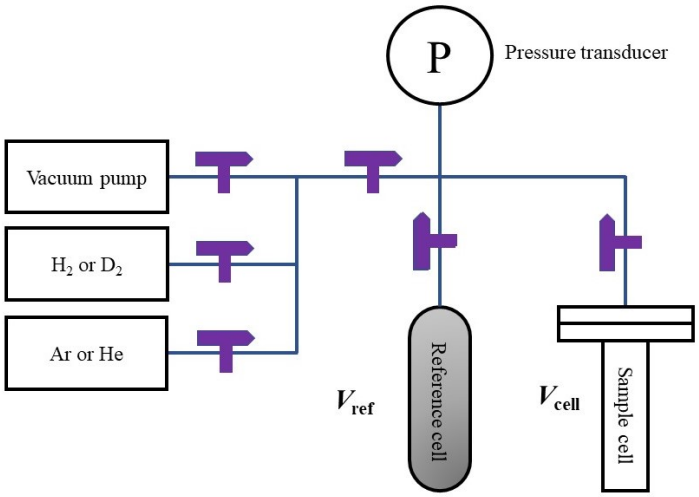


Figure 3.14 The schematic diagram (drawing based on T.P. Blach [224]) of the apparatus measuring the hydrogen uptake in GRINM.

I will detail the working process and principles in the case of the Sieverts-type apparatus in ICMPE. A certain quantity of hydrogen is introduced into a known volume at a given temperature. By measuring the starting pressure $P_{ini}$, the number of initial moles introduced into the hydrogenation chamber can be calculated. After thermal equilibrium, the gas is expanded in the sample holder. As shown in the Figure 3.15, the pressure drops to a value $P_{det}$ corresponding to the expansion of the gas in the empty volume. After this expansion, the changes of observed pressure correspond to the hydrogen absorption reaction of the sample. When equilibrium is reached, the final pressure $P_{fin}$ gives the equilibrium pressure and the number of final moles remaining in the sample. It is then possible to calculate the quantity absorbed by the difference between the initial and final moles.

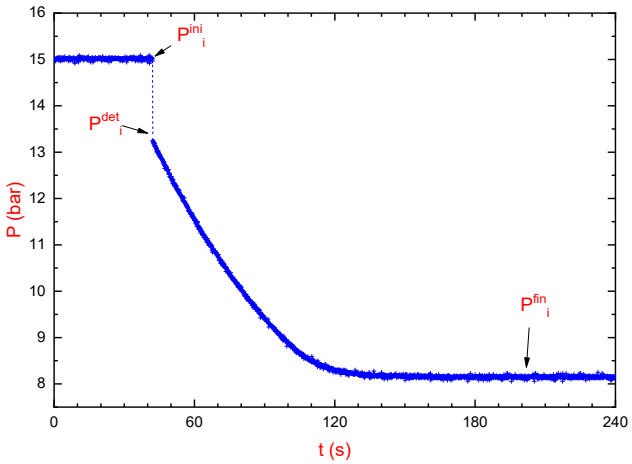


Figure 3.15 Pressure as function of time during one absorption point. The valve of the sample holder was opened at time t = 42 s. Equilibrium pressure is assumed to be reached after 200 s.

The calculation of hydrogen absorption capacities requires precise moles of hydrogen present in a volume at a given pressure and temperature. Considering the ideal gas model is not suitable for high pressures, Hemmes model is thus adopted because it takes into account the deviation from ideality of hydrogen at high pressure [225]. These two models are embedded into the Excel for calculation. Absorption capacity values can be calculated at room temperature with the ideal gas model for pressures up to 10 bar. Above that, it is preferable to use the Hemmes model to minimize the errors related to the deviation from the ideality of hydrogen at high pressure.

### 3.4.3 Sample preparing

The ingots were mechanically crushed and grounded into powder with size below 150 μm for hydrogenation measurements. The sample weights required for the apparatus in ICMPE and GRINM are around 0.5 g and 2.0 g respectively. Normally, there is a preliminary treatment on the sample before the measurements, using the high vacuum (~ $10^{-5}$ bar) and high temperature (150 ℃ ~ 200 ℃).

## 3.5 Thermal analysis

The thermal experiments in this thesis are commonly exerted on hydrogenated samples, to observe the structural evolution during hydrogen desorption. Differential Scanning Calorimetry (DSC 25 TA) (see Figure 3.16a) is used to observe and quantify the enthalpy changes of a material as a function of temperature or time during a controlled thermal cycle. The temperature of required for this equipment is normally below 600 ℃. Figure 3.16b shows the apparatus ATG, which is used to measure the change in mass of a sample when subjected to a programmable temperature change in a controlled atmosphere. We can calculate the amount of hydrogen released from the sample, thus determine the hydrogen absorption capacity and calculate the enthalpy.

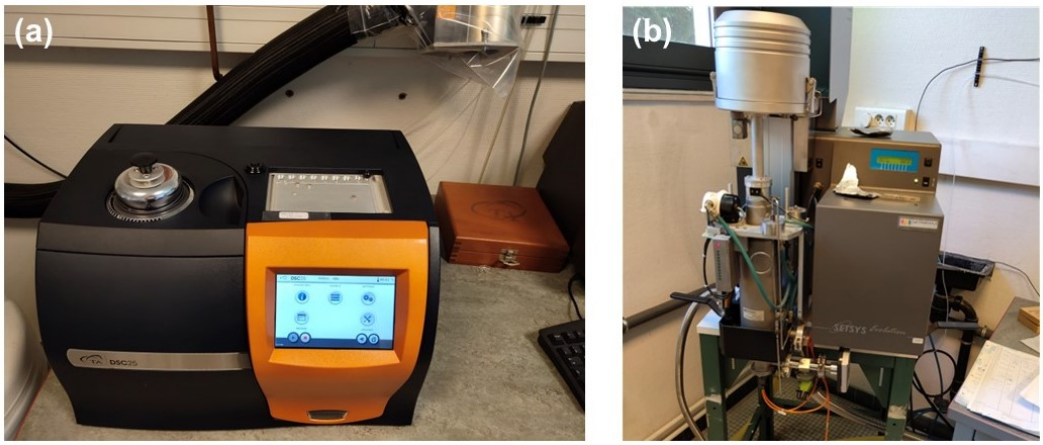


Figure 3.16 The DSC (a) and ATG (b) apparatus for thermal measurement.

Figure 3.17 shows the program of the thermal measurement. After the starting temperature which stabilizes at 40 ℃, the samples were heated to a target temperature. Upon cooling, the temperature decreased to a temporary temperature of 100 ℃ and the second cycle was carried out subsequently. Both the heating and cooling rate is 5 ℃/min, the starting and temporary temperatures are variable.

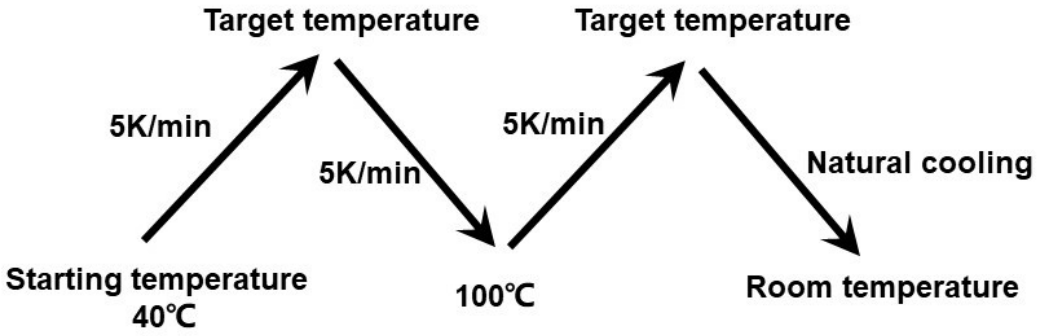


Figure 3.17 The experimental conditions and program settings of the thermal analysis.

## 3.6 Density Functional Theory calculations

DFT calculation was performed by University of New South Wales (UNSW), to ascertain the effect of vacancies and Mn anti-occupation on the stability of the structures. The programs and parameters used in this thesis are as follows.

Energies of all configurations were obtained employing DFT as implemented in the Vienna *ab initio* simulation program (VASP) [226], and the Perdew, Burke, and Ernzerhof (PBE) formulation of the generalized gradient approximation [227,228] from the VASP 5.3 repository. A plane-wave cut-off of 350 eV and k point grid of 2×4×4 was opted after a group of convergence tests on the optimized structures. The electronic wave functions in Brillouin zone were sampled via the Monkhorst-Pack method [229]. A first-order Methfessel-Paxton smearing function [230] of width 0.1 eV was applied to treat partial occupancies.

Thermodynamic properties associated with each configurational disorder was obtained using Boltzmann's statistics [231].

Enthalpy of formation of each structure, assuming forming from solid Yttrium, solid Nickel and alpha manganese, was calculated as:

$$\Delta E_f = \frac{\mu(Comp.) - (x)\mu(Y) - (y)\mu(Ni) - (z)\mu(Mn)}{x + y + z}$$

where $\mu$ is the chemical potentials of the compound and reference phases, taken from the DFT total energy of a unit cell containing $x$ Y, $y$ Ni and $z$ Mn atoms. Half of the DFT energy of a Yttrium hcp unit cell, one-fourth of the DFT energy of a bcc Ni unit cell and one-twenty ninth of $\alpha$-Mn unit cell were taken for $\mu$(Y), $\mu$(Ni) and $\mu$(Mn), respectively. Due to practical limitations, vibrational energy and entropy contributions to the enthalpy of formation were not included.

Finally, combining the calculation works performed by UNSW and the experimental works performed in ICMPE, we will systematically discuss the effects of vacancies and Mn anti-occupation on structural stability.

# 4 . *B*-substituted effects on structure and hydrogen sorption properties of $Y_xNi_{2-y}M_y$ (M = Al, Mn) compounds

Upon hydrogenation $AB_2$-type compounds suffer from hydrogen-induced amorphization (HIA) or hydrogen-induced disproportionation (HID) due to their poor structural stability. The structural stability is closely related to their atomic radii ratio $r_A/r_B$,= 1.37, above which HIA occurs. The rare earth based $RNi_2$ intermetallic compounds exhibit high $r_R/r_{Ni}$ value up to 1.4 because of the large atomic radii of lanthanides. Subsequently, a larger structural instability for light rare earths than for the heavy ones has been observed [123,201]. Therefore, we adopted $YNi_2$ as the initial compound because Y has a medium atomic radius of 1.8 Å (close to that of Gd) [136] and a much lower molar mass than ones of lanthanides. Thus, Y-based $AB_2$-type compounds with *C*15 Laves phase structure should provide better structural stability and larger gravimetric hydrogen absorption capacity than lanthanide-based compounds.

To further reduce the atomic radius ratio and improve the structural stability, the element substitution had been tried and proved its efficiency on suppressing HIA. This chapter will present the structural evolutions and hydrogen sorption properties of $YNi_2$-based compounds with *B*-side substitution. Al and Mn are considered as they have bigger atomic radius than Ni and are currently used to improve the hydrogen storage properties in $AB_5$ system.

## 4.1 Investigation of the phase occurrence and H sorption properties in the $YNi_{2-y}Al_y$ ($0 \leq y \leq 1$) compounds

### 4.1.1 Synthesis and characterization of the compounds

Compounds with nominal compositions $YNi_{2-y}Al_y$ ($y$ = 0, 0.05, 0.10, 0.15, 0.20, 0.25, 0.50, 0.75, 1) were prepared by induction melting of high-purity metals (Y: 99.9 wt.%, Ni: 99.995 wt.%, Al: 99.99 wt.% from Trillion Metals Co., Ltd.) in high purity argon atmosphere (5N) under a pressure of 0.04 MPa in a water-cooled copper crucible. The ingots were turned over and re-melted three times to ensure homogeneity. Then, parts of the as-cast ingots were mechanically crushed and ground into powder for hydrogenation measurements (< 150 µm) and for X-Ray diffraction (XRD) analysis (< 37 µm).

### 4.1.2 Phase compositions and structures for $YNi_{2-y}Al_y$ compounds

#### 4.1.2.1 $YNi_2$ ($y$ = 0)

The Rietveld refinement of the X-ray data for $YNi_2$ is shown in Figure 4.1a and the crystallographic data are summarized in Table 4.1. $YNi_2$ crystallizes in the previously described $Y_{0.95}Ni_2$ superstructure (space group $F\bar{4}3m$) [122,126]. The Rietveld analyses show that small amount of YNi (6 wt.%) and $Y_2O_3$ (2 wt.%) are also present as secondary phases as confirmed by EPMA analyses (Figure 4.1b). As already reported, the superstructure is related to a lowering of symmetry (space group $F\bar{4}3m$) due to formation of ordered yttrium vacancies on the 4*a* site, allowing to release the stress induced by the large $r_A/r_B$ ratio. Lattice parameter and atomic occupation obtained in this work are in good agreement with literature data [122,126]. The

observed vacancy ratio (0.6) on the 4*a* site is slightly smaller than published (0.7) [122], which yields to the stoichiometry $Y_{0.96}Ni_2$ in agreement with the EPMA analyses (Figure 4.1b).

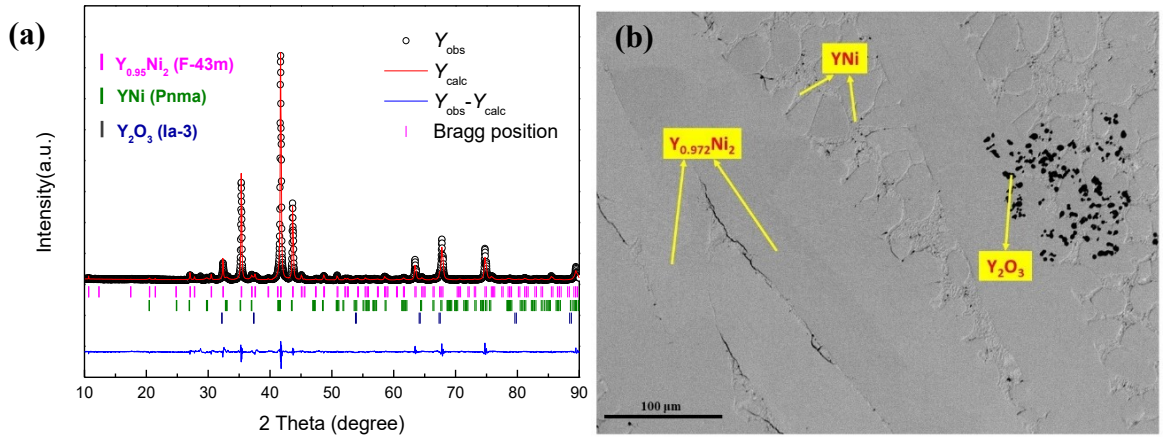


Figure 4.1 Rietveld refinement of X-ray diffraction pattern (a) and EPMA back scattered electron image (b) of $YNi_2$ ($y = 0$).

Table 4.1 Composition determined by ICP, EPMA and crystallographic data of $Y_{0.96}Ni_2$ from Rietveld refinement.

| | | | | |
|---|---|---|---|---|
| Composition by ICP | $Y_{0.96}Ni_2$ | | | |
| Composition by EPMA | $Y_{0.97(1)}Ni_2$ | | | |
| Composition by Rietveld | $Y_{0.96(1)}Ni_2$ | | | |
| Atom parameters | Site | Atom | Coordinates | Site occupation factors |
| | 4*a* | Y1 | $x = 0$ | 0.40 (1) |
| | 4*b* | Y2 | $x = 1/2$ | 1 |
| | 16*e* | Y3 | $x = 0.1028$ (3) | 1 |
| | 16*e* | Y4 | $x = 0.6287$ (3) | 1 |
| | 24*g* | Y5 | $x = 0.0075$ (5) | 1 |
| | 16*e* | Ni1 | $x = 0.3086$ (4) | 1 |
| | 16*e* | Ni2 | $x = 0.8136$ (5) | 1 |
| | 48*h* | Ni3 | $x = 0.0652$ (4) | 1 |
| | | | $x = 0.8073$ (6) | |
| | 48*h* | Ni4 | $x = 0.0626$ (4) | 1 |
| | | | $z = 0.3128$ (6) | |
| R-factors | $R_p = 6.02$, $R_{wp} = 8.23$, $R_{Bragg} = 5.51$ | | | |
| Space group | $F\bar{4}3m$ | | | |
| Cell parameter *a* (Å) | 14.3561 (3) | | | |
| Number of formula units Z | 64 | | | |
| Volume per formula *V* (Å3) | 46.23 (1) | | | |
| Phase abundance | 92% | | | |

### 4.1.2.2 $YNi_{2-y}Al_y$ ($0.05 \leq y \leq 0.25$)

The relevant XRD patterns and EPMA analyses of the $YNi_{2-y}Al_y$ ($0.05 \leq y \leq 0.25$) samples are shown in Figure 4.2 (Rietveld refinements are given in Figure 4.3), the results of Rietveld

and EPMA analysis are given in Table 4.2 ($0.05 \leq y \leq 0.25$). The absence of extra peaks related to the superstructure indicates that all Al-substituted compounds crystallize in the Y(Ni, Al)$_2$ ($AB_2$) type $C15$ structure. Meanwhile, Y(Ni, Al)$_3$ ($AB_3$) and YNi ($AB$) appear as secondary phases for $y = 0.05$ and 0.10 respectively. The percentages of secondary phases increase with Al content, and $AB_2$ type structure disappears for $y \geq 0.25$. Indeed, for samples with $y = 0.20$ and 0.25 Y(Ni, Al)$_3$ becomes the main phase (see Figure 4.3d and e). The crystal structure of Y(Ni, Al)$_3$ adopts the $R$-type stacking ($R\bar{3}m$) polymorph for high Al content ($y = 0.20$, 0.25) whereas the $H$-type stacking ($P6_3/mmc$) is favored at low Al content ($0.05 \leq y \leq 0.15$). As observed in the EPMA backscattered electron images (Figure 4.2b), the extent of dark gray regions, forming stripes and corresponding to the $AB_3$-type phase rises significantly with Al content, whereas that of light gray regions, attributed to $AB_2$-type phase, decreases. The $AB$-type YNi phase (white areas) is located within the light gray regions and its percentage grows gradually with Al content for $0.10 \leq y \leq 0.25$. $Y_2Ni_2Al$ (white areas) is another secondary phase with a similar phase abundance to YNi. However, after an increase percentage from 0 to 13 wt.%, the abundance of $Y_2Ni_2Al$ phase keeps unchanged for $0.15 \leq y \leq 0.25$. Furthermore, we notice the various solubilities of Al in $Y_2Ni_2Al$ phase ($Y_2Ni_2Al_{1-z}$), which deserves more discussion later.

Upon substitution, one can observe an increase of the lattice parameters and cell volumes with Al content for both $AB_2$ and $AB_3$ phases (Table 4.2). This is consistent with the increasing Al content substituted to Ni inside both $AB_2$ and $AB_3$ phases as measured by EPMA. Furthermore, the yttrium content analyzed by EPMA in all $AB_2$ phases remains sub-stoichiometric (around 0.95), confirming the existence Y-site vacancies, but disordered opposing to the Al-free superstructure phase. On the other hand, the lattice parameters of the $AB$ phase remain almost constant, showing that the Al content in the $AB$ phase is negligible in agreement with EPMA analyses.

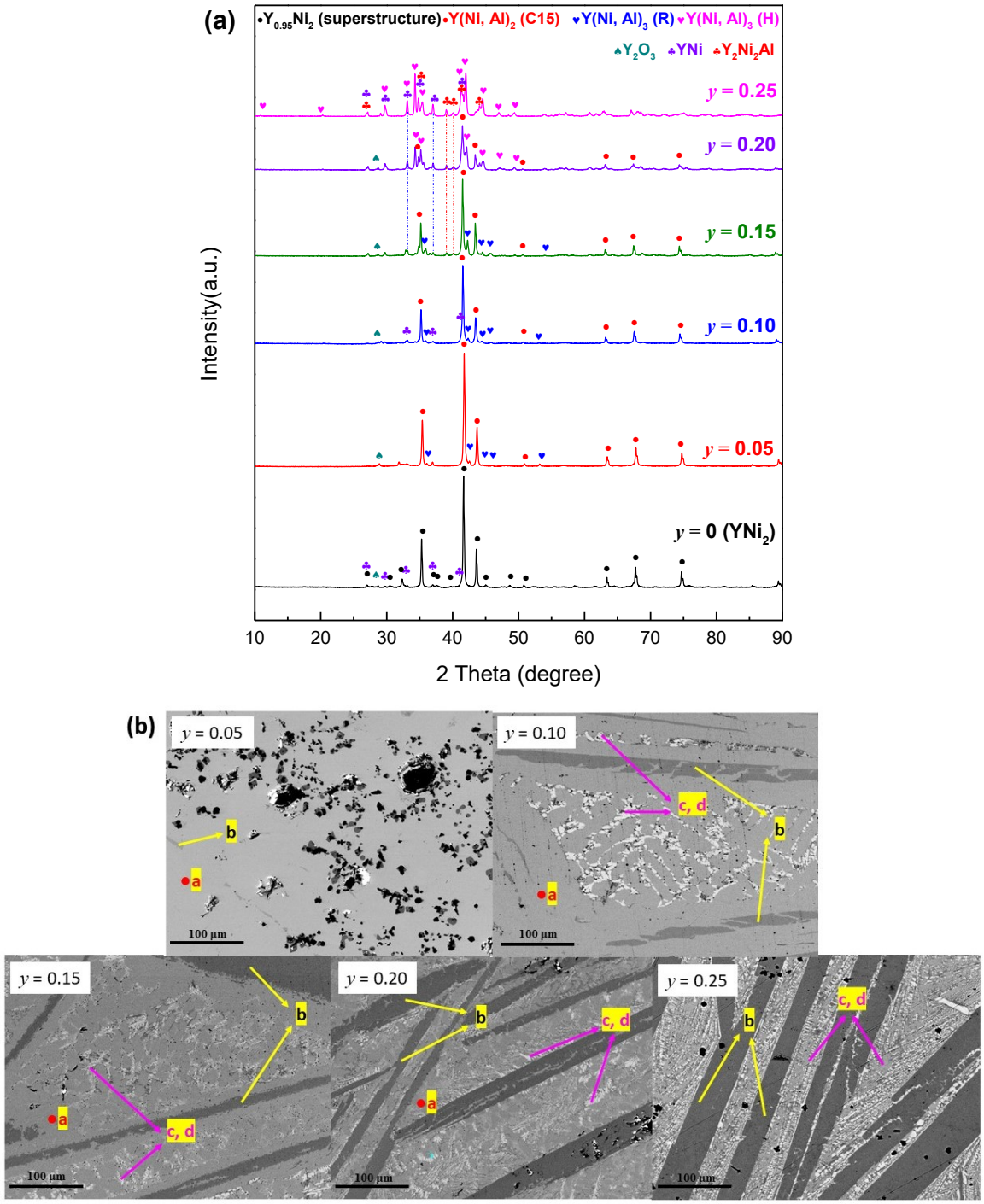


Figure 4.2 X-ray diffraction patterns (a) and EPMA back scattered electron images (b) for $0 \leq y \leq 0.25$: a - $AB_2$ phase (light gray); b - $AB_3$ phase (dark gray); c, d - $AB$ and $Y_2Ni_2Al$ phases (white). The deep-black regions are attributed to Y oxide and some cracks produced during grinding.

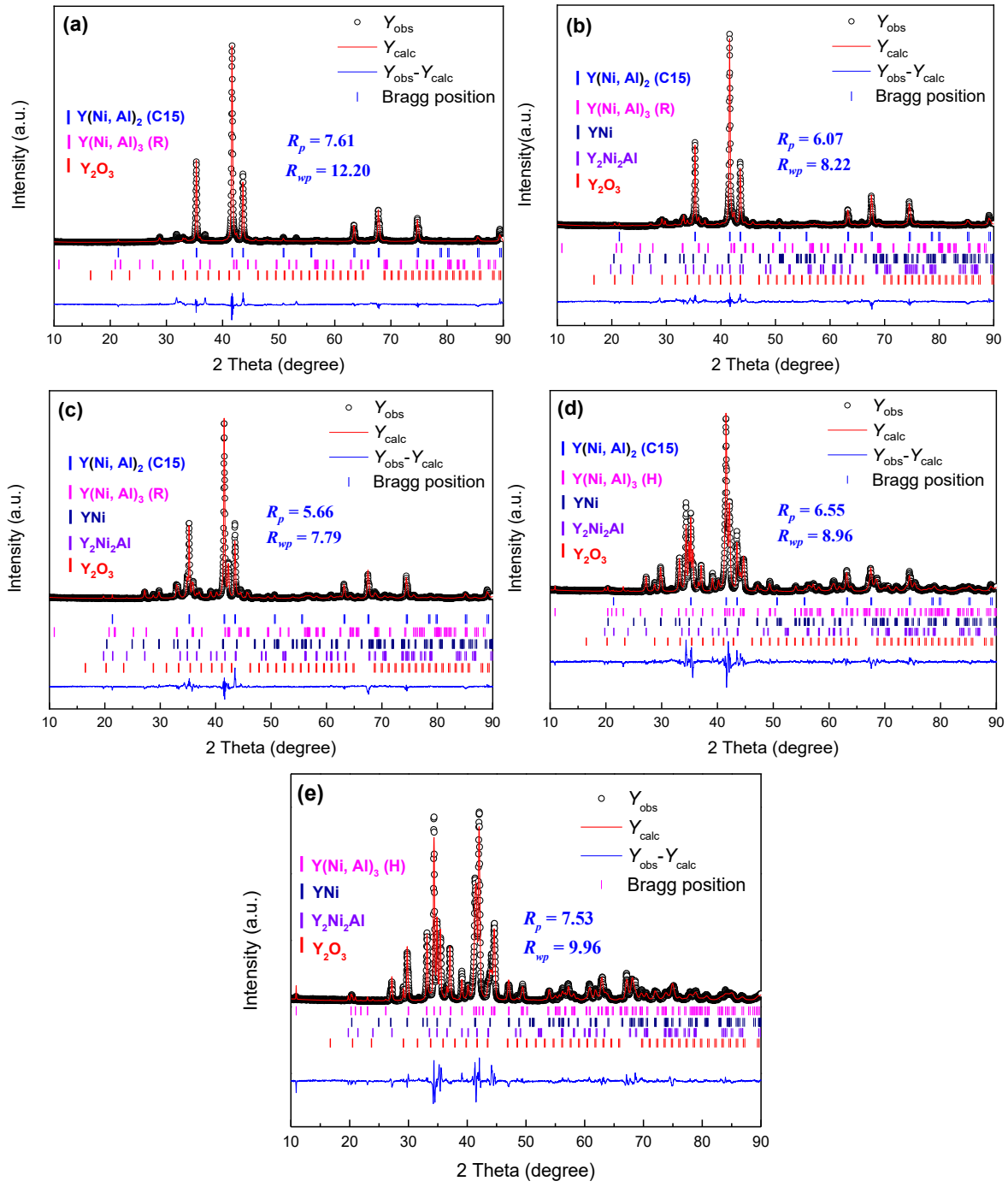


Figure 4.3 Rietveld refinements of the XRD patterns for $YNi_{2-y}Al_y$ compounds: a – $y = 0.05$, b – $y = 0.10$, c – $y = 0.15$, d – $y = 0.20$, e – $y = 0.25$.

Table 4.2 Phase compositions determined by ICP, EPMA, phase abundance and crystallographic data from Rietveld refinement for $YNi_{2-y}Al_y$ ($y$ = 0.05, 0.10, 0.15, 0.2, 0.25) samples.

| Compounds | | ***y*** | **0.05** | **0.10** | **0.15** | **0.20** | **0.25** |
|---|---|---|---|---|---|---|---|
| | | ICP (±0.01) | $Y_{0.95}Ni_{1.95}Al_{0.05}$ | $Y_{0.96}Ni_{1.90}Al_{0.10}$ | $Y_{0.97}Ni_{1.85}Al_{0.15}$ | $Y_{0.96}Ni_{1.80}Al_{0.20}$ | $Y_{0.99}Ni_{1.76}Al_{0.24}$ |
| Phases | Y (Ni, Al)$_2$ ($C15$, $Fd\bar{3}m$) | EPMA (±0.02) | $Y_{0.94}Ni_{1.94}Al_{0.05}$ | $Y_{0.95}Ni_{1.91}Al_{0.09}$ | $Y_{0.96}Ni_{1.89}Al_{0.15}$ | $Y_{0.95}Ni_{1.88}Al_{0.12}$ | |
| | | $a$ (Å) | 7.1822 (2) | 7.1985 (2) | 7.2073 (2) | 7.2072 (4) | |
| | | $V$ (Å$^3$) | 370.49 | 373.00 | 374.39 | 374.44 | |
| | | Abundance (wt.%) | 89% | 76% | 54% | 24% | |
| | | $R_{Bragg}$ | 6.64 | 5.63 | 6.44 | 7.05 | |
| | Y (Ni, Al)$_3$ $R\bar{3}m \leq 0.15$ $P6_3/mmc \geq 0.20$ | EPMA (±0.02) | - | $Y_{1.03}Ni_{2.85}Al_{0.15}$ | $Y_{1.03}Ni_{2.79}Al_{0.21}$ | $Y_{1.03}Ni_{2.70}Al_{0.30}$ | $Y_{1.03}Ni_{2.61}Al_{0.39}$ |
| | | $a$ (Å) | 4.988 (1) | 5.0019 (9) | 5.0208 (3) | 5.0457 (3) | 5.0667 (3) |
| | | $c$ (Å) | 24.427 (1) | 24.4410 (8) | 24.4006 (4) | 16.2664 (1) | 16.2349 (1) |
| | | $V$ (Å$^3$)/$AB_3$ | 175.58 | 176.50 | 177.57 | 179.34 | 180.48 |
| | | Abundance (wt.%) | 5% | 10% | 19% | 46% | 63% |
| | | $R_{Bragg}$ | | 23.30 | 8.72 | 7.63 | 4.06 |
| | YNi ($Pnma$) | EPMA (±0.02) | - | $YNi_{1.00}$ | $YNi_{1.02}Al_{0.01}$ | $YNi_{1.04}Al_{0.02}$ | $YNi_{0.99}$ |
| | | $a$ (Å) | | 7.121 (1) | 7.146 (1) | 7.137 (2) | 7.1365 (8) |
| | | $b$ (Å) | | 4.1377 (1) | 4.1394 (1) | 4.1296 (1) | 4.1280 (1) |
| | | $c$ (Å) | | 5.5134 (1) | 5.4938 (2) | 5.5096 (1) | 5.5140 (1) |
| | | $V$ (Å$^3$) | | 162.45 | 162.51 | 162.38 | 162.44 |
| | | Abundance (wt.%) | | 5% | 12% | 16% | 23% |
| | | $R_{Bragg}$ | | | 10.50 | 5.88 | 5.32 |
| | $Y_2Ni_2Al$ ($Immm$) | EPMA (±0.02) | - | $Y_2Ni_{2.48}Al_{0.18}$ | $Y_2Ni_{2.42}Al_{0.40}$ | $Y_2Ni_{2.42}Al_{0.42}$ | $Y_2Ni_{2.32}Al_{0.54}$ |
| | | $a$ (Å) | | 4.1615 (1) | 4.153 (1) | 4.154 (1) | 4.1545 (7) |
| | | $b$ (Å) | | 5.3478 (6) | 5.3374 (1) | 5.3323 (1) | 5.3385 (1) |
| | | $c$ (Å) | | 8.2247 (8) | 8.3008 (1) | 8.3015 (1) | 8.3049 (1) |
| | | $V$ (Å$^3$) | | 183.05 | 184.02 | 183.88 | 184.20 |
| | | Abundance (wt.%) | | 4% | 13% | 12% | 12% |
| | | $R_{Bragg}$ | | | 11.90 | 8.90 | 9.04 |
| | $Y_2O_3$ ($Ia\bar{3}$) | Abundance (wt.%) | 6% | 5% | 2% | 2% | 2% |

### 4.1.2.3 $YNi_{2-y}Al_y$ ($0.50 \leq y \leq 1.00$)

Figure 4.4a shows the XRD patterns for $0.50 \leq y \leq 1.00$. For $y = 0.50$, the XRD pattern can be indexed with cubic $Y_3Ni_6Al_2$ ($Ca_3Ag_8$-type, $Im\bar{3}m$) [232] and orthorhombic $Y_2Ni_2Al$ ($W_2CoB_2$-type, *Immm*) [233] structures beside a small quantity (< 5 wt.%) of $Y_2O_3$. For the sample with $y = 0.75$, the hexagonal YNiAl phase ($Fe_2P$-type, $P\bar{6}2m$) [234] appears as the main phase with some $Y_2Ni_2Al$ and $Y(Ni, Al)_5$ (*P6/mmm*) secondary phases. For the sample with $x = 1.00$, YNiAl is almost single-phase with very small amount (≤ 3 wt.%) of $Y_2Ni_2Al$ and $Y(Ni, Al)_5$ (see the refinements given in Figure 4.5). The lattice parameters, cell volumes and phase amount obtained from Rietveld analyses of the XRD patterns are given in Table 4.3. For this Al content region, the *AB*, $AB_2$, and $AB_3$ phases are not detected. EPMA back scattered electron images and corresponding analysis of the as-cast compounds with $y = 0.50, 0.75, 1.00$ are shown in Figure 4.4b and summarized in Table 4.3. The measured compositions for $Y_2Ni_2Al$ and YNiAl phases agree with previously reported ones, though there are deviations on Ni and Al contents from the stoichiometric composition of $Y_2Ni_2Al$. These deviations are accompanied by variations of the lattice parameters (Table 4.3), suggesting a homogeneity domain for this phase rather than a line compound.

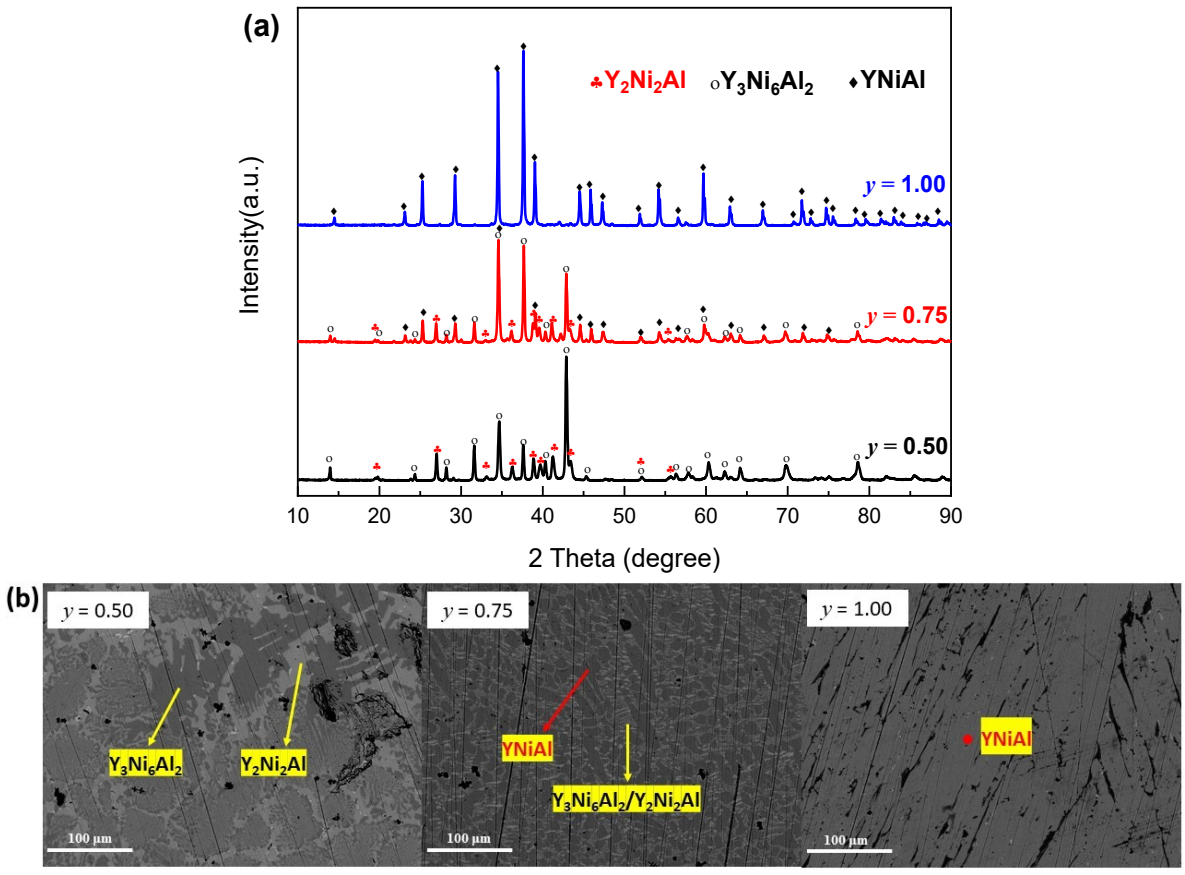


Figure 4.4 X-ray diffraction patterns (a) and EPMA back scattered electron images (b) for $YNi_{2-y}Al_y$ ($0.50 \leq y \leq 1.00$) samples.

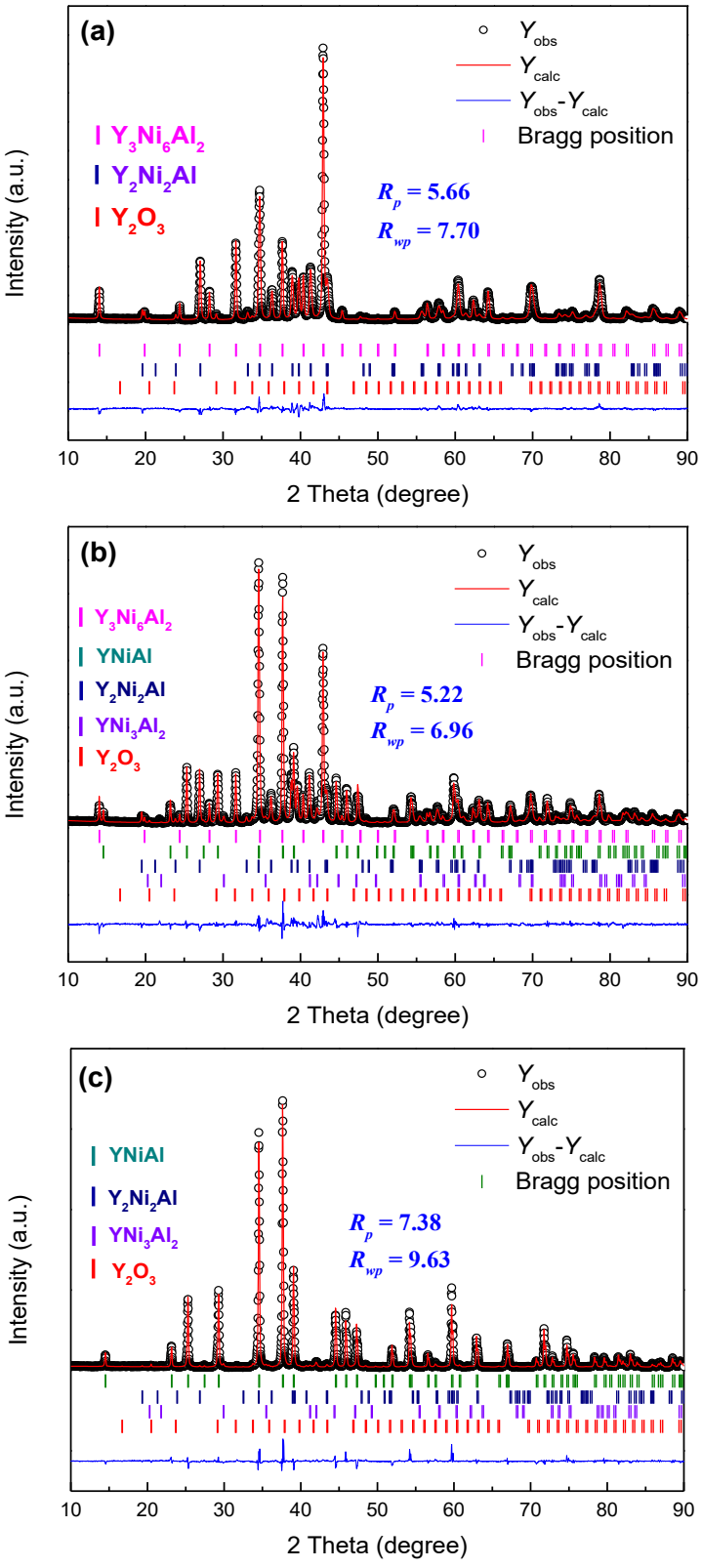


Figure 4.5 Rietveld refinements of the XRD patterns for $YNi_{2-y}Al_y$ compounds: (a) $y$ = 0.50, (b) $y$ = 0.75, (c) $y$ = 1.00.

Table 4.3 Phase composition determined by ICP, EPMA and crystallographic data from Rietveld refinement for $YNi_{2-y}Al_y$ ($0.50 \leq y \leq 1.00$) samples.

| **Compounds** | | ***y*** | **0.50** | **0.75** | **1.00** |
|---|---|---|---|---|---|
| | | ICP (±0.01) | $Y_{0.97}Ni_{1.51}Al_{0.49}$ | $Y_{0.96}Ni_{1.25}Al_{0.75}$ | $Y_{0.97}Ni_{1.01}Al_{0.99}$ |
| **Phases** | $Y_3Ni_6Al_2$ ($Im\bar{3}m$) | EPMA (± 0.02) | $Y_3Ni_{5.91}Al_{1.92}$ | $Y_3Ni_{5.34}Al_{1.95}$ | - |
| | | *a* (Å) | 8.9329 (1) | 8.9360 (2) | |
| | | *V* (Å$^3$) | 712.82 | 713.57 | |
| | | Abundance (wt.%) | 56% | 26% | - |
| | | $R_{Bragg}$ | 4.71 | 3.59 | |
| | $Y_2Ni_2Al$ (*Immm*) | EPMA (± 0.02) | $Y_2Ni_{2.28}Al_{0.70}$ | $Y_2Ni_{2.06}Al_{0.94}$ | - |
| | | *a* (Å) | 4.1593 (2) | 4.1680 (2) | 4.165 (2) |
| | | *b* (Å) | 5.3977 (1) | 5.4220 (3) | 5.509 (3) |
| | | *c* (Å) | 8.3450 (2) | 8.3706 (5) | 8.3413 (6) |
| | | *V* (Å$^3$) | 187.35 | 189.17 | 191.44 |
| | | Abundance (wt.%) | 42% | 26% | 1% |
| | | $R_{Bragg}$ | 5.86 | 4.35 | |
| | YNiAl *($P\bar{6}2m$)* | EPMA (± 0.02) | - | $YNi_{1.01}Al_{1.00}$ | $YNi_{0.95}Al_{0.98}$ |
| | | *a* (Å) | | 7.0306 (1) | 7.0410 (2) |
| | | *c* (Å) | | 3.8327 (1) | 3.8411 (3) |
| | | *V* (Å$^3$) | | 164.06 | 164.92 |
| | | Abundance (wt.%) | - | 42% | 95% |
| | | $R_{Bragg}$ | | 3.11 | 5.30 |
| | $Y(Ni, Al)_5$ *(P6/mmm)* | *a* (Å) | | 5.0298 (3) | 5.058 (1) |
| | | *c* (Å) | | 4.0711 (4) | 4.0827 (2) |
| | | *V* (Å$^3$) | | 89.20 | 90.48 |
| | | Abundance (wt.%) | - | 5% | 2% |
| | $Y_2O_3$ ($Ia\bar{3}$) | Abundance (wt.%) | 2% | 1% | 2% |

### 4.1.2.4 Discussion on structural properties

***$Y_{0.95}Ni_2$ phase with superstructure***

$YNi_2$ crystallizes in the superstructure described in the lower symmetry $F\bar{4}3m$ space group with Y:Ni stoichiometry 0.95:2. This superstructure is characterized by ordered Y vacancies on the 4*a* site and a doubling of the lattice parameter of the Laves phase (*a* = 14.35 Å). For $ANi_2$ (*A* = Y, rare earth) binary compounds, the instability of the *C*15 Laves phase structure ($Fd\bar{3}m$) is usually attributed to the large atomic radius ratio $r_A/r_{Ni}$ (up to 1.40) above the geometrical ideal one (1.225). The introduction of *A* vacancies allows relaxing constraints thus stabilizing the structure [123]. Therefore, the formation of $Y_{0.95}Ni_2$ superstructure with Y vacancies occurs instead of the ideal *C*15 Laves phase structure for *y* = 0. To allow chemical balance, some YNi

phase is formed. We observed 6 wt.% YNi and 2 wt.% yttrium oxide. This value closely agrees to the calculated 6.8 wt.% YNi expected from the stoichiometric reaction: $YNi_2 \Rightarrow 0.952\ Y_{0.95}Ni_2 + 0.095YNi$.

***$Y_{1-y}$(Ni, Al)$_2$ - C15 phase***

Figure 4.6 shows the phase abundance as the function of the nominal Al content for $0 \leq y \leq 0.25$, where the $AB_2$ amount decreases monotonously down to vanish at $y = 0.25$. For the sake of comparison, $Y_{0.95}Ni_2$ is accounted as an $AB_2$ phase even if it is off-stoichiometric with superlattice structure. As the nominal aluminum content increases to $y = 0.05$, a reversed structural transformation for Al-free $YNi_2$ ($y = 0$) from superstructure to $C15$ Laves phase structure for Y(Ni, Al)$_2$ solid solution ($0 < y \leq 0.15$) can be observed. Al-containing compounds are multiphase, but the main phase is indeed the $AB_2$ one for $y \leq 0.15$. Nevertheless, EPMA shows a systematic sub-stoichiometry for yttrium indicating the formation of disordered Y vacancies. Therefore, the substitution of Ni by Al favors the formation of the $C15$ structure without Y-vacancy ordering compared to the binary $Y_{0.95}Ni_2$. Similar behavior was observed with $B$ = Cu or Fe in the $Y_{0.95}Ni_{2-y}B_y$ system, showing for specific substitution ratio the $C15$ structure with disordered Y vacancies, *i.e.*, without superstructure [203].

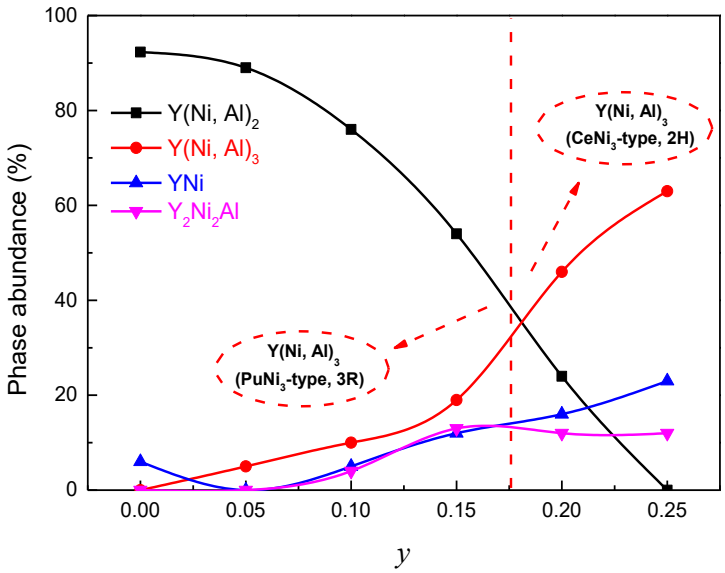


Figure 4.6 Phase abundance as the function of the nominal Al content for $0 \leq y \leq 0.25$. $AB_3$ phase exhibits $PuNi_3$-type structure below $y = 0.15$ and $Ce_3Co_8Si$-type structure above this value, the dashed line is a guide for eyes indicating the structure change of $AB_3$ phase.

Above $y = 0.15$, the $AB_2$ phase becomes secondary and disappears at $y = 0.25$ to the profit of $AB_3$ that increases up to 63 wt.%.

Figure 4.7 shows the evolution of the lattice constant and cell volume of the $AB_2$-type $YNi_{2-z}Al_z$ phase with nominal Al content (bottom-axis $y$) and Al content measured EPMA (top-axis $z$). The lattice constant increases linearly with Al as expected for a solid solution following the Vegard's law [204], except at low $y$ values (0 - 0.15) for which the structural change occurs

at nearly constant volume. For nominal contents $0.15 \leq y \leq 0.20$, both the Al content ($z = 0.11$ and 0.12, from EPMA, respectively) and the lattice constant ($a = 7.2073$ Å) of the $AB_2$-type phase remain constant. This indicates that the solubility limit of Al in $YNi_{2-z}Al_z$ $C15$ structure is reached and is limited to $z \approx 0.12$.

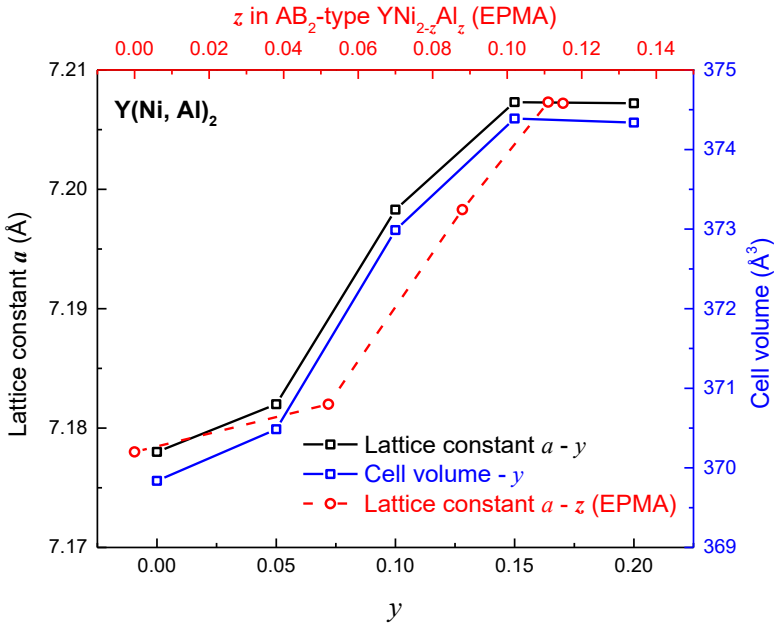


Figure 4.7 Lattice constants and cell volumes of $Y(Ni, Al)_2$ as function of nominal Al content in $YNi_{2-y}Al_y$ compounds (below) as well as Al content in the $Y(Ni, Al)_2$ phases obtained by EPMA (top).

### *Y(Ni, Al)$_3$ phase with stacking structure*

As shown in Figure 4.6, the $AB_3$ emerges as a second phase when Al content reaches $y = 0.05$ and becomes the main phase, increasing to 63 wt.%, for $y = 0.25$. It is interesting to note the structural change for $Y(Ni, Al)_3$ from rhombohedral ($PuNi_3$-type, $3R$) for $y \leq 0.15$ (*i.e.*, $YNi_{2.8}Al_{0.2}$) to hexagonal ($CeNi_3$-type, $2H$) for $y \geq 0.20$ (*i.e.*, $YNi_{2.7}Al_{0.3}$; see Table 4.2, Figure 4.3c and d). Similar results have been reported for $La(Ni, Mn)_3$ phase [235]. Indeed, Denys *et al.* found that substituting Ni for Mn in the $LaNi_{3-w}Mn_w$ system induces a structural transition from rhombohedral ($3R$) to hexagonal ($2H$) for $w > 0.1$. It can be hypothesized that Ni substitution by larger atoms like Al or Mn promotes the formation of the hexagonal structure rather than the rhombohedral one. Similar results have been also reported for the $A_2Ni_7$ ($A$ = Rare Earth) systems with stacking structure and they have been related to geometrical effects [81,236–238].

Figure 4.8 shows the lattice constant and cell volume evolutions for $Y(Ni, Al)_3$ with nominal Al content $y$ (bottom axis, solid line) and Al content $z$' obtained by EPMA (top axis, dashed line). For the sake of comparison between $R$ and $H$ crystal structures, the lattice constant $c$ of the hexagonal structure is multiplied by 3/2. One can notice that the lattice constant $a$ increases almost linearly with $y_{Al}$. The lattice constant $c$ tends to decrease, which means that the lattice expands along the *basal* plane and contracts slightly along the $c$ axis. This

phenomenon can be explained presuming that Al behaves like Mn in $LaNi_{3-w}Mn_w$ where Mn substitutes to Ni only in the [$AB_5$] slab [235]. This leads to an expansion of this slab, a reduced mismatch between the [$AB_5$]and [$A_2B_4$] slabs, and finally causes a lattice expansion in the *ab* plan and shrinkage of the *c* direction.

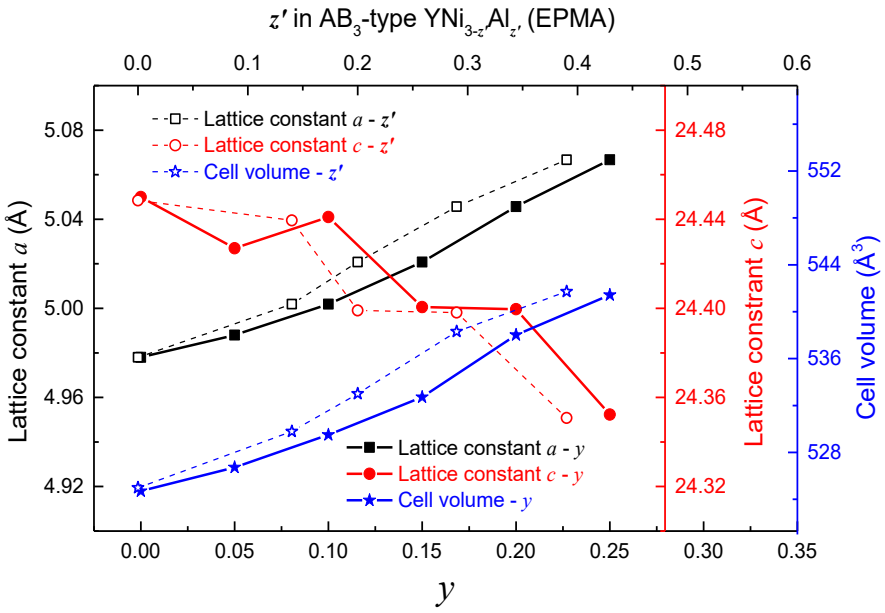


Figure 4.8 Lattice constants *a, c* and cell volumes *V* of $Y(Ni, Al)_3$ phases as function of nominal Al content *y* in $YNi_{2-y}Al_y$ compounds (bottom) as well as Al content obtained by EPMA in the $YNi_{3-z'}Al_{z'}$ phase (top).

For $y$ = 0.20 and 0.25, the EPMA compositions for $AB_3$ are $Y_{1.03}Ni_{2.70}Al_{0.30}$ and $Y_{1.03}Ni_{2.61}Al_{0.39}$ respectively, very close to the reported $Y_3Ni_8Al$ ternary phase [239]. This latter phase crystallizes in a $CeNi_3$-type stacking structure with ordered Al occupation on the 2*a* site. It can be represented as a stacking of $Y_2Ni_3Al$ ($AB_2$ type structure) and $YNi_5$ ($AB_5$-type structure) along the *c*-axis. Indeed, the stacking structure stability is related to the (mis)match of both [$AB_2$] and [$AB_5$] slabs. As the [$AB_2$] slab is originally larger than the [$AB_5$] one, only partial substitutions, either of *A* by smaller atoms (like Mg) in the [$AB_2$] [235,240] or/and of *B* by larger ones (Mn or Al) in the [$AB_5$] are reported to stabilize the stacking structure and improve their hydrogenation, forming a flatter plateau and higher reversibility [217,241,242]. From a first-principle study, the $Y_3Ni_8Al$ structure was determined and the calculation shows that the Al atom occupies the Wyckoff site 2*b* inside the [$AB_5$] slab [243]. Another experimental study on the Y-Ni-Ga system showed that Ga atoms, similar to Al, occupy the 2*c* site in [$AB_5$] slab [244]. Our Rietveld analyses also show that Al occupies preferably the sites in [$AB_5$] slab (Wyckoff sites 2*b* and 2*c*) and at the border between [$AB_2$] and [$AB_5$] slab (Wyckoff site 12*k*). So, from our results, $Y_{1.03}Ni_{2.70}Al_{0.30}$ and $Y_{1.03}Ni_{2.61}Al_{0.39}$ phases are solid solutions with Al occupying preferably the [$AB_5$] slab *B* sites in agreement with literature [235,240]. The result of Rietveld analyses is show in Figure 4.9 by comparison with Al atom occupying only the 2*a* site.

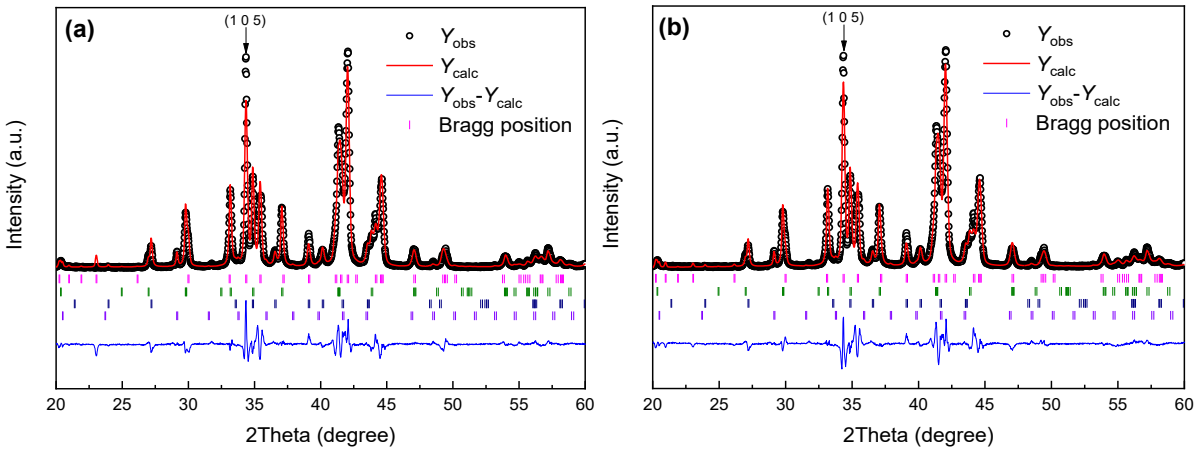


Figure 4.9 Rietveld refinements of the XRD patterns for Y(Ni, Al)$_3$ phase formed in $YNi_{1.75}Al_{0.25}$ compound as Al occupy preferably the site (Wyckoff site 2*a*) in [$AB_2$] slab (a) and the sites (Wyckoff site 2*b*, 2*c* and 12*k*) in [$AB_5$] slab or the border between [$AB_2$] and [$AB_5$] slab (b).

***YNi and $Y_2Ni_2Al$ phases***

As can be seen from Figure 4.6, for $y \leq 0.25$, beside the two main phases $AB_2$ and $AB_3$, two minor phases YNi and $Y_2Ni_2Al$ are formed for the compensation of additional Y induced by the formation of the $AB_3$-type phase. Interestingly, YNi is very poor in Al (see Al composition detected by EPMA from Table 4.2) and it can be considered as a binary compound with very low Al solubility. $Y_2Ni_2Al$ is a ternary compound reported in the literature [245] but not shown in the ternary phase diagram (800 °C) published by Ferro *et al.*[246]. In the present work, $Y_2Ni_2Al$ shows variable Al content. Once increasing the nominal Al content in $YNi_{2-y}Al_y$ samples, the Al content of the $Y_2Ni_2Al$ phase increases from 3.6 at. % to 20 at. % Al along a line joining $Y_2Ni_{2.5}Al_{0.2}$ for $y = 0.05$ to $Y_2Ni_2Al$ for $y = 0.75$.

***YNiAl phase***

As can be seen Figure 4.10, for $y$ values larger than 0.5, the ternary line compounds $Y_3Ni_6Al_2$ and YNiAl are formed instead of $AB_2$ or $AB_3$ pseudo-binary phases. Moreover, the abundances of $Y_3Ni_6Al_2$ and $Y_2Ni_2Al$ decrease rapidly as the Al content approaches the ternary composition YNiAl. In agreement with the Y-Ni-Al phase diagram [247], the composition of the observed compounds are located in the region where the three ternary phases coexist. For $y = 1.00$, expectedly the compound is almost single phase YNiAl with small amount of oxide. As a consequence, in the studied region, there are two-line compounds, YNi and YNiAl. For $YNi_{2-z}Al_z$ $AB_2$ and $YNi_{3-z}Al_z$ $AB_3$ phases, the solution limit of Al is $z = 0.11$ and $z = 0.4$, respectively. For $Y_2Ni_2Al$, the phase can form with Al content as low as $y = 0.2$.

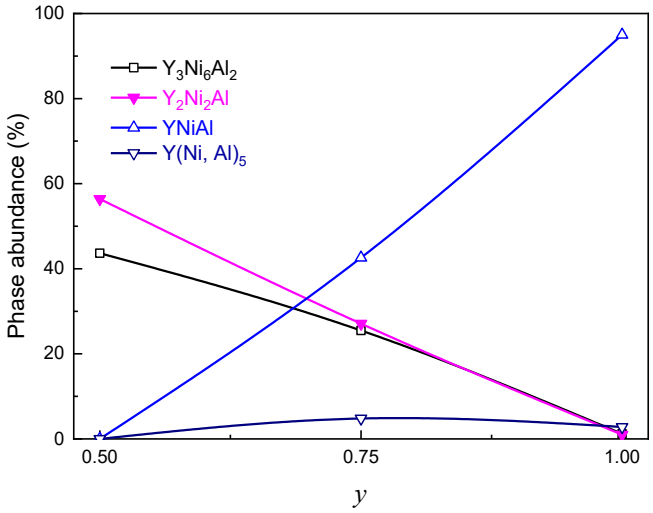


Figure 4.10 Phase abundance of $Y_3Ni_6Al_2$, $Y_2Ni_2Al$, YNiAl and $Y(Ni, Al)_5$ for $0.5 \leq y \leq 1.0$.

### 4.1.3 Hydrogenation sorption properties

Sorption kinetics and cycling stability of $H_2$ uptake/release reactions were tested in a homemade Sieverts-type apparatus under 2 MPa of hydrogen pressure at 25 ℃ for hydrogenation and dynamic vacuum during 1h at 400 ℃ for dehydrogenation. PCI curves were measured at 200 ℃ using the Sieverts' method.

#### 4.1.3.1 Kinetics and cycle properties

The hydrogenation kinetics of all compounds ($0 \leq y \leq 1$) for the first and the fourth hydrogen absorption cycles at 25 ℃ under 2 MPa $H_2$ are shown in Figure 4.11. For the first cycle (Figure 4.11a), after nearly 20 hours, the hydrogen storage capacity of $YNi_2$ attains 1.74 wt.%, which corresponds to the formation of the metal hydride $YNi_2H_{3.6}$. The hydrogen absorption kinetics are much faster at the fourth cycle with full uptake in 5 min (Figure 4.11b). The hydrogen absorption capacity decays significantly after the first cycle, then stabilizes at 1.08 wt.% for $YNi_2$. For Al-substituted compounds ($y > 0$), the kinetics of the first absorption is significantly improved as compared to the Al-free sample. The maximum capacity is reached in less than one hour for $y > 0.10$. As shown in Figure 4.11c, the maximum capacity is as high as 1.8 wt.% for $y = 0.05$ and then decreases monotonously with Al content to reach 0.75 wt.% for YNiAl ($y = 1.00$). After four cycles, the samples with $y = 0.05$, 0.10, 0.15, 0.25 show similar stable capacity around 1.2 wt.%, higher than for the binary $YNi_2$ (1.08 wt.%). For higher aluminum substitution, the capacity is lowered to 0.75 wt.%. It is noticed that YNiAl shows more stable hydrogen absorption behavior although its capacity is low (0.63 wt.%).

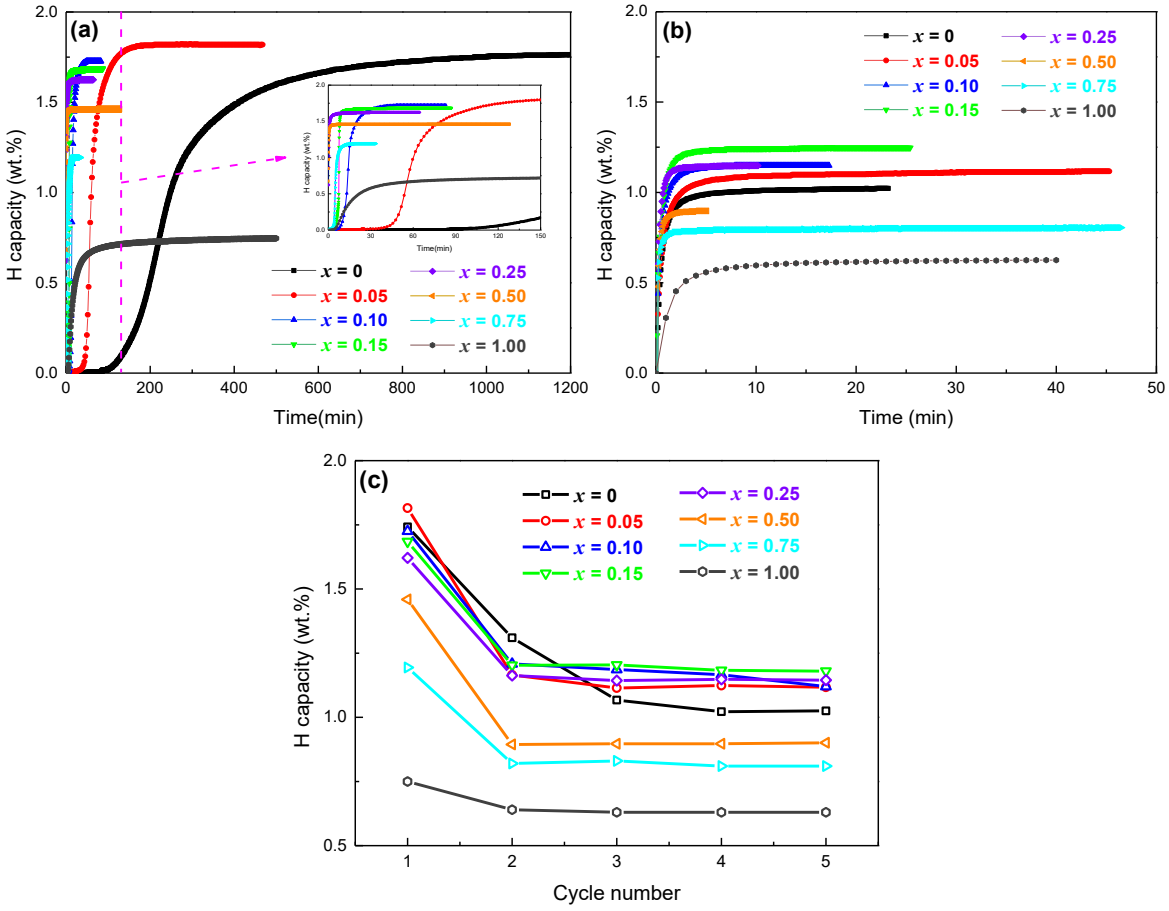


Figure 4.11 Time dependence of the hydrogen absorption for $0 \leq y \leq 1$ compounds at the first (a) and fourth (b) cycle (hydrogenation conditions: $P_{H2}$ = 2 MPa, 25 °C, dehydrogenation conditions: dynamic vacuum, 400 °C); The hydrogen absorption capacity as function of cycle number for $0 \leq y \leq 1$ (c) under same conditions.

### 4.1.3.2 Pressure-composition isotherms (PCI)

Due to the low equilibrium pressure at room temperature, the PCI were measured at 200 °C. For compound with $y$ = 0.05, the PCI shows similar profile to that of $YNi_2$ ($y$ = 0) with higher pressure for the first plateau (0.03 MPa) and sloping behavior for the second one. For $y$ = 0, the two-plateau behavior shows clearly, while for $y$ = 0.10 and 0.15, the first plateau remains present while second one is a sloped branch. At low hydrogen content, the PCI show sloping branches and narrow plateaus at 0.03 MPa between 0.4 H/M and 0.7 H/M, then a sloping curve raising up to 1.2 H/M is observed (Figure 4.12a). For $y$ = 0.25 (Figure 4.12b), up to 0.4 H/M the equilibrium pressure is too low, *i.e.*, below $10^{-5}$ MPa, to be determined by our Sieverts rig. However, a sloping plateau ranging from 0.5 to 1.2 H/M and with pressure of ~ 1 MPa appears, showing good reversibility and very small hysteresis. For $y$ = 1.00, the PCI shows a sloping branch and large hysteresis at 200 °C.

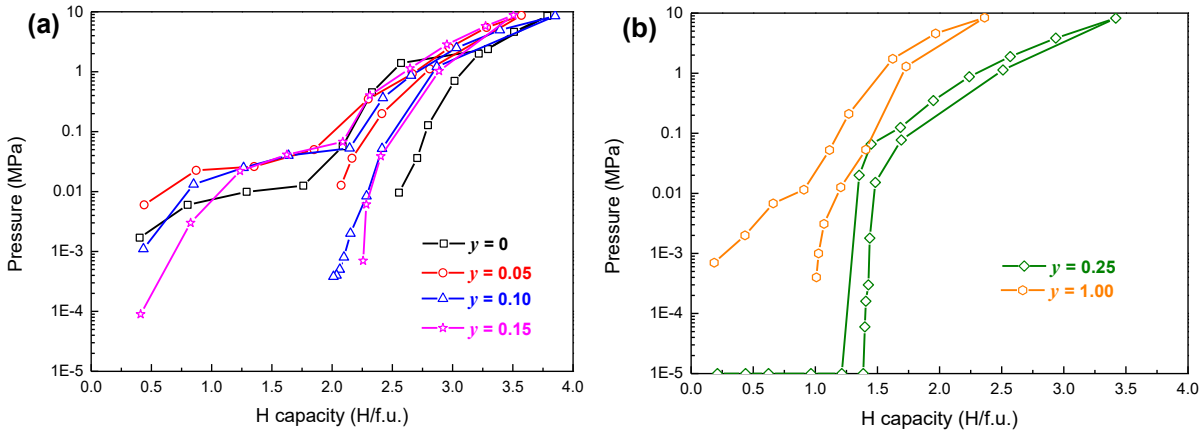


Figure 4.12 *P-C* isotherms measured at 200 °C for $YNi_{2-y}Al_y$ ($0 \leq y \leq 1$) samples.

### 4.1.3.3 Structural evolutions upon hydrogenation

To determine whether structural changes are induced by hydrogenation, the XRD patterns of hydrogenated $YNi_2$ (25 °C under 2 MPa of $H_2$) and dehydrogenated samples $0 \leq y \leq 1$ (dynamic vacuum at 400 °C) have been analyzed. As shown in Figure 4.13 and Table 4.4, for $YNi_2$, the Rietveld analyses of the hydrogenated sample show a cubic $Y_{0.96}Ni_2H_z$ structure with a lattice expansion $\Delta V/V = 18.5$ % in agreement with the literature [122]. After dehydrogenation under dynamic vacuum at 400 °C, the XRD pattern can be indexed with $YNi_3$ and $YH_2$, indicating a disproportionation reaction of the hydride upon hydrogenation cycling.

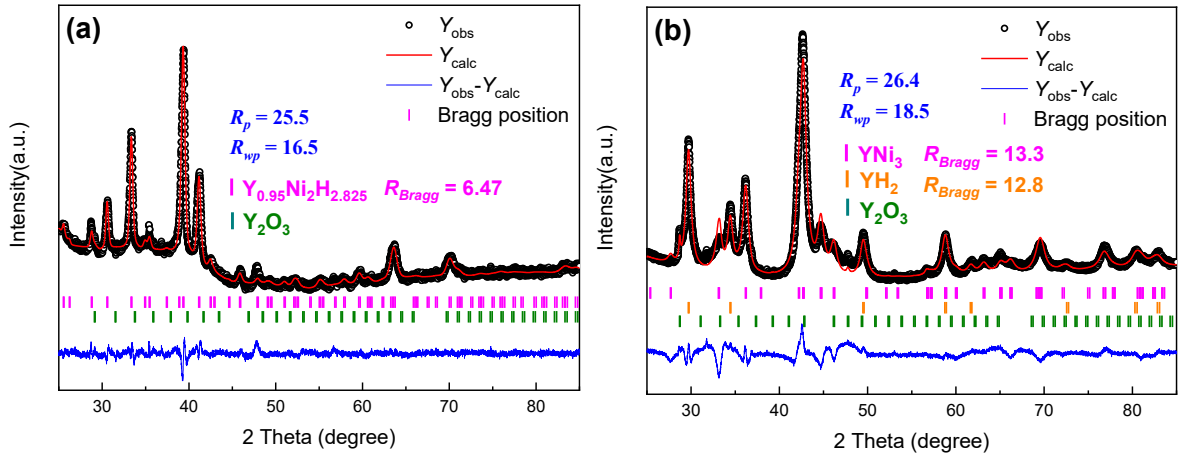


Figure 4.13 Rietveld refinements of XRD patterns for $YNi_2$ upon hydrogenation under hydrogen pressure of 2 MPa at 25 °C (a) and dehydrogenation under dynamic vacuum at 400 °C (b).

Table 4.4 Crystallographic data from Rietveld refinement for $YNi_2$ sample upon hydrogenation and dehydrogenation.

| **Condition** | **Phase** | **X-ray refined parameters** | | | | |
|---|---|---|---|---|---|---|
| | | ***a* (Å)** | ***c* (Å)** | ***V* (Å$^3$)** | **$\Delta V/V$ (%)** | **Occupation (Y: 4*a* site)** |
| Hydrogenated | $Y_{0.95}Ni_2D_{2.6}$ ($F\bar{4}3m$) [122] | 15.113 (1) | | 3451.7 (4) | 16.7% | 0 |
| | $Y_{0.96}Ni_2H_z$ ($F\bar{4}3m$) | 15.192 (1) | | 3506.4 (5) | 18.5% | 1.75 (1) |
| Dehydrogenated | $YNi_3$ ($R\bar{3}m$) | 4.9696 (8) | 24.3253 (4) | 520.2 (1) | | |
| | $YH_2$ ($Fm\bar{3}m$) | 5.210 (1) | | 141.4 (1) | | |

After dehydrogenation under dynamic vacuum at 400 °C, similar behavior is observed for $0.05 \leq y \leq 0.25$ (see Figure 4.14). The pristine compounds contain *C*15 $Y(Ni, Al)_2$, $(Y(Ni, Al)_3$ and few YNi, whereas after hydrogenation/dehydrogenation process, the *C*15 phase is no more observed, but the patterns are indexed with $Y(Ni, Al)_3$ and $YH_2$ (Figure 4.14a). $Y(Ni, Al)_3$ crystalizes in rhombohedral structure up to $y = 0.15$ and in hexagonal structure for $y \geq 0.20$. These results indicate a disproportion of $Y(Ni, Al)_2$ *C*15 phase into $AB_3$ phase and Y hydride upon hydrogenation/dehydrogenation. For higher Al content ($y = 0.50$, 0.75), $Y_3Ni_6Al_2$ and YNiAl phases are still observed after one hydrogenation cycle, but $Y_2Ni_2Al$ disappears and minor $YH_2$ is formed (Figure 4.14b). For $y = 1.00$ (YNiAl), neither structural changes, nor peak broadening are observed in the XRD patterns upon cycling, in agreement with the results reported by Kolomiets [248]. For the compounds containing initially $Y_2Ni_2Al$ and YNi, these two phases cannot be detected after one hydrogenation/dehydrogenation cycle.

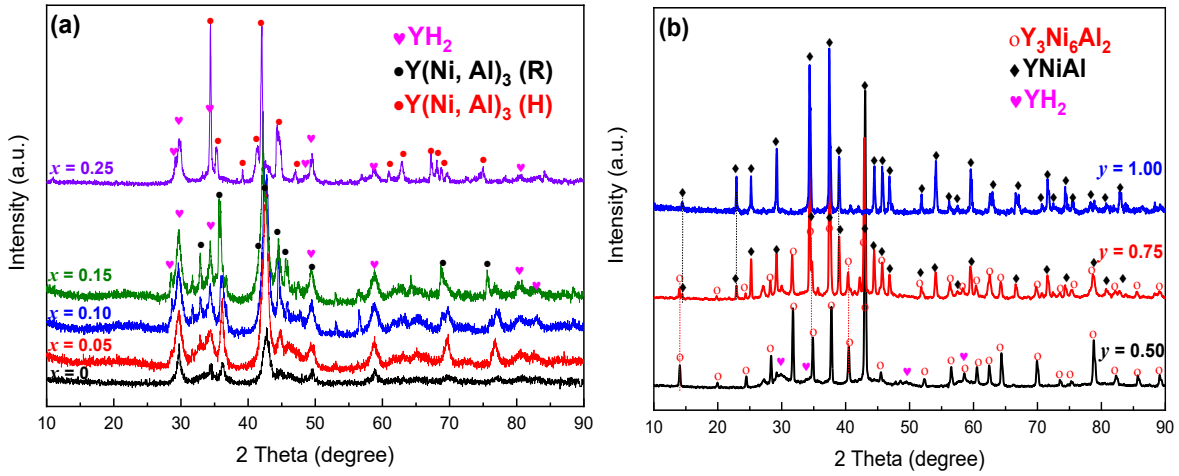


Figure 4.14 X-ray diffraction patterns for $YNi_{2-y}Al_y$ samples (a - $0 \leq y \leq 0.25$, b - $0.50 \leq y \leq 1.00$) after one hydrogenation/dehydrogenation cycle.

### 4.1.3.4 Discussion on hydrogen sorption properties

***The Pressure Composition Isotherm***

For $y = 0$, the hydrogenation and dehydrogenation properties can be attributed to $Y_{0.95}Ni_2$ ($F\bar{4}3m$) as it is the major phase (~ 92 wt.%). In the literature, the crystal structure of $Y_{0.95}Ni_2D_{2.6}$ prepared at room temperature with 1 bar of deuterium pressure has been reported [122]. Another work [183] reported a continuous increase of the pressure-composition curve in the range $10^{-3}$ to 1 MPa, without plateau pressure at room temperature. For the first time, we show here the complete PCI of $Y_{0.95}Ni_2$ at 200 °C. This is in good agreement with the results of reference [122], which state that high a large gap of pressure is necessary to increase the hydrogen content significantly. It probably means the end of the first plateau and the beginning of the second one. We consider that the two plateaus of the PCI correspond to two phase transformations, forming two hydrides $Y_{0.95}Ni_2D_{2.6}$ and $Y_{0.95}Ni_2H_3$, respectively. Then, $Y_{0.95}Ni_2D_{2.6}$ can be identified as a first hydride whereas the crystal structure of the second hydride at the end of the second

plateau remains unknown but could be amorphous as observed for other $R$Ni$_2$ hydrides. For confirmation, in-situ neutron diffraction studies under hydrogen (deuterium) pressure will be valuable.

For $y$ = 0.05, $Y_{0.95}$(Ni, Al)$_2$ ($Fd\bar{3}m$-$C15$) is the major phase (~ 90 wt.%), which allows a direct comparison of the PCI with $y$ = 0. At 200 °C, we observe that for $y$ = 0.05, the pressure of the low-pressure plateau (Figure 4.12a) is higher than that of $y$ = 0 though the lattice parameter of the former, $a$ = 7.182 Å, is close to the latter, $a$/2= 7.178 Å. This contradicts the geometrical rule obeyed by many metal-hydrogen systems [63,90,91] showing that the lower the cell parameter, the higher the pressure of the plateau. Such contradiction is commonly attributed to the predominancy of electronic versus geometric effects [249,250]. For $y$ = 0.10 and 0.15, the compounds contain other phases, and the PCI is expected to reflect the contribution of each component (Figure 4.12a). The sloped branch at low pressure could be assigned to YNi and $Y_2Ni_2Al$ phases. For $y$ = 0.25, the second plateau at 1 MPa and 0.7 H/M can be attributed to the hydrogenation of $YNi_{2.6}Al_{0.4}$ ($AB_3$ phase) (according to EPMA results, see Figure 4.12b), which shows very good reversibility. Accordingly, it will be worth to synthesis the single-phase compound $YNi_{2.6}Al_{0.4}$ for further investigation as hydrogen storage material.

At higher Al content ($y \geq 0.50$), the PCIs show very slopy behavior and lower absorption capacity due to the presence of the phases $Y_2Ni_2Al$, $Y_3Ni_6Al_2$ and YNiAl.

***Kinetics***

During absorption, the hydrogenation can be described as a sequential process comprising physisorption and chemisorption of hydrogen molecules at the surface, dissociation of dihydrogen, surface penetration of hydrogen atoms into the solid, diffusion of hydrogen atoms in the bulk and nucleation and growth of the hydride phase. Some models exist to identify the rate-determining steps [251]. For $YNi_2$, the sorption curve exhibits a sigmoidal shape (Figure 4.11a) indicating that the limiting step is the nucleation and growth of hydride nuclei [252]. The hydrogenation kinetics for $0.05 \leq y \leq 0.25$ are faster compared to Al-free compound. As for the Al-content ranging from $y$ = 0.05 to 0.15, both rates of hydride nucleation and growth increases. This can be attributed to the presence of the secondary phases Y(Ni, Al)$_3$, YNi and $Y_2Ni_2Al$ which may play a catalytic role on the dihydrogen dissociation process. The kinetic of compounds with higher Al ($y$ = 0.75, 1.00) contents is slower than that of $y$ = 0.50, all Al-contain compounds show better kinetic than the Al-free compound.

***Reversible capacity***

Regarding the maximum hydrogen sorption capacity (Figure 4.15), it increases slightly for $y$ = 0.05 as compared to the Al-free compound, which is attributed to the decrease of the molar weight by Al substitution in the $AB_2$ phase, thus augmenting the mass capacity. When further increasing Al content, the maximum absorption capacity decreases due to the formation of

secondary phases $Y_2Ni_2Al$, $Y_3Ni_6Al$ and YNiAl, which do not absorb large quantity of hydrogen.

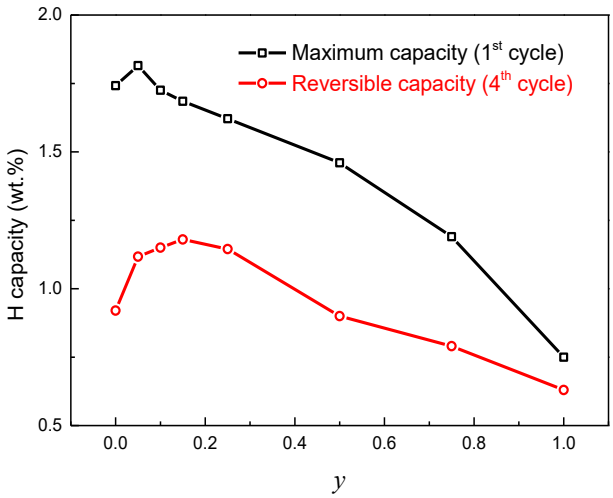


Figure 4.15 Maximum and reversible capacity as function of Al content in $YNi_{2-y}Al_y$ ($0 \leq y \leq 1$).

All compounds show a decay of their hydrogen absorption capacity between the first and the second cycle (Figure 4.11c), but the reason is different for each compound.

For $y = 0$, XRD patterns of the dehydrogenated samples can be indexed with $YNi_3$ and $YH_2$ (Figure 4.13). The capacity decay is mainly attributed to the disproportionation of $Y_{0.95}Ni_2H_z$. As a matter of fact, upon hydrogenation $AB_2$ ($A$ = Y, rare earth, $B$ = transition metals) binary compounds with $C15$ Laves phase structure suffer from HIA or HID [193,201]. Indeed, $Y_{0.95}Ni_2$ keeps the structural characteristics of the $C15$ Laves structure but needs ordered Y vacancies to stabilize. Despite this effect, any volume expansion induced by hydrogenation leads to interatomic distance distribution and weakening of atomic bounds [123], thus easier occurrence for HIA.

For $0.05 \leq y \leq 0.25$, the XRD patterns of the dehydrogenated samples can be indexed with $Y(Ni, Al)_3$ and $YH_2$ phases (Figure 4.14a). This result indicates that the same HID occurred for all present phases except $AB_3$-type $Y(Ni, Al)_3$ phase. Neither YNi nor $Y_2Ni_2Al$ phase contribute to the reversible hydrogen absorption capacity as for samples with Al content ranging between $0.10 \leq x \leq 0.25$, upon hydrogen absorption and desorption the diffraction peaks of YNi and $Y_2Ni_2Al$ phases cannot be detected. However, YNi could absorb approximately 3 hydrogen atoms per formula unit (H/f.u). under 1.1 MPa of hydrogen pressure at room temperature to form a $YNiH_3$ hydride [253]. $YNiH_3$ is unstable upon hydrogenation as it transforms into yttrium hydride and Ni. Regarding $Y_2Ni_2Al$ phase, although there are no studies on its hydrogenation properties, some works on the isostructural intermetallic compounds $A_2Ni_2Al$ ($A$ = Gd, Er, Lu) showed that their hydrogenation results in strong anisotropic cell expansion [233,254], which can eventually yield HIA.

The reversible capacity significantly increases for Al-containing compounds up to $y = 0.25$, which is due to the Y(Ni, Al)$_3$ phases after the first cycle. This indicates that Al-containing Y(Ni, Al)$_3$ provides higher hydrogen capacity than the binary $YNi_3$ one. The XRD patterns of compounds with $y$ = 0.50, 0.75 and 1.00 after dehydrogenation, show diffraction peaks belonging to $Y_3Ni_6Al_2$ and YNiAl (Figure 4.14b). This means that these two phases recover their crystal structure after dehydrogenation, which agrees with previous experimental results about the hydrides $A_3Ni_6AlGaH_z$ ($A$ = Y, Gd, Dy) [232] and $ANiAlH_z$ ($A$ = Y, Gd, Tb, Dy, Ho and Er) [248]. Figure 4.16 shows the $Y_2Ni_2Al$ phase abundance and capacity decay evolutions as a function of $y_{Al}$ in the region $0.50 \leq y \leq 1.00$. They display similar tendency, indicating that HIA of $Y_2Ni_2Al$ is the main reason for the capacity decay between $0.50 \leq y \leq 1.00$ Al content. The low reversible capacity is caused by the low hydrogen capacity of YNiAl and $Y_3Ni_6Al_2$.

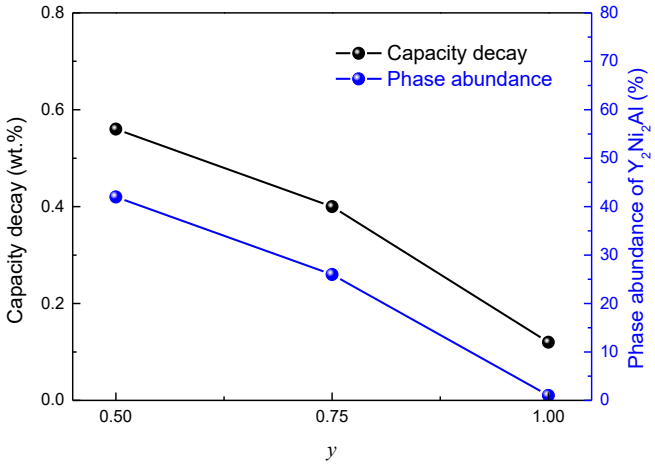


Figure 4.16 Evolution of $Y_2Ni_2Al$ abundance and capacity decay between cycles 1 and 4 as a function of the Al content ($0.50 \leq y \leq 1.00$).

## 4.1.4 Conclusions

We have investigated systematically the phase occurrence for $YNi_{2-y}Al_y$ in the range of $0 \leq y \leq 1$. We established that the Al substitution limit inside the $C15$ $YNi_{2-z}Al_z$ phase is $z = 0.11$. When increasing $y_{Al}$ from 0.15 to 0.20, the $AB_3$-type Y(Ni, Al)$_3$ phase occurs. Its structure switches from rhombohedral ($PuNi_3$-type, $3R$) to hexagonal ($CeNi_3$-type, $2H$) while the Al content increases, due to geometric effects. The Al solution limit for $YNi_{3-z'}Al_{z'}$ is estimated around $z' = 0.4$. The reported ordered $Y_3Ni_8Al$ ternary phase [239] is not observed but $YNi_{2.6}Al_{0.4}$ (with close composition, *i.e.*, $Y_3Ni_{7.8}Al_{1.2}$) crystallizes as a pseudo-binary in the same hexagonal structure, without any ordering of Al atoms in the $2d$ sites.

Al substitution enhances the hydrogen absorption kinetics of $YNi_{2-y}Al_y$ and improves the reversible hydrogen sorption capacity. The $Y_{0.95}Ni_2$ (superstructure phase), $Y_{0.95}$(Ni, Al)$_2$ ($C15$ structure), YNi and $Y_2Ni_2Al$ are not stable upon hydrogen absorption/desorption cycle. For compounds with Al content lower than 0.25, the reversible capacity is ensured by the $AB_3$ phase which forms after the first hydrogenation/dehydrogenation cycle. For higher Al content, the

reversible capacity comes from the hydrogenation of ternary phases $Y_3Ni_6Al_2$ and YNiAl. The $AB_3$-type $Y_{1.03}Ni_{2.61}Al_{0.39}$ phase shows interesting hydrogenation properties. A single-phase compound will be worth to synthesize to further investigate its hydrogen sorption properties.

## 4.2 Investigation of the phase occurrence and H sorption properties of the $Y_xNi_{2-y}Mn_y$ compounds ($0.75 \leq x \leq 1$, $0 \leq y \leq 0.5$)

Mn is one of the most common elements used in $AB_5$ or $AB_n$ ($3 \leq n \leq 3.8$) to modify their structural characteristics and enhance hydrogen sorption properties [89,93,255]. Compared to Al, Mn as a transition element, is located in the same group and exhibits similar chemical properties than Ni.

Another interesting phenomenon was observed: it was found that Mn is capable to occupy both *A*- and *B*-side sites in $Z_{rMn2}$-type Laves phase, allowing large over-stoichiometric domains $ZrMn_{2+y}$ [256]. For these reasons, the structural evolutions as well as structural stabilities of $Y_xNi_{2-y}Mn_y$ compounds are worth investigating.

### 4.2.1 Synthesis and characterization of the compounds

Intermetallic compounds with nominal composition $Y_xNi_{2-y}Mn_y$ ($x$ = 1, 0.95, 0.9, 0.86, 0.85, 0.825, 0.80, 0.75, $y$ = 0, 0.1, 0.2, 0.25, 0.3, 0.4, 0.5) were prepared by induction melting of high-purity metals (Y:99.9%, Ni:99.99%, Mn: 99.95% from *A*lfa *A*esar) in purified argon atmosphere (5N) under a pressure of 0.04 MPa in a cooled copper crucible. The ingots were turned over and re-melted three times to ensure homogeneity, The as-cast ingots were subsequently annealed 3 days at 850 °C.

The neutron diffraction (ND) patterns were collected at room temperature on at China Spallation Neutron Source (CSNS) using MPI in time-of-flight mode, the sample holder was in vanadium. The size of sample powder used for neutron diffraction is $\leq 100\ \mu m$ with mass of around $3\sim5\ g$. The diffraction patterns were then joint analyzed by using the program TOPAS [257].

### 4.2.2 Effect of Mn substitution on phase occurrence

To avoid confusing, the experimental results will be divided into three sections: compounds with Mn-changing and fixed Y content ($x$ = 0.9), Y-changing with fixed Mn content ($y$ = 0.3) and single *C*15-phase with changing both Y and Mn content.

#### 4.2.2.1 $Y_{0.9}Ni_{2-y}Mn_y$ (y = 0.1, 0.2, 0.3, 0.4, 0.5) compounds

The XRD patterns of $Y_{0.9}Ni_{2-y}Mn_y$ ($y$ = 0.1, 0.2, 0.3, 0.4, 0.5) compounds and Rietveld refinements are presented in Figure 4.17 and Figure 4.18. The relevant crystallographic data from Rietveld refinement and chemical compositions measured by EPMA are summarized in Table 4.5.

For $Y_{0.9}Ni_{2-y}Mn_y$ ($0.1 \leq y \leq 0.3$) compounds, *C*15 Laves phase $Y_{1-v}(Ni, Mn)_2$ was the main phase, YNi (*AB*-type, space group $Pnma$, No. 62) appears as the secondary phase and its abundance increases with the increasing Mn content $y$. $Y(Ni, Mn)_3$ (*AB*$_3$-type, space group $R\bar{3}m$,

No. 166) replaces *C*15 phase as the main phase for $y = 0.4$ and 0.5, *C*15 Laves phase disappeared for $y = 0.5$. Small amount of oxides $Y_2O_3$ ($Ia\bar{3}$, ~ 1 wt.%) and $Mn_2O_3$ ($Ia\bar{3}$, ~ 3 wt.%) were observed for $y = 0.1$, whereas only $Y_2O_3$ was observed in the other compounds with negligible amount (~ 1 wt.%).

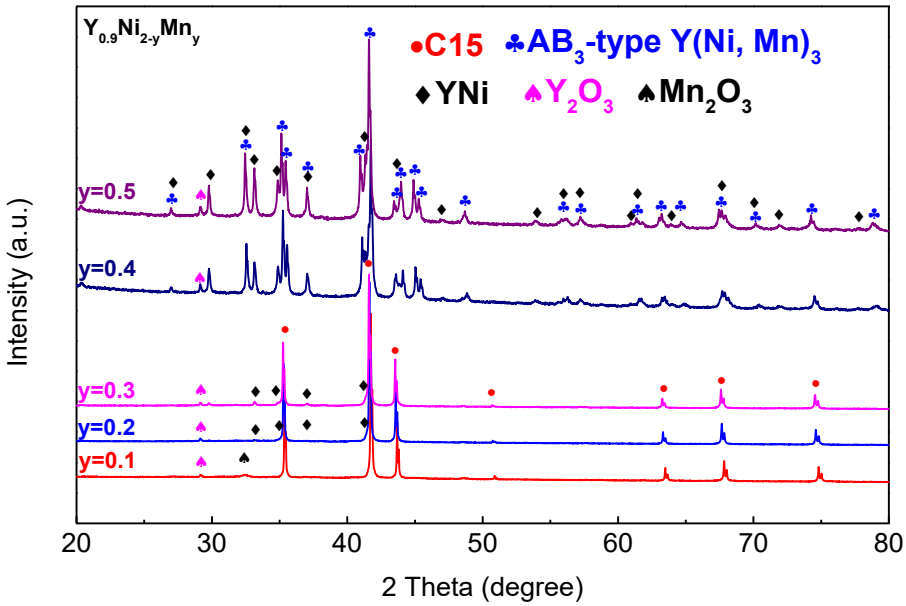


Figure 4.17 X-ray diffraction patterns of $Y_{0.9}Ni_{2-y}Mn_y$ ($y = 0.1$, 0.2, 0.3, 0.4, 0.5) compounds.

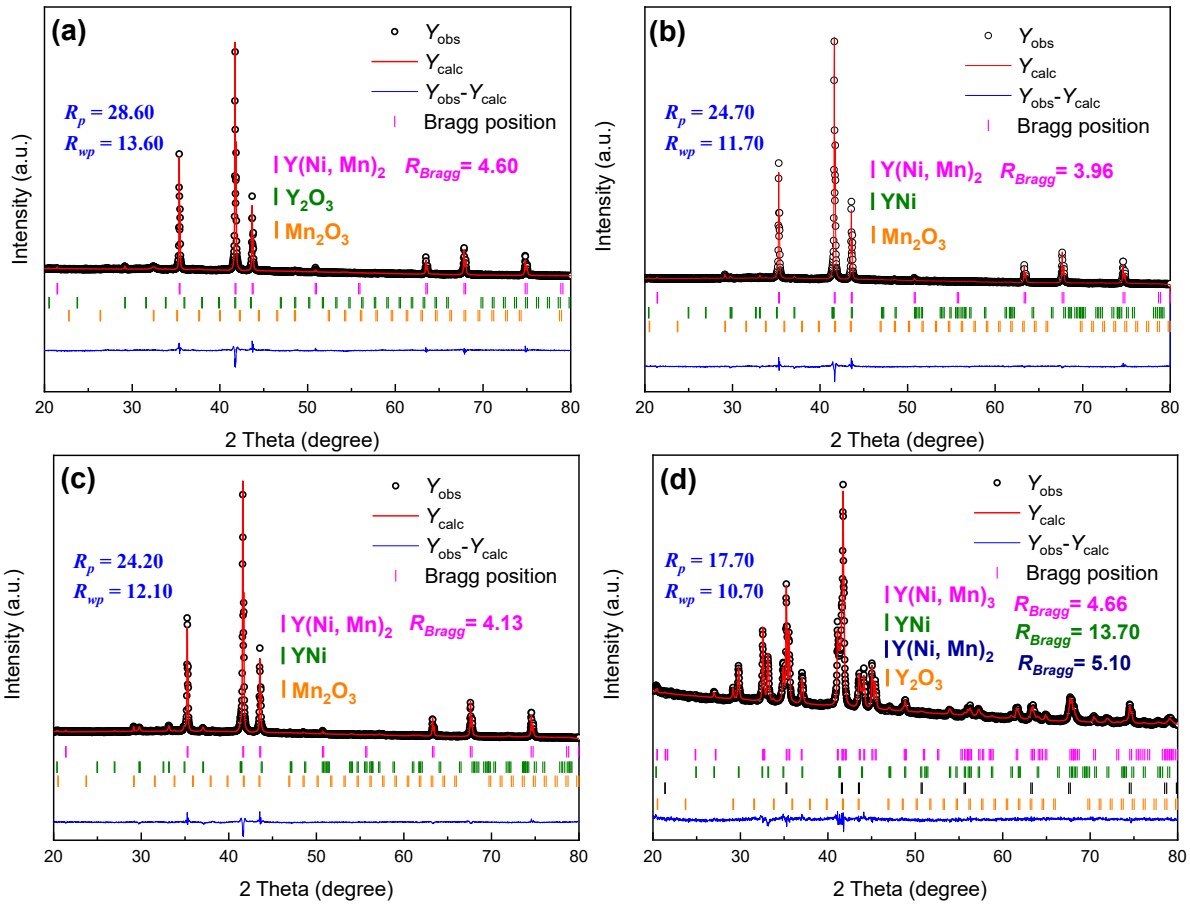

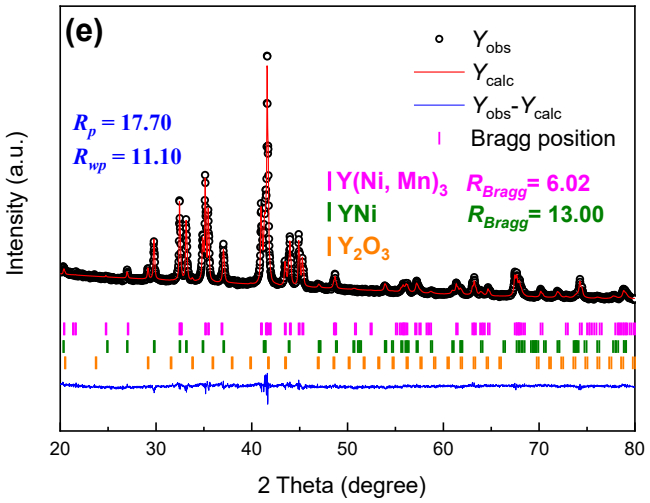


Figure 4.18 Rietveld refinements of the XRD patterns for $Y_{0.9}Ni_{2-y}Mn_y$ compounds: a – $y$ = 0.10, b – $y$ = 0.20, c – $y$ = 0.30, d – $y$ = 0.40, e – $y$ = 0.50.

Table 4.5 Phase compositions determined by EPMA and crystallographic data from Rietveld refinement of the XRD patterns of $Y_{0.9}Ni_{2-y}Mn_y$ ($y$ = 0.1, 0.2, 0.3, 0.4, 0.5) compounds.

| Sample | Phase | Crystal structure | Phase composition (EPMA) (±0.02) | Phase abundance (wt.%) | Lattice parameters (Å) | | |
|---|---|---|---|---|---|---|---|
| | | | | | *a* | *b* | *c* |
| $Y_{0.9}Ni_{1.9}Mn_{0.1}$ | $Y_{1-v}$(Ni, Mn)$_2$ | $MgCu_2$ ($Fd\bar{3}m$) | $Y_{0.86}Ni_{1.87}Mn_{0.13}$ | 96% (1) | 7.1736 (1) | - | - |
| | $Y_2O_3$ | $Ia\bar{3}$ | - | 4% (1) | - | - | - |
| | $Mn_2O_3$ | $Ia\bar{3}$ | | | | | |
| $Y_{0.9}Ni_{1.8}Mn_{0.2}$ | $Y_{1-v}$(Ni, Mn)$_2$ | $MgCu_2$ ($Fd\bar{3}m$) | $Y_{0.87}Ni_{1.79}Mn_{0.21}$ | 95% (1) | 7.1900 (1) | - | - |
| | YNi | FeB (*Pnma*) | - | 4% (1) | 7.131 (2) | 4.1505 (1) | 5.4858 (1) |
| | $Y_2O_3$ | $Ia\bar{3}$ | - | 1% (1) | - | - | - |
| $Y_{0.9}Ni_{1.7}Mn_{0.3}$ | $Y_{1-v}$(Ni, Mn)$_2$ | $MgCu_2$ ($Fd\bar{3}m$) | $Y_{0.83}Ni_{1.68}Mn_{0.32}$ | 90% (1) | 7.1951 (1) | - | - |
| | YNi | FeB (*Pnma*) | $YNi_{0.99}Mn_{0.02}$ | 9% (1) | 7.134 (2) | 4.1389 (1) | 5.5064 (1) |
| | $Y_2O_3$ | $Ia\bar{3}$ | - | 1% (1) | - | - | - |
| $Y_{0.9}Ni_{1.6}Mn_{0.4}$ | $Y_{1-v}$(Ni, Mn)$_2$ | $MgCu_2$ ($Fd\bar{3}m$) | $Y_{0.79}Ni_{1.60}Mn_{0.40}$ | 14% (1) | 7.2012 (4) | - | - |
| | YNi | FeB (*Pnma*) | $YNi_{0.99}Mn_{0.02}$ | 23% (1) | 7.1464 (6) | 4.1260 (1) | 5.5118 (1) |
| | Y(Ni, Mn)$_3$ | $PuNi_3$ ($R\bar{3}m$) | $YNi_{2.24}Mn_{0.72}$ | 62% (1) | 5.0890 (1) | | 24.6202 (1) |
| | $Y_2O_3$ | $Ia\bar{3}$ | - | 1% (1) | - | - | - |
| $Y_{0.9}Ni_{1.5}Mn_{0.5}$ | YNi | FeB (*Pnma*) | $YNi_{0.96}Mn_{0.02}$ | 27% (1) | 7.1481 (5) | 4.1266 (1) | 5.5133 (1) |
| | Y(Ni, Mn)$_3$ | $PuNi_3$ ($R\bar{3}m$) | $YNi_{2.09}Mn_{0.96}$ | 72% (1) | 5.1050 (1) | | 24.6890 (1) |
| | $Y_2O_3$ | $Ia\bar{3}$ | - | 1% (1) | - | - | - |

### 4.2.2.2 $Y_xNi_{1.7}Mn_{0.3}$ ($x$ = 1, 0.90, 0.85, 0.825, 0.80, 0.75) compounds

The XRD patterns and Rietveld analysis of $Y_xNi_{1.7}Mn_{0.3}$ ($x$ = 1, 0.90, 0.85, 0.825, 0.80, 0.75) compounds are presented in Figure 4.19 and Figure 4.20. The relevant crystallographic data from Rietveld refinement and chemical compositions measured by EPMA are summarized in Table 4.6.

For $Y_xNi_{1.7}Mn_{0.3}$ ($0.75 < x \leq 1.00$) compounds, $C15$ Laves phase $Y_{1-v}$(Ni, Mn)$_2$ ($v$ = rate of Y vacancies) is the main phase, and the secondary phases YNi and $AB_3$-type Y(Ni, Mn)$_3$ form depending on Y content. The quantity of YNi phase is positively associated with Y content, its abundance falls with $x$ ranging from 1 to 0.825 and disappears for $x$ = 0.825. The reverse trend can be observed for $AB_3$-type phase: when $x$ decreases from 0.825 to 0.75, the amount of Y(Ni, Mn)$_3$ phase increases from 0 to 54 wt.%. It is worth noticing that we didn't observe $AB_3$-type Y(Ni, Mn)$_3$ phase for $x$ = 0.825, 0.85 and 0.9, but 22 wt.% for $x$ = 1. This indicates that there is a domain where $MgCu_2$-type Y(Ni, Mn)$_2$ phase can be formed. For $x$ = 0.825, 0.85 and 0.9, the composition of the Laves phase is adjusted and only YNi is observed as secondary phase. While $YNi_{1.7}Mn_{0.3}$ should be located in the three-phase domain, it contains a mixture of $AB$, $AB_2$ and $AB_3$ phases. The equation can be written (Table 4.6):

$$YNi_{1.7}Mn_{0.3} \rightarrow 0.625\, Y_{0.8}Ni_{1.66}Mn_{0.34} + 0.37\, YNi + 0.12\, YNi_{2.3}Mn_{0.7}$$

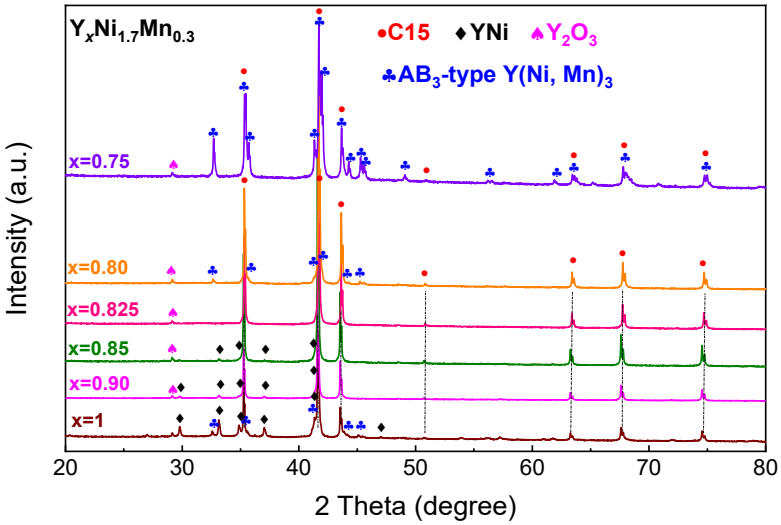


Figure 4.19 X-ray diffraction patterns of $Y_xNi_{1.7}Mn_{0.3}$ ($x$ = 1, 0.9, 0.85, 0.825, 0.80, 0.75) compounds.

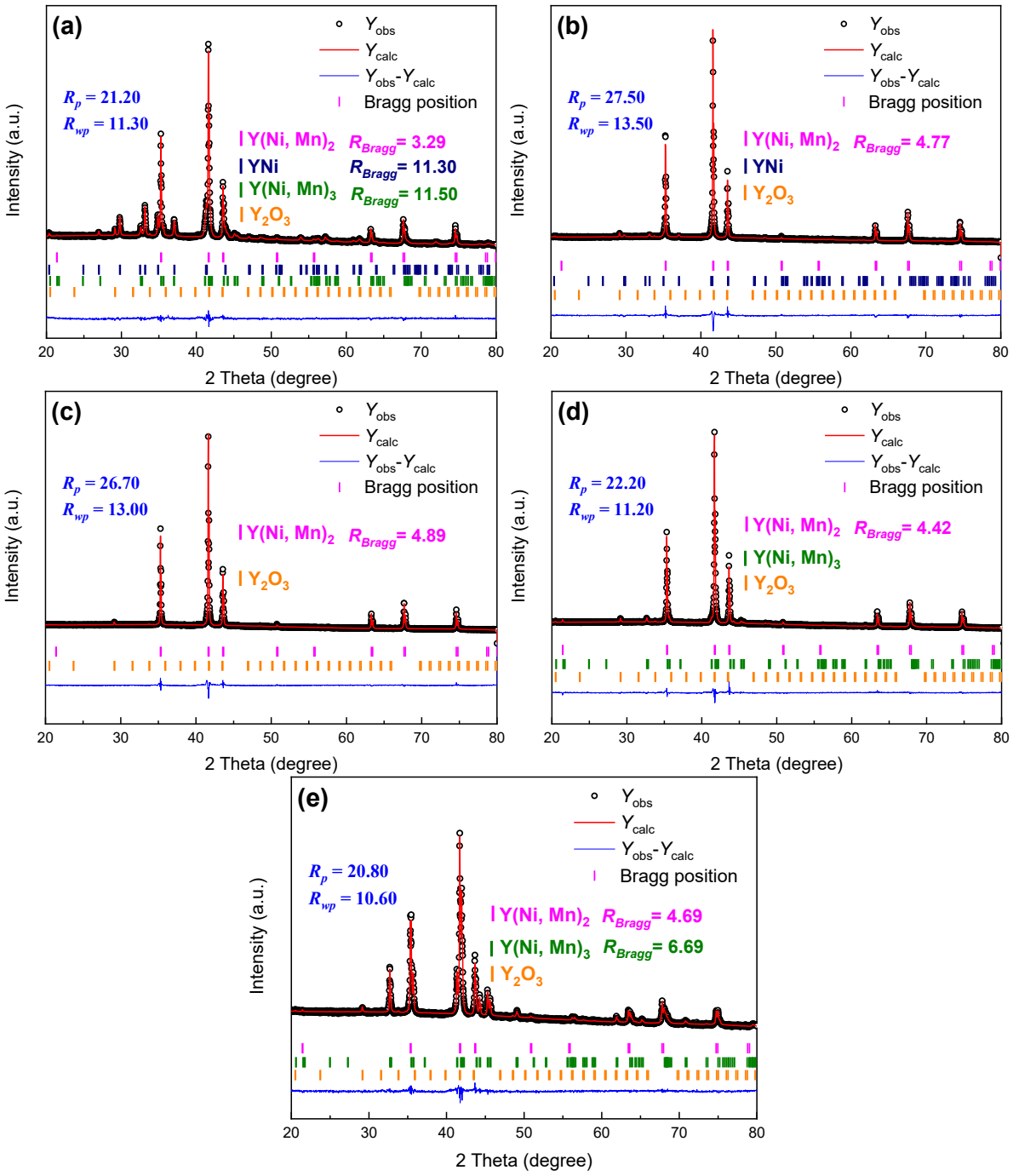


Figure 4.20 Rietveld refinements of the XRD patterns for $Y_xNi_{1.7}Mn_{0.3}$ compounds: a – $x$ = 1.0, b – $x$ = 0.85, c – $x$ = 0.825, d – $x$ = 0.80, e – $x$ = 0.75.

Table 4.6 Phase composition determined by EPMA and crystallographic data from Rietveld refinement of XRD patterns of $Y_xNi_{1.7}Mn_{0.3}$ ($x$ = 1, 0.9, 0.85, 0.825, 0.80, 0.75) compounds.

| Sample | Phase | Crystal structure | Phase composition (EPMA) (±0.02) | Phase abundance (wt.%) | Lattice parameters (Å) | | |
|---|---|---|---|---|---|---|---|
| | | | | | *a* | *b* | *c* |
| $YNi_{1.7}Mn_{0.3}$ | $Y_{1-v}(Ni, Mn)_2$ | $MgCu_2$ ($Fd\bar{3}m$) | $Y_{0.79}Ni_{1.66}Mn_{0.34}$ | 51% (1) | 7.1948 (1) | - | - |
| | YNi | FeB (*Pnma*) | $YNi_{1.01}Mn_{0.01}$ | 26% (1) | 7.1461 (5) | 4.1276 (1) | 5.5120 (1 ) |
| | $Y(Ni, Mn)_3$ | $PuNi_3$ ($R\bar{3}m$) | $YNi_{2.33}Mn_{0.65}$ | 22% (1) | 5.0857 (3) | | 24.6122 (3) |
| $Y_{0.9}Ni_{1.7}Mn_{0.3}$ | $Y_{1-v}(Ni, Mn)_2$ | $MgCu_2$ ($Fd\bar{3}m$) | $Y_{0.83}Ni_{1.68}Mn_{0.32}$ | 90% (1) | 7.1951 (1) | - | - |
| | YNi | FeB (*Pnma*) | $YNi_{0.99}Mn_{0.02}$ | 9% (1) | 7.134 (2) | 4.1389 (1) | 5.5064 (1) |
| | $Y_2O_3$ | - | - | 1% (1) | - | - | - |
| $Y_{0.85}Ni_{1.7}Mn_{0.3}$ | $Y_{1-v}(Ni, Mn)_2$ | $MgCu_2$ ($Fd\bar{3}m$) | $Y_{0.79}Ni_{1.67}Mn_{0.33}$ | 93% (1) | 7.1951 (1) | - | - |
| | YNi | FeB (*Pnma*) | $YNiMn_{0.01}$ | 6% (1) | 7.128 (3) | 4.1474 (1) | 5.4984 (1) |
| | $Y_2O_3$ | - | - | 1% (1) | - | - | - |
| $Y_{0.825}Ni_{1.7}Mn_{0.3}$ | $Y_{1-v}(Ni, Mn)_2$ | $MgCu_2$ ($Fd\bar{3}m$) | $Y_{0.82}Ni_{1.69}Mn_{0.31}$ | 99% (1) | 7.1912 (1) | - | - |
| | $Y_2O_3$ | - | - | 1% (1) | - | - | - |
| $Y_{0.80}Ni_{1.7}Mn_{0.3}$ | $Y_{1-v}(Ni, Mn)_2$ | $MgCu_2$ ($Fd\bar{3}m$) | $Y_{0.76}Ni_{1.69}Mn_{0.31}$ | 87% (1) | 7.1809 (1) | - | - |
| | $Y(Ni, Mn)_3$ | $PuNi_3$ ($R\bar{3}m$) | - | 12% (1) | 5.0678 (4) | | 24.5655 (4) |
| | $Y_2O_3$ | - | - | 1% (1) | - | - | - |
| $Y_{0.75}Ni_{1.7}Mn_{0.3}$ | $Y_{1-v}(Ni, Mn)_2$ | $MgCu_2$ ($Fd\bar{3}m$) | $Y_{0.80}Ni_{1.75}Mn_{0.25}$ | 45% (1) | 7.1778 (1) | - | - |
| | $Y(Ni, Mn)_3$ | $PuNi_3$ ($R\bar{3}m$) | $YNi_{2.52}Mn_{0.55}$ | 54% (1) | 5.0612 (1) | | 24.5362 (1) |
| | $Y_2O_3$ | - | - | 1% (1) | - | - | - |

### 4.2.2.3 Single C15 phase $Y_xNi_{2-y}Mn_y$ compounds

The XRD patterns and Rietveld analysis of $Y_{0.95}Ni_2$, $Y_{0.9}Ni_{1.9}Mn_{0.1}$, $Y_{0.86}Ni_{1.8}Mn_{0.2}$, $Y_{0.825}Ni_{1.7}Mn_{0.3}$ single phase compounds and $Y_{0.79}Ni_{1.6}Mn_{0.4}$ compound containing $Y_{0.79}Ni_{1.61}Mn_{0.39}$ as main phase are presented in Figure 4.21 and Figure 4.22 ($Y_{0.9}Ni_{1.9}Mn_{0.1}$ and $Y_{0.825}Ni_{1.7}Mn_{0.3}$ have been present in Figure 4.18 and Figure 4.20 respectively). The relevant crystallographic data from Rietveld refinement and chemical compositions measured by EPMA are summarized in Table 4.7.

$Y_{0.95}Ni_2$ presents a single $TmNi_2$-type $R_xNi_2$ ($R$ = Lanthanide, $0.9 < x < 1$) phase, which crystallizes in the previously described superstructure (space group $F\bar{4}3m$, No. 216) [122,126]. From above described two series compounds (Table 4.5 and Table 4.6), the single $C15$ Laves phase were only obtained with nominal compositions $Y_{0.9}Ni_{1.9}Mn_{0.1}$ and $Y_{0.825}Ni_{1.7}Mn_{0.3}$. For studying the formation and structural stability of $C15$-type $Y_{1-v}(Ni, Mn)_2$ phase, we prepared another two compounds with nominal compositions $Y_{0.86}Ni_{1.8}Mn_{0.2}$ and $Y_{0.79}Ni_{1.61}Mn_{0.39}$. As results, single $C15$ phase was observed for $Y_{0.86}Ni_{1.8}Mn_{0.2}$, whereas for $Y_{0.79}Ni_{1.61}Mn_{0.39}$ a small amount of $Y(Ni, Mn)_3$ phase was also detected (Figure 4.21 and Table 4.7).

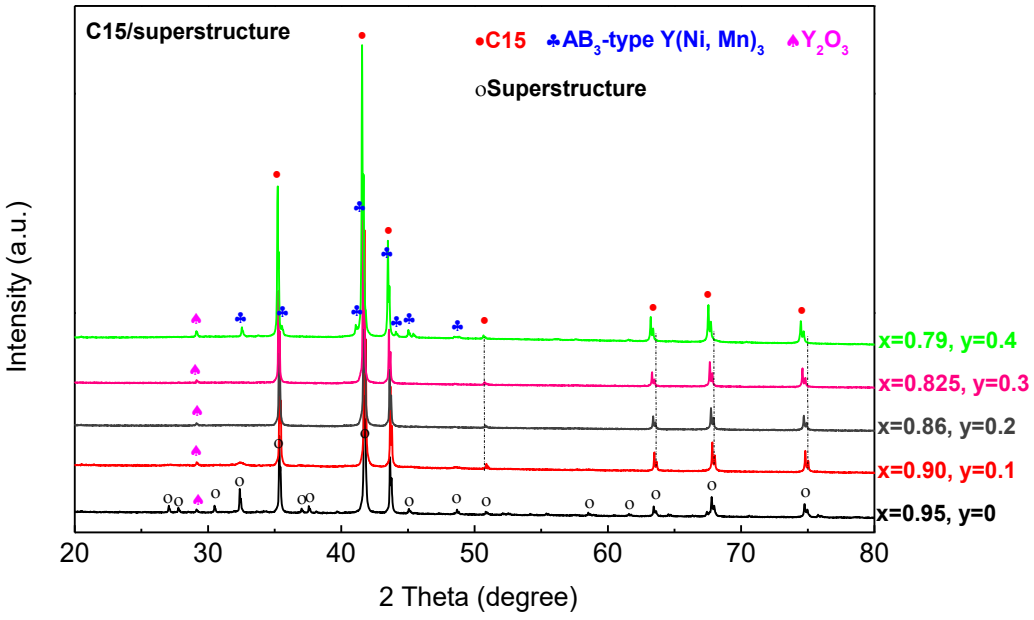


Figure 4.21 X-ray diffraction patterns of $Y_{0.95}Ni_2$, $Y_{0.9}Ni_{1.9}Mn_{0.1}$, $Y_{0.86}Ni_{1.8}Mn_{0.2}$, $Y_{0.825}Ni_{1.7}Mn_{0.3}$, $Y_{0.79}Ni_{1.6}Mn_{0.4}$ from bottom to top.

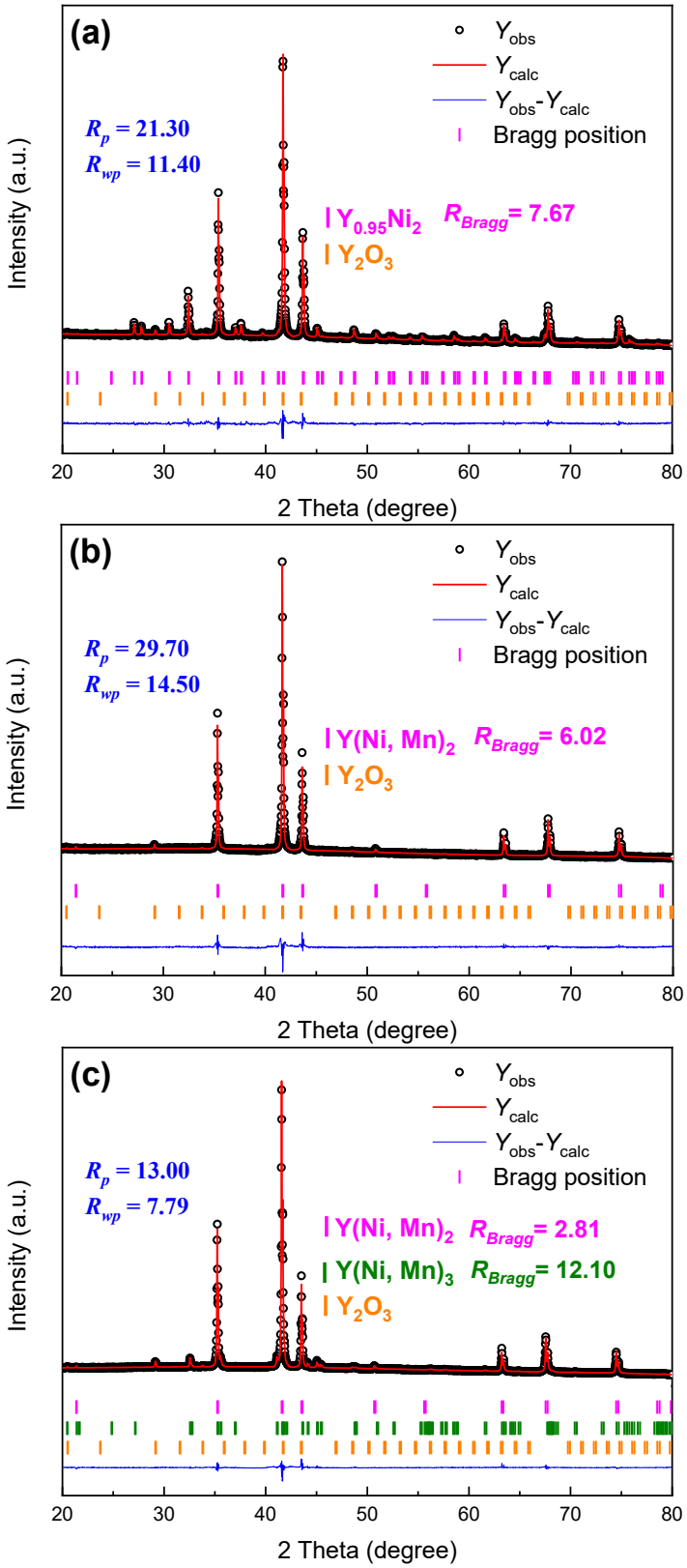


Figure 4.22 Rietveld refinements of the XRD patterns for $Y_xNi_{2-y}Mn_y$ compounds: a – $Y_{0.95}Ni_2$, b – $Y_{0.86}Ni_{1.8}Mn_{0.2}$, c – $Y_{0.79}Ni_{1.6}Mn_{0.4}$.

Table 4.7 Phase composition determined by EPMA and crystallographic data from Rietveld refinement for $Y_{0.95}Ni_2$, $Y_{0.9}Ni_{1.9}Mn_{0.1}$, $Y_{0.86}Ni_{1.8}Mn_{0.2}$, $Y_{0.825}Ni_{1.7}Mn_{0.3}$, $Y_{0.79}Ni_{1.6}Mn_{0.4}$.

| Sample | Phase | Crystal structure | Phase composition (EPMA) (±0.02) | Phase abundance (wt.%) | Lattice parameter(Å) | |
|---|---|---|---|---|---|---|
| | | | | | *a* | *c* |
| $Y_{0.95}Ni_2$ | $Y_{0.95}Ni_2$ | $TmNi_2$ ($F\bar{4}3m$) | $Y_{0.93}Ni_2$ | 99 (1) | 14.3557 (3) | = *a* |
| | $Y_2O_3$ | - | - | 1 (1) | - | - |
| $Y_{0.9}Ni_{1.9}Mn_{0.1}$ | $Y_{1-v}(Ni, Mn)_2$ | $MgCu_2$ ($Fd\bar{3}m$) | $Y_{0.86}Ni_{1.87}Mn_{0.13}$ | 96 (1) | 7.1733 (1) | = *a* |
| | $Y_2O_3/Mn_2O_3$ | - | - | 4 (1) | - | - |
| $Y_{0.86}Ni_{1.8}Mn_{0.2}$ | $Y_{1-v}(Ni, Mn)_2$ | $MgCu_2$ ($Fd\bar{3}m$) | $Y_{0.85}Ni_{1.79}Mn_{0.21}$ | 99 (1) | 7.1826 (1) | = *a* |
| | $Y_2O_3$ | | - | 1 (1) | - | - |
| $Y_{0.825}Ni_{1.7}Mn_{0.3}$ | $Y_{1-v}(Ni, Mn)_2$ | $MgCu_2$ ($Fd\bar{3}m$) | $Y_{0.82}Ni_{1.69}Mn_{0.31}$ | 99 (1) | 7.1912 (1) | = *a* |
| | $Y_2O_3$ | - | - | 1 (1) | - | - |
| $Y_{0.79}Ni_{1.71}Mn_{0.39}$ | $Y_{1-v}(Ni, Mn)_2$ | $MgCu_2$ ($Fd\bar{3}m$) | $Y_{0.80}Ni_{1.59}Mn_{0.41}$ | 83 (1) | 7.2001 (1) | = *a* |
| | $Y(Ni, Mn)_3$ | $PuNi_3$ ($R\bar{3}m$) | $YNi_{2.22}Mn_{0.78}$ | 16 (1) | 5.0884 (2) | 24.6168(1) |
| | $Y_2O_3$ | - | - | 1 (1) | - | - |

### 4.2.2.4 Discussion on phase occurrence

As discussed in section before, the binary $Y_{0.95}Ni_2$ compound crystalizes in $TmNi_2$-type superstructure with space group $F\bar{4}3m$. Once the substitution of Mn for Ni in $Y_xNi_{2-y}Mn_y$ up to $y \geq 0.1$, a reversed structural transformation from $TmNi_2$-type superstructure to $MgCu_2$-type $C15$ Laves phase structure occurred. One can note that EPMA analysis shows a systematic sub-stoichiometry for yttrium (see the $Y_{1-v}(Ni, Mn)_2$ phases presented in Table 4.5, Table 4.6 and Table 4.7), indicating that the substitution of Mn for Ni favors the formation of $C15$ structure with disordered Y vacancies. Similar behavior was also observed in $Y_{0.95}Ni_{2-y}B_y$ ($B$ = Cu, Fe, Al) systems [203,184].

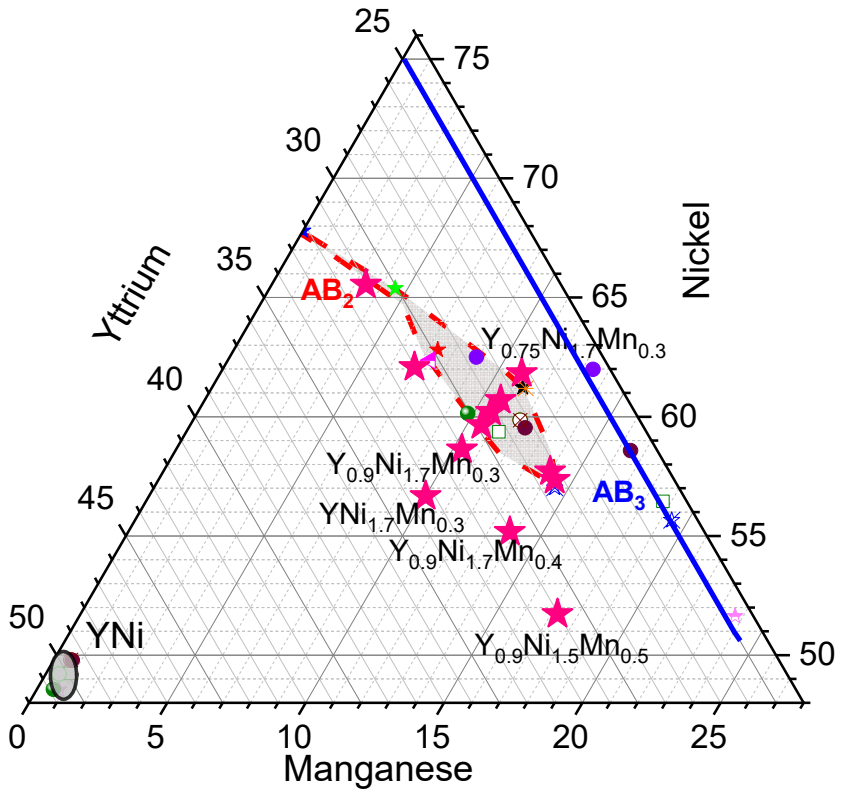


Figure 4.23 The ternary plot of compositions of $Y_{1-v}(Ni, Mn)_2$ compounds.

From EPMA data, the local phase diagram at 850 °C is shown in Figure 4.23. It shows that the $C15$ phase can be formed in a composition region, where the stoichiometry changes with Mn content. Up to 4 at.% of Mn (corresponding $Y_{0.9}Ni_{1.9}Mn_{0.1}$), the $C15$ phase forms with determined composition, above this content, it can be formed in a region by adjusting the three component. It cannot be formed with Mn content higher than 14 at. %, which corresponding to the composition of $Y_{0.8}Ni_{1.6}Mn_{0.4}$. The $AB$ phase does not contain Mn as the case observed in the Y-Ni-Al system, see section 4.1.2. The $AB_3$ phase crystalize all in rhombohedral structure, in contrary to the Y-Ni-Al system (section 4.1.2) non structure transition is observed. They follow the $Y(Ni_{3-w}Mn_w)$ line in our studied domain.

### 4.2.3 Effect of Mn substitution on crystal structure

#### 4.2.3.1 *C*15-type $Y_{1-v}(Ni, Mn)_2$ phase

Figure 4.24 shows the lattice parameters of the *C*15-type $Y_{1-v}(Ni, Mn)_2$ phase as function of Mn content and Y content. For $Y_{0.9}Ni_{2-y}Mn_y$ compounds (Figure 4.24a), the lattice parameter of *C*15 phase slightly decrease for $y = 0$ to 0.13, then increases significantly from 7.1733 Å ($y = 0.13$) to 7.1900 Å ($y = 0.21$), but as more Mn content inserted, the slope slow down for *a* ranging from 7.1900 Å ($y = 0.21$) to 7.2012 Å ($y = 0.40$).

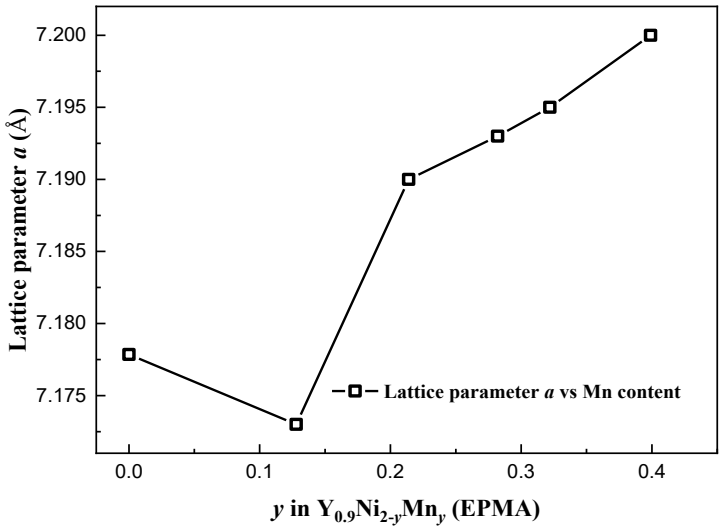


Figure 4.24 Lattice parameters of *C*15 Laves phase $Y_{1-v}(Ni, Mn)_2$ as function of Mn content.

For more clearly analyzing the evolution of lattice parameter of *C*15 $Y_{1-v}(Ni, Mn)_2$ phases, $YMn_{2-y}Ni_y$ compounds with $y = 0$, 0.2 [206] have been added in Figure 4.25 for comparation. Both $YMn_2$ and $YMn_{1.8}Ni_{0.2}$ crystalize in *C*15 Laves phase structure with Y:(Ni, Mn) stoichiometry of 1:2. The Ni for Mn substitution in $YMn_2$ leads to a strong reduction of the lattice parameter from 7.66 Å ($y = 0$) to 7.61 Å ($y = 0.2$). Whereas the increase of the lattice parameter for $Y_{0.9}Ni_{2-y}Mn_y$ compounds is much smaller, varying from 7.1736(1) Å ($y = 0.1$) to 7.1951(1) Å ($y = 0.3$). This difference of lattice parameter variation suggests that there is a competition between the expansion caused by Mn substitution on Ni site and the contraction caused either by Y vacancies [127] or by a possible anti-site occupation of Mn atoms (on Y site) as previously reported [256,258]. This hypothesis will be investigated by neutron diffraction and DFT calculations in the following section.

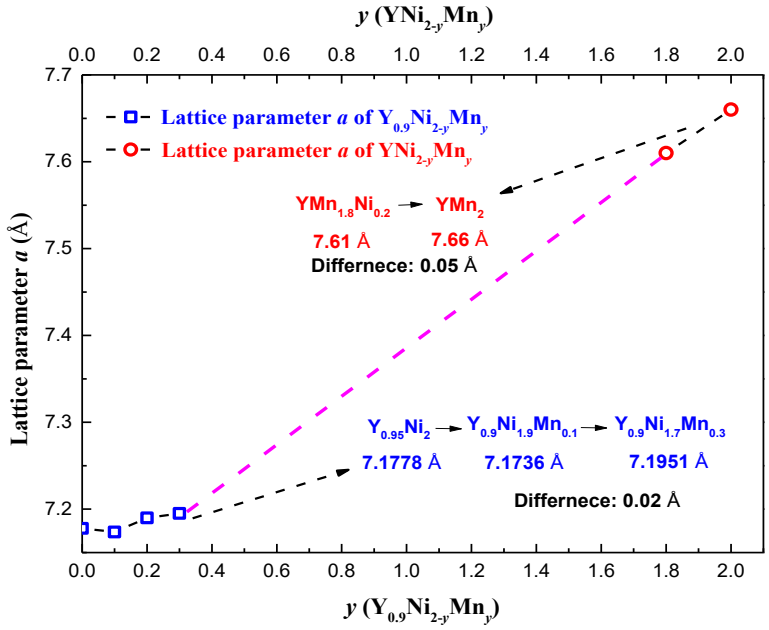


Figure 4.25 The evolution of lattice parameters of *C*15 phase in $Y_{0.9}Ni_{2-y}Mn_y$ ($y$ = 0.1, 0.2, 0.3), $YMn_{2-y}Ni_y$ ($y$ = 0, 0.2) [206].

### 4.2.3.2 $AB_3$ -type $YNi_{3-z}Mn_z$ phase

Figure 4.26 shows the lattice parameter of $AB_3$-type $YNi_{3-z}Mn_z$ phase with Mn content $z$ obtained by EPMA analyses. To follow the evolution of the $a$ and $c$ lattice parameter versus Mn content $z$, two other $YNi_{3-z}Mn_z$ compositions from the literatures ($z$ = 0, 0.33) [259,260] were added in Figure 4.26. Another series of $YNi_{3-z}Mn_z$ ($0 \leq z \leq 0.833$) pseudo-binary compounds reported by V. V. Berezovets' *et al.* [261] has been also added in this graph for comparison.

Both lattice parameters $a$ and $c$ increase dramatically as Mn content varies from $z$ = 0.55 to $z$ = 0.65. Surprisingly $a$ and $c$ remain almost constant ($a$: 5.0857 Å → 5.0884 Å, $c$: 24.6122 Å → 24.6168 Å) for $z$ = 0.65 to 0.78, then they increase again as more Mn content is inserted in $AB_3$ phase.

One can notice that both lattice parameter $a$ and $c$ do not follow a linear variation as expected from a typical Vegard's law [204]. Indeed, the lattice constant $a$ show a nearly linear increase for Mn content $z$ up to 0.65, whereas $c$ increases weakly for low Mn content ($0 \leq z \leq 0.33$), then starts to increase markedly for larger Mn content ($0.33 \leq z \leq 0.65$). This phenomenon can be interpreted that Mn substitutes to Ni only in the [$AB_5$] slab as reported in the literature [235]. This leads to an expansion of this slab, a reduced mismatch between the [$AB_5$] and [$A_2B_4$] slabs, and finally causes a lattice expansion in the $ab$ plane. However, between $z$ = 0.33 and $z$ = 0.65, both lattice parameter $a$ and $c$ show sharp increase, close to a Vegard's law, indicating Mn substitution may be equally distributed in [$AB_2$] and [$AB_5$] slabs, leading to a lattice expansion along both $ab$ plane and $c$ direction. This anomalous evolution occurring for $z$ < 0.65 is similar to the behavior observed for Mn in $Sm_2Ni_{7-w}Mn_w$ system [93]. It is also worth noticing

that the *a* and *c* lattice parameters remain almost unchanged for *z* between 0.65 and 0.78, then it starts to increase again for higher Mn content. Such anomalous behavior of the lattice parameters may be attributed to the rearrangement of Mn atoms distribution in [$AB_2$] and [$AB_5$] slabs at a larger Mn concentration.

Regarding pseudo-binary compounds $YNi_{3-z}Mn_z$ ($0 \leq z \leq 0.833$) reported from [261], the evolution of the *a* parameter is close to our work, including the nearly linear part ($0 \leq z \leq 0.67$) and the plateau region ($0.67 \leq z \leq 0.73$). Lattice parameter *c* shows a similar plateau region than for $YNi_{3-z}Mn_z$ ($z = 0$, 0.33) compounds [259,260], whereas for higher Mn content it exhibits a monotonous increase and no plateau region was observed until *z* reaches 0.833. So, to interpret these results, the site occupations of Mn and Ni atoms were determined combining neutron diffraction experiments in next section.

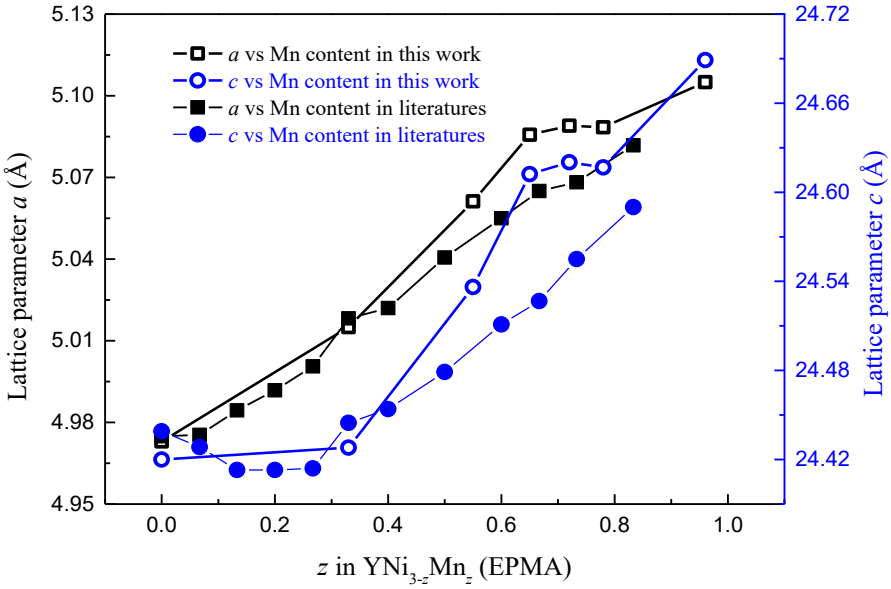


Figure 4.26 The lattice parameters *a* (black hollow box) and *c* (blue hollow circle) of $AB_3$-type $YNi_{3-z}Mn_z$ phases formed in $Y_xNi_{2-y}Mn_y$ ($0.75 \leq x \leq 1$, $y = 0.3$, 0.4, 0.5) compounds and from literatures ($z = 0$, 0.33) [259,260]. The black solid box and blue solid circle represent respectively the lattice parameters *a* and *c* of another series compounds $YNi_{3-z}Mn_z$ ($0 \leq z \leq 0.833$) [261].

### 4.2.3.3 *AB*-type YNi phase

*AB*-type YNi phase exhibits minor changes of *a*, *b* and *c* lattice parameters and cell volume ($162.3$ Å$^3 \leq V \leq 162.7$ Å$^3$), in agreement with EPMA analyses indicating that there is no Mn in the *AB* phase.

## 4.2.4 Vacancies and anti-site occupation of Mn

### 4.2.4.1 Neutron diffraction analysis

The contrast between Mn and Ni atoms is not sufficient by XRD, whereas neutron diffraction allows to discriminate between Ni and Mn and localize Mn position. Therefore, time of flight neutron diffraction has been performed at 25 °C for $Y_{0.9}Ni_{1.9}Mn_{0.1}$, $Y_{0.86}Ni_{1.8}Mn_{0.2}$, $Y_{0.825}Ni_{1.7}Mn_{0.3}$ and $Y_{0.79}Ni_{1.61}Mn_{0.39}$.

To better distinguish the occupations of Y vacancies and Mn atoms, the Neutron Powder Diffraction (NPD) and laboratory X-ray Powder Diffraction (XRPD) patterns are jointly refined. The following assumptions are done: the total Y, Ni and Mn contents are fixed to the value determined by EPMA, the yttrium atoms occupy only *A*-site, the nickel atoms occupy only *B*-sites. The refinement allows to distribute Mn atoms within *A* and *B* sites, keeping the sum $(m \cdot Mn\ (A) + (1-m) \cdot Mn\ (B))$ equal to EPMA measured content, and fitting only the parameter $m$. On the *A*-site possible vacancy rate (□) is also refined. The *A*/*B* ratio is fixed to the stoichiometry 1/2 as equation (1).

$$(Y + \square + m \cdot Mn)/(Ni + (1-m) \cdot Mn) = 1/2 \quad (1)$$

Figure 4.27 presents the refined patterns of the NPD (a), and XRD (b) of taking $Y_{0.825}Ni_{1.7}Mn_{0.3}$ for example. The detailed information of atomic occupations and lattice parameters refined from XRD and NPD patterns are listed in Table 4.8. For the low Mn content sample $y = 0.1$, the Y-site is filled with Y (86%) and vacancies (14%), while Mn occupy only Ni-site. For all another compounds, the Mn atoms are located in both *A* and *B* site and no more vacancies are present in the structure.

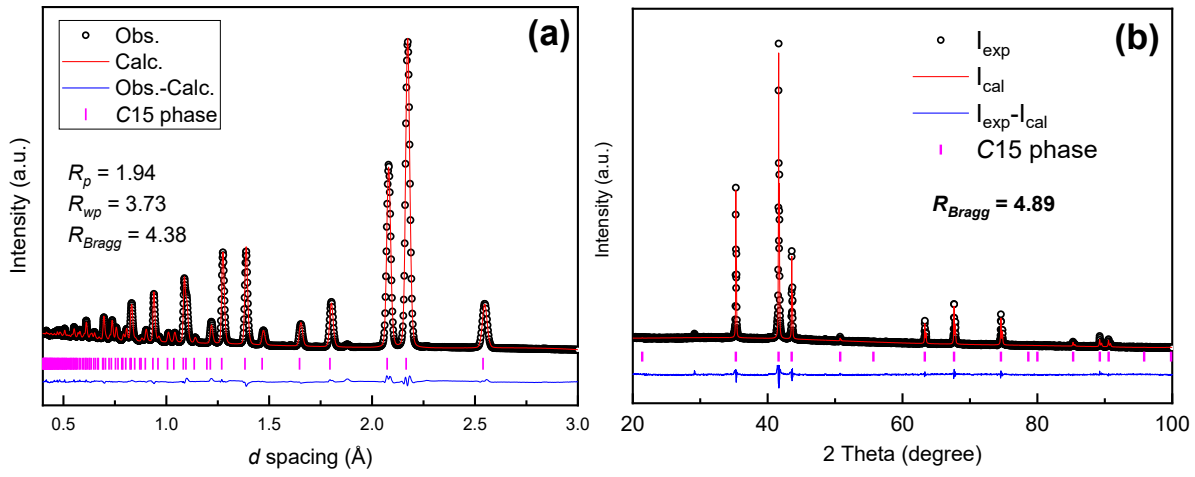


Figure 4.27 Neutron diffraction pattern (a) and X-ray diffraction (b) pattern of $Y_{0.825}Ni_{1.7}Mn_{0.3}$.

Table 4.8 Detailed structural information of *C*15 phases with the nominal composition $Y_{0.9}Ni_{1.9}Mn_{0.1}$, $Y_{0.86}Ni_{1.8}Mn_{0.2}$ and $Y_{0.825}Ni_{1.7}Mn_{0.3}$ and $Y_{0.79}Ni_{1.61}Mn_{0.39}$ from joint NPD and XRD refinement

| Nominal Composition | | $Y_{0.9}Ni_{1.9}Mn_{0.1}$ | $Y_{0.86}Ni_{1.8}Mn_{0.2}$ | $Y_{0.825}Ni_{1.7}Mn_{0.3}$ | $Y_{0.79}Ni_{1.61}Mn_{0.39}$ |
|---|---|---|---|---|---|
| | | $R_p$ = 2.23<br>$R_{wp}$ = 6.37<br>$R_{Bragg}$ (*C*15) = 4.25 | $R_p$ = 2.10<br>$R_{wp}$ = 3.46<br>$R_{Bragg}$ (*C*15) = 3.75 | $R_p$ = 1.94<br>$R_{wp}$ = 3.73<br>$R_{Bragg}$ (*C*15) = 4.38 | $R_p$ = 2.18<br>$R_{wp}$ = 3.71<br>$R_{Bragg}$ (*C*15) = 2.94 |
| Wykoff site 8*b* (3/8, 3/8, 3/8) atom occ.% | Y | 86 | 90 | 87 | 86 |
| | Mn | 0 | 10 | 13 | 14 |
| | □ | 14 | | | |
| Wykoff site 16*c* (0, 0, 0) atom occ.% | Ni | 93.5 | 94.5 | 90 | 85 |
| | Mn | 6.5 | 5.5 | 10 | 15 |
| Composition from diffraction | | $Y_{0.86}$□$_{0.14}Ni_{1.87}Mn_{0.13}$<br>($Y_{0.86}Ni_{1.87}Mn_{0.13}$) | $Y_{0.9}Mn_{0.1}Ni_{1.89}Mn_{0.11}$<br>($Y_{0.85}Ni_{1.79}Mn_{0.20}$) | $Y_{0.87}Mn_{0.13}Ni_{1.8}Mn_{0.2}$<br>($Y_{0.812}Ni_{1.68}Mn_{0.31}$) | $Y_{0.86}Mn_{0.14}Ni_{1.7}Mn_{0.3}$<br>($Y_{0.80}Ni_{1.59}Mn_{0.41}$) |
| Composition from EPMA (±0.02) | | $Y_{0.86}Ni_{1.87}Mn_{0.13}$ | $Y_{0.85}Ni_{1.79}Mn_{0.21}$ | $Y_{0.825}Ni_{1.68}Mn_{0.32}$ | $Y_{0.80}Ni_{1.59}Mn_{0.41}$ |
| *a* (Å) | | 7.1736 (1) | 7.1813 (1) | 7.1861 (1) | 7.1998 (1) |

## 4.2.5 DFT calculation

### 4.2.5.1 Computational methods

Figure 4.28 represents the structures investigated computationally (empty symbols), including structures with stoichiometries close to the samples synthesized (filled symbols), experimentally.

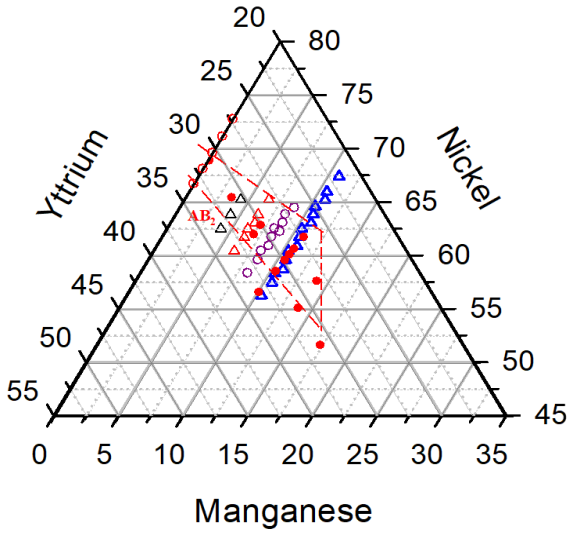


Figure 4.28 Ternary plot of the simulated compositions of (Y, □, Mn)(Ni, Mn)$_2$.(empty symbols) in comparison with experimental compositions (filled symbols).

Figure 4.29 represents formation energy of structures of (Y, □, Mn)(Ni, Mn)$_2$ in the composition range of 10.42-10.87 at.% Mn (a), 8.33-8.88 at.% Mn (b) and 6.25-6.52 at.% Mn (c), calculated at 500 K, including the wight of energy of each configurational disorder. It is worth noting that the effect of temperature on the trend of stability is negligible (see Figure 4.29d). From now on, all analyses are carried out on the basis of formation energies calculated at 500 K, to weigh each composition by their corresponding configurational degeneracy via the Boltzmann distribution.

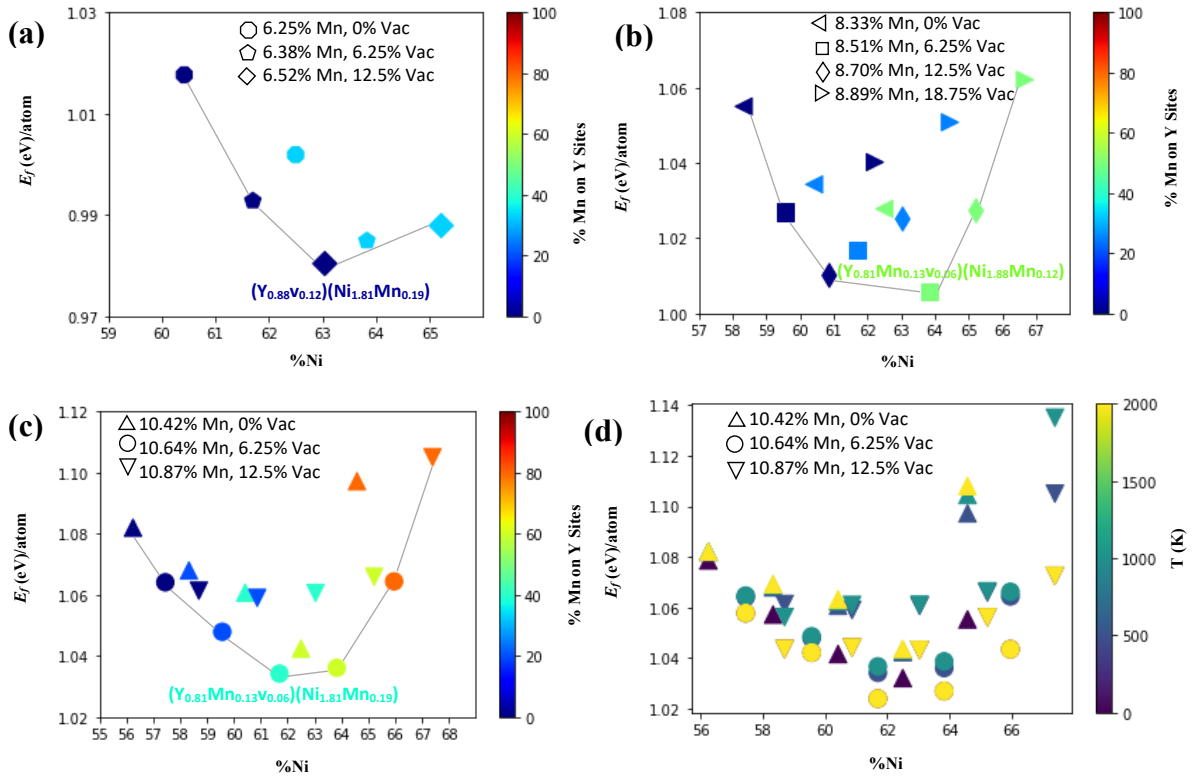


Figure 4.29. Formation energies of compounds of (Y, □, Mn)(Ni, Mn)$_2$ at 500 K, in the composition range of (a) 6.25-6.52 at.% Mn, (b) 8.33-8.88 at.% Mn and (c) 10.42-10.87 at.% Mn; color-coded by %Mn accommodated on the Y sites. (d) Formation energies of (Y, □, Mn)(Ni, Mn)$_2$ structures containing 10.42-10.87 at.% Mn at different temperatures.

As can be seen in Figure 4.29a, for the structures in the composition range of 6.25-6.52 at. %Mn, the lowest energy structure ($Y_{0.88}□_{0.12}$)($Ni_{1.81}Mn_{0.19}$) contains 12.5% Y vacancy (Figure 4.30) with all Mn atoms occupying Ni sites. In the composition range of 8.33 - 8.88 at.% Mn (see Figure 4.29b), *i.e.* the lowest energy compound ($Y_{0.81}Mn_{0.13}□_{0.06}$)($Ni_{1.88}Mn_{0.12}$) contains 6.25% Y vacancy, and around 50% of Mn atoms occupy Y sites in this structure (Figure 4.30), while we see that another configuration with 12.5 % vacancy of Y-sites and non-Mn occupy Y-site has slightly higher energy. For the fifteen structures investigated in the composition range of 10.42 - 10.87 at.% Mn (see Figure 4.29c), structure with compositions $Y_{0.81}Mn_{0.13}□_{0.06}$)($Ni_{1.81}Mn_{0.19}$) possesses the lowest formation energy. It contains 6.25% Y-site vacancy and roughly around 40% of Mn atoms occupy the Y sites in this structure (Figure 4.30),

and structure close to this one $(Y_{0.75}Mn_{0.19}\square_{0.06})(Ni_{1.87}Mn_{0.13})$ possess almost the same energy. Notably, neither of structures with no vacancies nor too many vacancies on the Y sites are preferable in these composition ranges.

Generally speaking, atomic scale simulations reveal that Mn may be accommodated on both Y and Ni sites, however, the partitioning between the two sites is strongly dependent on Mn concentration: at low concentrations (< 6.52 at.% Mn), Mn is preferentially accommodated on the Ni sites only, while as consequent quantity of vacancies is present at Y-sites. At higher Mn concentrations (8.33-10.87 at.% Mn), Mn atoms may be accommodated on both sites and the Y-site vacancies become less significant, the structures with difference Ni content, thus different anti-site occupation of Mn atoms possess very similar energy. And additionally, it is found that vacancies on Y sites are indispensable for stabilizing (Y, □)(Ni, $Mn)_2$, which is dominant at low Mn concentrations.

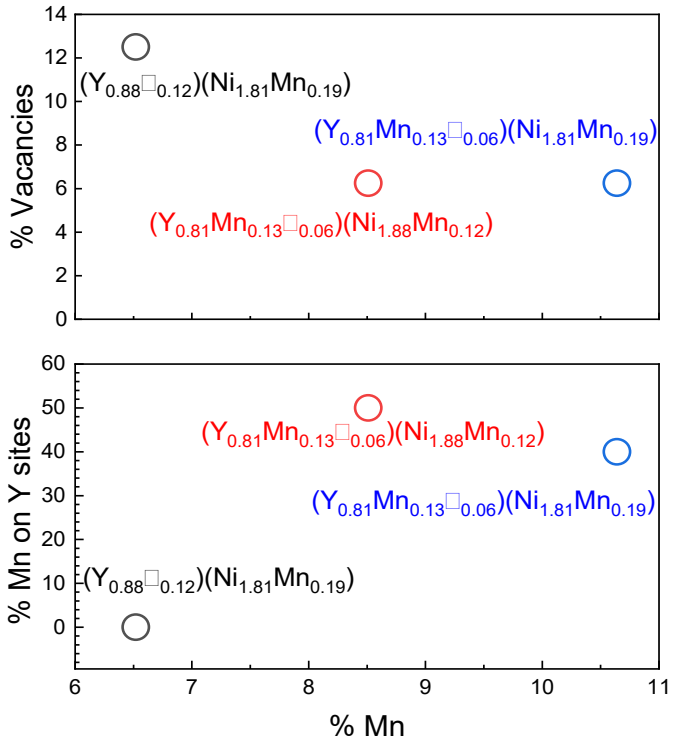


Figure 4.30. Percentage of vacancy on Y sites (upper panel) and percentage of Mn atoms occupied Y sites (lower panel).

### 4.2.5.2 Discussion on the phase formation

To better observe the evolution of the structure and composition of *C*15 phase, we analyzed EPMA compositions and lattice parameters of all the formed *C*15 Laves phase or superstructure phase. Their variation trends are shown in Figure 4.31. We can understand the ternary contour in two directions as follows:

Figure 4.31 shows ternary diagram of cell parameter as function of composition obtained by EPMA, indicating the domain of *C*15 phase formation increases with Mn content before

decreases again and rich the limit of solubility of Mn around 0.4. The lattice parameter exhibits a strong increase with the increasing Mn content following the "*b*" direction, where Y content stays the same. The changes of lattice parameter can be interpreted as a solid solution behavior, close to a Vegard's law [204]. Meanwhile, following the for "$a_1$" direction, within low Mn content range, the lattice parameter remains unchanged if Y content decreases tinnily accompanied with the increasing Mn content simultaneously. Similarly, in "$a_2$" directions, the Ni contents are basically unchanged, as the Y content decreases strongly and Mn content increase weakly, for the compositions with high Mn content, the lattice parameter remains unchanged. This three-dimension behavior indicates a more "complex" structure than we assumed before.

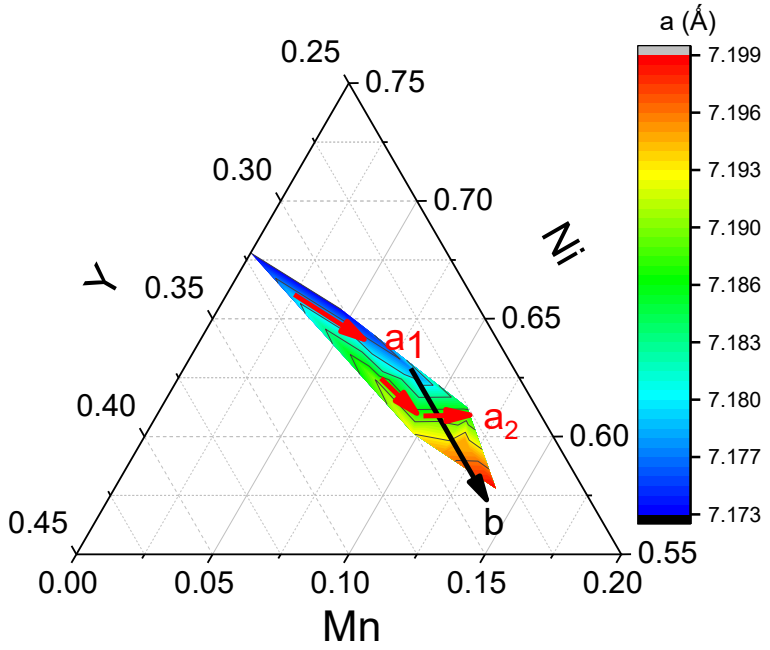


Figure 4.31 Ternary diagram of Y-Ni-Mn as function of lattice constant of *C*15 Laves phase.

The $Y_zNi_{2-y}Mn_y$ have been studied by combined diffraction techniques (X-ray and Neutron), EPMA and DFT calculations. The data analyses show that upon Mn substitution the $Y_zNi_{2-y}Mn_y$ compounds crystalize rather in *C*15 structure than superstructure as the case of $Y_{0.95}Ni_2$. For $z = 0.9$, the Mn content $y$ varies from 0.1 to 0.5. It was found that only with $y = 0.1$ we have obtained single-phase compound. By each given Mn content, alloys with different $x$ value have been synthesized. It is shown that with increasing of Mn content $y$, the stoichiometry $x$ should be decreased to obtain single phase. For $y = 0.4$, the *C*15 phase forms with large sub-stoichiometric $z = 0.79$.

To explain this phenomena, we propose two hypothesis: i) the Y-site vacancy, which is supported the presence of *A*-site vacancies in $RNi_2$ compounds (*R* = rare earth elements) already reported [119,124–126,210,262], ii) the anti-site occupation of Mn, which is supported by the ability of Mn to sit on the *A* sites in $ZrMn_2$-type Laves phase, allowing large over-stoichiometric

domains $ZrMn_{2+x}$ [256]. Moreover, ternary $RNi_2Mn$ ($R$ = Tb, Dy, Ho, Er) compounds [258] crystalize in the $C15$ Laves phase structure, where Mn occupying $A$- sites and $B$-sites.

The phases composition obtained by EPMA for all studied compounds are shown in the ternary diagram (Figure 4.32), the composition of $AB_2$ phases is inside the red frame and these of $AB_3$ phases are framed by two blue lines, the points of YNi phase are also shown in black squares. $AB_2$ phases coexist with $AB$ and $AB_3$ neighbouring phases for the multi-phase samples. This is a tentative phase diagram, it is shown the $AB_2$ phase domain varies with Mn content, at low Mn content, the phase forms with narrow stoichiometry, with increasing of Mn content, the composition region become wider up to the limit around $y \approx 0.4$. It is worth noting that all the $AB_2$ phases contain Mn locate above the ideal Y(Ni, Mn)$_2$ line assuming non vacancies and Mn plays the role of $B$-element. This suggests the presence of the vacancies on the Y-site, or the anti-site occupation of Mn on Y-site or co-existence of both. The compositions of ternary $AB_3$ phases locate around the stoichiometry Y(Ni, Mn)$_3$ line without large deviations. $AB$ (YNi) phase is very poor in Mn and it can be considered as a binary compound without Mn solubility.

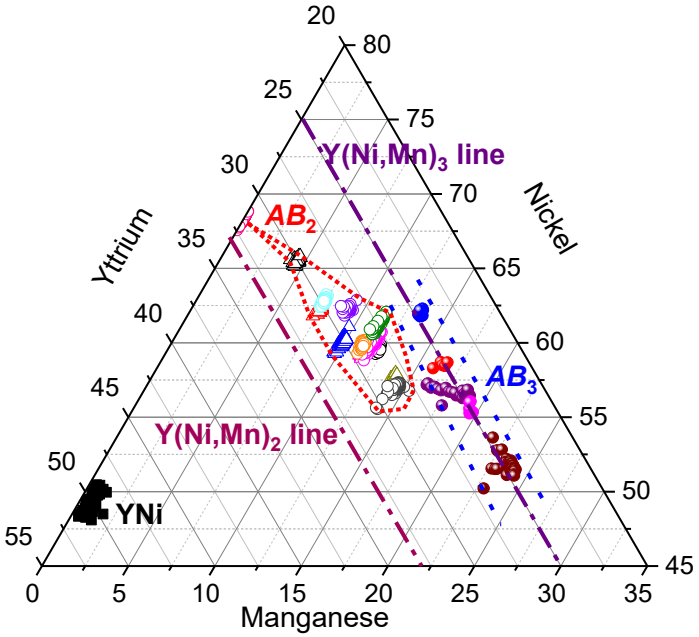


Figure 4.32 Ternary diagram of $Y_zNi_{2-y}Mn_y$ compounds: the opened symbols represent $AB_2$ phase; the closed balls represent $AB_3$ phase; the closed black boxes represent YNi phase.

Experimentally, the laboratory XRD give a good resolution of the structure, determining the lattice parameter but could not distinguish Ni, Mn occupation due to their very similar electron cloud. The neutron diffraction, specially by TOF technique gives a higher resolution of the atomic occupation. By using TOPAS package, a joint refinement of XRD and NPD allows us determine the Mn occupation and eventually $A$-site vacancies. From, the diffraction data, same tendency as DFT calculation has been observed, even the impossible direct comparison due to the composition difference. At low Mn concentration, the anti-site occupation can be neglected while the structure is stabilized by the Y-site vacancies, 14% of

they-site are vacates. This high-rate vacancy can explain the small lattice parameter change of $Y_{0.9}Ni_{1.9}Mn_{0.1}$ compound by comparison with the binary compound $Y_{0.95}Ni_2$ (direction *a*1 in Figure 4.31) where 5 % Y-site vacancy is established [122]. Even the atomic radium of Mn larger than that of Ni, the large proportion of vacancies 14% for $Y_{0.9}Ni_{1.9}Mn_{0.1}$ leads to a slight lattice contraction. At high Mn content, the vacancies on the *A*-sites decreases drastically see missing and 64 %, 56% and 48 % of Mn occupy the *A*-sites for the *C*15 phase with composition of $Y_{0.85}Ni_{1.79}Mn_{0.21}$, $Y_{0.825}Ni_{1.68}Mn_{0.32}$ and $Y_{0.80}Ni_{1.59}Mn_{0.41}$ respectively (see Table 4.8), which results in a Mn almost constant anti-site occupation rate (10%, 13% and 14% respectively) while a significant increase of the Mn content on the *B*-site (5.5%, 10% and 15 % respectively), globally leads to a lattice parameter increase (direction *b* in Figure 4.31). The results from DFT calculation agree with experimental: at low Mn content the *C*15 is stabilized by *A*-site vacancies. DFT calculation show that at high Mn content, the vacancies percentage decreases and a part of Mn atoms (50% for $Y_{0.81}Ni_{1.88}Mn_{0.28}$ and 40% for $Y_{0.81}Ni_{1.81}Mn_{0.32}$) go occupy the *A*-sites. And at high Mn content, *C*15 phase can be formed in a composition region by adjusting the anti-site occupation of Mn atoms, which is clearly indicated in the Figure 4.32. Also, the constant lattice parameter of *C*15 phase in the direction "*a*2" shown in Figure 4.31 indicates also the capability of adjustment of the Mn atoms either occupy *A*- or *B* – sites. This behavior is shown from DFT calculation results: for 10.64 at. % Mn, the composition with 61.5 at. % Ni and 64 at. % Ni show almost the same formation energy ( Figure 4.29c), the structure forms with different rate on Mn anti-site occupation.

## 4.2.6 Hydrogen sorption properties

### 4.2.6.1 Pressure-composition isotherms

After an activation pretreatment at 150 °C under vacuum, the PCI were measured at 150 °C for all $Y_xNi_{2-y}Mn_y$ ($0.75 \leq x \leq 0.95$, $0 \leq y \leq 0.5$) intermetallic compounds. As shown in

Figure 4.33a, for $Y_{0.9}Ni_{2-y}Mn_y$ ($y = 0.1, 0.2, 0.3$) compounds, the hydrogen storage capacity of Mn0.1 (~3.3 H/f.u.) compound is slightly lower than the one of Mn0.2 (~3.8 H/f.u.) and Mn0.3 (~3.8 H/f.u.) compounds. All the PCI curves present a first plateau between 0.25 H/f.u. and1.5 H/f.u., the plateau pressures are similar with a weak decrease from 0.0052 MPa ($y = 0.1$) to 0.0034 MPa ($y = 0.3$). For Mn0.2 and Mn0.3 compounds, the presence of a second sloping plateau with between 2 H/f.u. and 2.5 H/f.u. are prominent, and the corresponding equilibrium pressures reduces significantly (from 0.3135 MPa for Mn0.2 compound to 0.0795 MPa for Mn0.3 compound at hydrogen concentrations of around 2.5 H/f.u.).

For $Y_{0.9}Ni_{2-y}Mn_y$ ($y = 0.4, 0.5$) compounds (Figure 4.33b), the PCI curves show very different shapes. At low hydrogen concentration (< 1 H/f.u.), the equilibrium pressure is too low (below $10^{-5}$ MPa) to be measured in our laboratory. Besides that, we also observe a plateau ranging from 1.0 H/f.u. to 2.0 H/f.u. and a sloppy curve raising up to a maximum capacity of

3.8 H/f.u. and 3.0 H/f.u. for Mn0.4 and Mn0.5 respectively, showing good reversibility and very small hysteresis.

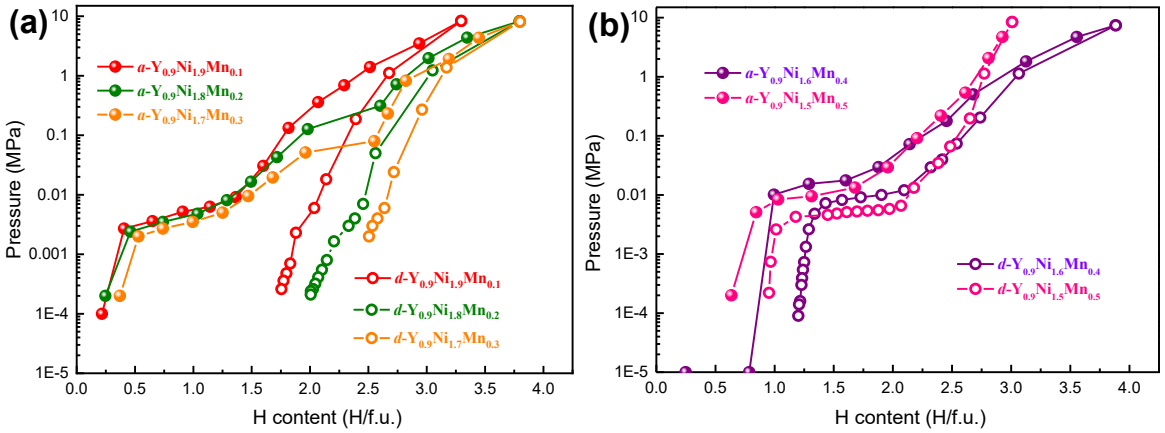


Figure 4.33 *P-C* isotherms measured at 150 ℃ for $Y_{0.9}Ni_{2-y}Mn_y$ ($y$ = 0.1, 0.2, 0.3) (a) and $Y_{0.9}Ni_{2-y}Mn_y$ ($y$ = 0.4, 0.5) (b) compounds, solid and open symbols represent the hydrogen absorption and desorption processes respectively.

The PCI curves of$Y_xNi_{1.7}Mn_{0.3}$ compounds ($x$ = 0.9, 0.85, 0.825, 0.80, 0.75) (Figure 4.34), except Y0.75, show two plateaus absorption behavior. As Y content reduces from 0.9 to 0.75, the corresponding hydrogen storage capacity decreases from 3.8 H/f.u. to 2.9 H/f.u., while the equilibrium pressure of the first plateau slightly increases. The second plateau pressure decreases first from 0.079 MPa for Y0.9 to 0.037 MPa for Y0.85, then increases markedly from 0.037 MPa for Y0.85 to 0.159 MPa for Y0.80. Finally, for Y0.75, a sloppy absorption branch and a good reversibility with residual hydrogen of 0.7 H/f.u. can be observed.

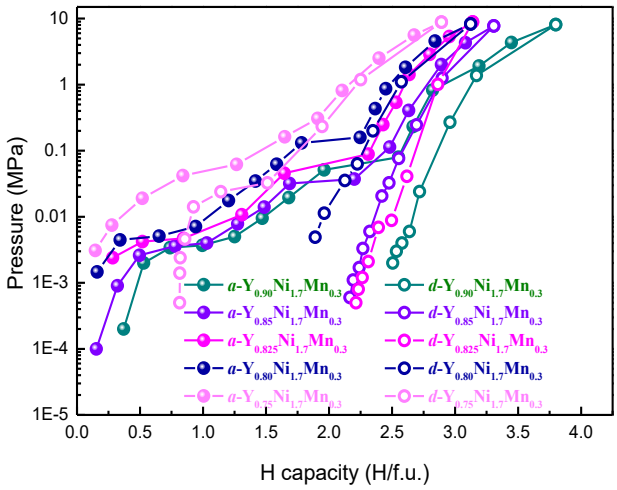


Figure 4.34 *P-C* isotherms measured at 150 ℃ for $Y_xNi_{1.7}Mn_{0.3}$ ($x$ = 0.9, 0.85, 0.825, 0.80, 0.75), solid and empty balls represent the hydrogen absorption and desorption processes respectively.

For the single-phase compounds with *C*15 structure or superstructure (Figure 4.35), one notice that the first plateaus overlap each other, showing the same equilibrium pressure of 0.005 MPa. In addition, the second plateau can be clearly observed for $Y_{0.95}Ni_2$, $Y_{0.86}Ni_{1.8}Mn_{0.2}$ and

$Y_{0.825}Ni_{1.7}Mn_{0.3}$ compounds, and the substitution of Mn for Ni slightly lowers the second plateau pressure. $Y_{0.9}Ni_{1.9}Mn_{0.1}$ shows different absorption behaviors at hydrogen concentration region 1.5 H/f.u. - 2.5 H/f.u., a sloppy branch is observed.

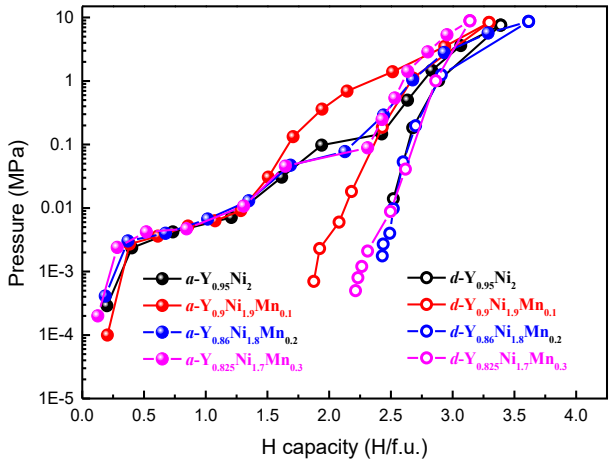


Figure 4.35 PCIs measured at 150 °C for $Y_xNi_{2-y}Mn_y$ compounds with single superstructure ($Y_{0.95}Ni_2$) or *C*15 Laves phase structure, solid and hollow balls represent the hydrogen absorption and desorption processes respectively.

### 4.2.6.2 Hydrides of $Y_{0.9}Ni_{2-y}Mn_y$ ($y$ = 0.1, 0.2, 0.3, 0.4, 0.5)

XRD have been performed on $Y_{0.9}Ni_{2-y}Mn_y$ ($y$ = 0.1, 0.2, 0.3, 0.4, 0.5) hydrides which have been hydrogenated at room temperature up to various hydrogen concentrations. Considering the different phases obtained for $y \leq 0.3$ and $y \geq 0.4$, we will present the hydrides evolution separately. The XRD patterns of their hydrides are shown in Figure 4.36 and Figure 4.37, the detailed crystallographic information obtained from Rietveld refinement are summarized in Table 4.9 and Table 4.10 respectively.

For Mn0.1, upon hydrogen uptake the *C*15 phase is changed to $TmNi_2$-type superstructure with double lattice parameter. Up to 2 H/f.u., the sample contains two phases, one intermetallic phase and a hydride phase with expanded lattice parameter, which corresponds to the plateau observed on PCI at 150 °C (even if it is not the same temperature) on Figure 4.34a. As the hydrogen concentration increases from 1.1 H/f.u. to 1.6 H/f.u., the lattice parameter of the hydrides phase remains almost constant (within the errors). Then between 1.6 H/f.u. and 2.0 H/f.u., the lattice parameter $a$ increases again from 15.051 Å to 15.229 Å, and the corresponding cell volume from 2952.8 (1) $Å^3$ to 3532.5 (5) $Å^3$ (with cell expansion of 19.6% as shown in Table 4.9), indicating the beginning of the solid-solution branch of the hydride phase.

For the compounds with larger Mn content ($y$ = 0.2, 0.3), the PCI show a “second plateau”. The XRD patterns for samples contain more than 1.1 H/f.u. show the formation of an unknown hydride. The intensity of Bragg peaks of this new hydride was markedly increased for $y$ = 0.3 at hydrogen concentration up to 1.9 H/f.u., indicating that the formation of such unknown hydride occurs more easily for compound with larger Mn content and moderate H concentration.

It is also obvious, that for Mn0.3, the relative decrease of the diffraction peaks intensity with H content may indicate a loss of crystallinity after hydrogen absorption.

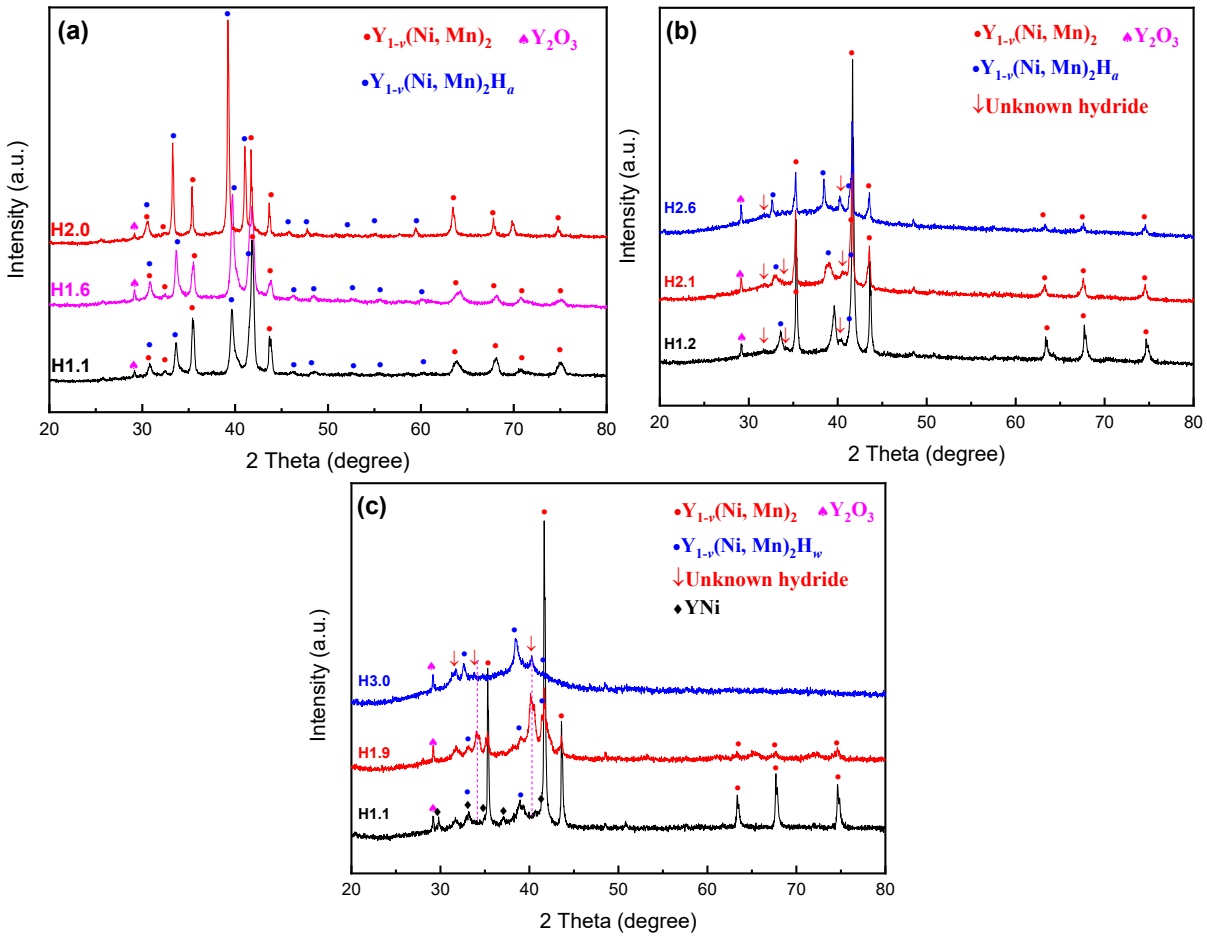


Figure 4.36 XRD patterns of the hydrides of $Y_{0.9}Ni_{1.9}Mn_{0.1}$ (a), $Y_{0.9}Ni_{1.8}Mn_{0.2}$ (b) and $Y_{0.9}Ni_{1.7}Mn_{0.3}$ (c) with different hydrogen concentration prepared at room temperature.

For both Mn0.4 and Mn0.5 compounds, it is interesting to observe that the lattice parameters of Y(Ni, Mn)$_3$ phase remain almost unchanged as hydrogen concentration increases to about 0.9 H/f.u. (Table 4.10). The hydride phase of YNi with $DyNiD_{3.8}$-type (*Cmcm*) structure was indexed in the pattern. This indicates that the un-measurable part of PCI curve at low pressure (Figure 4.33b) corresponds to the $YNiH_y$ formation. Similar results have been discussed in the Y-Ni-Al system, in the section 4.1.3. For hydrogen concentrations up to 2.80 H/f.u. for Mn0.4 and 2.53 H/f.u. for Mn0.5, the lattice parameters of Y(Ni, Mn)$_3$ phase increased drastically with volume expansion of 18.6% which correspond to the Y(Ni, Mn)$_3H_x$ hydride formation, (Figure 4.37 and Table 4.10).

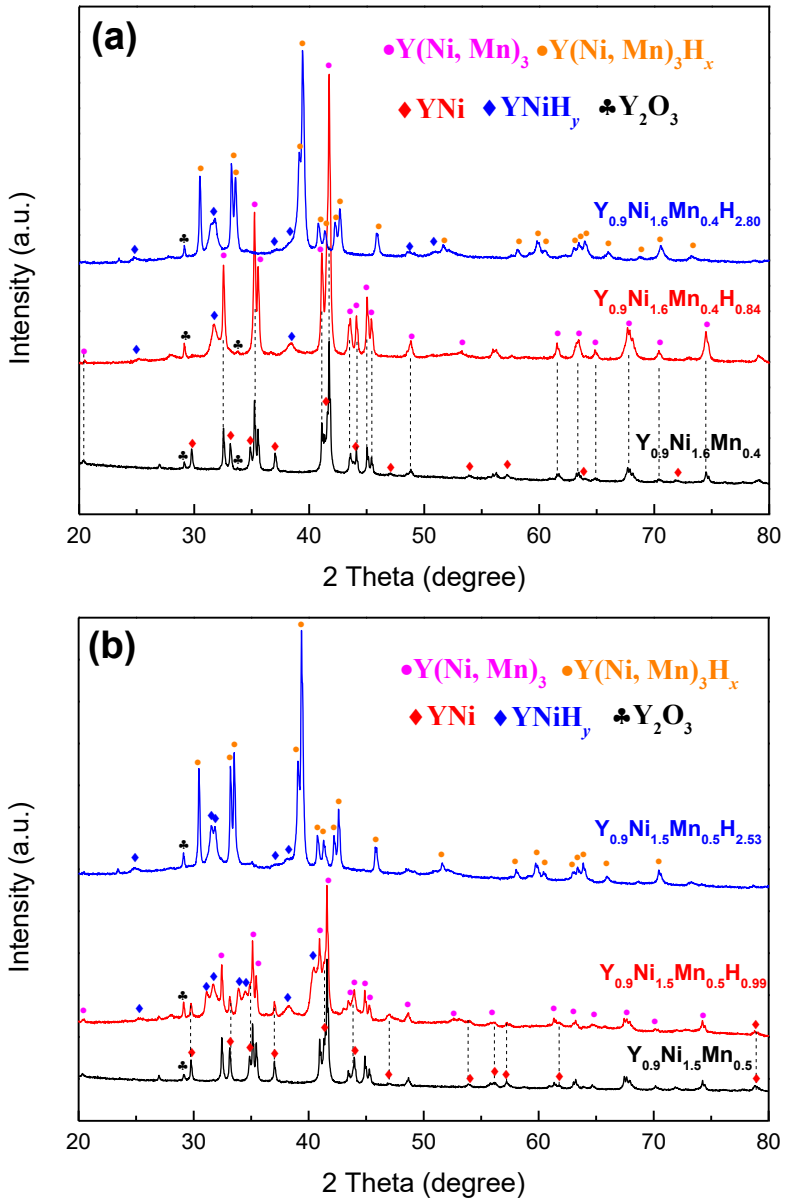


Figure 4.37 XRD patterns of the hydrides of $Y_{0.9}Ni_{1.6}Mn_{0.4}$ (a) and $Y_{0.9}Ni_{1.5}Mn_{0.5}$ (b) with different hydrogen concentrations prepared at room temperature.

Table 4.9 Crystallographic data of $Y_{0.9}Ni_{1.9}Mn_{0.1}$ compound and its hydrides

| Compound and hydrides | Phase | Abundance | Crystal structure | Lattice parameters *a* (Å) | Cell volume *V* (Å$^3$) | *ΔV/V* |
|---|---|---|---|---|---|---|
| $Y_{0.9}Ni_{1.9}Mn_{0.1}$ | $Y_{1-v}(Ni, Mn)_2$ | 96% | $MgCu_2$ ($Fd\bar{3}m$) | 7.1733 (1)/14.3466 (2) | 369.11 (1)/2952.8 (1) | |
| | $Y_2O_3$ | 4% | | | | |
| $Y_{0.9}Ni_{1.9}Mn_{0.1}H_{1.1}$ | $Y_{1-v}(Ni, Mn)_2$ | 47% | $TmNi_2$ ($F\bar{4}3m$) | 14.318 (1) | 2935.3 (5) | |
| | $Y_{1-v}(Ni, Mn)_2H_w$ | 52% | $TmNi_2$ ($F\bar{4}3m$) | 15.065 (1) | 3419.3 (7) | 15.8 % |
| | $Y_2O_3$ | 1% | | | | |
| $Y_{0.9}Ni_{1.9}Mn_{0.1}H_{1.6}$ | $Y_{1-v}(Ni, Mn)_2$ | 35% | $TmNi_2$ ($F\bar{4}3m$) | 14.320 (2) | 2936.7 (7) | |
| | $Y_{1-v}(Ni, Mn)_2H_w$ | 64% | $TmNi_2$ ($F\bar{4}3m$) | 15.051 (2) | 3409.7 (9) | 15.5 % |
| | $Y_2O_3$ | 1% | | | | |
| $Y_{0.9}Ni_{1.9}Mn_{0.1}H_{2.0}$ | $Y_{1-v}(Ni, Mn)_2$ | 21% | $TmNi_2$ ($F\bar{4}3m$) | 14.357 (1) | 2959.4 (4) | |
| | $Y_{1-v}(Ni, Mn)_2H_w$ | 78% | $TmNi_2$ ($F\bar{4}3m$) | 15.229 (1) | 3532.5 (5) | 19.6 % |
| | $Y_2O_3$ | 1% | | | | |

Table 4.10 Crystallographic data of $Y_{0.9}Ni_{1.6}Mn_{0.4}$ and $Y_{0.9}Ni_{1.5}Mn_{0.5}$ compounds and their hydrides

| Compounds and hydrides | Phase | Crystal structure | Lattice parameter (Å) | | | Cell volume $V$ (Å$^3$) |
|---|---|---|---|---|---|---|
| | | | *a* | *b* | *c* | |
| $Y_{0.9}Ni_{1.6}Mn_{0.4}$ | Y(Ni, Mn)$_3$ | PuNi$_3$ ($R\bar{3}m$) | 5.0890 (1) | | 24.6202 (1) | 552.19 (1) |
| | YNi | FeB (*Pnma*) | 7.1464 (6) | 4.1260 (1) | 5.5118 (1) | 162.52 (1) |
| | Y (Ni, Mn)$_2$ | MgCu$_2$ ($Fd\bar{3}m$) | 7.2012 (4) | | | 373.44 (3) |
| H0.84 | Y(Ni, Mn)$_3$ | PuNi$_3$ ($R\bar{3}m$) | 5.0897 (4) | | 24.6237 (2) | 552.42 (7) |
| | YNiH$_y$ | DyNiD$_{3.8}$ (*Cmcm*) | 3.699 (4) | 11.297 (1) | 4.7004 (5) | 196.4 (2) |
| H2.80 | Y(Ni, Mn)$_3$H$_x$ | PuNi$_3$ ($R\bar{3}m$) | 5.3367 (3) | | 26.529 (2) | 654.33 (8) |
| | YNiH$_y$ | DyNiD$_{3.8}$ (*Cmcm*) | 3.747 (1) | 11.376 (1) | 4.6345 (3) | 197.5 (1) |
| $Y_{0.9}Ni_{1.5}Mn_{0.5}$ | Y(Ni, Mn)$_3$ | PuNi$_3$ ($R\bar{3}m$) | 5.1050 (1) | | 24.6890 (1) | 557.24 (2) |
| | YNi | FeB (*Pnma*) | 7.1481 (5) | 4.1266 (1) | 5.5133 (1) | 162.63 (1) |
| H0.99 | Y(Ni, Mn)$_3$ | PuNi$_3$ ($R\bar{3}m$) | 5.120 (1) | | 24.704 (1) | 552.42 (7) |
| | YNiH$_y$ | Unknown | | | | |
| H2.53 | Y(Ni, Mn)$_3$H$_x$ | PuNi$_3$ ($R\bar{3}m$) | 5.3407 (2) | | 26.531 (1) | 655.38 (5) |
| | YNiH$_y$ | DyNiD$_{3.8}$ (*Cmcm*) | 3.763 (1) | 11.336 (1) | 4.5816 (3) | 195.45 (9) |

### 4.2.6.3 Phase occurrences and structural evolutions upon dehydrogenation

XRD characterization was performed after PCI measurements and subsequent hydrogen desorption under dynamic vacuum at 150 °C.

The XRD patterns of dehydrogenated $Y_{0.9}Ni_{2-y}Mn_y$ ($y$ = 0 - 0.3) show that, all these compounds have *C*15 phase as major phase (Figure 4.38a). It is clear that except for $Y_{0.9}Ni_{1.9}Mn_{0.1}$, the Bragg peaks of the initial intermetallic as well as hydride phases are not present upon dehydrogenation, indicating that full HIA occurs for these compounds. It is worth to note, that only $Y_{0.9}Ni_{1.9}Mn_{0.1}$ compound preserved the crystalline *C*15 phase after PCI measurement, showing better structural stability versus HIA. This should be related to its structural property, where only Y-site vacancies are present. All other compounds are suspected to have Mn anti-site occupation.

The XRD patterns of samples having $AB_3$ phase as major phase ($Y_{0.9}Ni_{2-y}Mn_y$ ($y$ = 0.4, 0.5) and $Y_xNi_{1.7}Mn_{0.3}$ ($x$ = 0.80, 0.75)) after dehydrogenation are presented in Figure 4.38b. The XRD patterns of $Y_{0.9}Ni_{2-y}Mn_y$ ($y$ = 0.4, 0.5) can be indexed with amorphous $YNiH_t$ hydride and the $AB_3$ intermetallic phase. The hydrogen cannot be released from $YNiH_t$ phase, thus leads to the uncompleted hydrogen desorption process shown in Figure 4.33. The crystallographic parameters of the $AB_3$ phase (pristine compound and dehydrogenated phase) are listed in Table 4.11. After dehydrogenation, the $AB_3$ phase presents an anisotropic lattice expansion along *c* axes with $\Delta c/c$ around 0.2%, indicating that some hydrogen atoms are trapped in the structure. However, for $Y_xNi_{1.7}Mn_{0.3}$ ($x$ = 0.80, 0.75) compounds, no obvious lattice expansion of $AB_3$ phases were observed, neither in *ab* plane nor along *c* axes. The lattice expansion behavior after hydrogen desorption may be attributed to the Mn content involved in $AB_3$ phase. The EPMA results (Table 4.11) show that the $AB_3$ phase in $Y_{0.9}Ni_{1.6}Mn_{0.4}$ and $Y_{0.9}Ni_{1.5}Mn_{0.5}$ contains more Mn than for $Y_{0.8}Ni_{1.7}Mn_{0.3}$ and $Y_{0.75}Ni_{1.7}Mn_{0.3}$. The literature [93,261,263] show that at low Mn content (normally $x < 0.5$), the hydrogen sorption properties as well as electrochemical performance of $AB_{n-x}Mn_x$ ($n$ = 3, 3.5, 3.8) alloys could be improved. Nevertheless, for higher Mn content, The $YNi_{3-x}Mn_x$ compounds show deteriorated electrochemical performance [261]. This behavior may be caused by the fact that at low Mn content the Mn atoms occupy only [$AB_5$] which contribute reducing the mismatch and enhance the structure stability and hydrogen absorption. At higher Mn-content, Mn atoms occupy also the sites in [$A_2B_4$] slabs, may results in instability of the structure.

The absence of crystalline peaks related to *C*15 phase in $Y_{0.80}Ni_{1.7}Mn_{0.3}$ indicates the hydrogen induced amorphization of *C*15 phase, which may contribute to the large wave on the XRD patterns.

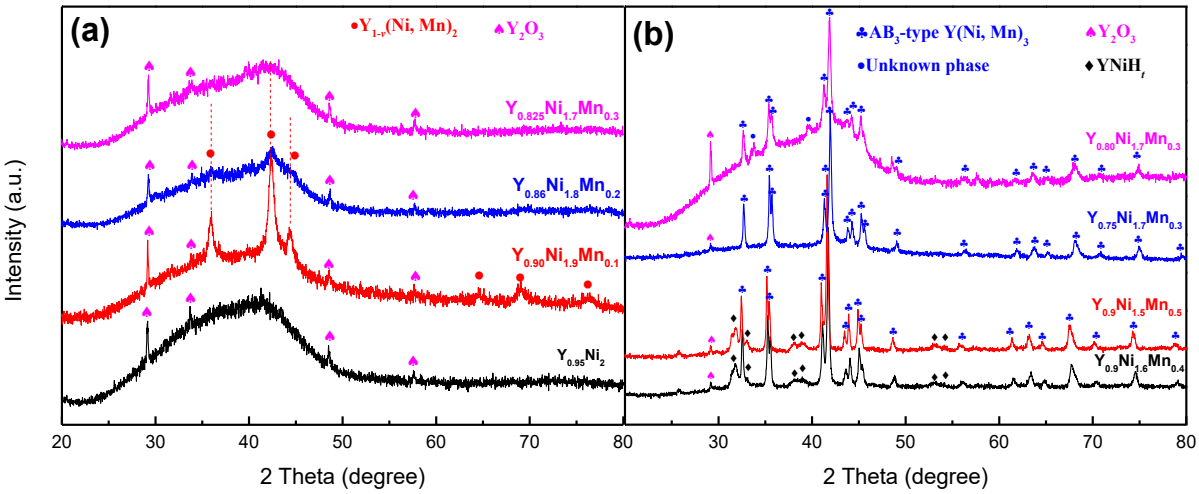


Figure 4.38 XRD patterns of the compounds with single-phase structure (superstructure or *C*15) (a) and $AB_3$-type Y(Ni, Mn)$_3$ (b) after PCI measurements and hydrogen desorption under dynamic vacuum at 150 °C.

Table 4.11 Crystallographic data of $AB_3$ phase (parent compound and dehydrogenated phase) in the $Y_{0.9}Ni_{2-y}Mn_y$ ($y$ = 0.4, 0.5) and $Y_xNi_{1.7}Mn_{0.3}$ ($x$ = 0.80, 0.75) compounds before and after PCI.

| Nominal composition | EPMA composition (±0.02) | Crystal structure | Lattice parameters (Å) | | | | | |
|---|---|---|---|---|---|---|---|---|
| | | | $AB_3$ phase (Compound) | | $AB_3$ phase (Dehydrogenated) | | | |
| | | | $a$ | $c$ | $a$ | $\Delta a/a$ (%) | $c$ | $\Delta c/c$ (%) |
| $Y_{0.9}Ni_{1.6}Mn_{0.4}$ | $YNi_{2.24}Mn_{0.72}$ | $PuNi_3$ ($R\bar{3}m$) | 5.0890 (1) | 24.6202 (1) | 5.0935 (4) | 0.09 | 24.6704 (2) | 0.20 |
| $Y_{0.9}Ni_{1.5}Mn_{0.5}$ | $YNi_{2.09}Mn_{0.96}$ | $PuNi_3$ ($R\bar{3}m$) | 5.1050 (1) | 24.6890 (1) | 5.1060 (3) | 0.02 | 24.7465 (2) | 0.23 |
| $Y_{0.75}Ni_{1.7}Mn_{0.3}$ | $YNi_{2.52}Mn_{0.55}$ | $PuNi_3$ ($R\bar{3}m$) | 5.0612 (1) | 24. 5362 (4) | 5.0650 (6) | 0.08 | 24.5389 (3) | 0.01 |
| $Y_{0.80}Ni_{1.7}Mn_{0.3}$ | - | $PuNi_3$ ($R\bar{3}m$) | 5.0678 (4) | 24.5655 (1) | 5.0742 (8) | 0.12 | 24.5725 (4) | 0.03 |

### 4.2.6.4 DSC studies of the amorphous hydrides

After PCI tests and subsequent hydrogen desorption at 150 °C under dynamic vacuum, thermal analysis was performed for $Y_xNi_{2-y}Mn_y$ compounds. The TG/DSC curves are shown in Figure 4.39. According to loss of weight of the samples (TG curves) we calculated the desorbed mol $H_2$ per mol samples. Then, by integrating the endothermic peaks (shadow area) we could calculate the enthalpy changes during releasing one mole of $H_2$. The crystallization temperature and enthalpy changes are listed in Table 4.12. All the DSC curves of compounds with single superstructure or *C*15 phase show a large broad endothermic peak followed by a sharp exothermic peak, corresponding to the trapped hydrogen desorption of amorphous and phase crystallization. The shaded area below the broken line corresponds to enthalpy changes during the release of hydrogen from amorphous hydrides. This temperature does not vary with Mn content. As temperature varying from T1 to T2, the hydrogen content released from the amorphous phase increases with the increasing Mn content (Mn0.1 to Mn0.3). The maximum

amount of desorbed hydrogen can be observed for Mn0.3, whereas the Mn0.2 compound shows maximum enthalpy.

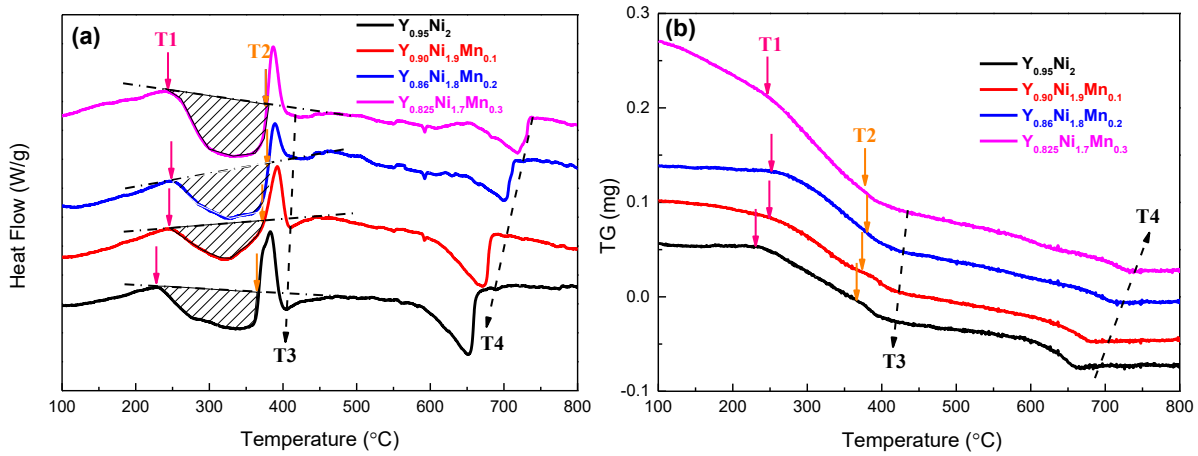


Figure 4.39 DSC (a) and TG (b) curves of $Y_xNi_{2-y}Mn_y$ compounds ($x$ = 0.95, 0.9, 0.86, 0.825, $y$ = 0, 0.1, 0.2, 0.3) samples upon PCI tests and hydrogen desorption under dynamic vacuum. T1 and T2 are the beginning and end temperature for hydrogen desorption of amorphous hydrides, T3 is the end temperature of crystallization, T4 is the end temperature of the second endothermic peak which should correspond to the hydrogen desorption from $YH_2$.

Table 4.12 The hydrogen content released from the amorphous phase and the enthalpy changes per mol $H_2$.

| Samples | Hydrogen desorption (mol $H_2$/mol sample) | $\Delta H$ (kJ/mol $H_2$) |
|---|---|---|
| *a*-$Y_{0.95}Ni_2H_w$ | 0.39 | 41.58 |
| *a*-$Y_{0.90}Ni_{1.9}Mn_{0.1}H_w$ | 0.34 | 35.16 |
| *a*-$Y_{0.86}Ni_{1.8}Mn_{0.2}H_w$ | 0.39 | 52.80 |
| *a*-$Y_{0.825}Ni_{1.7}Mn_{0.3}H_w$ | 0.59 | 39.48 |

At higher temperature, the exothermic peak should correspond to recrystallization, T3 being the temperature at which ends the crystallization. T4 is the end temperature of the second endothermic peak which may correspond to the hydrogen desorption from $YH_2$. Interestingly, this temperature increases with Mn content, but the raison should be clarified.

To understand the structural evolution upon heating, the XRD analysis was carried out for the samples upon thermal analysis at temperatures T3 and T4. As shown in Figure 4.40a, after crystallization at T3, all the XRD patterns contains $AB_3$-type Y(Ni, Mn)$_3$, $YH_2$ phase and a small amount of $AB_2$ and $Y_2O_3$, indicating a disproportionation reaction of the hydride upon hydrogenation and dehydrogenation. After heating at T4 temperature, the absence of $YH_2$ phase and presence of $C15$ or superstructure Y (Ni, Mn)$_2$ phase indicates a reaction between $YH_2$ and $AB_3$-type Y(Ni, Mn)$_3$ phase (Figure 4.40b) which can explain the sensitivity of T4 to the Mn content. The prominent oxide $Y_2O_3$ and remaining $AB_3$ phase means an incomplete reaction.

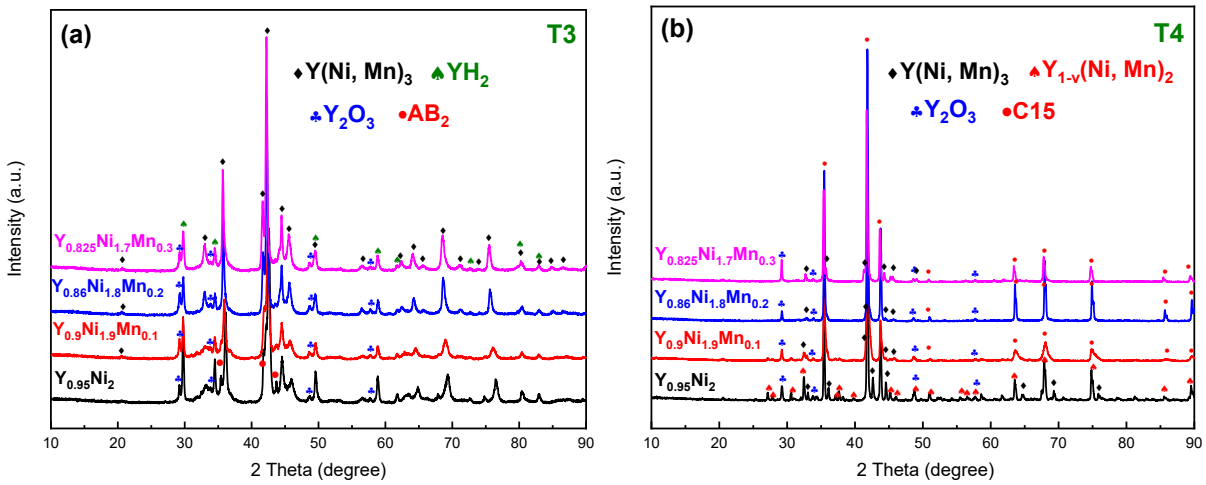


Figure 4.40 The XRD patterns of $Y_xNi_{2-y}Mn_y$ ($x$ = 0.95, 0.9, 0.86, 0.825, $y$ = 0, 0.1, 0.2, 0.3) compounds upon thermal analysis at different temperature: T3, the end temperature of crystallization (a); T4, the end temperature of the second endothermic peak (b).

The DSC analyses of $Y_{0.9}Ni_{2-y}Mn_y$ ($y$ = 0.4, 0.5) compounds show a broad endothermic peak followed by a small exothermic peak, which may represent desorption of trapped hydrogen of $AB_3$-type $Y(Ni, Mn)_3H_z$ and $YNiH_z$ phase respectively. The XRD patterns after DSC measurements show that the YNi phase has disappeared and that a new $YNi_3$ phase ($a$ = 4.9792 $c$ = 24.5766, space group $R\bar{3}m$ [264]) was formed upon crystallization indicating the instability of YNi phase. Furthermore, Table 4.13 shows the lattice parameters of $Y(Ni, Mn)_3$ phase upon dehydrogenation and thermal analysis. Both $a$ and $c$ parameters exhibit a slight drop after heating to 600 °C, and recovering the initial value. This means that the trapped hydrogen atoms could be released up to 600 °C.

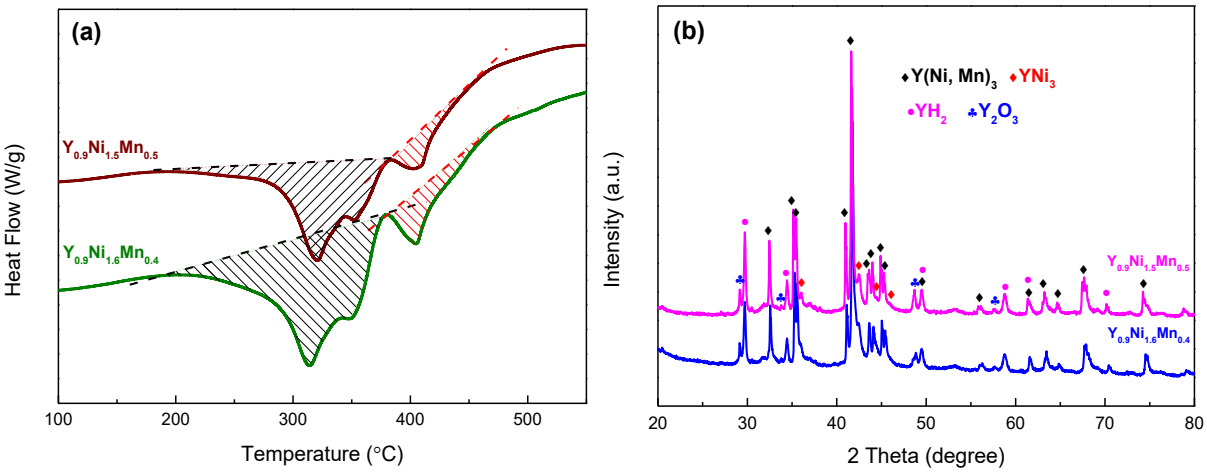


Figure 4.41 DSC curves of $Y_xNi_{2-y}Mn_y$ compounds ($x$ = 0.9, $y$ = 0.4, 0.5) samples upon PCI measurements and hydrogen desorption under dynamic vacuum (a), and the corresponding XRD patterns of the samples upon thermal analysis (b).

Table 4.13 Crystallographic data of $AB_3$ phase in the $Y_{0.9}Ni_{2-y}Mn_y$ ($y$ = 0.4, 0.5) compounds, initial, after PCI and after DSC analysis.

| Compounds | Samples | Phase | Crystal structure | Lattice parameters (Å) | |
|---|---|---|---|---|---|
| | | | | *A* | *c* |
| $Y_{0.9}Ni_{1.6}Mn_{0.4}$ | Initial | $YNi_{2.24}Mn_{0.72}$ | $PuNi_3$ ($R\bar{3}m$) | 5.0890 (1) | 24.6202 (1) |
| | Dehydrogenated | $Y(Ni, Mn)_3$ | $PuNi_3$ ($R\bar{3}m$) | 5.0935 (4) | 24.6704 (2) |
| | After thermal analysis | $Y(Ni, Mn)_3$ | $PuNi_3$ ($R\bar{3}m$) | 5.0865 (2) | 24.6308 (1) |
| $Y_{0.9}Ni_{1.5}Mn_{0.5}$ | Initial | $YNi_{2.09}Mn_{0.96}$ | $PuNi_3$ ($R\bar{3}m$) | 5.1050 (1) | 24.6890 (1) |
| | Dehydrogenated | $Y(Ni, Mn)_3$ | $PuNi_3$ ($R\bar{3}m$) | 5.1060 (3) | 24.7465 (2) |
| | After thermal analysis | $Y(Ni, Mn)_3$ | $PuNi_3$ ($R\bar{3}m$) | 5.1015 (3) | 24.6952 (2) |

### 4.2.6.5 Discussion of the hydrogen sorption properties

***Hydrogen absorption***

The Mn substitution in $Y_{0.9}Ni_{2-y}Mn_y$ up to 0.3 shows similar PCI curves, even if they contain *C*15 phase as major phase with a lattice parameter increases with Mn content, the change of equilibrium pressures of the first plateau are not visible. This can be related to the structural properties, like the anti-site occupation of Mn. As the Mn does not have the same affinity with hydrogen than Y, the partial substitution of Mn for Y makes the compounds less favorable for hydrogen insertion. On the other hand, the increased lattice parameter gives opposite effect. The balancing of both effects can be responsible to the unchanged plateau pressure. For the second plateau, it is more complicated to explain as they do not have the same hydrides.

The XRD patterns of hydrides show that an unknown hydride appeared and HIA has already started during the second hydrogen absorption plateaus of $Y_{0.9}Ni_{1.8}Mn_{0.2}$ (Mn0.2) and $Y_{0.9}Ni_{1.7}Mn_{0.3}$ (Mn0.3) compounds. Whereas $Y_{0.9}Ni_{1.9}Mn_{0.1}$ (Mn0.1) preserved the crystalline hydride and compound phase at the similar hydrogen concentration (around 2 H/f.u.). This means that the structural stability of $Y_{0.9}Ni_{1.9}Mn_{0.1}$ was improved, but that higher amount of Mn yields negative effects on structural stability, which cannot be explained only by the size effect.

For Mn0.2 and Mn0.3, upon hydrogen absorption of 1 H/f.u., the lattice parameters of the crystalline hydride $Y_{1-v}(Ni, Mn)H_w$ and the unknown hydride do non increase with further H-absorption, but the intensities of the Bragg peaks of these two phases decreases and becomes broader. Such behaviors are similar to $GdNi_2$-H system, which is named as a solid solution type amorphization [193]. In those cases, the crystalline hydrides form upon H-sorption with markedly increased lattice parameters, then the amorphous hydride nucleates and growths with the increasing H concentration without further changes of the lattice parameter.

For $Y_{0.9}Ni_{2-y}Mn_y$ ($y$ = 0.4, 0.5) compounds, the low pressure part of PCI with hydrogen concentration below 0.75 H/f.u. can be attributed to hydrogenation of YNi phase [184]. The high plateau pressure can be attributed to the hydrogen absorption process of $YNi_{3-z}Mn_z$ phase, showing a substantial decrease in hysteresis and good reversibility as compared to $YNi_3$-H system [260].

***Hydrogen desorption***

Regarding the hydrogen desorption part, most of the hydrogen cannot be released in the PCI measurement conditions. The XRD patterns of the dehydrogenated samples indicate that fully or partially amorphous hydrides were formed upon hydrogen absorption desorption. As a matter of fact, the $AB_2$ compounds with $A/B$ atomic size ratio above 1.37 will be amorphized by hydrogenation [201]. In this case, considering the anti-site occupation of Mn, the atomic size ratio of the calculated composition $Y_{0.87}Mn_{0.13}Ni_{1.79}Mn_{0.21}$ by NPD is $r_{Y+Mn}/r_{Ni+Mn} = 1.39$, still slightly higher than 1.37, and another effect like valance electron concentration may also play a role here. However, we observed a crystalline phase for $Y_{0.9}Ni_{1.9}Mn_{0.1}$ compound during both hydrogen absorption or desorption, this could be explained by the fact that the high-rate Y-site vacancies for $Y_{0.9}Ni_{1.9}Mn_{0.1}$ makes the atomic size ration lower to $r_{Y+\square}/r_{Ni+Mn} = 1.29$, which make it more stable regarding hydrogenation.

### 4.2.6.6 Thermal analysis for the amorphous hydrides

The overall phase evolution of the amorphous hydride $a$-$Y_{1-v}(Ni, Mn)_2H_z$ upon heating can be summarized into three steps as follows ($a$-: amorphous, $c$-:crystalline):

$$a\text{-}Y_{1-v}(Ni, Mn)_2H_w \xrightarrow[\text{1st endothermic}]{} a\text{-}Y_{1-v}(Ni, Mn)_2H_{w'} + H_2 \xrightarrow[\text{exothermic}]{} c\text{-}Y(Ni, Mn)_3 + c\text{-}YH_2 + H_2 \xrightarrow[\text{2nd endothermic}]{} c\text{-}Y_{1-v}(Ni, Mn)_2 + H_2$$

The hydrogen desorption and crystallization processes of the amorphous hydrides normally end before 400 °C. During these two processes, intermetallic containing some hydrogen goes to disproportionation to Y forming stable metal hydride $YH_2$ and more stable intermetallic $AB_3$-type $Y(Ni, Mn)_3$ phase. Such behaviors are commonly found in amorphous $a$-$RNi_2H_x$ compounds [193,265,266]. Moreover, it is worth noting that the temperature of reaction between $Y(Ni, Mn)_3$ and $YH_2$ phases increases with Mn content. The reaction includes the decomposition of $YH_2$ and rearrangement of Y, Ni and Mn atoms to form $C15$ phase. Therefore, the increased reaction temperature can be attributed to the lower enthalpy of formation of $C15$ phase with higher Mn content, which also indicates the less stable structure [132].

## 4.2.7 Conclusions

Intermetallic compounds with nominal composition $Y_xNi_{2-y}Mn_y$ ($x$ = 1, 0.95, 0.9, 0.86, 0.85, 0.825, 0.80, 0.75, $y$ = 0, 0.1, 0.2, 0.25, 0.3, 0.4, 0.5) were investigated systematically in

this section. Their phase occurrence, structural properties and hydrogen sorption properties have been well studied and discussed.

The solubility limit of Mn doping in *C*15 phase formed in $Y_{0.9}Ni_{2-y}Mn_y$ compounds is around $y = 0.4$. The boundary of Y content forming $AB_2$ phase in $Y_xNi_{1.7}Mn_{0.3}$ compounds is close to $x = 0.825$. Single superstructure phase was obtained for $Y_{0.95}Ni_2$ and single *C*15 Laves phase was obtained for $Y_{0.9}Ni_{1.9}Mn_{0.1}$, $Y_{0.86}Ni_{1.8}Mn_{0.2}$ and $Y_{0.825}Ni_{1.7}Mn_{0.3}$.

The anti-site occupation of Mn in $Y_xNi_{2-y}Mn_y$ system were confirmed combining neutron diffraction and DFT calculation. They agree that the Mn content significantly affects the accommodation of Mn atoms and number of vacancies in $Y_xNi_{2-y}Mn_y$ compounds. When the Mn content increases, Mn atoms preferentially occupy both Y and Ni sites while for low content Mn, they are accommodated only on the Ni sites, meanwhile a high rate of vacancies on Y sites occurs to stabilize the structure. A tentative phase diagram of $AB_2$ phase in Y-Ni-Mn system is given.

The lattice parameter of *C*15 $Y_{1-v}(Ni, Mn)_2$ phase increases weakly with increasing Mn content. This can be interpreted that at low Mn content the size reduction caused by Y vacancies compensates the expected increase of cell volume caused by Mn substitution, whereas for higher Mn content, anti-occupation of Mn leads to a weak increase of lattice parameter, rather than a decrease due to vacancies.

This structural property leads to an almost unchanged first absorption plateau pressure at low hydrogen content (< 1.5 H/f.u.), but a markedly decreased equilibrium pressure for high hydrogen content (> 1.5 H/f.u.). More Mn substituting Y on *A* site helps the formation of another unknown hydride, which is represented by the more prominent second hydrogen absorption plateau. The reversible capacity is ensured by the $AB_3$ phase, which show interesting hydrogenation properties and are worth for further investigation.

# 5 . *A*-side elemental substitution effects on $YNi_2$ compound

In the preceding chapter, we introduced the *B*-side elemental substitution effects on phase occurrence, structural evolution, and hydrogen sorption properties of $YNi_2$ compound. As expected, the structural stability was enhanced partly by the substitution of Al ($r_{Al} = 143\ pm$) and Mn ($r_{Mn} = 135\ pm$) for Ni ($r_{Ni} = 124\ pm$) but do not suppress HIA due to their close atomic radius to that of Ni and limited solid solution in $YNi_2$ compound. It was found that rare earth elements are responsible of the structural instability and HIA effect due to their large atomic radius compared to Ni. Therefore, modifying the *A*-side elemental components may be an effective way to improve structural stability substantially and eliminate HIA.

Mg ($r_{Mg} = 160\ pm$) and Sc ($r_{Sc} = 164\ pm$) were chosen for their much smaller atomic radius than Y ($r_Y = 180\ pm$), to lower the *A*/*B* atomic radius ratio markedly. According to the empirical critical value $r_A/r_B = 1.37$ determining HIA occurrence [201], we can optimize the ratio between Y and Mg or Sc elements, to approach this critical value and suppress HIA effect.

For Mg substitution, we adopted $YNi_2$ directly as the based alloy, investigating the $Y_{1-x}Mg_xNi_2$ ($x$ = 0.1 - 0.5) alloys. Due to the low melting point and high evaporation pressure of Mg, it is hard to control Mg evaporation during induction melting. As a result, the real compositions commonly deviate from the target values. Therefore, the less constituent elements the smaller errors during melting, $YNi_2$ could be more suitable in studying Mg substitution rather than $YNi_{2-y}Al_y$ or $Y_xNi_{2-y}Mn_y$ alloys.

Compared to Mg, Sc evaporation remains limited upon induction melting, so we adopted $Y_{0.9}Ni_{1.9}Mn_{0.1}$ as the starting composition Sc for Y substitution. $Y_{0.9}Ni_{1.9}Mn_{0.1}$ alloy has already been studied thoroughly, showing interesting capacity (3.2 H/f.u.), incomplete amorphization and better structural stability versus HIA (The crystalline *C*15 type phase of $Y_{0.9}Ni_{1.9}Mn_{0.1}$ alloy was preserved after hydrogen absorption and desorption) as compared to other Mn-containing $AB_2$ compounds. The further substitution of Sc for Y can therefore enhance the structural stability and improve hydrogen sorption properties.

# 5.1 The effects of Mg substitution for Y on structural stability and hydrogen sorption properties of $Y_{1-x}Mg_xNi_2$ ($x$ = 0.1 - 0.5) alloys

## 5.1.1 Phase occurrence and crystal structures

### 5.1.1.1 Synthesis and measurements

The $Y_{1-x}Mg_xNi_2$ compounds ($0.1 \leq x \leq 0.5$) were synthesized using induction melting in an Ar atmosphere (5N). Mg has a high vapor pressure and is easy to evaporate, therefore, we added excess Mg (around 150% of the designate Mg content) before the first melting. The ingots were turned over and re-melted several times to ensure their homogeneity. After each melting, a part of Mg was lost, and the mass of ingot was measured to judge if the quantity of Mg in the ingot had reached the target value.

The global compositions of as-cast $Y_{1-x}Mg_xNi_2$ compounds were determined by ICP-AES (Axial View Inductively Coupled Plasma Spectrometer from SPECTRO Analytical Instruments GmbH) and are given in Table 5.1. The compositions of as-cast compounds deviate from the target values due to the unmanageable Mg evaporation. For Mg0.4 and Mg0.5 compounds, the Mg contents are higher than the amount in classical reported $YMgNi_4$ compound ($x = 0.5$) [213].

Table 5.1 Global compositions measured by ICP-AES for the as-cast $Y_{1-x}Mg_xNi_2$ compounds.

| $x$ | Y (±0.01) | Mg (±0.01) | Ni (±0.01) | Composition |
|---|---|---|---|---|
| 0.1 | 0.84 | 0.18 | 2.00 | $Y_{0.84}Mg_{0.18}Ni_2$ |
| 0.2 | 0.73 | 0.28 | 2.00 | $Y_{0.73}Mg_{0.28}Ni_2$ |
| 0.3 | 0.65 | 0.38 | 2.00 | $Y_{0.65}Mg_{0.38}Ni_2$ |
| 0.4 | 0.56 | 0.61 | 2.00 | $Y_{0.56}Mg_{0.61}Ni_2$ |
| 0.5 | 0.47 | 0.73 | 2.00 | $Y_{0.47}Mg_{0.73}Ni_2$ |

### 5.1.1.2 Phase occurrence

Figure 5.1 shows the XRD patterns of the as-cast $Y_{1-x}Mg_xNi_2$ ($x$ = 0.1, 0.2, 0.3, 0.4, 0.5) compounds. The Rietveld refinement of XRD patterns is shown in Figure 5.2 and the obtained crystallographic data such as phase abundance and lattice constants are summarized in Table 5.2. Without surprise, for all compounds, $A_2B_4$-type $(Y, Mg)_2Ni_4$ phase in *C*15*b* structure is the main phase instead the *C*15 structure for the *B*-side substituted compounds. The *C*15*b* structure (space group: $F\bar{4}3m$, No. 216) differs to the C15 structure by the ordered *A*-site occupation: 8*a* sites split in 4*a* (prefer to be occupied by rare earth atoms) and 4*c* (prefer to be occupied by Mg atoms) sites. Despite the small amount of $Y_2O_3$ (≤ 3 wt.%), the single-phase *C*15*b* structure are observed for Mg0.1 and Mg0.2 compounds, the secondary $AB_3$-type $(Y, Mg)Ni_3$ phase (5 wt.%) and $Mg_2Ni$ phase (6 wt.%) were presented respectively in Mg0.3 and Mg0.4 compounds.

It is worth noting that the XRD pattern of Mg0.4 compound exhibits different relative peak intensities (two peaks shown between 20° and 30°) as compared to the other compounds. Indeed, the relative peak intensities of $A_2B_4$ phase are closely related to the exchange occupation phenomenon at 4*a* and 4*c* sites, which is commonly observed in $REMgNi_4$ compounds [215,216]. In our case, the Y and Mg may simultaneously occupy 4*a* and 4*c* sites because of the exceeding Y ($Y_{1.4}Mg_{0.3}Ni_4$) content, showing similar relative peak intensities for all compounds except Mg0.4 one. Considering the excess of Y and Mg content shown in ICP result, we tried to refine its XRD pattern by using various possible occupation of Y and Mg based on a single $A_2B_4$ phase. Nevertheless, the refinement is not good, though any hypothesis about another phase is too forward from the unsatisfactory of one peak intensity (blue arrow on Figure 5.1).

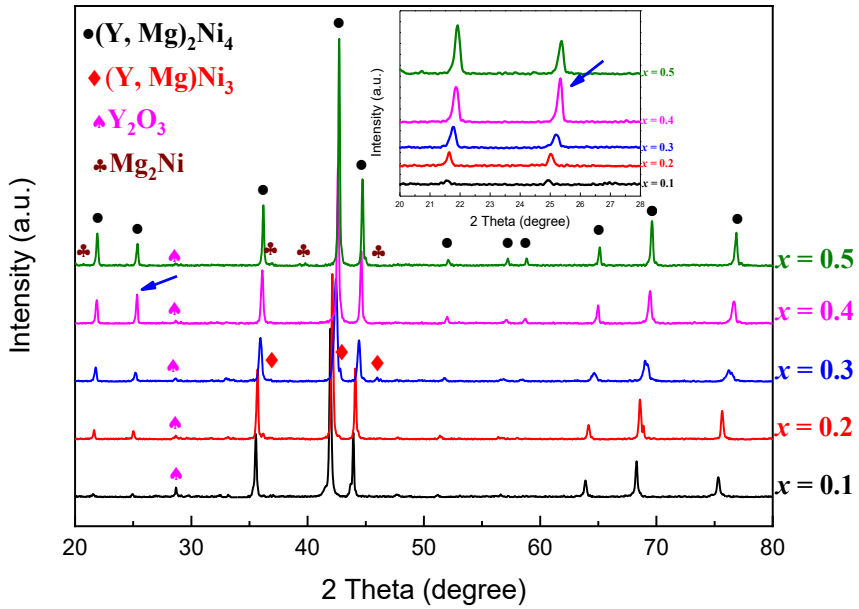


Figure 5.1 XRD patterns of the as-cast $Y_{1-x}Mg_xNi_2$ ($0.1 \leq x \leq 0.5$) compounds.

Table 5.2 Phase occurrence and crystal structures of as-cast $Y_{1-x}Mg_xNi_2$ ($0.1 \leq x \leq 0.5$) compounds.

| $x$ | Phase | Abundance (±1%) | Crystal structure | Space group |
|---|---|---|---|---|
| 0.1 | $(Y, Mg)_2Ni_4$ | 97% | *C*15*b* | $F\bar{4}3m$ |
| | $Y_2O_3$ | 3% | | $Ia\bar{3}$ |
| 0.2 | $(Y, Mg)_2Ni_4$ | 98% | *C*15*b* | $F\bar{4}3m$ |
| | $Y_2O_3$ | 2% | | $Ia\bar{3}$ |
| 0.3 | $(Y, Mg)_2Ni_4$ | 93% | *C*15*b* | $F\bar{4}3m$ |
| | $(Y, Mg)Ni_3$ | 5% | $PuNi_3$ | $R\bar{3}m$ |
| | $Y_2O_3$ | 2% | | $Ia\bar{3}$ |
| 0.4 | $(Y, Mg)_2Ni_4$ | ~99% | *C*15*b* | $F\bar{4}3m$ |
| | $Y_2O_3$ | ~1% | | $Ia\bar{3}$ |
| 0.5 | $(Y, Mg)_2Ni_4$ | 93% | *C*15*b* | $F\bar{4}3m$ |
| | $Mg_2Ni$ | 6% | | P6222 |
| | $Y_2O_3$ | 1% | | $Ia\bar{3}$ |

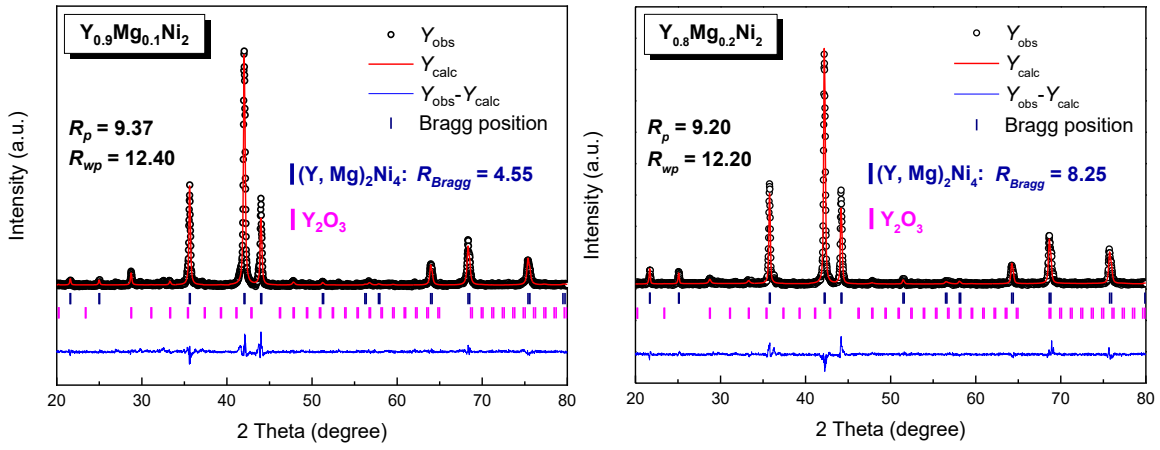

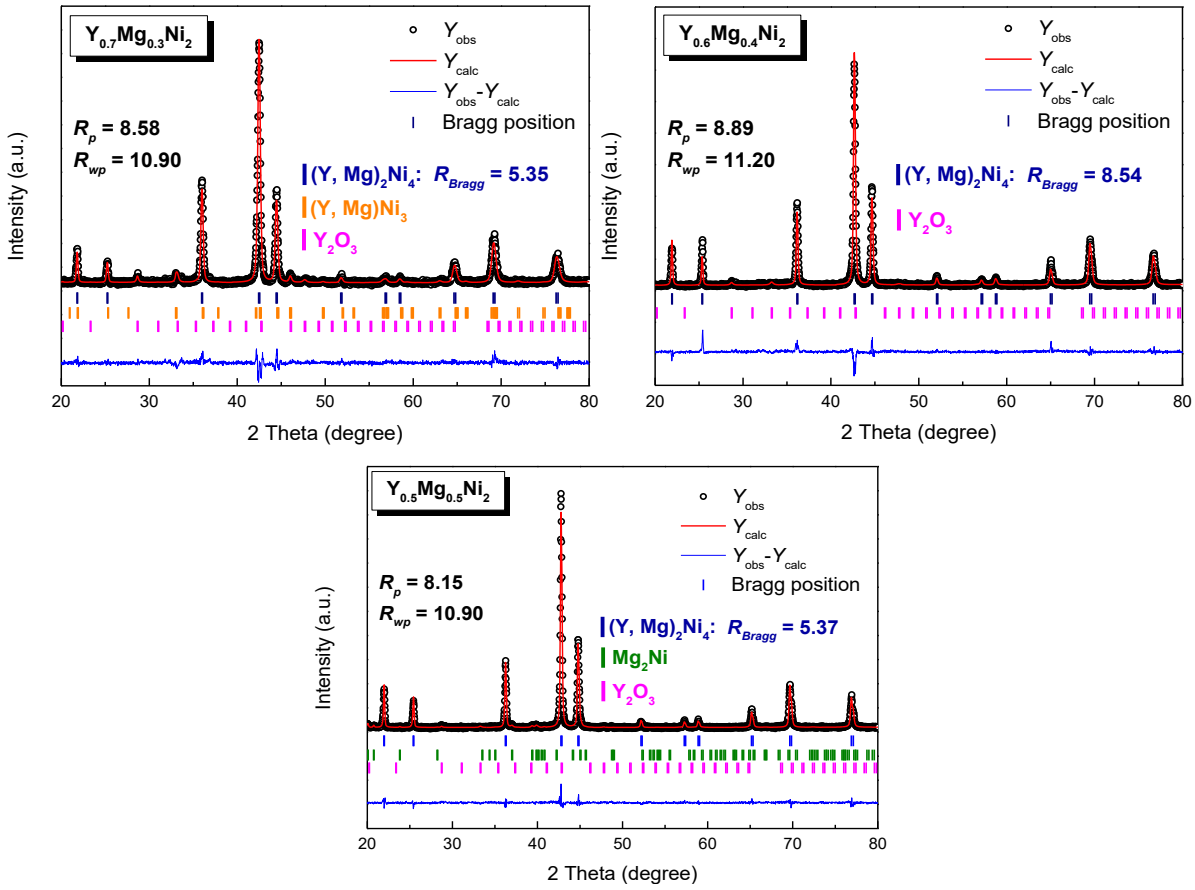


Figure 5.2 Rietveld refinements of the XRD patterns for as-cast $Y_{1-x}Mg_xNi_2$ ($0.1 \leq x \leq 0.5$) compounds.

### 5.1.1.3 Lattice constants of $A_2B_4$ phase

Figure 5.3 shows the lattice parameters as function of Mg content calculated by Rietveld analysis. For sake of contrast, the Mg content measured by ICP ($Y_{1-x}Mg_xNi_2$) was also present in this figure. The crystallographic data of *C*15*b* phase obtained from Rietveld refinement are listed in Table 5.3. The lattice parameter refined by Rietveld analysis decreases linearly with Mg content (according to the site occupations of Y and Mg shown in Table 5.3) as expected for a solid solution following the Vegard's law [204]. Due to the synthesis method, the Mg content (determined by ICP) is higher than designed ones, thus leads to an over *A*-stoichiometry (Y+Mg) and causes the formation of secondary phases. For Mg0.1 and Mg0.2 compounds, a small amount of oxide $Y_2O_3$ is observed. Mg0.3 compound contains secondary phase $AB_3$-type (Y, Mg)$Ni_3$. Indeed, the lattice parameter of $AB_3$ phase formed in this alloy are $a$ = 4.973 (1) Å, $c$ = 24.405 (1) Å, which corresponds to an adjacent $YNi_3$ composition ($a$ = 4.9779 (4) Å, $c$ = 24.449 (3) Å) from literature [267]. Which means the amount of substitution of Mg for Y in $AB_3$ phase is negligible, so, the Mg content in $A_2B_4$ phase is a bit larger than the values measured by ICP (which is average value of the two phases). For Mg0.4 and Mg0.5 compounds, the occurrence of $Mg_2Ni$ and some magnesium oxide MgO, often in lower crystalline state, can explain the higher Mg content measured by ICP.

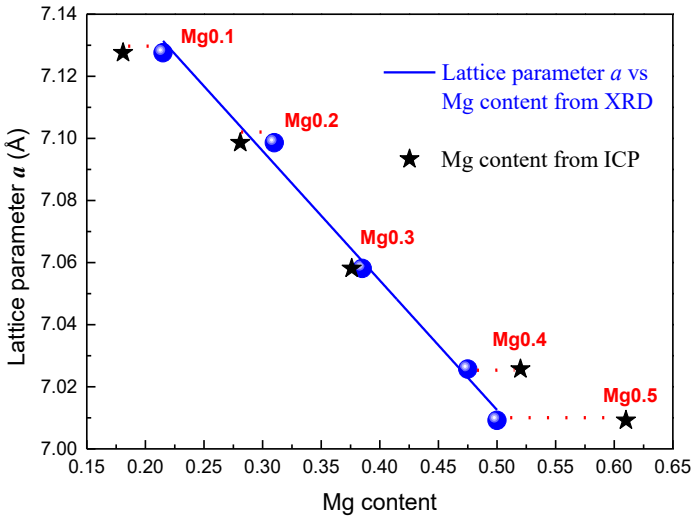


Figure 5.3 Lattice parameters of $(Y, Mg)_2Ni_4$ phase as function of Mg content calculated by Rietveld analysis (blue line). The black stars represent the Mg content measured by ICP.

The crystal structure of $YMgNi_4$ has been determined by K. Aono [213]. $YMgNi_4$ crystalizes in the *C*15*b* ($AuBe_5$)-type Laves phase structure, where Y and Mg exclusively occupy 4*a* and 4*c* sites respectively. While for *C*15 Laves phase structure, these two sites are merged in one site and can be occupied by Y and Mg randomly.

In our work, although nominal Mg content is designed varying from 0.1 to 0.5, the measured ICP compositions are generally higher than the designate ones (Table 5.3). At low Mg content, a partial occupation of Y on the 4*c* sites was observed. With the increasing Mg content, the Y occupation ratio on 4*c* sites decrease and vanish for Mg0.5 compound. This can be explained by the increasing of Mg contents, and up to Mg0.5 the Mg content is high enough to occupy entirely the 4*c* site. The lattice parameter of $A_2B_4$ phase ($a$ = 7.0092 Å) in Mg0.5 compound agrees well with literature ($a$ = 7.01 Å) [213]. For Mg0.4 compound, its XRD pattern cannot be well refined only by $A_2B_4$ phase. The lattice parameter of $A_2B_4$ phase ($a$ = 7.0257) in Mg0.4 compound is a bit higher than 7.01 Å, indicating the incomplete occupation of Mg at 4*c* sites although global composition shows excess of Y and Mg content, as confirmed by Rietveld refinement (see Table 5.3). Another hypothesis is the disorder on the site occupation. Indeed, there are many ternary intermetallic compounds with unknown structures shown in Y-Mg-Ni system [268], the determination of phase composition and site occupation requires other techniques such as measurement of single crystal by neutron diffraction.

Table 5.3 Composition measured by ICP and crystallographic data from Rietveld refinement for as-cast $Y_{1-x}Mg_xNi_2$ ($0.1 \leq x \leq 0.5$) compounds (the compositions from Rietveld analysis are calculated by combining phase abundance, chemical constitution and occupations).

| $x$ | Global compositions | Phase | Lattice parameters (Å) | Occupation | | | Refined composition of $A_2B_4$ phase |
|---|---|---|---|---|---|---|---|
| | | | | 4*a* | *4c* | 16*e* | |
| 0.1 | XRD: $Y_{0.84}Mg_{0.22}Ni_2$<br>ICP: $Y_{0.84}Mg_{0.18}Ni_2$ | $A_2B_4$ | $a$ = 7.1276 (2) | 100%Y | 57%Y + 43%Mg | 100%Ni | $Y_{1.57}Mg_{0.43}Ni_4$ |
| 0.2 | XRD: $Y_{0.74}Mg_{0.31}Ni_2$<br>ICP: $Y_{0.73}Mg_{0.28}Ni_2$ | $A_2B_4$ | $a$ = 7.0986 (2) | 100%Y | 38%Y + 62%Mg | 100%Ni | $Y_{1.38}Mg_{0.62}Ni_4$ |
| 0.3 | XRD: $Y_{0.67}Mg_{0.36}Ni_2$<br>ICP: $Y_{0.65}Mg_{0.31}Ni_2$ | $A_2B_4$ | $a$ = 7.0581 (1) | 100%Y | 23%Y + 77%Mg | 100%Ni | $Y_{1.23}Mg_{0.77}Ni_4$ |
| | | $AB_3$ | $a$ = 4.973 (1)<br>$c$ = 24.405 (1) | | | | |
| 0.4 | XRD: ~<br>ICP: $Y_{0.56}Mg_{0.61}Ni_2$ | $A_2B_4$ | $a$ = 7.0257 (2) | 100%Y | 5%Y + 95%Mg | 100%Ni | $Y_{1.05}Mg_{0.95}Ni_4$ |
| 0.5 | XRD: $Y_{0.49}Mg_{0.67}Ni_2$<br>ICP: $Y_{0.47}Mg_{0.73}Ni_2$ | $A_2B_4$ | $a$ = 7.0092 (1) | 100%Y | 100% Mg | 100%Ni | $YMgNi_4$ |
| | | $Mg_2Ni$ | $a$ = 5.223 (1)<br>$c$ = 13.2758 (5) | | | | |

## 5.1.2 Hydrogen sorption properties

The hydrogenation kinetics of all as-cast $Y_{1-x}Mg_xNi_2$ ($0.1 \leq x \leq 0.5$) compounds for the first and the third hydrogen absorption cycles at 25 °C under 2 MPa $H_2$ are shown in Figure 5.4. For the first cycle (Figure 5.4a), the compounds with Mg content up to 0.3 show good absorption capacity (around 1.6 wt.%, higher than 1.05 wt.% reported capacity of $YMgNi_4$). The hydrogen absorption kinetics become slower with increasing of Mg content from Mg0.1 to Mg0.4; whereas the hydrogen absorption kinetic of Mg0.5 compound is improved though remaining inferior to Mg0.1. Meanwhile, as compared to the first cycle, faster full hydrogen uptake can be observed for the subsequent cycles (Figure 5.4b, c, d, e, f).

For the compounds with low Mg content (Mg0.1, Mg0.2), the hydrogen absorption capacity decays significantly after the first cycle, then stabilizes at 1.07 wt.% and 1.33 wt.% for Mg0.1 and Mg0.2 compounds respectively which are still higher that the reported capacity of $YMgNi_4$ [213,269]. It was attributed to the ratios of Y and Mg, that lower amounts of Mg caused the lower hydrogen absorption pressures, thus more hydrogen storage capacities [269]. As shown in Figure 5.4d, once Mg content increases to $x'$ = 0.38 (Mg0.3), after 3 cycles, the capacity decay is negligible, with stable capacity locating around 1.22 wt.% (Table 5.4). For higher Mg substitution, although no capacity decay was observed, the stable capacity is lowered to around 0.94 wt.% (Table 5.4).

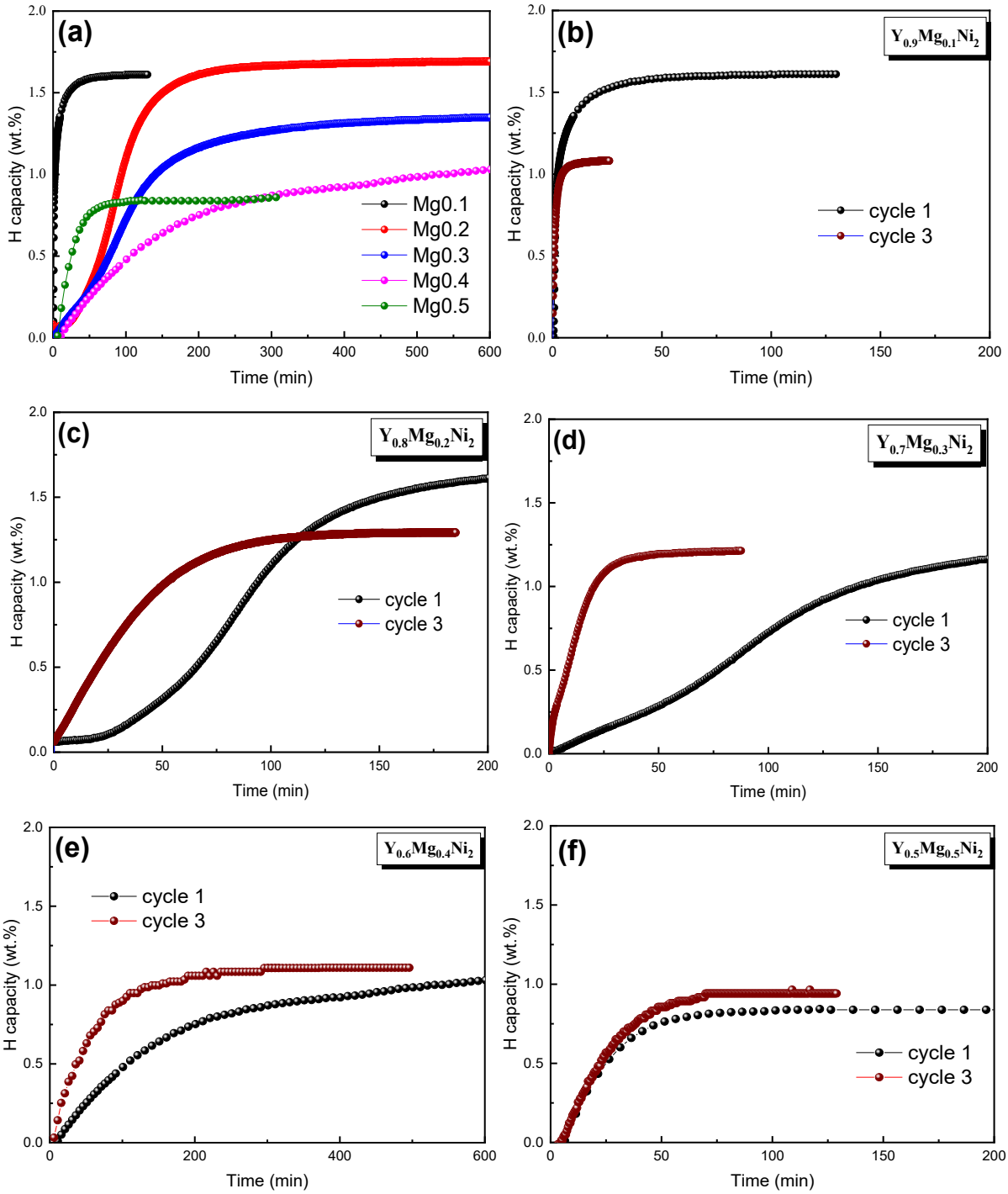


Figure 5.4 Time dependence of the hydrogen absorption for $Y_{1-x}Mg_xNi_2$ ($0.1 \leq x \leq 0.5$) alloys at the first cycle (a) (hydrogenation conditions: $P_{H2}$ = 2 MPa, 25 °C, dehydrogenation conditions: dynamic vacuum, 400 °C); Time dependence of the hydrogen absorption for $0.1 \leq x \leq 0.5$ alloys (b, c, d, e, f) upon three cycles under same hydrogenation and dehydrogenation conditions.

Table 5.4 Hydrogen absorption capacities at the first and third cycle for $Y_{1-x}Mg_xNi_2$ ($0.1 \leq x \leq 0.5$) alloys.

| $x$ | $1^{st}$ hydrogen absorption capacity | | $3^{th}$ hydrogen absorption capacity (wt.%) | Capacity loss (wt.%) |
|---|---|---|---|---|
| | (wt.%) | (H/f.u.) | | |
| 0.1 | 1.61 | 3.22 | 1.07 | 0.67 |
| 0.2 | 1.70 | 3.27 | 1.33 | 0.37 |
| 0.3 | 1.38 | 2.58 | 1.22 | 0.16 |
| 0.4 | 1.10 | 1.73 | 1.11 | ~ |
| 0.5 | 0.86 | 1.27 | 0.94 | ~ |

## 5.1.3 Heat treatment and HIA

### 5.1.3.1 Heat treatment

To improve their homogeneity, an annealing at 1000 °C for 1 h was carried out in a silica tube with Ar atmosphere (5N, pressure of 100 mbar) for Mg0.2 and Mg0.3 compounds. As shown in Figure 5.5 and Table 5.5, we obtained a mixture of phase component, including main phase $A_2B_4$-type (Y, Mg)$_2$Ni$_4$, secondary phase $AB_3$-type (Y, Mg)Ni$_3$ and a small amount of impurities of $Y_2O_3$ and YN (≤ 3 wt.%). The compositions determined by ICP are also given in Table 5.5. A loss of Mg during annealing changed the stoichiometry and is the reason for the small augmentation of the lattice constants of $A_2B_4$ phases, as well as the increase of $AB_3$ phase abundance.

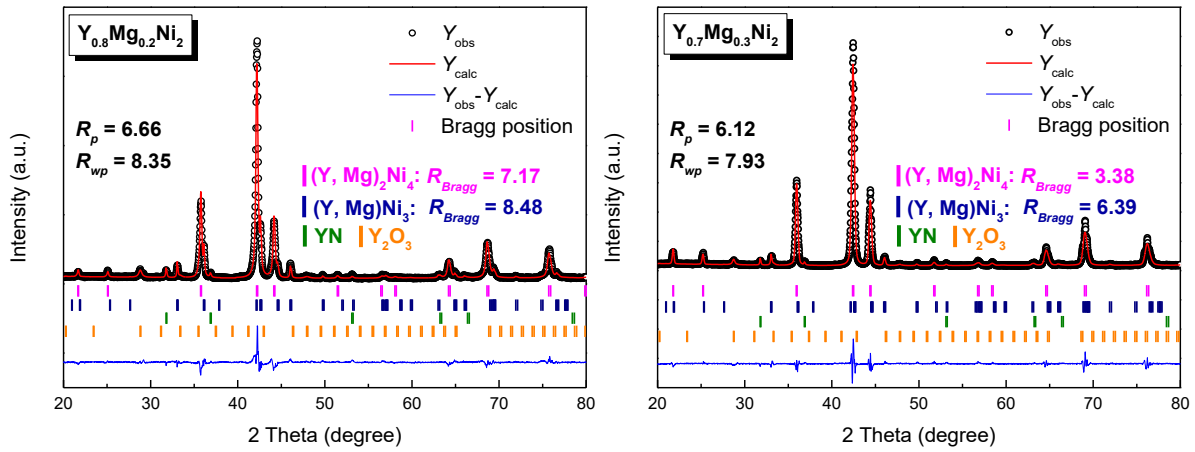


Figure 5.5 XRD patterns of $Y_{0.8}Mg_{0.2}Ni_2$ and $Y_{0.7}Mg_{0.3}Ni_2$ alloys upon heat treatment.

Table 5.5 Phase occurrence and crystal structures of the annealed $Y_{1-x}Mg_xNi_2$ ($x$ = 0.2, 0.3) compounds obtained by Rietveld analysis.

| $x$ | ICP | Phase | Abundance | Crystal structure | Lattice constant (Å) | |
|---|---|---|---|---|---|---|
| | | | | | As-cast | Annealed |
| 0.2 | Annealed: $Y_{0.75}Mg_{0.17}Ni_2$ As-cast: $Y_{0.73}Mg_{0.28}Ni_2$ | $(Y, Mg)_2Ni_4$ | 82% (1) | $C15b$ ($F\bar{4}3m$) | $a$=7.0986 (2) | $a$=7.1013 (2) |
| | | $(Y, Mg)Ni_3$ | 15% (1) | $PuNi_3$ ($R\bar{3}m$) | | $a$=4.9705 (3) $c$=24.3882 (2) |
| | | YN | 1% (1) | | | |
| | | $Y_2O_3$ | 2% (1) | | | |
| 0.3 | Annealed: $Y_{0.66}Mg_{0.23}Ni_2$ As-cast: $Y_{0.65}Mg_{0.31}Ni_2$ | $(Y, Mg)_2Ni_4$ | 83% (1) | $C15b$ ($F\bar{4}3m$) | $a$=7.0581 (1) | $a$=7.0665 (2) |
| | | $(Y, Mg)Ni_3$ | 14% (1) | $PuNi_3$ ($R\bar{3}m$) | $a$=4.973 (1) $c$=24.405 (1) | $a$=4.9707 (4) $c$=24.4216 (3) |
| | | YN | 1% (1) | | | |
| | | $Y_2O_3$ | 2% (1) | | | |

### 5.1.3.2 HIA

The annealed samples are cycled under the same hydrogenation conditions with as-cast samples. Figure 5.6 presents the hydrogenation kinetics of the annealed Mg0.2 and Mg0.3 compounds and their cycling properties. The hydrogen absorption capacities are summarized in Table 5.6. For two and more cycles, both the two annealed compounds show stable capacities and faster hydrogen absorption rate than the first cycle. Annealed Mg0.2 compound exhibits higher hydrogen storage capacity of 1.35 wt.%, while Mg0.3 shows better capacity retention. The reversible capacities are still higher than that of $YMgNi_4$ at fifth cycle [213,269]. In our case, both $A_2B_4$ and $AB_3$ phases would contribute the reversible capacities according to the phase occurrence shown in Table 5.5, whereas which phase leads to the capacity decay is unknown. To understand whether the capacity decay is induced by structural changes, the XRD analyses of dehydrogenated Mg0.2 and Mg0.3 samples (dynamic vacuum at 400 °C) were carried out.

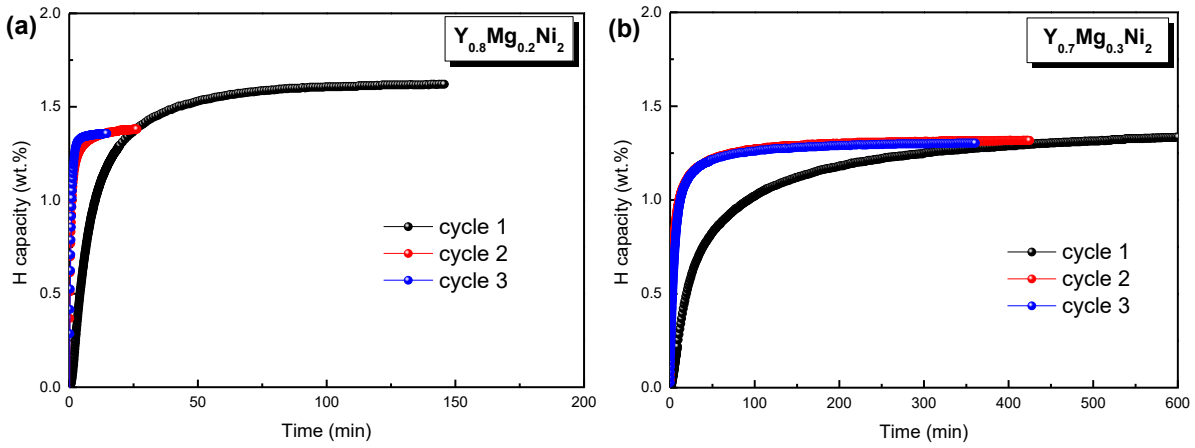

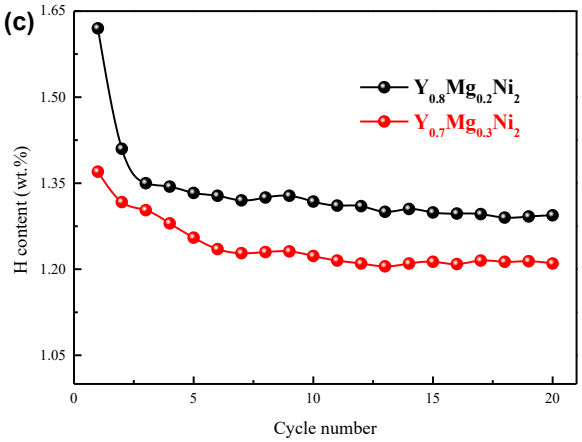


Figure 5.6 Kinetics of hydrogen absorption for annealed Mg0.2 (a) and Mg0.3 (b) compounds upon three hydrogen absorption and desorption cycles (hydrogenation conditions: $P_{H2}$ = 2 MPa, 25 ℃, dehydrogenation conditions: dynamic vacuum, 400 ℃). (c) Hydrogen absorption capacity as function of the cycle-number to twenty cycles of Mg0.2 and Mg0.3 compounds.

Table 5.6 Hydrogen absorption capacities at the first and third cycle for as-cast and annealed Mg0.2 and Mg0.3 alloys.

| *x* | Sample | Hydrogen absorption capacity (wt.%) | | Capacity loss (wt.%) |
|---|---|---|---|---|
| | | $1^{st}$ | $20^{th}$ | |
| 0.2 | Heat treatment | 1.62 | 1.35 | 0.27 |
| 0.3 | Heat treatment | 1.36 | 1.20 | 0.16 |

Figure 5.7 shows the XRD patterns of the parent Mg0.2 and Mg0.3 compounds and their dehydrogenated samples (dynamic vacuum at 400 ℃). For Mg0.2 compound, it's clear to see that the secondary phase (Y, Mg)$Ni_3$ and impurities $Y_2O_3$ and YN remained upon hydrogen absorption and desorption cycles. The presence of $YH_2$ (Figure 5.7) and the decreased $A_2B_4$ phase content indicating a disproportion reaction of the $A_2B_4$ hydride upon hydrogenation cycling occurred. Meanwhile, we observe a broadening of diffraction peaks, an intensity decreases and a shift to higher angle for $A_2B_4$-type (Y, Mg)$_2Ni_4$ phase. This structural change can be interpreted that the loss of Y leads to a smaller lattice parameter and less crystalized structure due to the disproportion. In contrast, higher Mg-containing Mg0.3 compound exhibits good crystalline character upon hydrogen absorption and desorption cycles. No obvious broadening neither shift of the diffraction peaks was observed, indicating more stable *C*15*b* structure. Meanwhile, as shown in Figure 5.8 and Table 5.7, the Rietveld analyses show very small amount (2 wt.%) of $YH_2$ for Mg0.3 compound, further suggesting the more stable structure upon hydrogenation cycling.

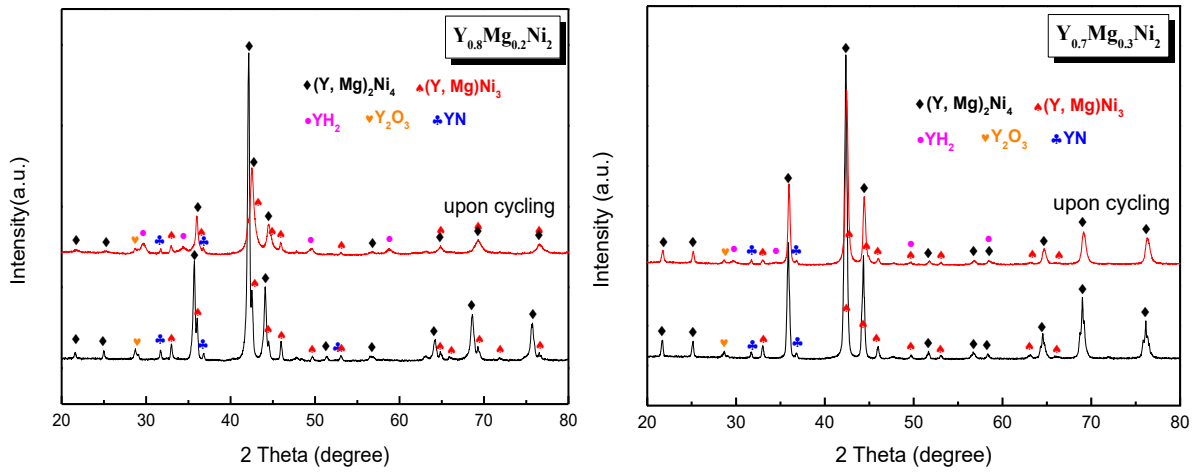


Figure 5.7 XRD patterns of initial $Y_{1-x}Mg_xNi_2$ ($x$ = 0.2, 0.3) compounds and samples upon hydrogen absorption and desorption cycling.

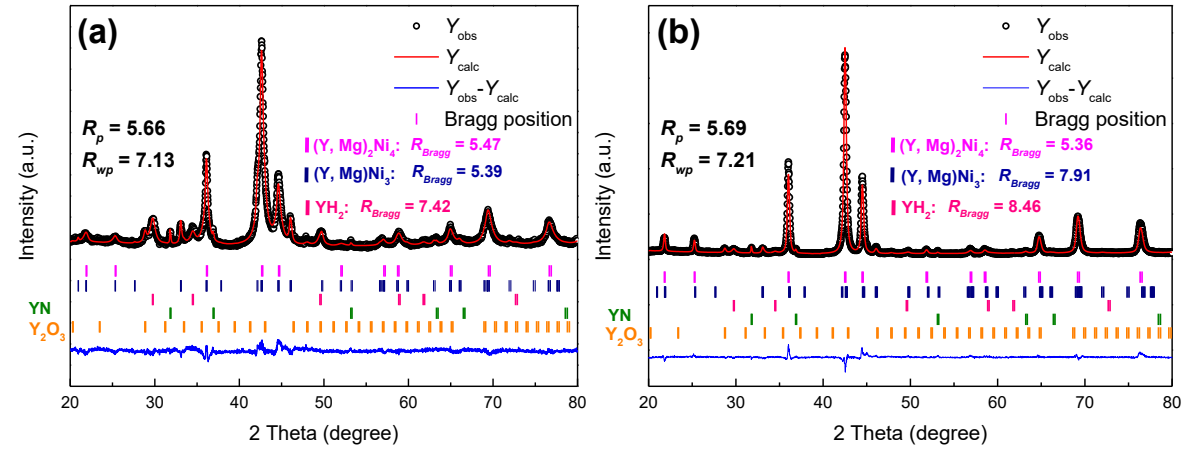


Figure 5.8 Rietveld refinements for the XRD patterns of dehydrogenated $Y_{0.8}Mg_{0.2}Ni_2$ (a) and $Y_{0.7}Mg_{0.3}Ni_2$ (b) alloys.

By Rietveld analysis for dehydrogenated $Y_{0.7}Mg_{0.3}Ni_2$ sample, we obtained the ratio of Y occupying at 4$c$ site is around 28%, corresponding to the composition $Y_{0.64}Mg_{0.36}Ni_2$. The atomic radius ratio of $Y_{0.64}Mg_{0.36}Ni_2$ is calculated to be $r_{Y+Mg}/r_{Ni} = 1.39$, whereas HIA was not occurred but slight disproportionation. Therefore, the controlling factor for HIA occurrence is not only the atom radius ratio, but there could also be another factor, like YOUNG's module or electronic factor like valence electron concentration.

Table 5.7 Phase occurrence and crystal structures of the dehydrogenated $Y_{1-x}Mg_xNi_2$ ($x$ = 0.2, 0.3) compounds.

| $x$ | ICP | Phase | Abundance | Crystal structure | Lattice constant (Å) |
|---|---|---|---|---|---|
| 0.2 | $Y_{0.746}Mg_{0.174}Ni_2$ | $(Y, Mg)_2Ni_4$ | 61% (1) | $C15b$ ($F\bar{4}3m$) | $a$ = 7.0251 (6) |
| | | $(Y, Mg)Ni_3$ | 28% (1) | $PuNi_3$ ($R\bar{3}m$) | $a$ = 4.9736 (5)<br>$c$ = 24.3790 (4) |
| | | $YH_2$ | 8% (1) | Cubic ($Fm\bar{3}m$) | $a$ = 5.2011 (8) |
| | | $YN/Y_2O_3$ | 3% (1) | | |
| 0.3 | $Y_{0.654}Mg_{0.327}Ni_2$ | $(Y, Mg)_2Ni_4$ | 86% (1) | $C15b$ ($F\bar{4}3m$) | $a$ = 7.0513 (2) |
| | | $(Y, Mg)Ni_3$ | 10% (1) | $PuNi_3$ ($R\bar{3}m$) | $a$ = 4.9658 (8)<br>$c$ = 24.3930 (6) |
| | | $YH_2$ | 2% (1) | Cubic ($Fm\bar{3}m$) | $a$ = 5.1994 (5) |
| | | $YN/Y_2O_3$ | 2% (1) | | |

## 5.1.4 Partial conclusion

In this section, we have discussed the influence of the substitution of Mg for Y in $YNi_2$ compound on structural stability and hydrogen sorption properties. The structural stability upon hydrogenation cycling increases with Mg content. Mg0.3 compound ($Y_{0.654}Mg_{0.327}Ni_2$) exhibits stable capacity (1.30 wt.%) and prominent structural stability, without hydrogen induced amorphization (HIA) but weak hydrogen induced disproportionation (HID) (2 wt.% $YH_2$).

The HIA was suppressed by Mg substitution. This could be explained by the decreased atomic radius ratio $r_{Y+Mg}/r_{Ni}$ 1.39 for the refined composition $Y_{0.64}Mg_{0.36}Ni_2$. Thus, the cell shrinks and structural stability was significantly enhanced. K. Aoki *et al.* [201,181] first explicitly proposed the correlation between atomic size and HIA that the $r_A/r_B$ is the most important factor for determining HIA in $AB_2$ compounds with $C15$ structure with a critical value of $r_A/r_B = 1.37$. The atomic radius ratios obtained in our work are slightly higher than 1.37 ($Y_{1-x}Mg_xNi_2$ compounds, Mg0.5 is excepted), whereas HIA was markedly suppressed (the XRD patterns of the pristine compound and sample upon three hydrogen absorption and desorption cycles are almost the same).

## 5.2 The effects of Sc substitution for Y on structural stability and hydrogen sorption properties of $Y_{0.9-x}Sc_xNi_{1.9}Mn_{0.1}$ ($x$ = 0.20, 0.45, 0.60, 0.75, 0.90) alloys

Scandium (Sc) is the lightest element with the smallest atomic radius ($r_{Sc} = 164\ nm$) among rare earth metals. The previous section showed that the *A*-side substitution by Mg can effectively suppress the HIA and achieve reversible hydrogen storage capacity of 1.30 wt.%, although the $r_{Y+Mg}/r_{Ni} \approx 1.39$. The limit of solubility for Mg in this phase is 50%, while Sc possesses similar chemical properties and can substitute total Y in the *C*15 phase. In this section, we conducted the Sc alloying on $Y_{0.9}Ni_{1.9}Mn_{0.1}$ compound to explore the structural evolution and hydrogen sorption properties. Meanwhile, Sc substituting effects on suppressing HIA or HID is also the motivation of this section.

### 5.2.1 Phase occurrence and crystal structures

#### 5.2.1.1 Synthesis

Intermetallic compounds with nominal composition $Y_{0.9-x}Sc_xNi_{1.9}Mn_{0.1}$ ($x$ = 0.2, 0.45, 0.6, 0.75, 0.9) were prepared by induction melting of high-purity metals (Y: 99.9%, Ni: 99.99%, Mn: 99.95% from *A*lfa *A*esar) in purified argon atmosphere (5N) under a pressure of 0.04 MPa in a cooled copper crucible. The ingots were turned over and re-melted three times to ensure homogeneity, the as-cast ingots were subsequently annealed 3 days at 850°C.

#### 5.2.1.2 Phase occurrence and structural properties

The XRD patterns of annealed $Y_{0.9-x}Sc_xNi_{1.9}Mn_{0.1}$ ($x$ = 0.20, 0.45, 0.60, 0.75, 0.90) compounds are presented in Figure 5.9. Rietveld refinements for these five compounds are presented in Figure 5.10. All the compounds crystallize purely in *C*15-type Laves phase structure ($MgCu_2$-type structure, space group $Fd\bar{3}m$), only tiny amount of $Y_2O_3$ is observed for $x$ = 0.2, 0.45 and 0.6 compounds.

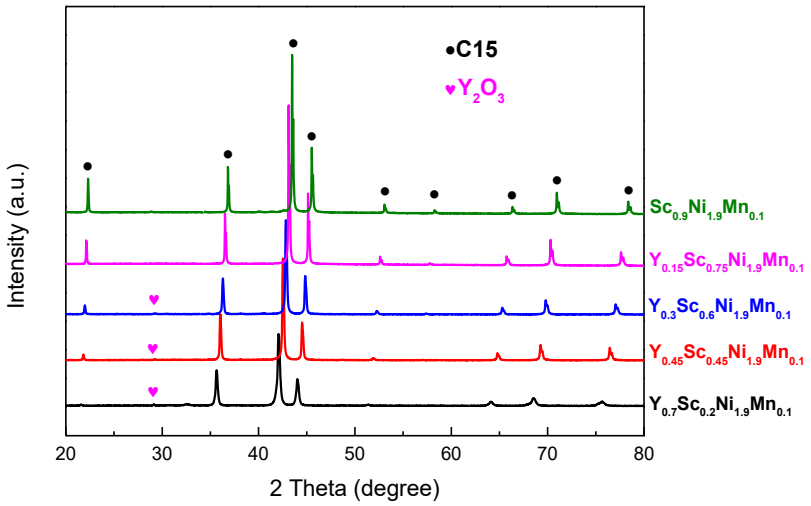


Figure 5.9 XRD patterns of $Y_{0.9-x}Sc_xNi_{1.9}Mn_{0.1}$ ($x$ = 0.20, 0.45, 0.60, 0.75, 0.90) compounds.

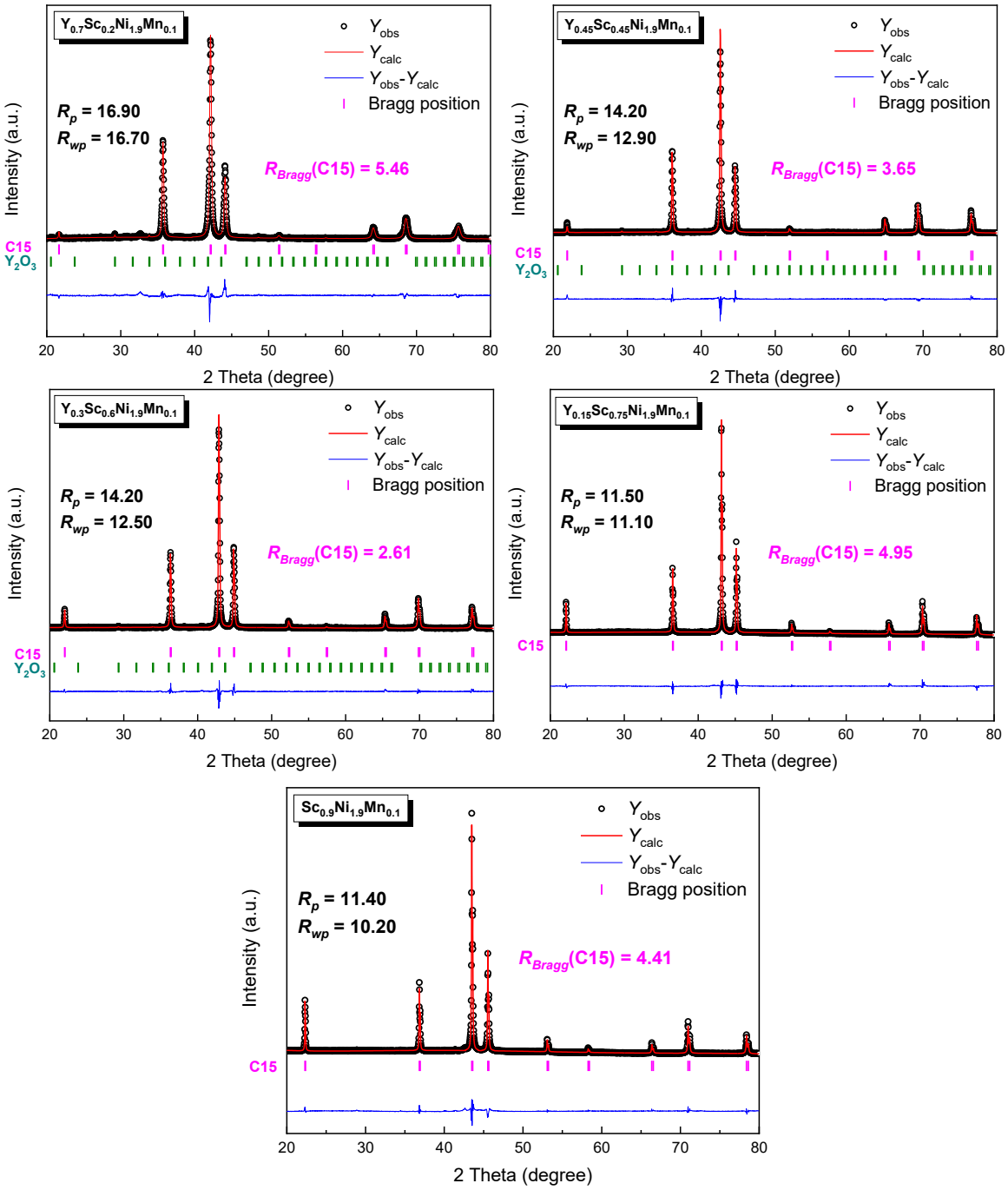


Figure 5.10 Rietveld refinements for the XRD patterns of $Y_{0.9-x}Sc_xNi_{1.9}Mn_{0.1}$ ($x$ = 0.20, 0.45, 0.60, 0.75, 0.90) compounds.

The lattice constant and unit cell volume derived from Rietveld refinement are summarized in Table 5.8. The evolution of the cubic lattice constant of the *C*15-type $Y_{0.9-x}Sc_xNi_{1.9}Mn_{0.1}$ phase with Sc content is shown in Figure 5.11. With the increasing Sc content, the lattice constants of *C*15 Laves phases decrease linearly as expected for a solid solution following the Vegard's law [204], Consequently, there is a contraction of the unit cell volume from 359.48 Å$^3$ for $Y_{0.9}Ni_{1.9}Mn_{0.1}$ to 327.88 Å$^3$ for $Sc_{0.9}Ni_{1.9}Mn_{0.1}$. This can be interpreted that Sc atoms ($r_{Sc} = 164\ nm$), which substitute Y atoms, are much smaller than Y ($r_Y = 180\ nm$). Therefore,

the more Sc introducing in the *C*15 Laves phase structure, the more contraction of the cell volume is observed.

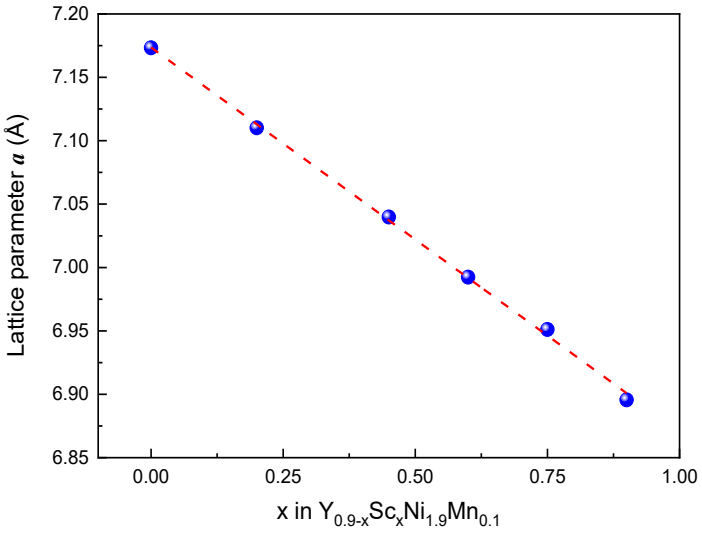


Figure 5.11 Lattice constants of *C*15 phase as function of Sc content in $Y_{0.9-x}Sc_xNi_{1.9}Mn_{0.1}$ compounds.

Table 5.8 Lattice constants and unit cell volumes of the $Y_{0.9-x}Sc_xNi_{1.9}Mn_{0.1}$ compounds.

| Compositions | Lattice constant *a* (Å) | Cell volume *V* (Å$^3$) |
|---|---|---|
| $Y_{0.7}Sc_{0.2}Ni_{1.9}Mn_{0.1}$ | 7.1103 (4) | 359.48 (3) |
| $Y_{0.45}Sc_{0.45}Ni_{1.9}Mn_{0.1}$ | 7.0397 (1) | 348.88 (1) |
| $Y_{0.3}Sc_{0.6}Ni_{1.9}Mn_{0.1}$ | 6.9925 (1) | 341.90 (1) |
| $Y_{0.15}Sc_{0.75}Ni_{1.9}Mn_{0.1}$ | 6.9511 (1) | 335.87 (1) |
| $Sc_{0.9}Ni_{1.9}Mn_{0.1}$ | 6.8956 (1) | 327.88 (1) |

### 5.2.1.3 Chemical analysis

EPMA was performed to check the chemical compositions of $Y_{0.9-x}Sc_xNi_{1.9}Mn_{0.1}$ compounds. The compositions of the *C*15 Laves phases are shown in ternary diagram Figure 5.12. The detailed phase compositions and crystallographic data from Rietveld refinement are summarized in Table 5.9. These compositions are mostly in line with the designated values (the red dot line shown in Figure 5.12). According to Rietveld analyses, at low Sc content ($x$ = 0, 0.2) the *A*-sites are not full occupied (86 % and 89 %, respectively) which agrees well the results of chemical analysis. For higher Sc content, $x \geq 0.45$, the Rietveld analyses indicates 100 % occupation of the *A*-site, whereas the chemical analysis indicates the contrary. We suppose anti-site occupation (Mn on the *A* - sites) should take place for these compounds. Another hypothesis is the *B* site vacancies (for $x$ = 0.9). Similar results has been reported early, where $ScMgNi_{3.4}$ forms the *C*15*b* structure with Ni-sites vacancies [270].

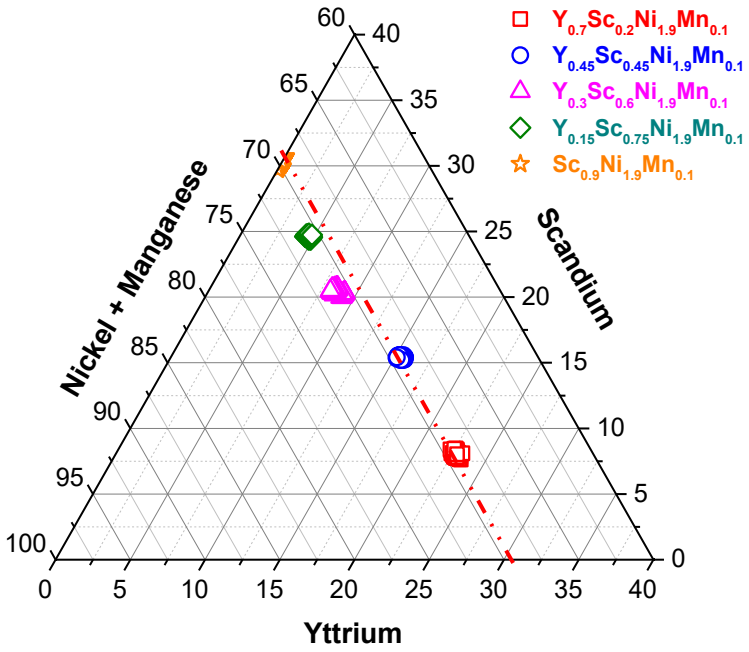


Figure 5.12 Ternary plot of the compositions of *C*15-type $Y_{0.9-x}Sc_xNi_{1.9}Mn_{0.1}$ compounds measured by EPMA.

Table 5.9 Phase compositions measured by EPMA and crystallographic data derived from Rietveld refinement.

| $x$ | Phase composition EPMA (±0.02) | Ratio (Ni+Mn) / (Y+Sc) | $r_A/r_B$ | Atoms at 8*b* site | 8*b* site occup. factor | Phase composition Rietveld |
|---|---|---|---|---|---|---|
| 0 | $Y_{0.86}Ni_{1.87}Mn_{0.13}$ | 2/0.86 | 1.440 | 100%Y | 86% | $Y_{0.86}Ni_{1.87}Mn_{0.13}$ |
| 0.2 | $Y_{0.66}Sc_{0.23}Ni_{1.89}Mn_{0.11}$ | 2/0.89 | 1.411 | 78%Y+22%Sc | 88% | $Y_{0.69}Sc_{0.19}Ni_{1.89}Mn_{0.11}$ |
| 0.45 | $Y_{0.45}Sc_{0.45}Ni_{1.89}Mn_{0.11}$ | 2/0.9 | 1.376 | 55%Y+45%Sc | 100% | $Y_{0.55}Sc_{0.45}Ni_{1.89}Mn_{0.11}$ |
| 0.6 | $Y_{0.26}Sc_{0.57}Ni_{1.90}Mn_{0.10}$ | 2/0.83 | 1.354 | 30%Y+70%Sc | 100% | $Y_{0.30}Sc_{0.70}Ni_{1.90}Mn_{0.10}$ |
| 0.75 | $Y_{0.13}Sc_{0.69}Ni_{1.90}Mn_{0.10}$ | 2/0.82 | 1.333 | 16%Y+84%Sc | 100% | $Y_{0.16}Sc_{0.84}Ni_{1.90}Mn_{0.10}$ |
| 0.9 | $Sc_{0.87}Ni_{1.89}Mn_{0.11}$ | 2/0.87 | 1.312 | 100%Sc | 100% | $Sc_{1.0}Ni_{1.89}Mn_{0.11}$ |

## 5.2.2 Hydrogen sorption properties

### 5.2.2.1 Pressure-composition isotherms

*P-C* isotherms at 150 °C of $Y_{0.9-x}Sc_xNi_{1.9}Mn_{0.1}$ compounds were measured using Sievert's method up to 10 MPa and shown in Figure 5.13. For $x$ = 0.20, 0.45 and 0.60, we observe two plateaus, first one short but flat followed by a sloppy one. With the increase of Sc content, both plateau pressures increase and measured hydrogen storage capacities decrease. For

$Y_{0.7}Sc_{0.2}Ni_{1.9}Mn_{0.1}$, the first plateau is very short and appears at 0.015 MPa with hydrogen content lying between 0.5 and 1.0 H/f.u.. Then, from 1 H/f.u., the second sloppy plateau starts up to 3.1 H/f.u. at 10 MPa. For Sc0.45 and Sc0.6 compound, the first plateaus exhibit longer hydrogen content region than Sc0.2 one, lying in the region from 0.3 to 1.3 H/f.u.. The second ones start around 1.8 MPa and 3.7 MPa of hydrogen pressure for Sc0.45 and Sc0.6 compounds, respectively. However, for both compounds, the pressure of the second plateau is too high to be entirely measured. Furthermore, for Sc0.75 and Sc0.9 compounds, even the first plateau is not completed up 10 MPa (see the magnified diagram in Figure 5.13). To obtain the complete hydrogen absorption and desorption processes, these PCI could be performed at lower temperature, but then the first plateau pressure could be too low to be measured for Sc0.2.

Meanwhile, we can observe that for low Sc-containing compounds (Sc0.2 and Sc0.45), most of hydrogen cannot be released from the formed hydrides, whereas once Sc content $x \geq 0.6$, hydrogen desorption was obtained although a small amount of hydrogen remains (< 0.4 H/f.u.). The well-performed hydrogen desorption for $x \geq 0.6$ can be explained by their higher equilibrium pressure and lower H content. To understand the HIA effect caused by Sc substitution, using X-ray diffraction to detect the structural evolution upon hydrogen absorption and desorption is essential.

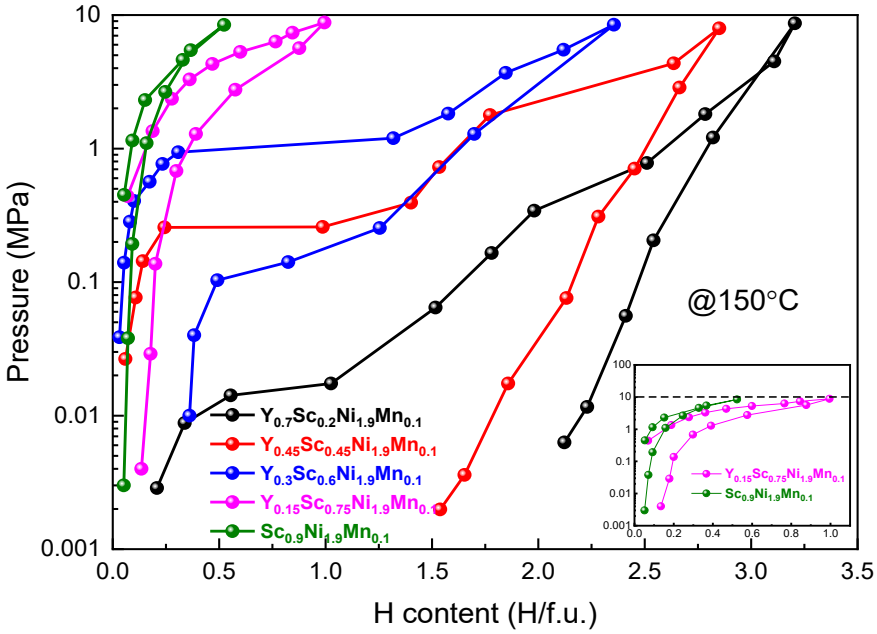


Figure 5.13 Comparison of *P-C* isotherms measured at 150 °C for $Y_{0.9-x}Sc_xNi_{1.9}Mn_{0.1}$ compounds. The embedded diagram is the magnified PCI curves of Sc0.75 and Sc0.9 compounds.

### 5.2.2.2 XRD patterns of the dehydrogenated samples

XRD patterns measured after PCI measurements of $Y_{0.9-x}Sc_xNi_{1.9}Mn_{0.1}$ compounds are presented in Figure 5.14. For high Sc-containing compounds (Sc0.60, Sc0.75 and Sc0.90), the *C*15 structure is preserved after dehydrogenation with no shift for the diffraction peaks. This result also illustrates that residual hydrogen in Sc0.6 compound after PCT (Figure 5.13) was

released under dynamic vacuum at 150 °C. Nevertheless, for Sc0.20 and Sc0.45 compounds, hydrogen induced amorphization occurred and only small crystalline diffraction peaks of *C*15 phase were observed (Figure 5.14).

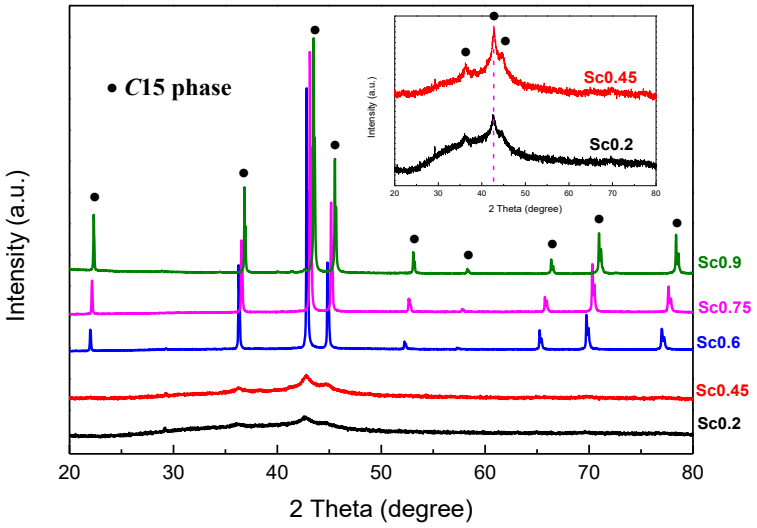


Figure 5.14 XRD patterns of dehydrogenated $Y_{0.9-x}Sc_xNi_{1.9}Mn_{0.1}$ compounds upon PCI measurements and subsequent dynamic vacuum at 150 °C.

Figure 5.16 displays the *P-C* isotherms measured at three different temperatures for Sc0.45, Sc0.6 and Sc0.75 compounds. The XRD patterns of each dehydrogenated $Y_{0.9-x}Sc_xNi_{1.9}Mn_{0.1}$ ($x$ = 0.20, 0.45, 0.60, 0.75) samples after PCI measurements under three different temperatures are shown in Figure 5.15 (hydrogen desorption was performed at the measuring temperature of PCI under dynamic vacuum), $Sc_{0.9}Ni_{1.9}Mn_{0.1}$ is not shown for its minor changes during hydrogen absorption and desorption.

For Sc0.20 and Sc0.45 compounds, except the amorphous phases (Figure 5.15), we can also observe the remained crystalline $\beta$ hydrides upon hydrogen absorption and desorption at 70 °C and 100 °C, whereas crystalline hydrides were not present at 150 °C. This can be interpreted that at 150 °C the desorption pressure is high enough for totally hydrogen desorption, while at 70 °C and 100 °C, even the primary vacuum cannot allow hydrogen desorption due to the low desorption pressure.

For Sc0.6 compound, similar phenomenon is observed. But instead to Sc0.2 and Sc0.45 at 150 °C, 100 °C is high enough for hydrogen desorption under vacuum. While Sc0.75 compound totally desorb the absorbed hydrogen even at 70 °C.

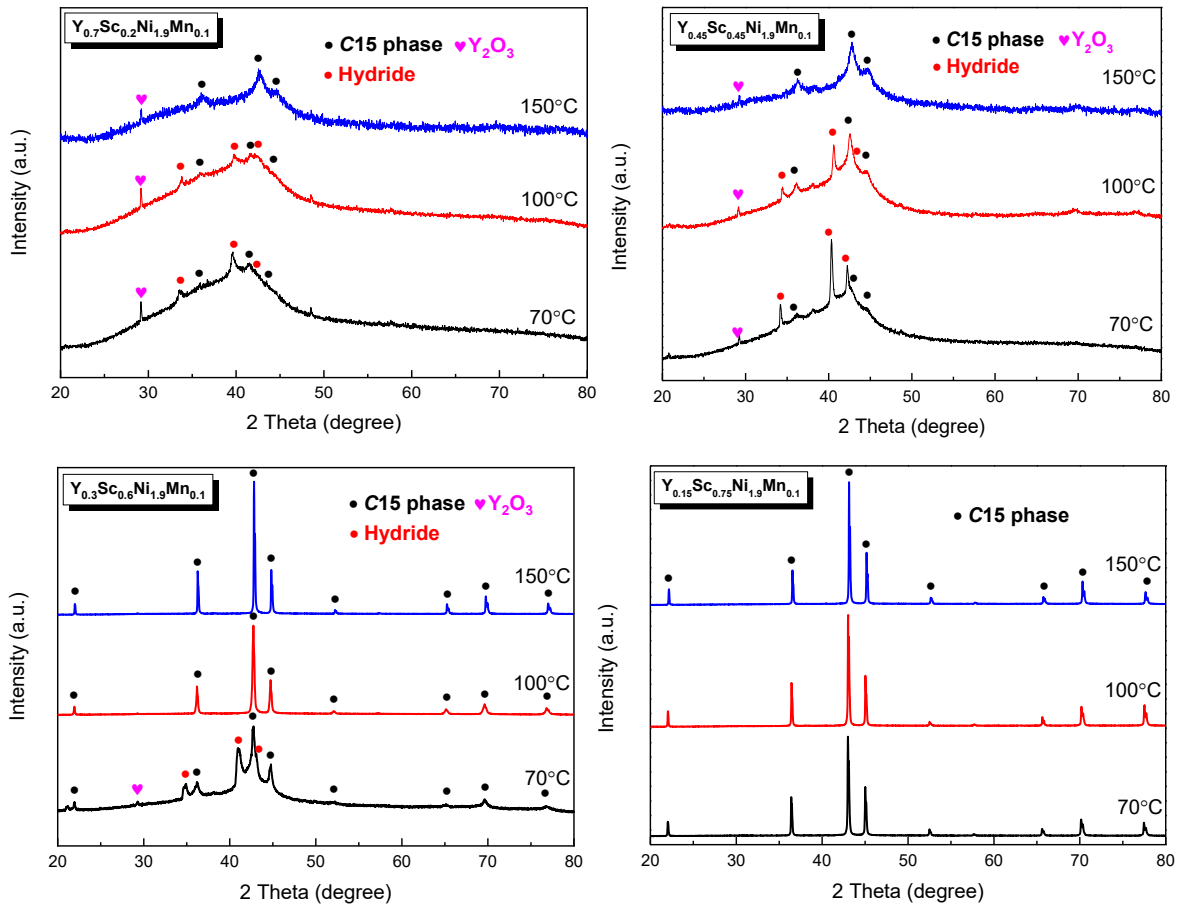


Figure 5.15 XRD patterns of the dehydrogenated samples after PCI measurements under different temperatures for $Y_{0.9-x}Sc_xNi_{1.9}Mn_{0.1}$ ($x$ = 0.2, 0.45, 0.6, 0.75) compounds.

### 5.2.2.3 Van't Hoff plots

Sc0.2 goes hydrogen induced amorphization, Sc0.9 does not absorb significant quantity of hydrogen. We measured the *P-C* isotherms at different temperatures for Sc0.45, Sc0.6 and Sc0.75 compounds (Figure 5.16). Their Van't Hoff plots for hydrogen absorption are shown in Figure 5.16 d and Table 5.10. The absolute values of $\Delta H$ and $\Delta S$ of the first plateau decreased significantly with the increasing Sc content, indicating the stability of *C*15 hydrides were enhanced markedly. The hydrogen absorption $\Delta H$ and $\Delta S$ calculated for $Y_{0.25}Sc_{0.7}Ni_2$ have been reported that $\Delta H = -24.53\ kJ/mol\ H_2$, $\Delta S = -80.69\ J/mol\ H_2/K$ [209]. Our calculated values of $\Delta H$ and $\Delta S$ for $Y_{0.3}Sc_{0.6}Ni_{1.9}Mn_{0.1}$ compound are $-36.69\ kJ/mol\ H_2$ and $-75.00\ J/mol\ H_2/K$ respectively. It is worth noting that the lattice parameter of $Y_{0.25}Sc_{0.7}Ni_2$ is $a$ = 6.98 Å, very closing to $Y_{0.3}Sc_{0.6}Ni_{1.9}Mn_{0.1}$ with $a$ = 6.99 Å. Thus, the higher $\Delta H$ may attribute to the difference in chemical compositions, that relatively lower presence ratio of Sc than $Y_{0.25}Sc_{0.7}Ni_2$, also the Mn partial substitution for Ni. As a result, the stability of hydrides of $Y_{0.25}Sc_{0.7}Ni_2$ are inferior to ones of $Y_{0.3}Sc_{0.6}Ni_{1.9}Mn_{0.1}$.

One should notice that the entropy obtained here is different from the conventional value (~130.6 J/mol $H_2$/K), especially for the Sc0.75 compound, this can be a consequence of the incomplete PCI leading to under-estimated plateau pressure.

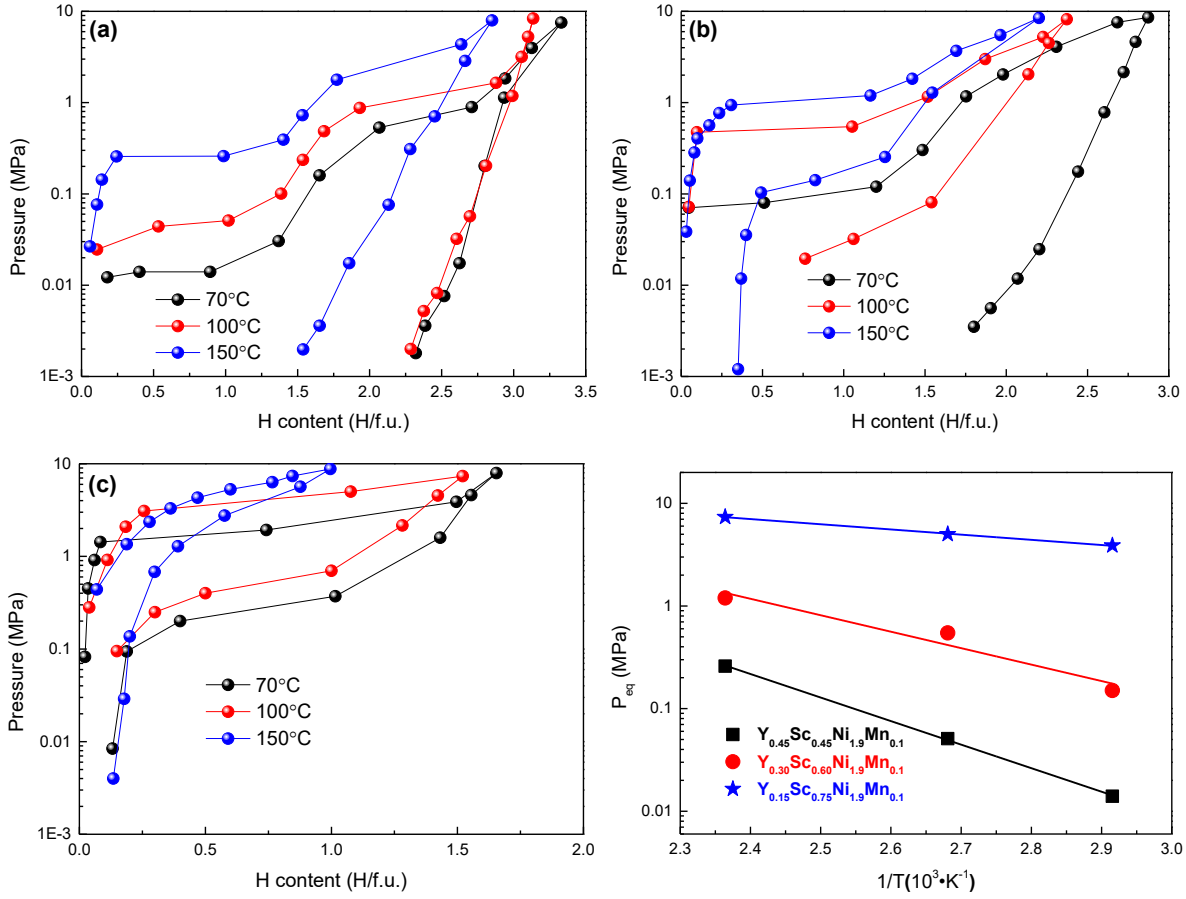


Figure 5.16 PCI curves measured at 70 °C (black), 100 °C (red) and 150 °C (blue) for $Y_{0.45}Sc_{0.45}Ni_{1.9}Mn_{0.1}$ (a), $Y_{0.3}Sc_{0.6}Ni_{1.9}Mn_{0.1}$ (b) and $Y_{0.15}Sc_{0.75}Ni_{1.9}Mn_{0.1}$ (c) compounds and their Van't Hoff plots (d) fitting at the first plateau during hydrogenation.

Table 5.10 Variation of enthalpy and entropy of $Y_{0.9-x}Sc_xNi_{1.9}Mn_{0.1}$ ($x$ = 0.45, 0.6, 0.75) compounds during hydrogen absorption.

| **Hydrides** | $\Delta H(KJ/mol\ H_2)$ | $\Delta S(J/mol\ H_2/K)$ |
|---|---|---|
| $Y_{0.45}Sc_{0.45}Ni_{1.9}Mn_{0.1}H_x$ | -43.92 | -92.72 |
| $Y_{0.3}Sc_{0.6}Ni_{1.9}Mn_{0.1}H_x$ | -36.69 | -75.00 |
| $Y_{0.15}Sc_{0.75}Ni_{1.9}Mn_{0.1}H_x$ | -9.68 | -39.45 |

## 5.2.3 Thermal analysis for the dehydrogenated samples

### 5.2.3.1 DSC analysis

After PCI measurements at 150 °C and the subsequent hydrogen desorption under primary dynamic vacuum, the thermal analysis with heating rate of 5 °C/min up to 600 °C was

performed for Sc0.20, Sc0.45 and Sc0.60 compounds. The DSC curves are shown in Figure 5.17. The measurement of Sc0.20 compound shows a large broad endothermic peak followed by a sharp exothermic peak, corresponding to the trapped hydrogen desorption and phase crystallization respectively. Similar behavior was observed for Sc0.45 compound, but the markedly decreased endothermic peak which indicates less trapped hydrogen release. The shifted crystallization temperature indicates a different chemistry of involved crystallization process, the more Sc content, the compound crystallizes more easily. To decide the products of crystallization and understand the changes of temperature, XRD patterns of the samples after DSC analysis were analyzed in detail in next section.

For Sc0.60 ($a$ = 6.99 Å) compound, neither endothermic hydrogen desorption nor crystallization peak were present in the DSC curves (blue line in Figure 5.17), means neither HIA nor residues trapping hydrogen happened for this compound. This is similar to the DSC curves for $Y_{0.25}Sc_{0.7}Ni_2$ compound [12]. In contrary, for $Y_{0.35}Sc_{0.6}Ni_2$ ($a$ = 7.01 Å) compound, the DSC curve exhibits a broad endothermic (hydrogen desorption) peak followed by a sharp exothermic peak (crystallization) [12], similar to Sc0.45 ($a$ = 7.03 Å) compound in our case (red line in Figure 5.17). This means the structural stability of Sc0.60 is similar to that of reported $Y_{0.25}Sc_{0.7}Ni_2$ compound, which could be the contribution of Mn substitution for Ni. It shows the structure stabilization can be achieved by both site substitution.

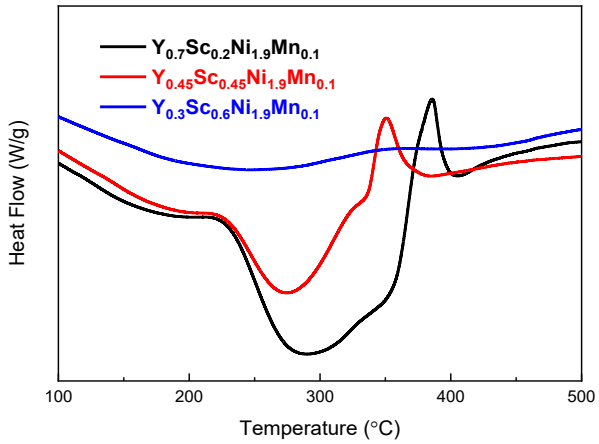


Figure 5.17 The DSC curves of dehydrogenated $Y_{0.9-x}Sc_xNi_{1.9}Mn_{0.1}$ ($x$ = 0.20, 0.45, 0.60) compounds with heating rate of 5 °C/min.

### 5.2.3.2 X-ray diffraction analysis after DSC measurement

The XRD of the samples after DSC measurement (heating to 600 °C and then cooling down to room temperature) were carried out (Figure 5.18). The detailed crystallographic data obtained from Rietveld analysis are summarized in Table 5.11. The XRD pattern of Sc0.20 compound can be indexed with the mixture of $C$15-type $AB_2$ phase, $PuNi_3$-type $AB_3$ phase, $YH_2$ and $Y_2O_3$ phases (Table 5.11), indicating the occurrence of hydrogen induced disproportionation (HID). Indeed, HID typically appears in the rare earth-based $AB_2$ compounds. We have observed the HID in $AB_2$-type $Y_x(Ni, Al)_2$ and $Y_x(Ni, Mn)_2$ systems, amorphous

hydrides recrystallized in $YH_2$ and $AB_3$ phases during hydrogen desorption upon heating [184]. HID also means the structural stability is poor during hydrogen absorption and desorption. For Sc0.45 compound, minor amount of $YH_2$ is present, which suggests the weak HID and its structural stability was enhanced upon more Sc doping. The decreased crystallization temperature for more Sc doping (Sc0.2→Sc0.45, see Figure 5.17) also indicates the lowered formation enthalpy of *C*15-type $AB_2$ phase, thus the more stable structure. Moreover, for Sc0.6 compound the XRD pattern is in good agreement with the initial compound, the lattice constant keeps almost unchanged (Table 5.11).

In addition, it is worth noting that after hydrogen desorption, the low Sc-containing compounds show a lowered lattice constant (Table 5.11). Especially for Sc0.2 compound, the lattice constant decreases from 7.11 Å for pristine compound to 7.07 Å for dehydrogenated compound. This could be explained by the fact that the $YH_2$ formation pump some Y out of the pristine *C*15 phase and results to a higher Sc containing *C*15 phase after hydrogen absorption and desorption. Furthermore, Sc0.45 compound exhibits much smaller changes of lattice constant and Sc0.6 compounds shows no lattice constant change, indicating better stability of the *C*15 structure with larger Sc content.

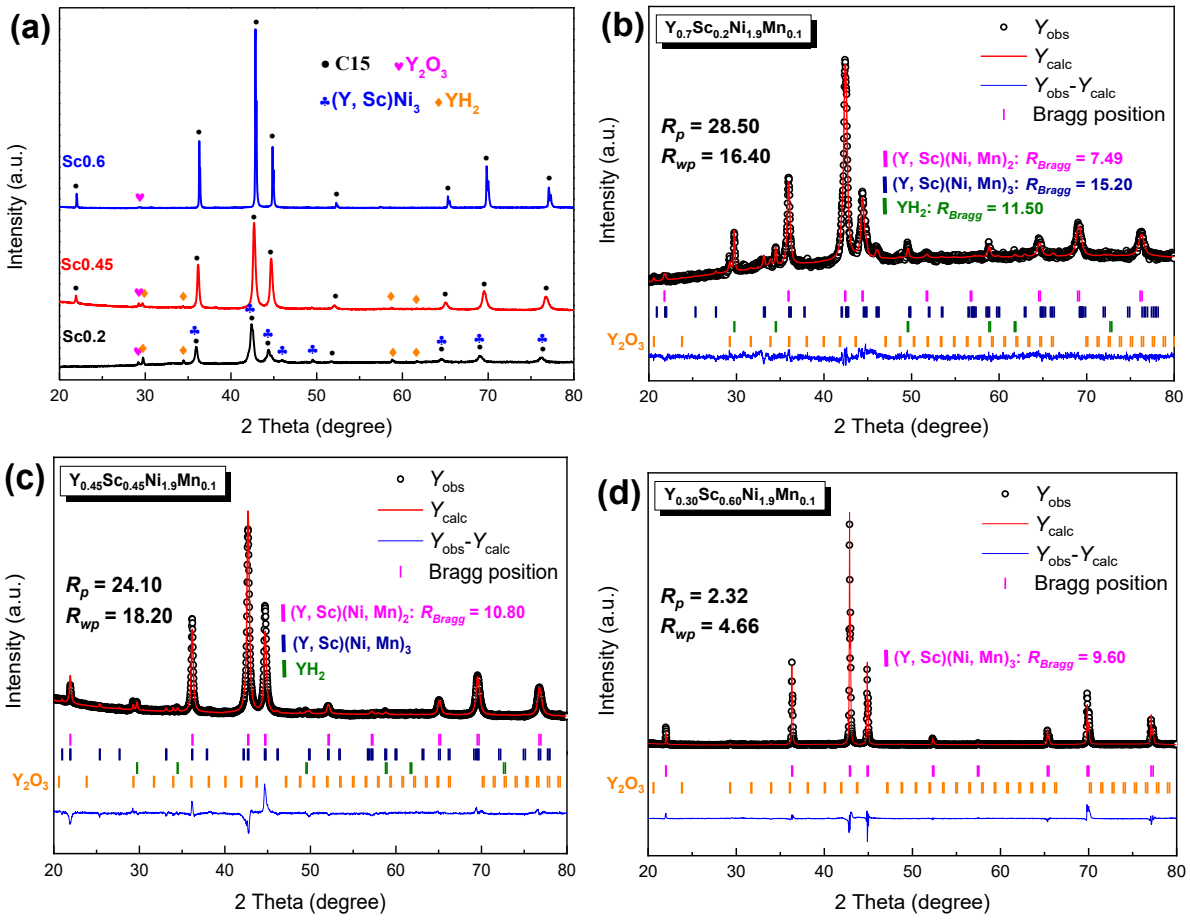


Figure 5.18 XRD patterns of the dehydrogenated samples upon heating to 600 °C with heating rate of 5 °C/min (a) and their Rietveld refinement fits: (b) – (d).

Table 5.11 The phase abundance and crystallographic data derived from Rietveld refinement of the dehydrogenated samples upon heating to 600 ℃ with heating rate of 5 ℃/min.

| Samples | Phase | Phase abundance | Crystal structure | Lattice constant |
|---|---|---|---|---|
| Sc0.2 | $AB_2$ | 73(1)% | *C*15 ($Fd\bar{3}m$) | $a$ = 7.0685 (2) |
| | $AB_3$ | 19(1)% | $PuNi_3$ ($R\bar{3}m$) | $a$ = 4.9856 (6)<br>$c$ = 24.2685 (5) |
| | $YH_2$ | 4(1)% | Cubic ($Fm\bar{3}m$) | |
| | $Y_2O_3$ | 4(1)% | | |
| Sc0.45 | $AB_2$ | 98(1)% | *C*15 ($Fd\bar{3}m$) | $a$ = 7.0203 (1) |
| | $YH_2$ | 1(1)% | Cubic ($Fm\bar{3}m$) | |
| | $Y_2O_3$ | 1(1)% | | |
| Sc0.6 | $AB_2$ | 100% | *C*15 ($Fd\bar{3}m$) | $a$ = 6.9923 (1) |

### 5.2.4 Summary

In this section, we synthesized and obtained the $Y_{0.9-x}Sc_xNi_{1.9}Mn_{0.1}$ ($x$ = 0.2, 0.45, 0.6, 0.75, 0.9) compounds with single *C*15 Laves phase structure. Sc substitution brings great effects on structural stability and hydrogen sorption properties.

The lattice constants of *C*15 Laves phases decrease linearly with the increasing Sc content. No *A* - site vacancies were found for Sc content from $x$ = 0.45 according to the Rietveld refinement and possible anti-site occupation of Mn may exist in $Y_{0.9-x}Sc_xNi_{1.9}Mn_{0.1}$ system. For compounds with Sc content $x \geq 0.6$, reversible hydrogen absorption and desorption at 150 ℃ was realized with a small amount of hydrogen remains (< 0.4 H/f.u.). The formation enthalpy for the mono-hydride (first plateau) decreases with the increasing Sc content, indicating the stability of *C*15 hydrides were markedly decreased. HIA and HID were markedly suppressed since Sc content $x \geq 0.6$, whereas the hydrogen absorption capacities decrease with increasing Sc content under experimental condition (10 MPa room temperature).

## 5.3 Conclusions

In this chapter, we synthesized compounds with Mg and Sc substitution for Y in $YNi_2$ and $Y_{0.9}Ni_{1.9}Mn_{0.1}$ respectively, to study their influence on structural stability and hydrogen sorption properties. The structural stability upon hydrogen and desorption cycling increases with the increase of Mg and Sc content. Mg0.3 compound ($Y_{0.654}Mg_{0.327}Ni_2$) exhibits modest stable capacity (1.30 wt.%) and prominent structural stability, without hydrogen induced amorphization but weak hydrogen induced disproportionation (2 wt.% $YH_2$). Meanwhile, Sc0.6 compound ($Y_{0.26}Sc_{0.57}Ni_{1.90}Mn_{0.11}$) shows excellent reversible hydrogen absorption and desorption properties and structural stability. As expected, for both Mg and Sc substituted compounds the hydrogen absorption capacity decreases linearly with increasing Mg and Sc content. This is attributed to the lattice contraction induced by substitution on *A*- side of atoms

with smaller atomic radius than Y. As a result, when the *A*/*B* atomic radius ratio approaches to 1.37, the structural stability is enhanced during hydrogen absorption and desorption, and the HIA is suppressed.

It is worth noting that the atomic radius ratio $r_A/r_B$ of $Y_{0.654}Mg_{0.327}Ni_2$ is around 1.39, which is higher than the empirical value 1.37, but no hydrogen induced amorphization occurrence. In contrast, the turning point of hydrogen induced amorphization occurrence for Sc-substituted compounds is from $Y_{0.45}Sc_{0.45}Ni_{1.89}Mn_{0.11}$ to $Y_{0.26}Sc_{0.57}Ni_{1.90}Mn_{0.11}$, the corresponding atomic radius ratio $r_A/r_B$ changes from 1.376 to 1.354, follows well the empirical rule of 1.37. Such difference between Mg- and Sc-substituted compounds may due to their structures: *C*15*b*- and *C*15-type. Indeed, the literature [271] has reported the critical atomic radius ratio for HIA in $Pr_{1-x}Mg_xNi_2$ compounds is larger than 1.37. We suppose besides the geometric effect, the electronic structure of Mg-substituted *C*15*b* structure also plays a role on the structural stability facing to hydrogen sorption.

For Mg-containing $Y_{1-x}Mg_xNi_2$ compounds, the atomic radius ratio $r_A/r_B$ can be additionally decreased by *B*-side substitution Ni by larger atoms. Therefore, additional substitution of Al or Mn for Ni could be effective to optimize the structural and hydrogen sorption properties.

# 6. *A*/*B* side substitution effects on structural stability and hydrogen sorption properties of (Y, Mg)$Ni_2$-based compounds

Synthesizing the former studies of element substitution effects on structural stability and hydrogen sorption properties of $YNi_2$ compound, *B*-side substitution may increase hydrogen absorption capacity slightly but still suffers from HIA and HID, showing minor effects on improvement of structural stability and reversible hydrogen absorption capacity. On the contrary, *A*-side substitution could suppress HIA and HID effectively, whereas hydrogen absorption capacities are too low due to the high plateau pressure. Therefore, in this chapter, we investigate the *A*/*B*-side substitution simultaneously, aiming to find a compound with better hydrogen absorption capacity and structural stability without HIA and HID occurrence.

## 6.1 Effects of Al substitution in $Y_{0.7}Mg_{0.3}Ni_{2-y}Al_y$ ($0.05 \leq y \leq 0.25$) compounds

In this section, the effects of Al substitution on structural stability and hydrogen sorption properties of pseudo-binary $Y_{0.7}Mg_{0.3}Ni_{2-y}Al_y$ compounds ($0.05 \leq y \leq 0.25$) are investigated. According to the studies of $A_2B_4$-type $Y_{1-x}Mg_xNi_2$ ($0.1 \leq x \leq 0.5$) compounds shown in previous chapter, the $Y_{0.7}Mg_{0.3}Ni_2$ compound is located at the middle point between $YNi_2$ with a modified *C*15 ($MgCu_2$)-type Laves phase structure and $YMgNi_4$ with *C*15*b*-type Laves phase structure, crystalizing in the same *C*15*b* superstructure, but with simultaneous occupation of Y and Mg in 4*c* site. Al is often used as a substitute for Ni to optimize the hydrogen sorption properties of $AB_5$ or $AB_n$ ($3 \leq n \leq 4$)-type alloys [91,272,273]. Moreover, Al substitution for Ni in $Y_{0.7}Mg_{0.3}Ni_2$ compound could further enhance the structural stability upon hydrogenation according to the empirical atomic radius ratio of 1.37 for HIA occurrence. For these reasons, the $Y_{0.7}Mg_{0.3}Ni_{2-y}Al_y$ compounds were synthesized and investigated.

### 6.1.1 Synthesis of the $Y_{0.7}Mg_{0.3}Ni_{2-y}Al_y$ compounds

The $Y_{0.7}Mg_{0.3}Ni_{2-y}Al_y$ compounds ($0.05 \leq y \leq 0.25$) were synthesized by induction melting in an Ar atmosphere (5N). The as-cast ingots were obtained using the same pretreatment of raw materials with $Y_{1-x}Mg_xNi_2$ compounds: 150% excess of Mg for the first melting. The ingots were turned over and re-melted several times to ensure their homogeneity. After each melting, a part of Mg would be lost, then the weight of ingot was weighed by assuming the weight loss is due to Mg evaporation and add Mg in the ingot to reach the target value. After melting, the as-cast ingots were annealed at 850 °C under argon atmosphere in a closed steel crucible for 3 days to obtain the uniformity of microstructure and distribution of composition.

### 6.1.2 Characteristics of synthesized $Y_{0.7}Mg_{0.3}Ni_{2-y}Al_y$ compounds

#### 6.1.2.1 ICP Compositions

The global compositions of prepared $Y_{0.7}Mg_{0.3}Ni_{2-y}Al_y$ compounds were examined by inductively coupled plasma-optical emission spectroscopy (ICP-OES, Agilent 5800) and the experimentally observed average compositions are presented in Table 6.1. They are close to the

target compositions with relatively lower Y content and higher Mg content. Indeed, Mg evaporation is hard to be controlled effectively, which results in various excess of Mg content as compared to designate value $x = 0.3$.

Table 6.1 Chemical compositions measured by ICP for $Y_{0.7}Mg_{0.3}Ni_{2-y}Al_y$ compounds.

| Target composition | Y (±0.01) | Mg (±0.01) | Ni (±0.01) | Al (±0.01) |
|---|---|---|---|---|
| $Y_{0.7}Mg_{0.3}Ni_{1.95}Al_{0.05}$ | 0.67 | 0.31 | 1.95 | 0.05 |
| $Y_{0.7}Mg_{0.3}Ni_{1.90}Al_{0.10}$ | 0.68 | 0.33 | 1.90 | 0.10 |
| $Y_{0.7}Mg_{0.3}Ni_{1.85}Al_{0.15}$ | 0.67 | 0.36 | 1.86 | 0.15 |
| $Y_{0.7}Mg_{0.3}Ni_{1.80}Al_{0.20}$ | 0.67 | 0.31 | 1.81 | 0.20 |
| $Y_{0.7}Mg_{0.3}Ni_{1.75}Al_{0.25}$ | 0.67 | 0.33 | 1.75 | 0.25 |

### 6.1.2.2 XRD patterns and refinements

The relevant XRD patterns of the $Y_{0.7}Mg_{0.3}Ni_{2-y}Al_y$ samples and the corresponding Rietveld refined patterns are displayed in Figure 6.1a and b-f respectively, the crystallographic data obtained from refinements and EPMA analysis are summarized in Table 6.2. It is observed that for all compounds, that the main phase is the $A_2B_4$-type phase with *C*15*b*-type Laves phase structure (space group $F\bar{4}3m$). In our case, the *C*15*b* structure shows that 4*a* site is entirely occupied by Y, while the 4*c* site is occupied by both Y and Mg. The calculated compositions (Rietveld analysis of the XRD patterns) are close to the compositions determined by EPMA. Indeed, similar results have been reported in $Gd_xMg_{2-x}Ni_4$ [215] and $CeMgNi_4$ [216] compounds, where the rare earth atoms occupy the 4*a* and 4*c* sites with Mg. Another case is that in Mg-rich $Mg_{2-x}R_xNi_4$ (*R* = La, Pr, Nd, Sm, Gd) compounds [274–276], the Mg occupies the 4*c* site and co-occupy the 4*a* site with *R* atom. We can conclude that in $Mg_{2-x}R_xNi_4$ system, the $A_2B_4$-type phase forms in a large composition range, Mg atoms preferably occupying the 4*c* sites and the *R* atoms the 4*a* sites. Nonetheless, Mg atoms on the 4*a* sites and *R* atoms on the 4*c* sites are observed when $x \neq 1$.

For the compounds with Al content below 0.2, the absence of extra diffraction peaks indicates the single-phase nature of these compounds. While for the compounds with $y = 0.2$ and 0.25, a secondary phase $Y_3Ni_6Al_2$ is observed. Its abundance increases with the increasing Al content, accounting 2 wt.% and 4 wt.% for $y = 0.2$ and 0.4 respectively. In addition, small amount of $Y_2O_3$ is present as impurity phase with abundance around 1 wt.%.

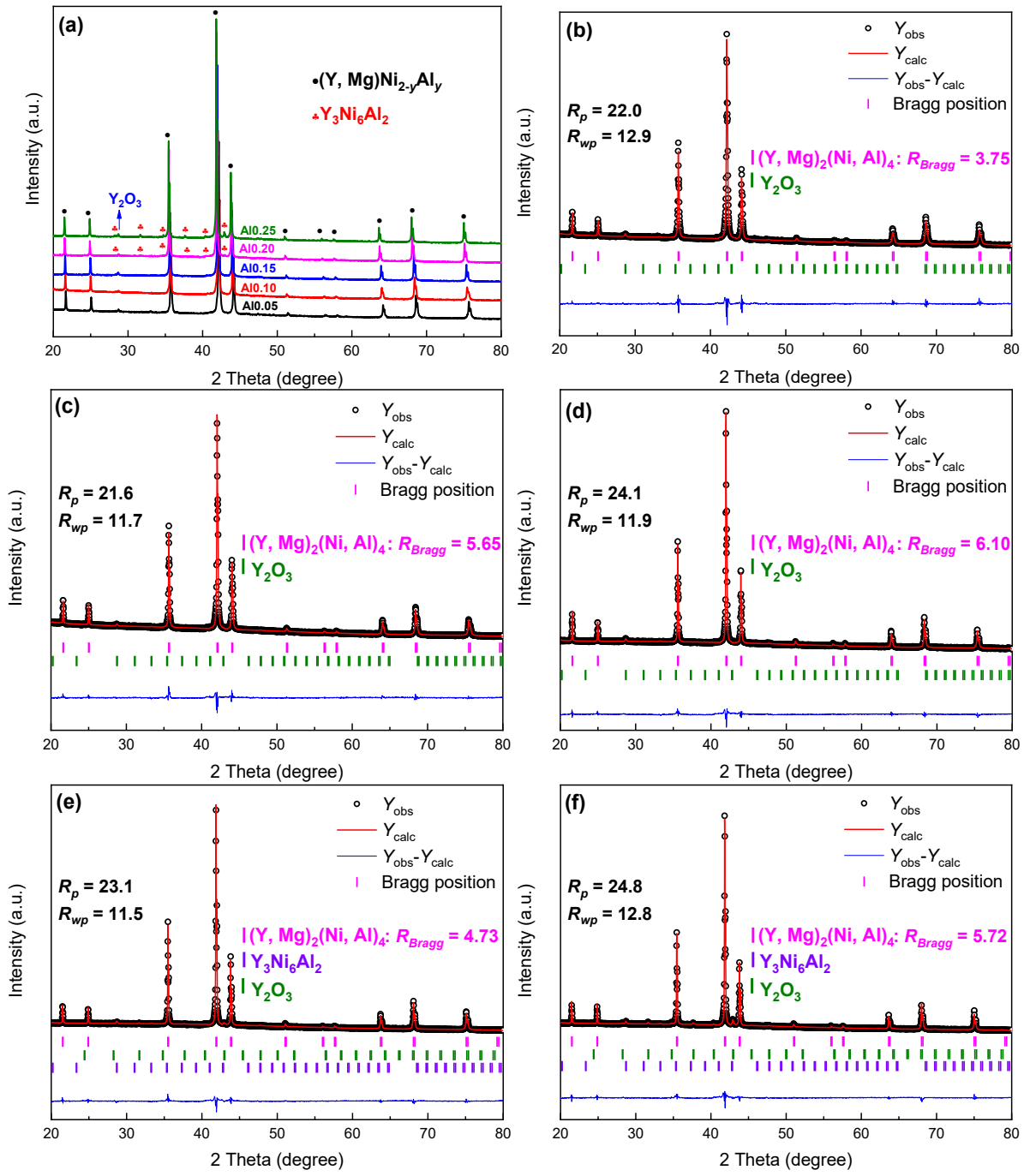


Figure 6.1 XRD patterns (a) and Rietveld analysis of $Y_{0.7}Mg_{0.3}Ni_{2-y}Al_y$ compounds: (b) $y = 0.05$, (c) $y = 0.10$, (d) $y = 0.15$, (e) $y = 0.20$, (f) $y = 0.25$.

### 6.1.2.3 EPMA analysis

The phase composition and microstructures of prepared compounds were examined by Electron Probe Micro-Analysis (EPMA) in a JEOL-JXA8230 device. The corresponding results of surface morphology and quantitative composition analysis are shown in Figure 6.2 and summarized in Table 6.2. It is composed of a homogeneous matrix and some cracks produced during grinding (the black area). The chemical compositions of the matrix were determined by EPMA on around 60 points distributed over the whole area of the picture. The average atomic

compositions show that Mg concentration in $A_2B_4$-type $Y_{0.7}Mg_{0.3}(Ni, Al)_2$ ($F\bar{4}3m$) phase is higher than the nominal one, consistent with the ICP results. The formation of $A_2B_4$ phase with various Mg concentrations indicates the existence of a homogeneity domain for this phase rather a line compound, in agreement with the ternary Y-Mg-Ni phase diagram [268]. Meanwhile, $Ca_3Ag_8$-type $Y_3Ni_6Al_2$ ($Im\bar{3}m$) appears as the secondary phase for $y = 0.2$ and 0.25. The measured compositions agrees with previously reported one [277], though there is a deviation on Al content from the stoichiometric composition of $Y_3Ni_6Al_2$.

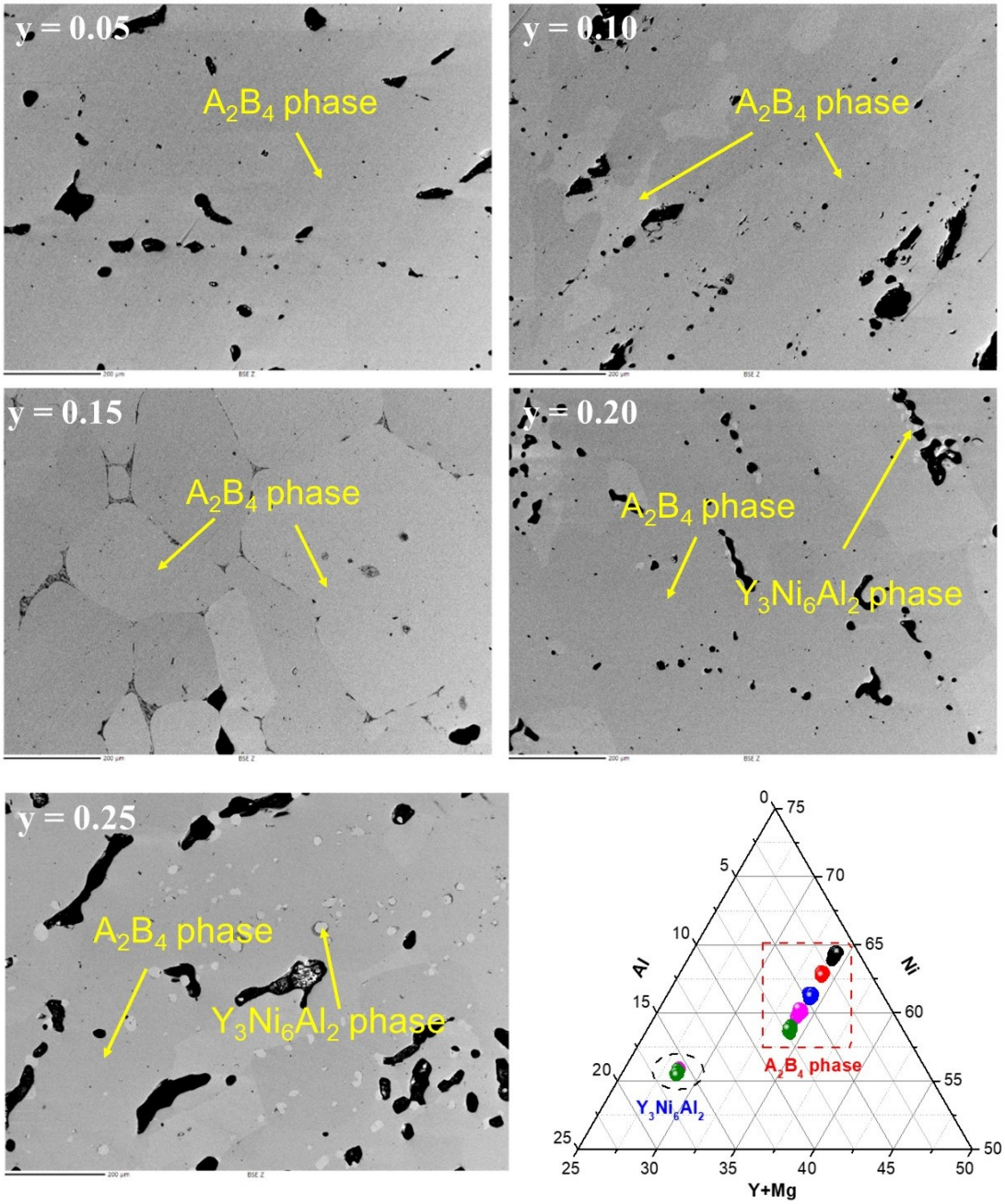


Figure 6.2 EPMA back scattered electron images for $Y_{0.7}Mg_{0.3}Ni_{2-y}Al_y$ compounds. The matrix refers to the $A_2B_4$-type $Y_{0.7}Mg_{0.3}(Ni, Al)_2$ phase. $Y_3Ni_6Al_2$ phase appears as white areas shaped as a small cycle. The deep-black regions are attributed to some cracks produced during grinding.

Table 6.2 Phase compositions determined by EPMA and crystallographic data obtained from Rietveld refinement for $Y_{0.7}Mg_{0.3}Ni_{2-y}Al_y$ compounds ($0.05 \leq y \leq 0.25$).

| $y$ | Phase | Compositions (EPMA and XRD) | Phase abundance | Crystal structure | Space group | Lattice parameter $a$ (Å) | Cell volume $V$ (Å$^3$) | Occupation | |
|---|---|---|---|---|---|---|---|---|---|
| | | | | | | | | 4*a* | 4*c* |
| 0.05 | $A_2B_4$ | XRD : $Y_{0.67}Mg_{0.33}Ni_{1.95}Al_{0.05}$ | 99% | $AuBe_5$ (*C*15*b*) | $F\bar{4}3m$ | 7.1031 (1) | 358.38 (1) | Y | 1.4(1)Y+2.6(1)Mg |
| | | EPMA (±0.02) : $Y_{0.69}Mg_{0.34}Ni_{1.95}Al_{0.05}$ | | | | | | | |
| 0.10 | $A_2B_4$ | XRD : $Y_{0.66}Mg_{0.34}Ni_{1.91}Al_{0.09}$ | 99% | $AuBe_5$ (*C*15*b*) | $F\bar{4}3m$ | 7.1200 (1) | 360.94 (1) | Y | 1.3(1)Y+2.7(1)Mg |
| | | EPMA (±0.02): $Y_{0.71}Mg_{0.32}Ni_{1.91}Al_{0.09}$ | | | | | | | |
| 0.15 | $A_2B_4$ | XRD : $Y_{0.64}Mg_{0.36}Ni_{1.86}Al_{0.14}$ | 99% | $AuBe_5$ (*C*15*b*) | $F\bar{4}3m$ | 7.1291 (1) | 362.336 (8) | Y | 1.1(1)Y+2.9(1)Mg |
| | | EPMA (±0.02): $Y_{0.70}Mg_{0.34}Ni_{1.86}Al_{0.14}$ | | | | | | | |
| 0.20 | $A_2B_4$ | XRD : $Y_{0.68}Mg_{0.32}Ni_{1.82}Al_{0.18}$ | 97% | $AuBe_5$ (*C*15*b*) | $F\bar{4}3m$ | 7.1501 (1) | 365.546 (8) | Y | 1.4(1)Y+2.6(1)Mg |
| | | EPMA (±0.02): $Y_{0.71}Mg_{0.32}Ni_{1.82}Al_{0.18}$ | | | | | | | |
| | $Y_3Ni_6Al_2$ | EPMA (±0.02): $Y_{3.00}Mg_{0.05}Ni_{6.00}Al_{1.67}$ | 2% | $Ce_3Ni_6Si_2$ | $Im\bar{3}m$ | 8.9304 (9) | 712.2 (2) | ~ | ~ |
| 0.25 | $A_2B_4$ | XRD : $Y_{0.65}Mg_{0.35}Ni_{1.78}Al_{0.22}$ | 95% | $AuBe_5$ (*C*15*b*) | $F\bar{4}3m$ | 7.1575 (1) | 366.677 (8) | Y | 1.2(1)Y+2.8(1)Mg |
| | | EPMA (±0.02): $Y_{0.70}Mg_{0.33}Ni_{1.78}Al_{0.22}$ | | | | | | | |
| | $Y_3Ni_6Al_2$ | EPMA (±0.02): $Y_{3.03}Mg_{0.04}Ni_{6.00}Al_{1.72}$ | 4% | $Ce_3Ni_6Si_2$ | $Im\bar{3}m$ | 8.9363 (9) | 713.6 (1) | ~ | ~ |

### 6.1.2.4 Lattice parameters

The evolution of the lattice parameters as function of Al content measured by EPMA for $A_2B_4$ phase is shown in Figure 6.3. Upon Al substitution, as expected, an increase of the lattice parameter with increasing Al content is observed, which is consistent with other previous works [214,272,278]. The lattice parameter increases linearly with Al content as expected for a solid solution following the Vegard's law [204], the deviation from the straight line could result from the difference of Mg contents which are given on the figure.

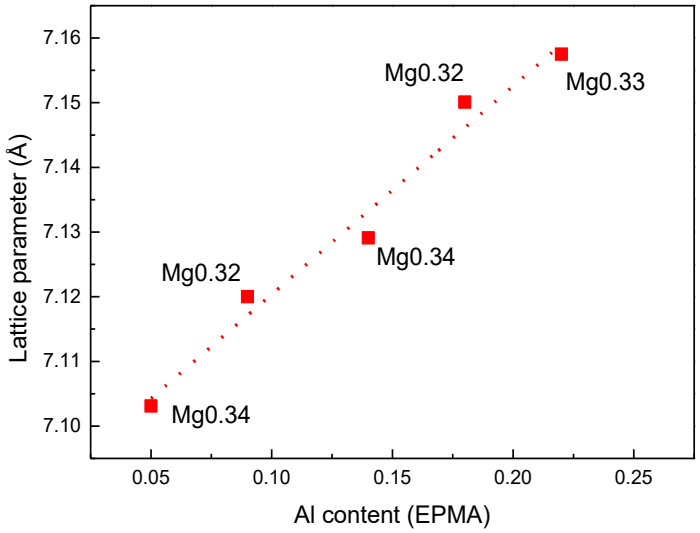


Figure 6.3 Evolution of the lattice parameter as a function of Al content measured by EPMA for $Y_{0.7}Mg_{0.3}Ni_{2-y}Al_y$ compounds ($0.05 \leq y \leq 0.25$), the measured corresponding Mg contents for each compound are given on the figure.

## *6.1.3* Hydrogen sorption properties

### 6.1.3.1 Thermodynamics: PCI curves

The *P-C* Isotherms of the $Y_{0.7}Mg_{0.3}Ni_{2-y}Al_y$ compounds ($0.05 \leq y \leq 0.25$) during the first cycle at 150 °C up to 2.5 MPa (10 MPa for $y = 0.1$) are shown in Figure 6.4 and the detailed data are listed in Table 6.3. A first flat plateau is observed for all compounds, followed by a sloping plateau with hydrogen concentration raising up to around 3 H/f.u for compounds containing Al higher than 0.05. In addition, the PCI curves indicate a decrease of hydrogen equilibrium pressure with increasing Al content, which are in good agreement with the results obtained for $AB_5$ and $AB_n$ ($3 \leq n \leq 3.8$) compounds [89,90,278,279]. The maximum capacity shows an increase first as $y \leq 0.15$, then a decrease for larger Al content. We suppose that the capacity increase may be correlated to the larger cell volume which lower the plateau pressure. For compounds with larger Al content, the capacity decrease could be due to the lower affinity of Al with hydrogen. For the compound with $y = 0.25$, a two-plateau behavior is clearly observed. We can consider that the two-plateau of the PCI corresponds to the formation of two hydrides which we will discuss later.

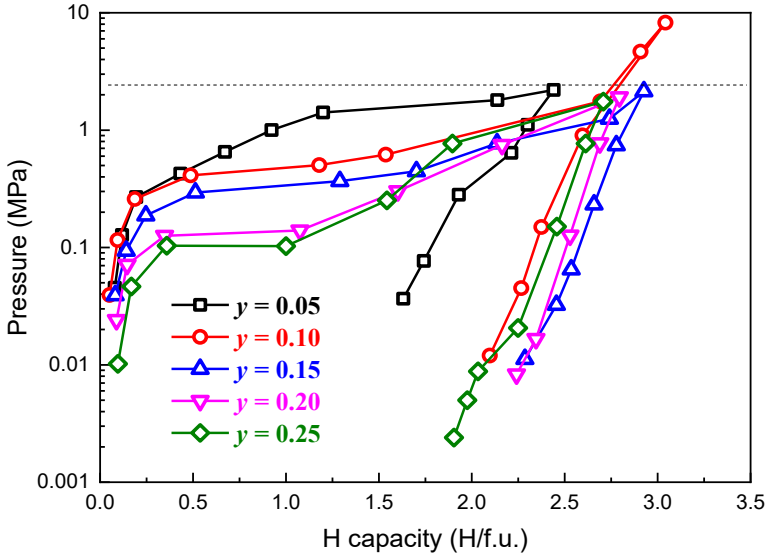


Figure 6.4 *P-C* isotherms measured at 150 °C for $Y_{0.7}Mg_{0.3}Ni_{2-y}Al_y$ compounds ($0.05 \leq y \leq 0.25$) during the first hydrogen absorption and desorption.

Table 6.3 Equilibrium pressure and hydrogen absorption capacity for $Y_{0.7}Mg_{0.3}Ni_{2-y}Al_y$ compounds ($0.05 \leq y \leq 0.25$) at 150 °C.

| $y$ | $P_{eq}$ (MPa) | Maximum capacity (H/f.u.) | Temperature (°C) |
|---|---|---|---|
| 0.05 | 1.42 | 2.45 | 150 |
| 0.10 | 0.50 | 2.69 | 150 |
| 0.15 | 0.45 | 2.93 | 150 |
| 0.20 | 0.14 | 2.79 | 150 |
| 0.25 | 0.10 | 2.70 | 150 |

### 6.1.3.2 Evolutions of hydrides of $Y_{0.7}Mg_{0.3}Ni_{2-y}Al_y$ compounds

Several hydrides with different hydrogen concentrations have been prepared in order to identify the structural evolution and phase occurrence during hydrogenation of $Y_{0.7}Mg_{0.3}Ni_{2-y}Al_y$ compounds. Due to the bad kinetic properties of Mg-containing compounds the PCI curves were measured at 150 °C. However, the hydrides have to be prepared at room temperature for further XRD measurements. For the sake of comparison, we put the PCT curves measured at 150 °C and the three points (hydrogen content and equilibrium pressures) used for hydrides synthesis on the same figure. As shown in Figure 6.5, for Al0.05-Al0.15 compounds, the three points normally follow the variation trends of PCT curves measured at 150 °C, the first two points being located at the first plateau region. For Al0.20 and Al0.25 compounds, the second points are out of the plateau region, which also means the hydrogen absorption plateau regions of Al0.20 and Al0.25 compounds would be very short at 25 °C.

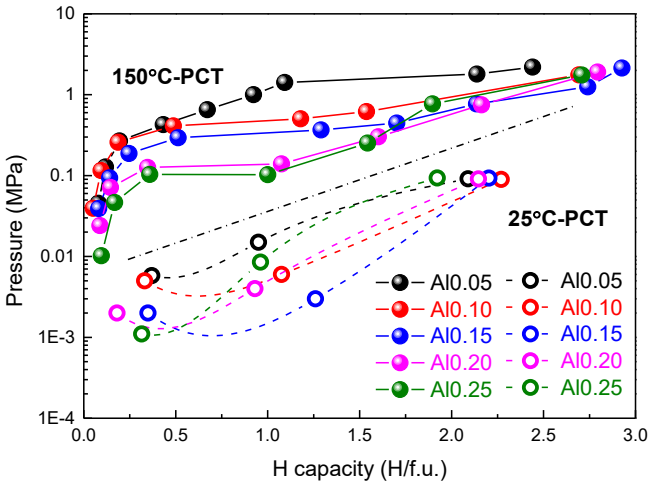


Figure 6.5 The PCT curves measured at 150 ℃ (solid spheres and lines) and the three equilibrium points for hydrogen absorption at 25 ℃ (hollow spheres and dotted lines) of $Y_{0.7}Mg_{0.3}Ni_{2-y}Al_y$ compounds.

As the system $Y_{0.7}Mg_{0.3}Ni_{2-y}Al_y$ shows various structural evolutions in the domain $0.05 \leq y \leq 0.25$, the analysis of $Y_{0.7}Mg_{0.3}Ni_{1.95}Al_{0.05}$ compound will be presented first, then the hydrogenation properties of other $Y_{0.7}Mg_{0.3}Ni_{2-y}Al_y$ compounds ($0.1 \leq y \leq 0.25$) and the effect of Al substitution will be discussed.

***$Y_{0.7}Mg_{0.3}Ni_{1.95}Al_{0.05}$***

This compound has been fully hydrogenated under 0.1MPa of hydrogen pressure at room temperature, reaching a maximum capacity of 2.09 H/f.u.. The XRD patterns of the hydrides of $Y_{0.7}Mg_{0.3}Ni_{1.95}Al_{0.05}$ with different hydrogen concentrations (determined by Sievert's method) are shown in Figure 6.6, and the results of Rietveld analysis are given in Table 6.4. At low hydrogen concentration of 0.37 H/f.u. the $YNi_3H_{1.6}$-type hydride [261] and $YNi_3$-type intermetallic phase are observed, whereas the $A_2B_4$ hydride phase remains small, accounting for 6 wt.%. There is clearly a hydrogenation induced disproportion reaction. The hydride of $A_2B_4$ phase is mainly formed on the plateau (from 1.0 to 2.0 H/f.u.) and finally the initial line $A_2B_4$ phase progressively disappeared for the highest hydrogen concentration (2.09 H/f.u.).

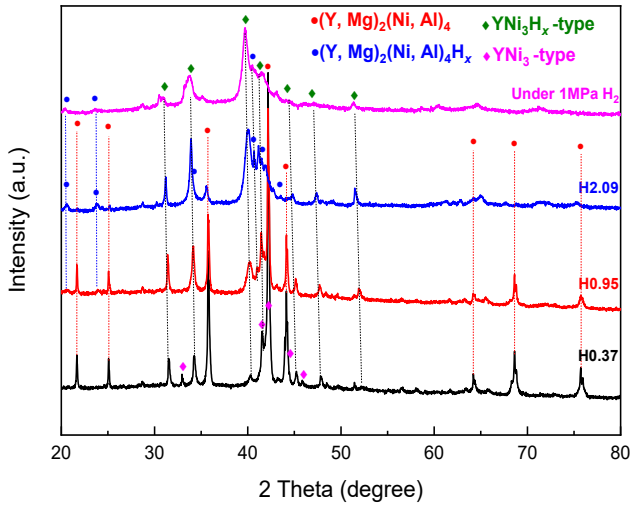


Figure 6.6 XRD patterns of the $Y_{0.7}Mg_{0.3}Ni_{1.95}Al_{0.05}$ compound with different hydrogen concentrations.

Table 6.4 Rietveld refinement results of partially hydrogenated $Y_{0.7}Mg_{0.3}Ni_{1.95}Al_{0.05}$ compounds.

| Compound | Phase | Space group | Phase abundance (wt.%) | Lattice parameter (Å) | $R_{Bragg}$ | $R_p/R_{wp}$ |
|---|---|---|---|---|---|---|
| $AB_2H_{0.37}$ | $A_2B_4$ | $F\bar{4}3m$ | 56 (1) | $a$ = 7.1018 (3) | 5.45 | 23.2/15.7 |
| | $A_2B_4H_x$ | $F\bar{4}3m$ | 6 (1) | $a$ = 7.421 (2) | 14.0 | |
| | $AB_3H_x$ | $R\bar{3}m$ | 32 (1) | $a$ = 5.0079 (4)<br>$c$ = 26.2489 (3) | 11.5 | |
| | $AB_3$ | $R\bar{3}m$ | 5 (1) | $a$ = 4.9965 (6)<br>$c$ = 24.4328 (5) | 10.4 | |
| | $Y_2O_3$ | $Ia$-3 | 1 (1) | $a$ = 10.772 (4) | | |
| $AB_2H_{0.95}$ | $A_2B_4$ | $F\bar{4}3m$ | 30 (1) | $a$ = 7.1022 (2) | 6.12 | 22.1/14.5 |
| | $A_2B_4H_x$ | $F\bar{4}3m$ | 29 (1) | $a$ = 7.4323 (8) | 7.06 | |
| | $AB_3H_x$ | $R\bar{3}m$ | 40 (1) | $a$ = 5.0144 (3)<br>$c$ = 26.3825 (2) | 9.25 | |
| | $Y_2O_3$ | $Ia$-3 | 1 (1) | $a$ = 10.774 (4) | | |
| $AB_2H_{2.07}$ | $A_2B_4$ | $F\bar{4}3m$ | 3 (1) | $a$ = 7.085 (3) | 13.1 | ~ |
| | $A_2B_4H_x$ | $F\bar{4}3m$ | 69 (1) | $a$ = 7.4651 (6) | 5.85 | |
| | $AB_3H_x$ | $R\bar{3}m$ | 27 (1) | $a$ = 5.0487 (4)<br>$c$ = 26.5809 (4) | 8.44 | |
| | $Y_2O_3$ | $Ia$-3 | 1 (1) | $a$ = 10.775 (4) | | |

Such structural transformation with different symmetry from the *C*15*b*-type structure was observed for $YMgNi_4$ compounds where Y and Mg elements are ordered [213]. The XRD patterns of hydrogenated samples show three phases: intermetallic $YMgNi_4$ phase, its hydride and an unknown third phase. This unknown phase is very probably the $AB_3$ hydride phase. Indeed, as shown in Table 6.5, upon hydrogenation the amount of Y atoms occupying the 4*c* site decreases with the increasing hydrogen concentration. Finally, the remained $A_2B_4$ phase exists in the chemical composition $Y_{0.5}Mg_{0.5}(Ni, Al)_2$. Thus, the structural transformation is linked to the Mg homogeneity range of this phase [280], leading to the preferential transformation from $Y_{0.7}Mg_{0.3}Ni_{1.95}Al_{0.05}$ phase with poor structural stability to $YMgNi_4$ phase. *i.e.*, the occupation of Mg prefers to be ordered upon hydrogenation.

Table 6.5 Rietveld refinement results of partially hydrogenated $Y_{0.7}Mg_{0.3}Ni_{1.95}Al_{0.05}$ compound.

| Compound | Occupation (4*c*) | |
|---|---|---|
| | Y | Mg |
| $Y_{0.7}Mg_{0.3}Ni_{1.95}Al_{0.05}$ | 1.35 | 2.65 |
| $AB_2H_{0.37}$ | 1.10 | 2.90 |
| $AB_2H_{0.95}$ | 0.56 | 3.44 |

### *$Y_{0.7}Mg_{0.3}Ni_{2-y}Al_y$ compounds ($0.1 \leq y \leq 0.25$)*

The hydrides of $Y_{0.7}Mg_{0.3}Ni_{2-y}Al_y$ compounds ($0.1 \leq y \leq 0.25$) obtained at different hydrogen concentrations are shown in Figure 6.7, the crystallographic data of these hydrides are summarized in Table 6.6. All the four compounds with various Al contents exhibit similar evolution of hydrides as a function of hydrogen concentration. At low hydrogen concentration (0.18 H/f.u.~0.35 H/f.u.), the β-hydride phases have been formed, meaning that the formation of α-hydride phases have already occurred at lower hydrogen concentration. The transition from α- to β-hydride phases continues until hydrogen concentration up to around 2 H/f.u., where α-hydride phases disappear completely. Then, once further rise hydrogen pressure to obtain higher hydrogen concentration in the compounds, the Bragg diffraction peaks of β-hydride phases start to broaden, the hydrides exhibit worsening crystalline character. It is worth noting that the more Al content, the better crystalline character of hydrides formed under 1 MPa hydrogen pressure, indicating the structural stability during hydrogenation is enhanced by Al substitution.

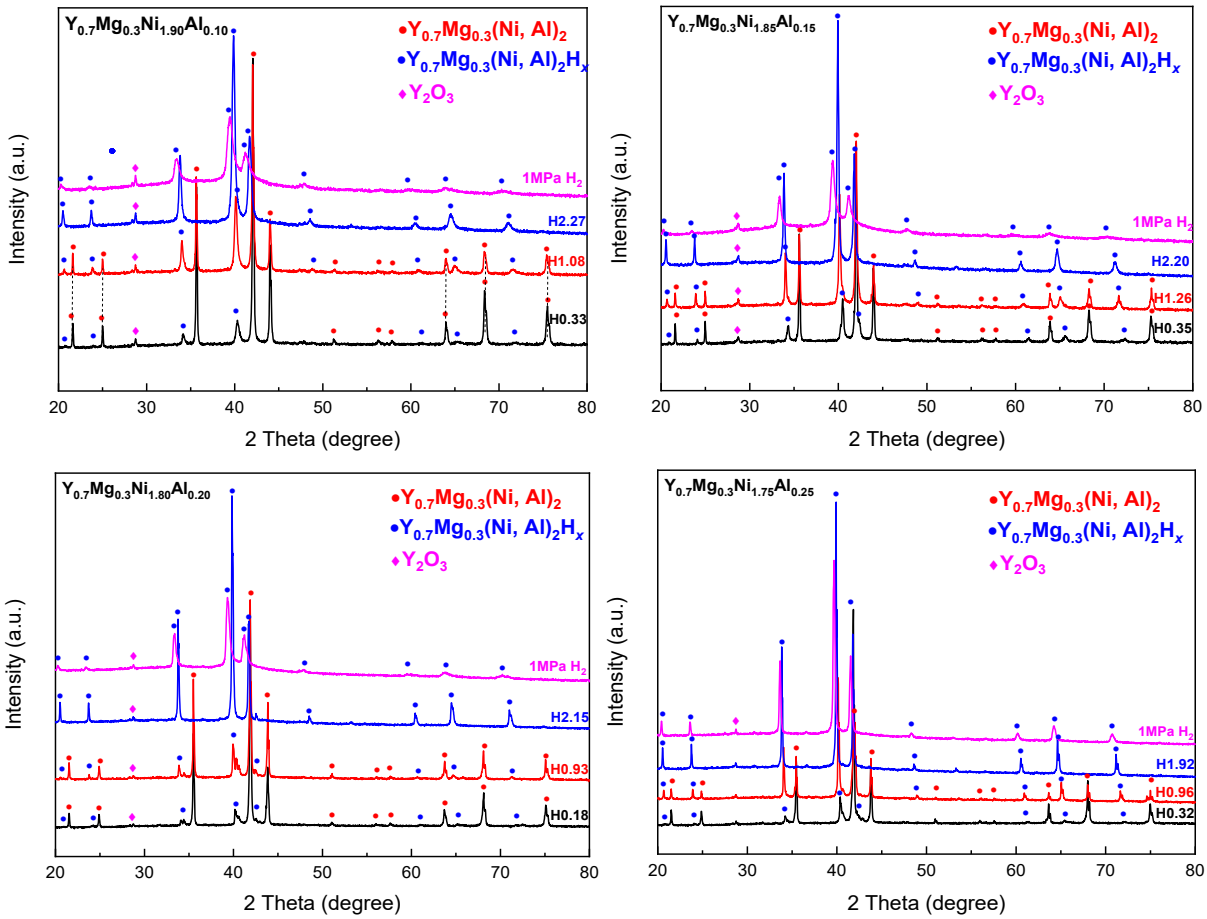


Figure 6.7 XRD patterns of the $Y_{0.7}Mg_{0.3}Ni_{2-y}Al_y$ ($0.10 \leq y \leq 0.25$) hydrides with different hydrogen concentration.

Table 6.6 Rietveld refinement results of the hydrides for $Y_{0.7}Mg_{0.3}Ni_{2-y}Al_y$ ($y$ = 0.10, 0.15, 0.20, 025) compounds (1 wt.% $Y_2O_3$ was remained in all hydrides).

| Compound | | Phase | Space group | Phase abundance (wt.%) | Lattice parameter (Å) | $R_{Bragg}$ |
|---|---|---|---|---|---|---|
| Al0.1 | $AB_2$ | $A_2B_4$ | $F\bar{4}3m$ | 99 (1) | $a$ = 7.1200 (1) | 5.65 |
| | $AB_2H_{0.33}$ | $A_2B_4$ | $F\bar{4}3m$ | 81 (1) | $a$ = 7.1252 (1) | 8.86 |
| | | $A_2B_4H_x$ | $F\bar{4}3m$ | 18 (1) | $a$ = 7.4223 (8) | 10.1 |
| | $AB_2H_{1.08}$ | $A_2B_4$ | $F\bar{4}3m$ | 54 (1) | $a$ = 7.1265 (2) | 5.59 |
| | | $A_2B_4H_x$ | $F\bar{4}3m$ | 45 (1) | $a$ = 7.4549 (3) | 8.54 |
| | $AB_2H_{2.27}$ | $A_2B_4H_x$ | $F\bar{4}3m$ | 99 (1) | $a$ = 7.4990 (8) | 16.0 |
| | 1MPa $H_2$ | $A_2B_4H_x$ | $F\bar{4}3m$ | 99 (1) | $a$ = 7.557 (2) | 9.98 |
| Al0.15 | $AB_2$ | $A_2B_4$ | $F\bar{4}3m$ | 99 (1) | $a$ = 7.1291 (1) | 6.10 |
| | $AB_2H_{0.35}$ | $A_2B_4$ | $F\bar{4}3m$ | 76 (1) | $a$ = 7.1354 (3) | 9.80 |
| | | $A_2B_4H_x$ | $F\bar{4}3m$ | 23 (1) | $a$ = 7.3910 (4) | 10.30 |
| | $AB_2H_{1.26}$ | $A_2B_4$ | $F\bar{4}3m$ | 50 (1) | $a$ = 7.1334 (3) | 5.90 |
| | | $A_2B_4H_x$ | $F\bar{4}3m$ | 49 (1) | $a$ = 7.4494 (4) | 4.73 |
| | $AB_2H_{2.20}$ | $A_2B_4H_x$ | $F\bar{4}3m$ | 99 (1) | $a$ = 7.4866 (4) | 15.20 |
| | 1MPa $H_2$ | $A_2B_4H_x$ | $F\bar{4}3m$ | 99 (1) | $a$ = 7.577 (2) | 15.1 |
| Al0.20 | $AB_2$ | $A_2B_4$ | $F\bar{4}3m$ | 97 (1) | $a$ = 7.1501 (1) | 4.07 |
| | $AB_2H_{0.18}$ | $A_2B_4$ | $F\bar{4}3m$ | 85 (1) | $a$ = 7.1499 (2) | 4.58 |
| | | $Y_3Ni_6Al_2$ | $Im\bar{3}m$ | 1 (1) | $a$ = 9.005 (5) | ~ |
| | | $A_2B_4H_x$ | $F\bar{4}3m$ | 7 (1) | $a$ = 7.4334 (6) | 20.3 |
| | | $A_2B_4H_{x'}$ | $F\bar{4}3m$ | 6 (1) | $a$ = 7.368 (1) | 16.1 |
| | $AB_2H_{0.93}$ | $A_2B_4$ | $F\bar{4}3m$ | 71 (1) | $a$ = 7.1520 (3) | 17.2 |
| | | $Y_3Ni_6Al_2$ | $Im\bar{3}m$ | 1 (1) | $a$ = 9.0214 (5) | ~ |
| | | $A_2B_4H_x$ | $F\bar{4}3m$ | 15 (1) | $a$ = 7.4838 (5) | 14.8 |
| | | $A_2B_4H_{x'}$ | $F\bar{4}3m$ | 8 (1) | $a$ = 7.416 (1) | 36.7 |
| | | $A_2B_4H_{x''}$ | $F\bar{4}3m$ | 4 (1) | $a$ = 7.362 (1) | 18.7 |
| | $AB_2H_{2.15}$ | $A_2B_4H_x$ | $F\bar{4}3m$ | 97 (1) | $a$ = 7.5050 (3) | 14.4 |
| | | $Y_3Ni_6Al_2$ | $Im\bar{3}m$ | 2 (1) | $a$ = 9.021 (3) | ~ |
| | 1MPa $H_2$ | $A_2B_4H_x$ | $F\bar{4}3m$ | 99 (1) | $a$ = 7.5050 (3) | 24.2 |
| Al0.25 | $AB_2$ | $A_2B_4$ | $F\bar{4}3m$ | 95 (1) | $a$ = 7.1575 (1) | 5.72 |
| | $AB_2H_{0.32}$ | $A_2B_4$ | $F\bar{4}3m$ | 75 (1) | $a$ = 7.1604 (1) | 9.87 |
| | | $Y_3Ni_6Al_2$ | $Im\bar{3}m$ | 2 (1) | $a$ = 8.940 (2) | ~ |
| | | $A_2B_4H_x$ | $F\bar{4}3m$ | 15 (1) | $a$ = 7.4075 (4) | 11.1 |
| | | $A_2B_4H_{x'}$ | $F\bar{4}3m$ | 7 (1) | $a$ = 7.353 (1) | 15.4 |
| | $AB_2H_{0.96}$ | $A_2B_4$ | $F\bar{4}3m$ | 42 (1) | $a$ = 7.1596 (3) | 8.44 |
| | | $Y_3Ni_6Al_2$ | $Im\bar{3}m$ | 2 (1) | $a$ = 8.921 (4) | ~ |
| | | $A_2B_4H_x$ | $F\bar{4}3m$ | 49 (1) | $a$ = 7.4452 (2) | 6.85 |
| | | $A_2B_4H_{x'}$ | $F\bar{4}3m$ | 6 (1) | $a$ = 7.362 (1) | 20.1 |
| | $AB_2H_{1.92}$ | $A_2B_4H_x$ | $F\bar{4}3m$ | 97 (1) | $a$ = 7.4882 (2) | 15.5 |
| | | $Y_3Ni_6Al_2$ | $Im\bar{3}m$ | 2 (1) | $a$ = 8.930 (5) | ~ |
| | 1MPa $H_2$ | $A_2B_4H_x$ | $F\bar{4}3m$ | 99 (1) | $a$ = 7.5326 (3) | 15.1 |

According to the phase abundance of each hydride, we can calculate the real hydrogen concentration absorbed in β-hydride phases. The evolution of lattice parameters of β-hydride as function of hydrogen concentration is shown in Figure 6.8, for the sake of comparison, the lattice parameters of initial compounds are also present on this figure. All the lattice parameters increase at the beginning, and then remain almost constant. The increase is in good agreement with the beginning of the PCI curves, which represents the formation of α-hydride phase. Nevertheless, the evolution of lattice parameters for the hydrides with higher hydrogen concentration did not behave in an expected way. For the solution of hydrogen in α-hydride (β-hydride), no well-marked increase of the lattice parameters is observed. Therefore, we assumed that the hydride saturates in hydrogen in the plateau region, the β-hydride range is very short or close to zero. The almost unchanged or slightly increasing lattice parameter of the higher hydrogen-containing hydrides can attribute to the formation of γ-hydride (hydrogen solution of β-hydride). Considering the errors during PCI measurements, the plateau range with high hydrogen concentration may belong to the formation of γ-hydride, rather than β-hydride.

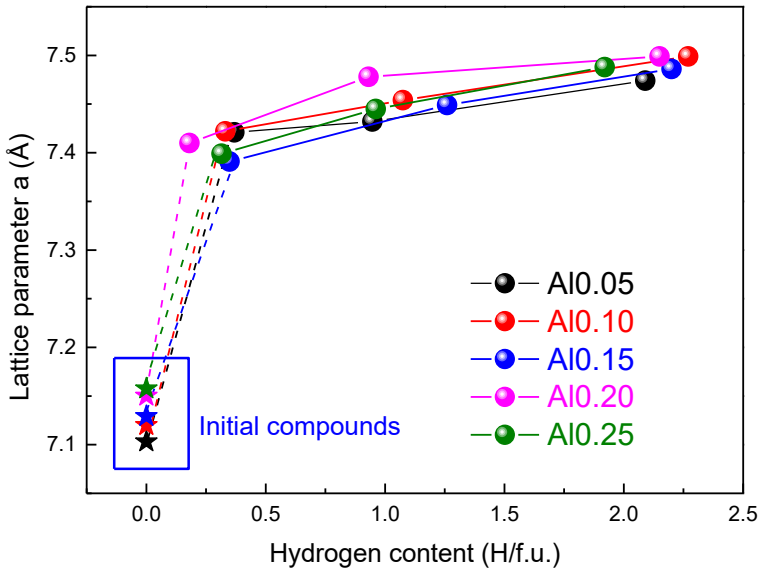


Figure 6.8 Lattice parameters of β-hydrides of $A_2B_4$ phases as function of hydrogen concentration (solid balls). The stars represent the lattice parameters of the initial $Y_{0.7}Mg_{0.3}Ni_{2-y}Al_y$ compounds.

### 6.1.3.3 Van't Hoff plots

To study the hydrogen absorption and desorption thermodynamics, the *P-C* isotherms of the activated $Y_{0.7}Mg_{0.3}Ni_{2-y}Al_y$ compounds ($y$ = 0.10, 0.15, 0.20, 0.25) were measured at 90 °C, 120 °C and 150 °C respectively, with hydrogen pressure ranging from 0.001 MPa to 10 MPa. The results are shown in Figure 6.10a - d. Al0.05 compound is not presented here as its phase changes upon hydrogen absorption, so its PCI curve will not perfectly represent the hydrogen absorption behavior of $A_2B_4$ phase.

At 90 °C and 120 °C, two plateaus can be clearly observed for all the four Al-containing compounds. The first plateau locating at low-pressure region is flat and obvious, whereas the

second one is sloppy and very short. At 150 °C, the two plateaus behavior is not evident for the compounds with low Al content ($y$ = 0.1 and 0.15). With increasing Al content, the first plateau become shorter, indicating the lowering of hydrogen concentration in β-hydrides. According to an empirical rule, the equilibrium pressures of hydrogen absorption depend on the cell volume of the compound. Figure 6.9e presents the evolution of equilibrium pressures in hydrogen absorption process at 150 °C as function of cell volumes. As expected, the equilibrium pressures exhibit nearly linear decrease with the increase of cell volumes.

For hydrogen desorption, all the compounds cannot release all absorbed hydrogen even at 150 °C.

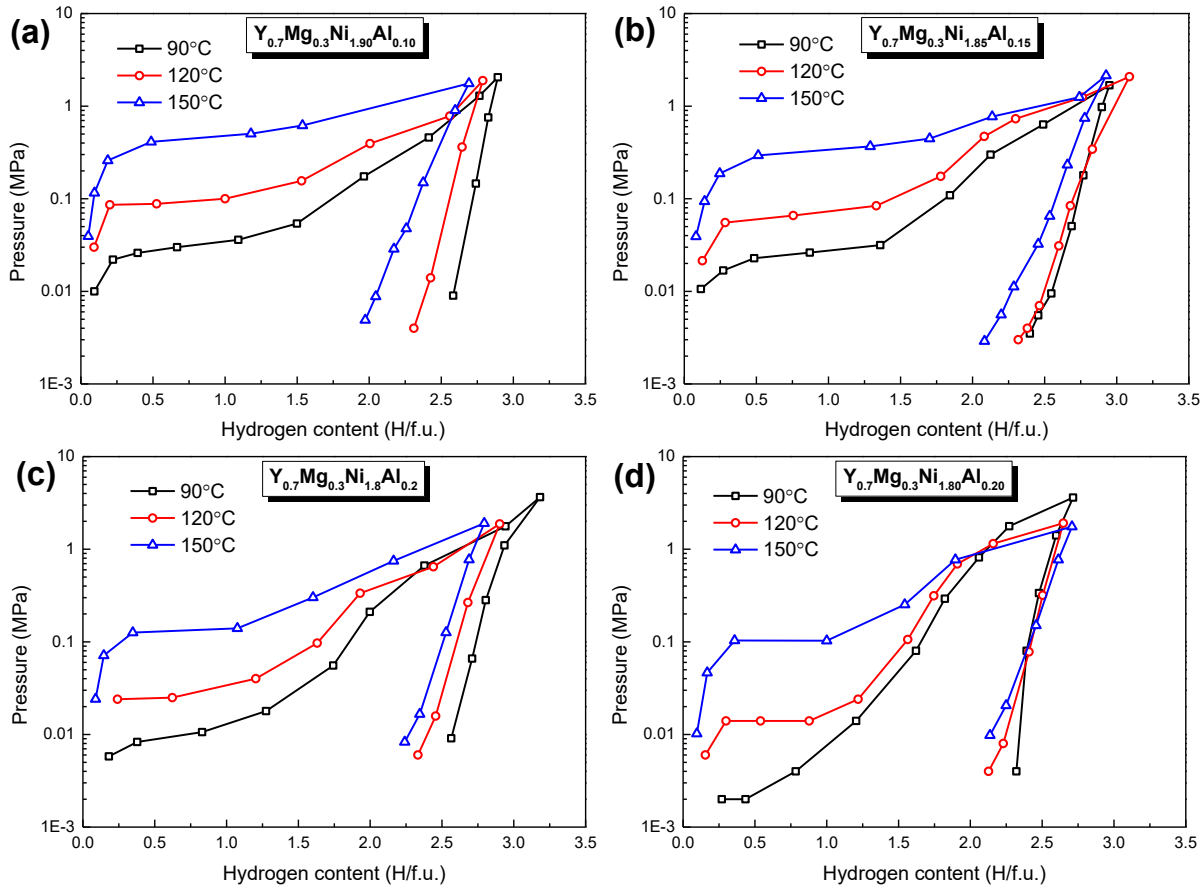

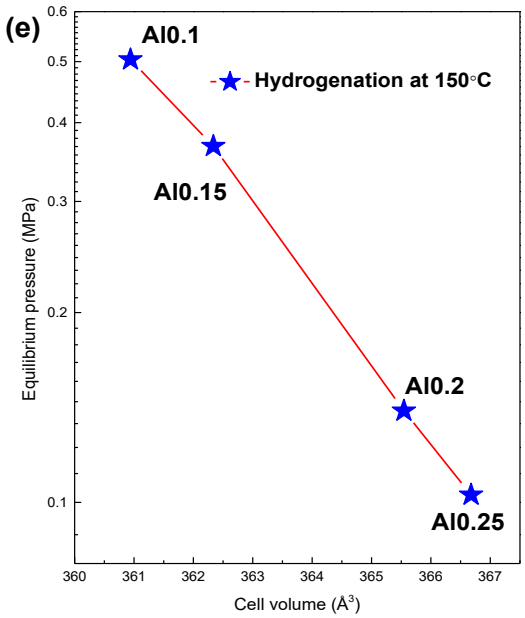


Figure 6.9 *P-C* isotherms of hydrogen absorption and desorption measured at150 °C for $Y_{0.7}Mg_{0.3}Ni_{2-y}Al_y$ compounds ($y$ = 0.10, 0.15, 0.20, 0.25) (a - d). (e) Equilibrium pressures of the first plateau as function of cell volumes of $A_2B_4$ phases.

Figure 6.10 shows the Van't Hoff plots of the first absorption plateau for $Y_{0.7}Mg_{0.3}Ni_{2-y}Al_y$ compounds ($y$ = 0.10, 0.15, 0.20, 0.25) and the results are listed in Table 6.7. Considering the measured errors, it can be seen that the absolute values of hydriding enthalpy increase with Al content, which means that the stability of hydrides is enhanced by Al substitution. This could be explained by the geometric factor as show in Figure 6.9f. Indeed, the enthalpies and entropies of hydride formation of $YMgNi_4$ compound has been calculated by K. Aono *et al.* [213] and V.V. Shtender *et al* [220]: $\Delta H$ = -35.8 ± 0.4 kJ/mol $H_2$, $\Delta S$ = -106 ± 1 kJ/mol $H_2$ and $\Delta H$ = -33.1 kJ/mol $H_2$, $\Delta S$ = -117.6 ± 2.4 kJ/mol $H_2$, respectively. The higher enthalpies in our case are due to the ratio of Mg to Y (0.7/0.3), which leads to a higher atomic radius ratio. Thus, the more stable $A_2B_4$ hydrides were formed. The influence of geometric factor was also observed for the $Mg_{2-x}Pr_xNi_4$ system as the absolute values of enthalpies of hydride formation increased with the amount of Pr content [275]. In addition, the enthalpy and entropy of hydrides formation of Al-substituted $Y_{0.5}Mg_{0.5}Ni_{1.75}Al_{0.25}$ compound ($r_{Y+Mg}/r_{Ni+Al} = 1.345$) are evaluated to be -29.1 kJ/mol $H_2$ and -110.6 J/mol $H_2$/K [272]. In contrast, $Y_{0.7}Mg_{0.3}Ni_{1.75}Al_{0.25}$ ($Y_{0.70}Mg_{0.33}Ni_{1.78}Al_{0.22}$) compound ($r_{Y+Mg}/r_{Ni+Al} = 1.377$) shows in this study higher absolute values of calculated $\Delta H$ = -72.66 kJ/mol $H_2$ and $\Delta S$ = -151.56 J/mol $H_2$/K, which can also be attributed to relatively higher atomic radius ratio.

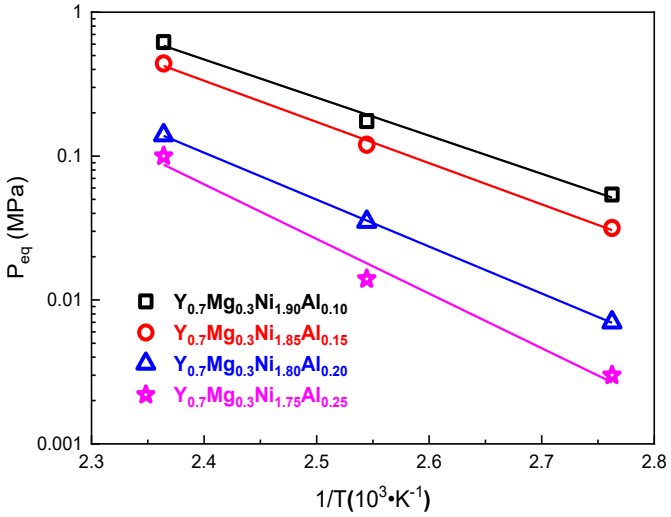


Figure 6.10 Van't Hoff plots for $Y_{0.7}Mg_{0.3}Ni_{2-y}Al_y$ compounds ($y$ = 0.10, 0.15, 0.20, 0.25).

Table 6.7 Thermodynamics parameters of $Y_{0.7}Mg_{0.3}Ni_{2-y}Al_y$ compounds ($y$ = 0.10, 0.15, 0.20, 0.25)

| Sample | $\Delta H$ (kJ/mol $H_2$) | $\Delta S$ (J/mol $H_2$/K) |
|---|---|---|
| $y$ = 0.10 | -50.70 | -115.39 |
| $y$ = 0.15 | -54.83 | -122.46 |
| $y$ = 0.20 | -62.44 | -131.16 |
| $y$ = 0.25 | -72.66 | -151.56 |

## 6.1.4 Dehydrogenation mechanism

### 6.1.4.1 XRD patterns of the dehydrogenated samples

As shown in the PCI curves, large amount of hydrogen cannot be released from the formed hydrides even at 150 °C. To determine whether structural changes are induced by hydrogenation, the XRD patterns of dehydrogenated samples ($x$ = 0.05, 0.10, 0.15, 0.20, 0.25) have been analysed. In addition, to obtain detailed structural evolution upon dehydrogenation, the thermal analysis has been performed and analysed.

As shown in Figure 6.11, the crystalline diffraction peaks are visible for Al0.05 compound, which can be indexed with a mixture of $AB_2$-type phase and $AB_3$-type phase. The $AB_3$ phase is originated from hydrogen desorption of $AB_3$-type hydrides formed during hydrogenation (see the formation of hydrides at different hydrogen concentration discussed above). For $x \geq 0.1$, we observed similar XRD patterns after hydrogen desorption. The diffraction peaks are severely broadened, indicating a decrease of the crystallinity, but without exhibit thorough amorphization like hydrogenation behaviours of $Y(Ni, Al)_2$ and $Y_x(Ni, Mn)_2$ compounds. This means that the formation of the hydride leads to rearrangement of the microstructure of the compounds. In this case, the stabilities of hydrides lie between crystalline and amorphous ones,

and the hydrogen cannot be released upon hydrogen desorption under dynamic vacuum at 150 °C.

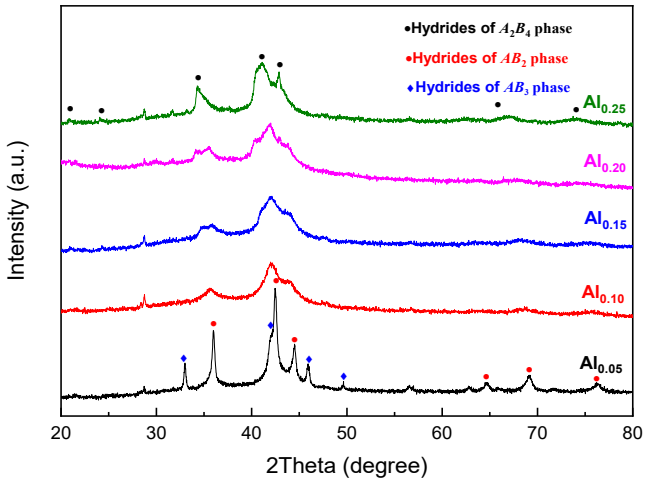


Figure 6.11 X-ray diffraction patterns for $Y_{0.7}Mg_{0.3}Ni_{2-y}Al_y$ ($0 \leq y \leq 0.25$) upon dehydrogenation under dynamic vacuum at 150 °C.

### 6.1.4.2 DSC analysis for the dehydrogenated samples

To identify the hydrogen desorption temperatures, the thermal analysis was performed by DSC for the partially dehydrogenated samples. The DSC curves in Figure 6.12a, show a large broad endothermic peak, corresponding to the trapped hydrogen desorption from the rearranged microstructure. Compared to $Y_xNi_{2-y}Mn_y$-H system, the sharp exothermic peak which represents the phase crystallization process is not visible. This further indicates that HIA did not occur in $Y_{0.7}Mg_{0.3}Ni_{2-y}Al_y$-H system.

The final phase components were detected after heating the samples in DSC up to 600 °C. As shown in Figure 6.12b and Table 6.8, the XRD patterns are indexed with the $A_2B_4$ phase and a small amount of $YH_2$ (the impurity phase $Y_2O_3$ is negligible). The phase components are almost recovered after heating at 600 °C, although the minor amount of $YH_2$ indicates the very weak hydrogen induced disproportionation (HID). Therefore, we can conclude that HIA and HID is negligible in $Y_{0.7}Mg_{0.3}Ni_{2-y}Al_y$-H system. However, the atomic radius ratio is $r_A/r_B = 1.372$ in the case of $Y_{0.7}Mg_{0.3}Ni_{1.75}Al_{0.25}$ compound, (according to the EPMA composition: $Y_{0.70}Mg_{0.33}Ni_{1.78}Al_{0.22}$), close to the empirical value 1.37, whereas it is larger for $Y_{0.7}Mg_{0.3}Ni_{1.90}Al_{0.10}$ (EPMA composition: $Y_{0.71}Mg_{0.32}Ni_{1.91}Al_{0.09}$), with $r_A/r_B = 1.387$. Therefore, the empirical limit of 1.37 for HIA reported by Aoki *et al.* [201] is not suitable for Mg-containing $AB_2$ systems.

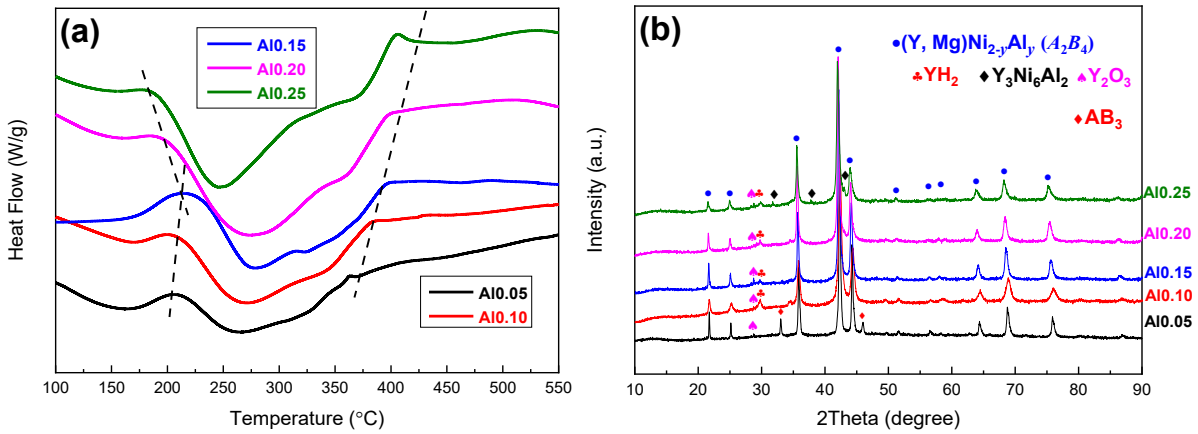


Figure 6.12 DSC curves of the dehydrogenated samples (a) and the XRD patterns of the dehydrogenated samples upon thermal analysis with temperature heating to 600 ℃ (b).

Table 6.8 Phase components of the dehydrogenated samples after heating to 600 ℃.

| Compound | Phase | Space group | Phase abundance (wt.%) | Lattice parameter *a* (Å) |
|---|---|---|---|---|
| Al0.05 | $A_2B_4$ | $F\bar{4}3m$ | 98 (1) | 7.0929 (3) |
| | $Y_2O_3$ | | 2 (1) | |
| Al0.10 | $A_2B_4$ | $F\bar{4}3m$ | 96 (1) | 7.0743 (7) |
| | $YH_2$ | | 3 (1) | |
| | $Y_2O_3$ | | 1 (1) | |
| Al0.15 | $A_2B_4$ | $F\bar{4}3m$ | 97 (1) | 7.1082 (4) |
| | $YH_2$ | | 2 (1) | |
| | $Y_2O_3$ | | 1 (1) | |
| Al0.20 | $A_2B_4$ | $F\bar{4}3m$ | 97 (1) | 7.1223 (4) |
| | $YH_2$ | | 2 (1) | |
| | $Y_2O_3$ | | 1 (1) | |
| Al0.25 | $A_2B_4$ | $F\bar{4}3m$ | 97 (1) | 7.1322 (4) |
| | $YH_2$ | | 2 (1) | |
| | $Y_2O_3$ | | 1 (1) | |

## 6.1.5 Cycle properties

Finally, we investigated the hydrogen absorption and desorption cycles and structural evolution of this series of compounds taking $Y_{0.7}Mg_{0.3}Ni_{1.9}Al_{0.1}$ compound as an example. Figure 6.13 shows the H capacity of $Y_{0.7}Mg_{0.3}Ni_{1.9}Al_{0.1}$ compound after several hydrogen absorption and desorption cycles (Hydrogen pressure: ~ 4 MPa, measuring temperature: 25 ℃; Hydrogen desorption: 400 ℃, dynamic vacuum, 1h). After four cycles the hydrogen absorption capacity stabilizes at around 2.5 H/f.u. (1.37 wt.%).

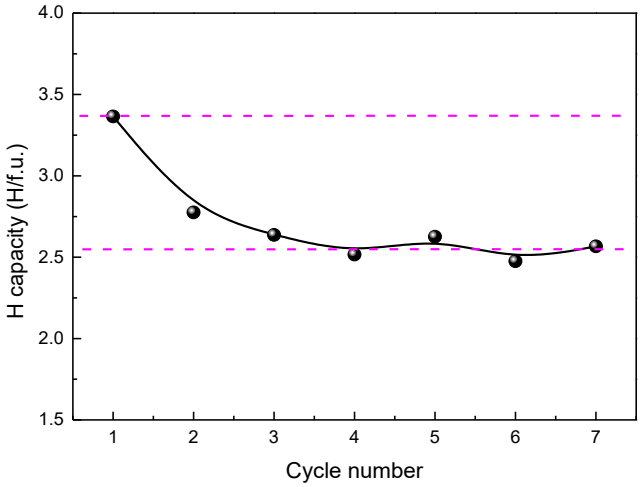


Figure 6.13 Cycle properties of $Y_{0.7}Mg_{0.3}Ni_{1.9}Al_{0.1}$ compound (Hydrogen pressure: ~ 4 MPa, measuring temperature: 25 ℃; Hydrogen desorption: 400 ℃, dynamic vacuum, 1 h).

We observed the evolution of phase crystal structure before and after capacity decay by XRD. As shown in Figure 6.14, new $A_2B_4$ phase accompanied by a small amount of $YH_2$ phase is formed, indicating that weak hydrogen induced disproportionation (HID) occurred. The new $A_2B_4$ phase shows much smaller lattice parameter with $a$ = 7.0377 (9) Å, compared to the parent compound ($a$ = 7.1200 (1) Å), but still higher than for $YMgNi_4$ compound ($a$ = 7.01 Å). This can be interpreted by the partial loss of Y leading to the formation of new $A_2B_4$ phase with higher proportion of Mg in the 4*c* site.

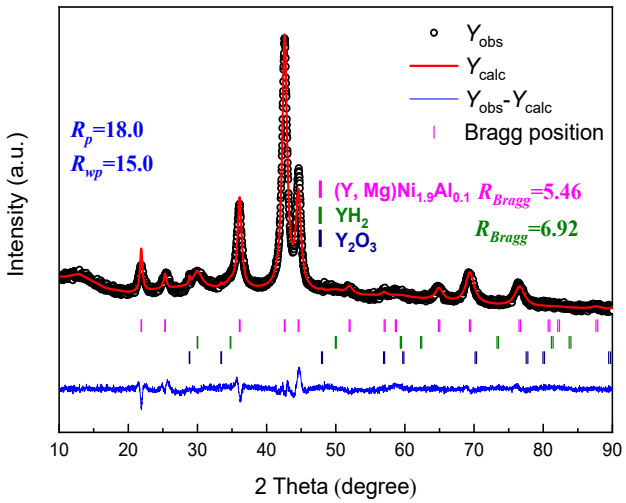


Figure 6.14 Rietveld refinement of XRD pattern of $Y_{0.7}Mg_{0.3}Ni_{1.9}Al_{0.1}$ compound upon 7 hydrogen absorption and desorption cycles.

On the whole, the stable hydrogen absorption capacity of $Y_{0.7}Mg_{0.3}Ni_{2-y}Al_y$ hydrides (1.37 wt.%) is relatively low compared to that of $AB_5$-type hydrogen storage materials (around 1.5 wt.%). The capability resisting to structural changes during the first hydrogen absorption and desorption cycle decides their subsequent hydrogen sorption performance. However, the absent of $AB_3$-type phase suggests that the HID occurrence in this case is different from $Y(Ni, Al)_2$ or

$Y(Ni, Mn)_2$ alloys without Mg. $Y_{0.7}Mg_{0.3}(Ni, Al)_2$ phase with disordered Mg occupation prefer to convert to $Y_{0.5}Mg_{0.5}(Ni, Al)_2$ phase with ordered Mg occupation. Meanwhile, we also observed the effects of Al substitution on suppressing such conversion (Al0.25 compound). Therefore, increasing the Al content may show more effective effects to enhance structural stability.

### 6.1.6 Summary

The $Y_{0.7}Mg_{0.3}Ni_{2-y}Al_y$ ($y$ = 0.05, 0.1, 0.15, 0.2, 0.25) compounds were investigated in this section. After heat treatment, single-$A_2B_4$ phase structure was observed for $y$ = 0.05, 0.1, 0.15, while a small amount of $Y_3Ni_6Al_2$ phase in $y$ = 0.2 and 0.25 compounds.

The maximum hydrogen absorption capacity is around 3 H/f.u. (1.63 wt.%) for $y$ = 0.15 (EPMA: $Y_{0.70}Mg_{0.34}Ni_{1.86}Al_{0.14}$). By increasing the Al content, the stability of hydrides is enhanced. $A_2B_4$ phase in $Y_{0.7}Mg_{0.3}Ni_{1.95}Al_{0.05}$ compound is not stable upon hydrogen absorption, during which the structure turns from single $A_2B_4$-type into $AB_3$ one. For $y \geq 0.1$, crystalline hydrides can be obtained with hydrogen concentration higher than 2 H/f.u..

The H-containing compounds upon hydrogen absorption and desorption at 150 ℃ exhibit rearranged microstructure, and hydrogen cannot be released at such temperature. Thermal analysis suggests that the hydrogen can be totally released before 300 ℃. The $A_2B_4$-type structures could be recovered from microcrystalline state upon heating to 400 ℃. For $y$ = 0.1, 0.15 and 0.2, the lattice parameters show minor changes, whereas a marked decrease of lattice parameters was observed for $y$ = 0.25 compound, in agreement with appearance of the second plateau.

## 6.2 Effects of La substitution on $Y_{0.7-x}La_xMg_{0.3}Ni_2$ ($0.1 \leq x \leq 0.3$)

For Mg-containing $A_2B_4$ compounds with $C15b$-type structure, we have found that their hydrogen sorption behaviors are different from $AB_2$ compounds with $C15$ Laves phase structure, especially showing a stronger resistance for HIA. Meanwhile, the hydrogen absorption capacity is lowered due to the lattice contraction. Considering these facts, we adopted small amount of La to further substitute Y. Although the empirical value of atomic radius ratio is higher than 1.37, La substitution may weaken the structural stability of $A_2B_4$ phase because of its much larger atomic radius (1.879 Å) than Y (1.801 Å) one. Therefore, the amount of La should be limited. In addition, heat treatment may contribute to the substitution of La for Y.

In this chapter, the La substitution and heat treatment effects on structural stability and hydrogen sorption properties of $Y_{0.7-x}La_xMg_{0.3}Ni_2$ compounds are discussed in detail.

All the as-cast ingots were prepared by induction melting in high purity argon atmosphere (5N) under a pressure of 0.04 MPa in a water-cooled copper crucible. $Y_{0.5}La_{0.2}Ni_2$ precursor alloy was prepared firstly by induction melting for Y, La and Ni metals (purity ≥ 99.9%, from Trillion Metals Co.,Ltd.), the ingot was turned over and re-melted three times to insure their homogeneity. Then, $Y_{0.5}La_{0.2}Mg_{0.3}Ni_2$ was prepared by induction melting for the precursor and Mg (purity ≥ 99.9%, from Trillion Metals Co.,Ltd.), the ingot were re-melted few times until we got the target weight.

### 6.2.1 As-cast compounds

#### 6.2.1.1 Phase occurrences and crystal structures

Rietveld refinements for the XRD patterns of as-cast $Y_{0.7-x}La_xMg_{0.3}Ni_2$ ($x$ = 0.1, 0.2, 0.3) compounds are shown in Figure 6.15, the phase abundance and crystallographic data obtained from refinements are summarized in Table 6.9. Few phases are indexed for the as-cast La0.1 sample, including $AB_3$-type (Y, La, Mg)$Ni_3$ (space group $R\bar{3}m$), $A_2B_4$-type (Y, La, Mg)$_2Ni_4$ ($C15b$, space group $F\bar{4}3m$), $La_2Ni_2Mg$ (space group $P4/mbm$) and LaNi (space group $cmcm$). All phases presented in La0.1 sample also appears in La0.2 and La0.3 samples, the only difference is the appearance of $AB_2$-type (Y, La, Mg)$Ni_2$ ($C15$, space group $Fd\bar{3}m$) phase for La0.3 compound. By increasing the La content from $x$ = 0.1 to $x$ = 0.2 and 0.3, the abundance of $AB_3$ phase increases while the amount of $A_2B_4$ phase decrease. Meanwhile, trace of $LaYO_3$ (space group $Ia\bar{3}$) is also observed in all as-cast samples.

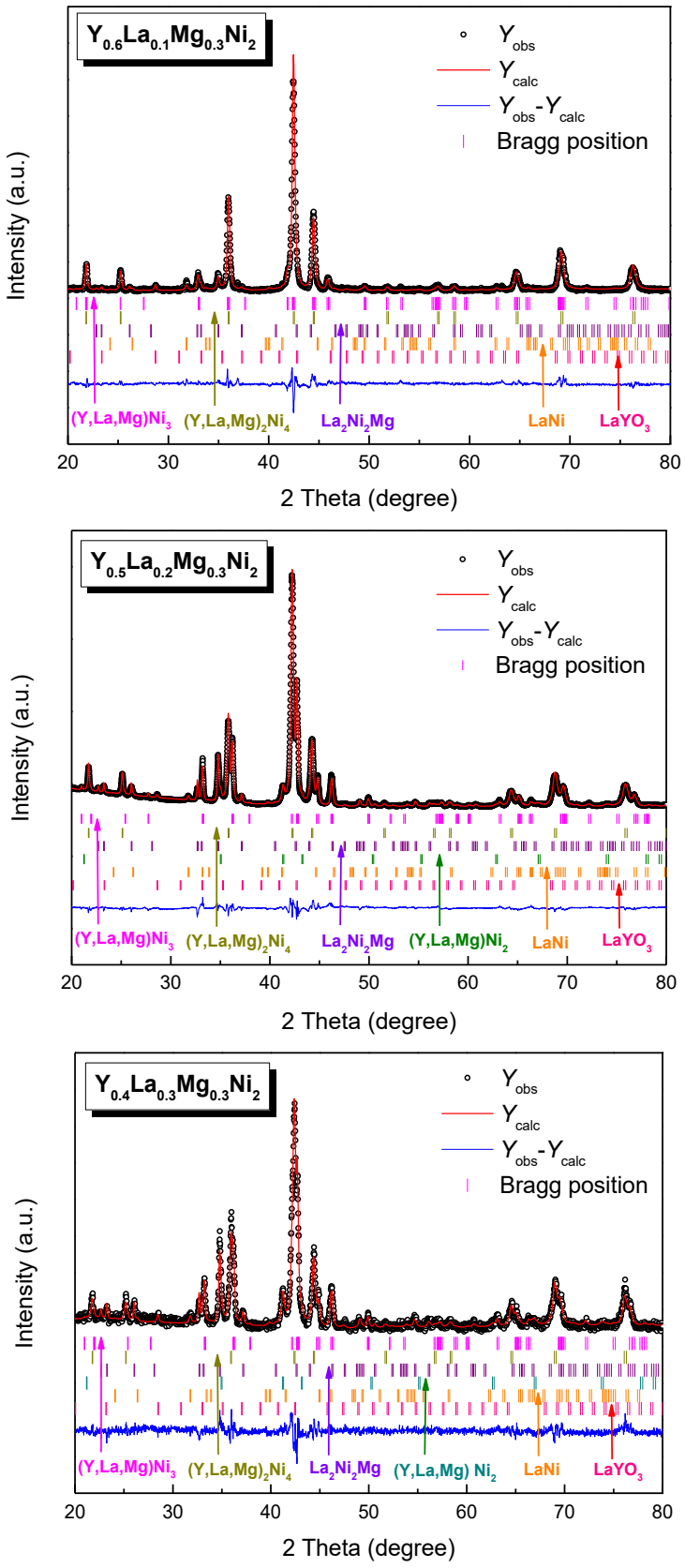


Figure 6.15 Rietveld refinements of the XRD patterns for as-cast $Y_{0.7-x}La_xMg_{0.3}Ni_2$ ($x$ = 0.1, 0.2, 0.3) compounds.

Table 6.9 Phase abundance and crystallographic data from Rietveld refinement for as-cast $Y_{0.7-x}La_xMg_{0.3}Ni_2$ ($x$ = 0.1, 0.2, 0.3) compounds.

| Sample | Phase | Phase abundance (±1%) | R-Bragg | Space group | Lattice parameters (Å) |
|---|---|---|---|---|---|
| La0.1<br>$R_p$ = 7.95<br>$R_{wp}$ = 9.80 | (Y, La, Mg)$_2$Ni$_4$ | 74% | 5.02 | $F\bar{4}3m$ | $a$ = 7.0575 (5) |
| | (Y, La, Mg)Ni$_3$ | 19% | 9.66 | $R\bar{3}m$ | $a$ = 5.0022 (5)<br>$c$ = 24.383 (6) |
| | La$_2$Ni$_2$Mg | 4% | | $P_4/mbm$ | $a$ = 7.623 (2)<br>$c$ = 3.8961 (1) |
| | LaNi | 2% | | $Cmcm$ | $a$ = 3.922 (2)<br>$b$ = 10.623 (4)<br>$c$ = 4.368 (5) |
| | YLaO$_3$ | 1% | | | |
| La0.2<br>$R_p$ = 9.72<br>$R_{wp}$ = 8.26 | (Y, La, Mg)$_2$Ni$_4$ | 59% | 3.55 | $F\bar{4}3m$ | $a$ = 7.0915 (1) |
| | (Y, La, Mg)Ni$_3$ | 29% | 7.20 | $R\bar{3}m$ | $a$ = 4.9637 (1)<br>$c$ = 24.2467 (1) |
| | La$_2$Ni$_2$Mg | 7% | | $P_4/mbm$ | $a$ = 7.6541 (4)<br>$c$ = 3.9226 (1) |
| | (Y, La, Mg)Ni$_2$ | 3% | | $Fd\bar{3}m$ | $a$ = 7.2468 (4) |
| | LaNi | 1% | | $Cmcm$ | $a$ = 3.929 (2)<br>$b$ = 10.8029 (6)<br>$c$ = 4.3591 (3) |
| | YLaO$_3$ | 1% | | | |
| La0.3<br>$R_p$ = 14.3<br>$R_{wp}$ = 9.81 | (Y, La, Mg)$_2$Ni$_4$ | 52% | 3.65 | $F\bar{4}3m$ | $a$ = 7.0706 (6) |
| | (Y, La, Mg)Ni$_3$ | 30% | 8.19 | $R\bar{3}m$ | $a$ = 4.9702 (5)<br>$c$ = 24.217 (3) |
| | La$_2$Ni$_2$Mg | 9% | | $P_4/mbm$ | $a$ = 7.650 (1)<br>$c$ = 3.925 (1) |
| | (Y, La, Mg)Ni$_2$ | 6% | | $Fd\bar{3}m$ | $a$ = 7.261 (1) |
| | LaNi | 2% | | $Cmcm$ | $a$ = 3.935 (8)<br>$b$ = 10.722 (9)<br>$c$ = 4.352 (9) |
| | YLaO$_3$ | 1% | | | |

### 6.2.1.2 Hydrogen storage capacities and kinetic properties

Kinetic properties of the as-cast $Y_{0.7-x}La_xMg_{0.3}Ni_2$ ($x$ = 0.1, 0.2, 0.3) compounds were measured at 25 °C, with initial hydrogen pressure of around 6 MPa and final pressure around 4 MPa. The kinetic curves and hydrogen absorption capacities are shown in Figure 6.16 and Table 6.10 respectively. The hydrogenation kinetics for $x$ = 0.2 and 0.3 are faster compared to La0.1 compound (see Figure 6.16d), they reach full capacity in few minutes while La0.1 need more one hour for the first cycle. Furthermore, La0.2 and La0.3 compounds exhibit higher hydrogen storage capacity 1.43 wt.% than 1.33 wt.% for La0.1. To understand this difference, the XRD analyses of the cycled compounds are carried out.

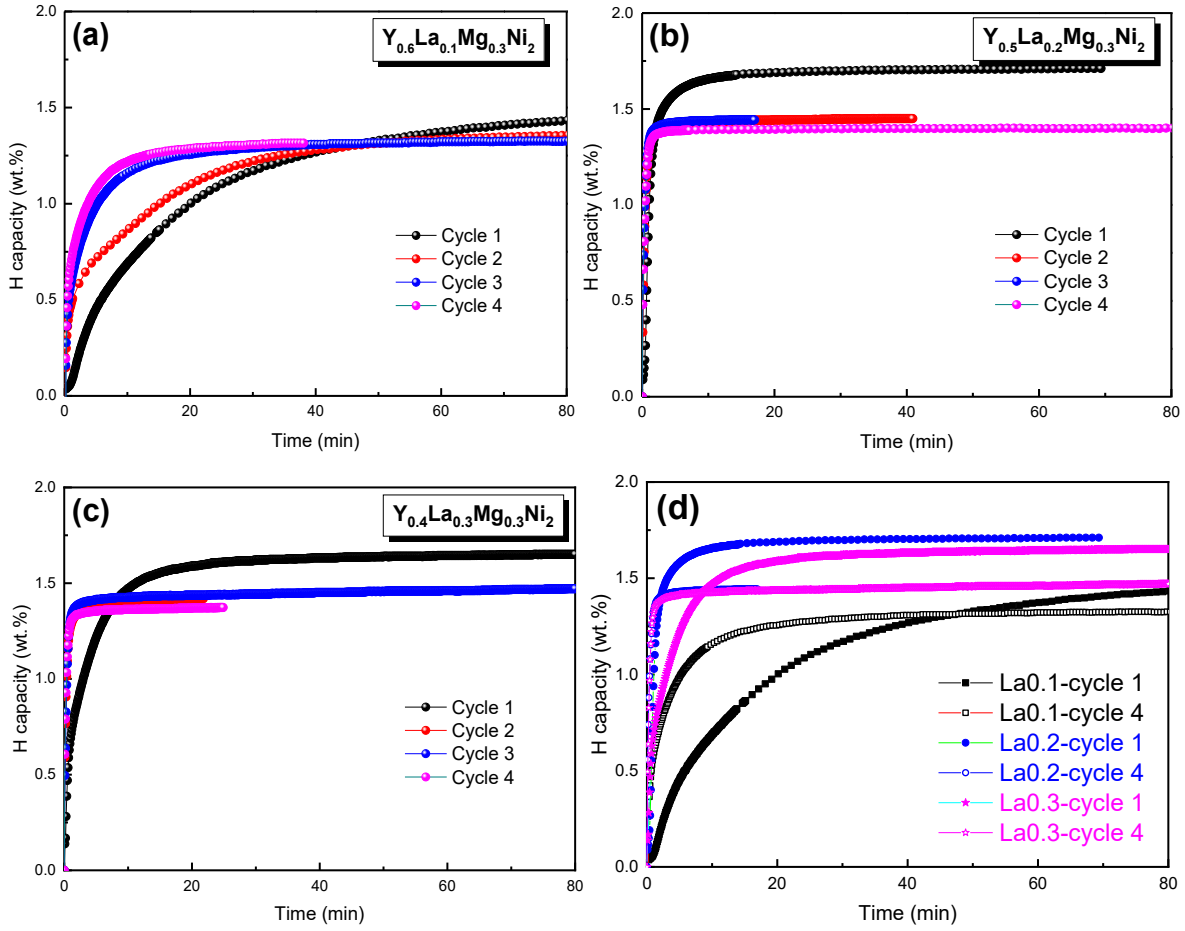


Figure 6.16 kinetic curves of as-cast $Y_{0.7-x}La_xMg_{0.3}Ni_2$ ($x$ = 0.1, 0.2, 0.3) (a, b, c) compounds for 1 to 4 cycles and their comparison of the first and the fourth cycle (d) (initial hydrogen pressure: ~6 MPa, final hydrogen pressure: ~4 MPa, measuring temperature: 25 °C).

Table 6.10 Hydrogen absorption capacities of the as-cast $Y_{0.7-x}La_xMg_{0.3}Ni_2$ ($x$ = 0.1, 0.2, 0.3) compounds during the first and the fourth hydrogenation.

| Sample | Maximum capacity $C_{1st}$ (wt.%) | Reversible capacity $C_{4th}$ (wt.%) | Capacity decay |
|---|---|---|---|
| $Y_{0.6}La_{0.1}Mg_{0.3}Ni_2$ | 1.60 | 1.33 | 17% |
| $Y_{0.5}La_{0.2}Mg_{0.3}Ni_2$ | 1.71 | 1.44 | 16% |
| $Y_{0.4}La_{0.3}Mg_{0.3}Ni_2$ | 1.65 | 1.43 | 13% |

### 6.2.1.3 The XRD studies of cycled compounds

To explain the hydrogen absorption capacity decay, we analyzed the phase occurrence and crystal structures of dehydrogenated $Y_{0.7-x}La_xMg_{0.3}Ni_2$ ($x$ = 0.1, 0.2, 0.3) samples. These samples were prepared by hydrogen absorption and desorption for four cycles (hydrogenation: with initial hydrogen pressure of around 6 MPa and final pressure around 4 MPa at room temperature; dehydrogenation: dynamic vacuum at 400 °C for 1 h). As shown in Figure 6.17, the XRD and Rietveld analysis indicate that $A_2B_4$-type (Y, La, Mg)$_2$Ni$_4$ and $AB_3$-type (Y, La,

Mg)$Ni_3$ account for the main phases. The stable hydride (La, Y)$H_2$ is the product of HID, appearing in all samples of different La contents. The oxide $LaYO_3$ is left unacted upon hydrogen absorption and desorption cycles.

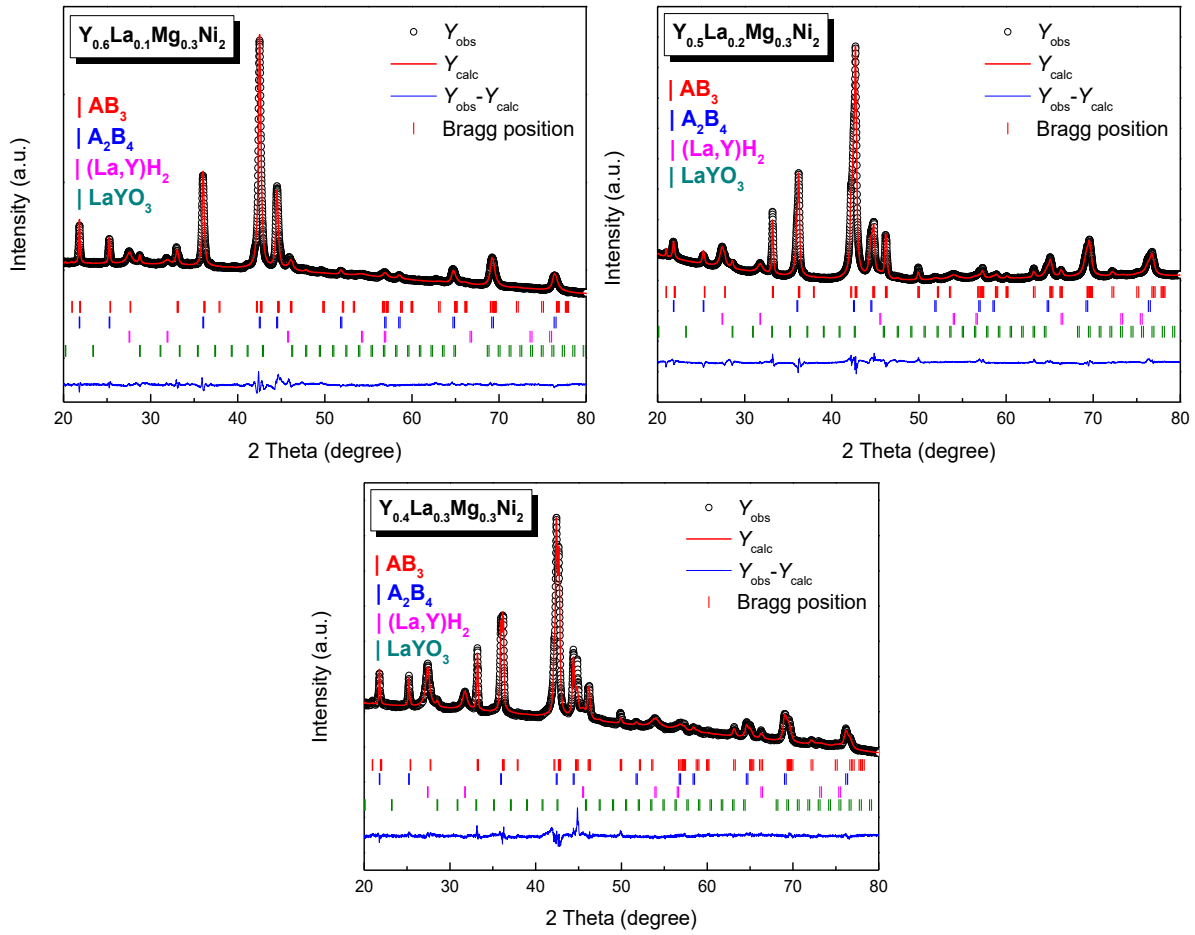


Figure 6.17 Rietveld refinements of the XRD patterns for as-cast $Y_{0.7-x}La_xMg_{0.3}Ni_2$ ($x$ = 0.1, 0.2, 0.3) compounds upon hydrogen absorption and desorption cycles.

The phase abundance and lattice parameters for each phase obtained from Rietveld refinements for the dehydrogenated samples are summarized in Table 6.11. The reversible hydrogen absorption capacities are closely related with the phase composition after hydrogen absorption and desorption cycles. $AB_2$-type, $La_2Ni_2Mg$ and LaNi phases are invisible for all compounds upon hydrogen absorption, desorption cycles, while the stable hydride (La, Y)$H_2$ emerged (Figure 6.17 and Table 6.11). Meanwhile, $AB_3$ phase is formed during hydrogenation cycling by chemical balancing, as an increase of its abundance is observed after cycling. Therefore, the reversible hydrogen capacity is controlled by relative phase abundance of $AB_3$- and $A_2B_4$-type phases. 77 wt.% of $A_2B_4$ phase is present as main phase in La0.1, whereas in La0.2 and La0.3 compounds $A_2B_4$ and $AB_3$ phases have similar percentage. It is known that $A_2B_4$ phases have lower capacity (~1 wt.%) [220] than Mg substituted $AB_3$ phase (~1.5 wt.%) [281]. We can conclude that the low reversible hydrogen capacity of La0.1 compound is due to

the relative higher content of $A_2B_4$-type (Y, La, Mg)$_2$Ni$_4$ phase. The capacity decay is caused by the HIA or HID of $AB_2$-type, La$_2$Ni$_2$Mg and LaNi phases.

It is worth noting that the lattice parameter of (La, Y)H$_2$ is around 5.6 Å (see Table 6.11), which is far larger than that of YH$_2$ ($a$ = 5.21Å) but close to LaH$_2$ ($a$ = 5.67Å). Therefore, it should be a La-rich solid-solution (La, Y)H$_2$, in agreement with the fact that hydrogen induced disproportionation La$_2$Ni$_2$Mg and LaNi phases are La-rich.

Table 6.11 Phase abundance and crystallographic data obtained from Rietveld refinements for as-cast $Y_{0.7-x}La_xMg_{0.3}Ni_2$ ($x$ = 0.1, 0.2, 0.3) compounds upon four hydrogen absorption and desorption cycles.

| Sample | Phase | Phase abundance (±1%) | R-Bragg | Space group | Lattice parameters (Å) |
|---|---|---|---|---|---|
| La0.1<br>$R_p$ = 14.6<br>$R_{wp}$ = 9.97 | $A_2B_4$ | 77% | 4.30 | $F\bar{4}3m$ | $a$ = 7.0522 (2) |
| | $AB_3$ | 18% | 8.34 | $R\bar{3}m$ | $a$ = 4.9663 (6)<br>$c$ = 24.3690 (5) |
| | (La, Y)H$_2$ | 4% | | $Fm3m$ | $a$ = 5.6071 (9) |
| | LaYO$_3$ | 1% | | | |
| La0.2<br>$R_p$ = 15.3<br>$R_{wp}$ = 9.62 | $A_2B_4$ | 46% | 8.55 | $F\bar{4}3m$ | $a$ = 7.0512 (2) |
| | $AB_3$ | 48% | 6.19 | $R\bar{3}m$ | $a$ = 4.9643 (1)<br>$c$ = 24.2562 (1) |
| | (La, Y)H$_2$ | 5% | | $Fm3m$ | $a$ = 5.6332 (7) |
| | LaYO$_3$ | 1% | | | |
| La0.3<br>$R_p$ = 14.8<br>$R_{wp}$ = 11.4 | $A_2B_4$ | 41% | 3.42 | $F\bar{4}3m$ | $a$ = 7.0657 (3) |
| | $AB_3$ | 49% | 6.84 | $R\bar{3}m$ | $a$ = 4.9697 (2)<br>$c$ = 24.2360 (5) |
| | (La, Y)H$_2$ | 9% | | $Fm3m$ | $a$ = 5.6371 (6) |
| | LaYO$_3$ | 1% | | | |

To sum up, La0.2 and La0.3 compounds exhibit relative higher reversible hydrogen absorption capacities than La0.1 one, which deserve to be further studied. However, the Rietveld analysis of La0.3 compound indicates that larger amount of $AB_2$-type phase appeared, which suffers HIA and HID and leads to the capacity decay according to the studies shown in chapter 4. Meanwhile, the atomic radius ratio rule mentioned in chapter 2 suggests in Y-based $AB_2$-type alloys, the more La, the worse structural stability of $C$15-type $AB_2$ phase or [$A_2B_4$] unit in $AB_3$ phase. Therefore, the La0.2 compound was chosen for further studies. Furthermore, to eliminate the unstable phases such as $C$15-type $AB_2$, La$_2$Ni$_2$Mg and LaNi, and help the dissolution of La in $A_2B_4$ phases, the annealing treatment is essential.

### 6.2.2 Heat treatment effects on crystal structure and hydrogen sorption properties of $Y_{0.5}La_{0.2}Mg_{0.3}Ni_2$ compound

For La0.1 compound, the hydrogen absorption capacities are relatively low compared to other La contents. Meanwhile, the higher La content in La0.3 compound may induce the structural instability due to its large atomic radius. Therefore, $Y_{0.5}La_{0.2}Mg_{0.3}Ni_2$ compound was selected to study the effects of heat treatment on structural and hydrogen sorption properties.

Heat treatment of $Y_{0.5}La_{0.2}Mg_{0.3}Ni_2$ compound was performed at 700 ℃ and 900 ℃ for 8 h and 24 h respectively in a silica tube under Ar atmosphere (5N, pressure of 100 mbar). Powder samples < 150 μm were used for hydrogenation measurements. Initially the samples were activated at 400 ℃ under dynamic vacuum for 1h. Hydrogen absorption and desorption cycles were performed in a Sieverts-type apparatus under a starting hydrogen pressure 6 MPa at 25 ℃ for hydrogenation, then 1 h dynamic vacuum at 400 ℃ for dehydrogenation. PCI curves were also measured at 25 ℃ using the Sieverts' method.

#### 6.2.2.1 Chemical compositions

The global chemical compositions of the annealed samples measured by ICP-AES are listed in Table 6.12, for comparison the composition before annealing is also given. One can see that the La, Y content do not change, whereas Mg content is sensitive to the annealing temperature and time. The sample annealed at 700 ℃ for 8 hours does not present visible loss of magnesium, whereas sample annealed 24 h shows a decrease of Mg content. For samples annealed at 900 ℃, the loss of Mg is rather important, leading to stoichiometry *B*/*A* increase from the cast alloy of 2.04/1 to 2.48/1 and 2.59/1 for annealing time of 8 h and 24 h, respectively.

Indeed, the Mg loss during annealing is due to the experimental conditions. The as-cast samples were sealed in a silica tube in where the space is very large as compared to sample volume, and the inner pressure is negative. As a result, during annealing, partial Mg resides in the silica tube in the form of steam and condenses on the inside walls of the tube. Normally, the higher temperature, the more amount of Mg loss.

Table 6.12 Global compositions measured by ICP-AES for the as-cast and annealed $Y_{0.5}La_{0.2}Mg_{0.3-z}Ni_2$ compounds.

| Elements | Y (±0.01) | La (±0.01) | Mg(±0.01) | Ni(±0.01) | Composition | *B*/*A* |
|---|---|---|---|---|---|---|
| Target value | 0.50 | 0.20 | 0.30 | 2.00 | $Y_{0.50}La_{0.20}Mg_{0.30}Ni_2$ | 2.00 |
| Cast | 0.48 | 0.21 | 0.29 | 2.00 | $Y_{0.48}La_{0.21}Mg_{0.29}Ni_2$ | 2.04 |
| 700℃-8h | 0.49 | 0.19 | 0.31 | 2.00 | $Y_{0.49}La_{0.19}Mg_{0.31}Ni_2$ | 2.02 |
| 700℃-24h | 0.48 | 0.19 | 0.26 | 2.00 | $Y_{0.48}La_{0.19}Mg_{0.26}Ni_2$ | 2.13 |
| 900℃-8h | 0.47 | 0.19 | 0.15 | 2.00 | $Y_{0.47}La_{0.19}Mg_{0.15}Ni_2$ | 2.48 |
| 900℃-24h | 0.48 | 0.19 | 0.10 | 2.00 | $Y_{0.48}La_{0.19}Mg_{0.10}Ni_2$ | 2.59 |

### 6.2.2.2 Phase occurrence and structural properties

The XRD patterns of the as-cast and annealed $Y_{0.5}La_{0.2}Mg_{0.3-z}Ni_2$ compounds are shown in Figure 6.18. Numerous phases are indexed for the as-cast sample, including $AB_3$-type (Y, La, Mg)$Ni_3$ (space group $R\bar{3}m$), $A_2B_4$-type (Y, La, Mg)$_2Ni_4$ ($C15b$, space group $F\bar{4}3m$), $AB_2$-type (Y, La, Mg)$Ni_2$ ($C15$, space group $Fd\bar{3}m$), $La_2Ni_2Mg$ (space group $P4/mbm$) and LaNi (space group $cmcm$). Trace of $LaYO_3$ (space group $Ia\bar{3}$) is also observed in as-cast sample and 700 °C annealed samples. For samples annealed at 700 °C, all phases presented in as-cast sample transformed into $A_2B_4$-type (Y, La, Mg)$_2Ni_4$ phase and $AB_2$-type (Y, La, Mg)$Ni_2$ phase. By extending the heating time to 24 h, $AB_3$-type (Y, La, Mg)$Ni_3$ phase appears. For the samples annealed at 900 °C, the abundance of $AB_3$ phase increased while the amount of $A_2B_4$ phase decreased.

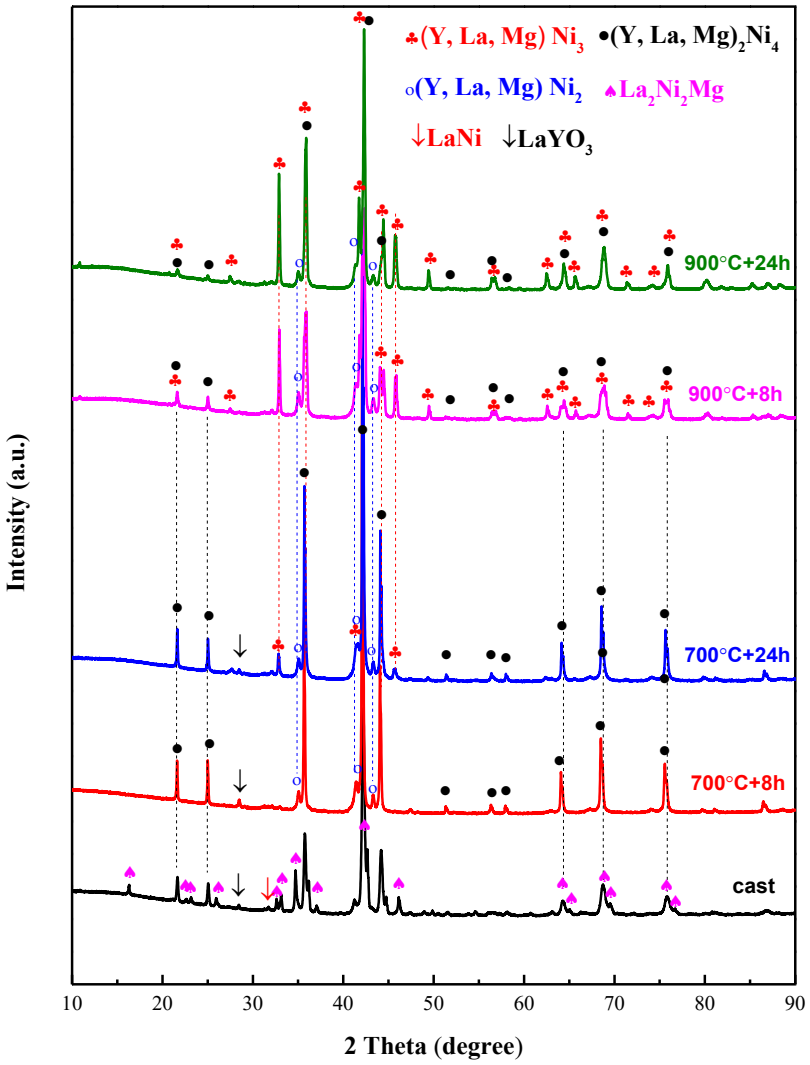


Figure 6.18 X-ray diffraction patterns of the as-cast and annealed samples.

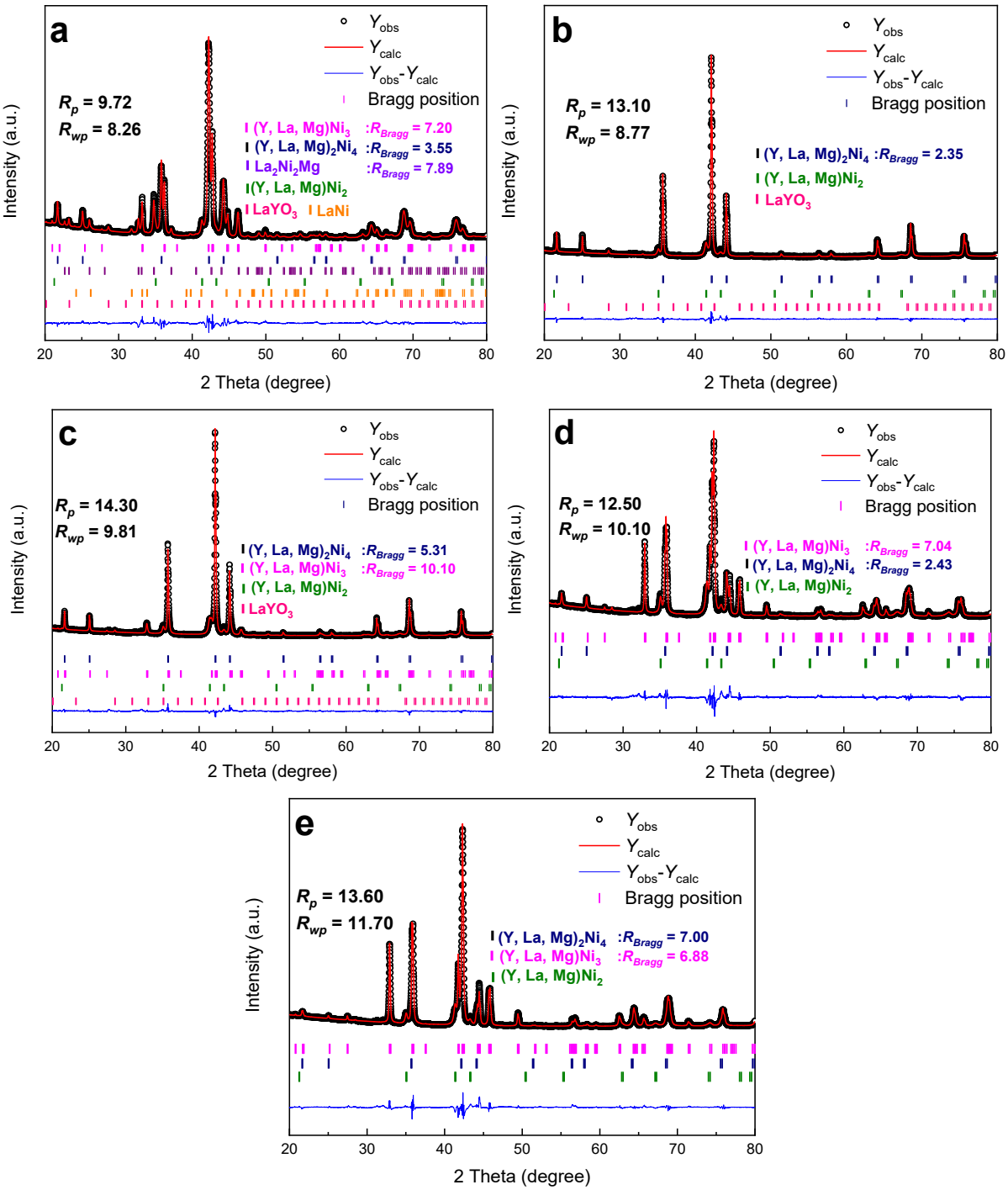


Figure 6.19 Rietveld refinements of the XRD patterns for $Y_{0.5}La_{0.2}Mg_{0.3-z}Ni_2$ compounds: a – as-cast, b – annealed at 700 °C for 8 h, c – annealed at 700 °C for 24 h, d – annealed at 900 °C for 8 h, e – annealed at 900 °C for 24 h.

The phase abundance and crystallographic data obtained from Rietveld analysis are given in Table 6.13, the Rietveld refinements of the XRD patterns are shown in Figure 6.19. With annealing time increases from 8 h to 24 h, $AB_3$ phase amount increases from zero to 25 wt.% for 700 °C and 50 wt.% to 82 wt.% for 900 °C. Whereas $A_2B_4$ phase amount decreases from 84 wt.% to 59 wt.% and 35 wt.% to 10 wt.%, respectively.

Upon heat treatment, one can observe there is little variation in the lattice parameters of $A_2B_4$ phases. Meanwhile, the lattice parameters of $AB_3$ phase increase significantly after annealing, especially the *c* parameter which increases from 24.2 Å (as-cast sample) to 24.4 Å (annealed samples). This can be due to the loss of Mg and increases of La content, and will be discussed later. $AB_2$ type (Y, La, Mg)$Ni_2$ phase with *C*15 structure shows larger lattice parameters 7.23 ~7.24 Å, than parent $YNi_2$ (*a* = 7.18 Å) compound [282].

Table 6.13 Crystallographic data from Rietveld refinement for as cast and annealed $Y_{0.5}La_{0.2}Mg_{0.3-z}Ni_2$ compounds.

| Sample | Phase | Compositions (EPMA) (±0.02) | Phase abundance (±1%) | Space group | Lattice parameters (Å) |
|---|---|---|---|---|---|
| Cast | (Y, La, Mg)$_2$Ni$_4$ | $Y_{0.53}La_{0.11}Mg_{0.31}Ni_2$ | 59% | $F\bar{4}3m$ | *a* = 7.0915 (1) |
| | (Y, La, Mg)$Ni_3$ | $Y_{0.73}La_{0.08}Mg_{0.18}Ni_3$ | 29% | $R\bar{3}m$ | *a* = 4.9637 (1)<br>*c* = 24.2467 (1) |
| | (Y, La, Mg)$Ni_2$ | $Y_{0.49}La_{0.35}Mg_{0.13}Ni_2$ | 3% | $Fd\bar{3}m$ | *a* = 7.2468 (4) |
| | $La_2Ni_2Mg$ | $La_{2.53}Ni_{2.55}Y_{0.1}Mg$ | 7% | $P_4/mbm$ | *a* = 7.6541 (4)<br>*c* = 3.9226 (1) |
| | LaNi | $La_{1.04}Y_{0.03}Mg_{0.01}Ni$ | 1% | *Cmcm* | *a* = 3.929 (2)<br>*b* = 10.8029 (6)<br>*c* = 4.3591 (3) |
| 700°C-8h | (Y, La, Mg)$_2$Ni$_4$ | $Y_{0.51}La_{0.16}Mg_{0.32}Ni_2$ | 84% | $F\bar{4}3m$ | *a* = 7.1098 (1) |
| | (Y, La, Mg)$Ni_2$ | $Y_{0.46}La_{0.35}Mg_{0.14}Ni_2$ | 15% | $Fd\bar{3}m$ | *a* = 7.2298 (2) |
| 700°C-24h | (Y, La, Mg)$_2$Ni$_4$ | ¬ | 59% | $F\bar{4}3m$ | *a* = 7.1032 (4) |
| | (Y, La, Mg)$Ni_3$ | ¬ | 25% | $R\bar{3}m$ | *a* = 5.0201 (2)<br>*c* = 24.4715 (1) |
| | (Y, La, Mg)$Ni_2$ | ¬ | 15% | $Fd\bar{3}m$ | *a* = 7.2278 (3) |
| 900°C-8h | (Y, La, Mg)$_2$Ni$_4$ | ¬ | 35% | $F\bar{4}3m$ | *a* = 7.1113 (2) |
| | (Y, La, Mg)$Ni_3$ | ¬ | 50% | $R\bar{3}m$ | *a* = 5.0075 (1)<br>*c* = 24.4144 (1) |
| | (Y, La, Mg)$Ni_2$ | ¬ | 15% | $Fd\bar{3}m$ | *a* = 7.2326 (4) |
| 900°C-24h | (Y, La, Mg)$_2$Ni$_4$ | $Y_{0.53}La_{0.16}Mg_{0.26}Ni_2$ | 10% | $F\bar{4}3m$ | *a* = 7.1120 (3) |
| | (Y, La, Mg)$Ni_3$ | $Y_{0.71}La_{0.26}Mg_{0.12}Ni_3$ | 82% | $R\bar{3}m$ | *a* = 5.0133 (1)<br>*c* = 24.4379 (1) |
| | (Y, La, Mg)$Ni_2$ | $Y_{0.54}La_{0.31}Mg_{0.11}Ni_2$ | 8% | $Fd\bar{3}m$ | *a* = 7.2401 (5) |

### 6.2.2.3 EPMA mapping analysis

The EPMA elemental mapping analysis of as-cast and one of annealed (900 °C + 24 h) samples is shown in Figure 6.20. For as-cast compounds, the chemical segregation is clear. La is mainly distributed in the $La_2Ni_2Mg$ and LaNi phases, whereas Mg prefer to go to in $A_2B_4$ and $La_2Ni_2Mg$ phases.

Upon annealing at 900 °C for 24 h, the element is distributed homogeneously, only that the Mg is mainly located in the $A_2B_4$ phases and less in $AB_3$ and $AB_2$ phase (Table 6.13). The homogeneous distribution of La and Y, can be the main raison for changes of lattice parameter of $AB_3$ phase before and after annealing.

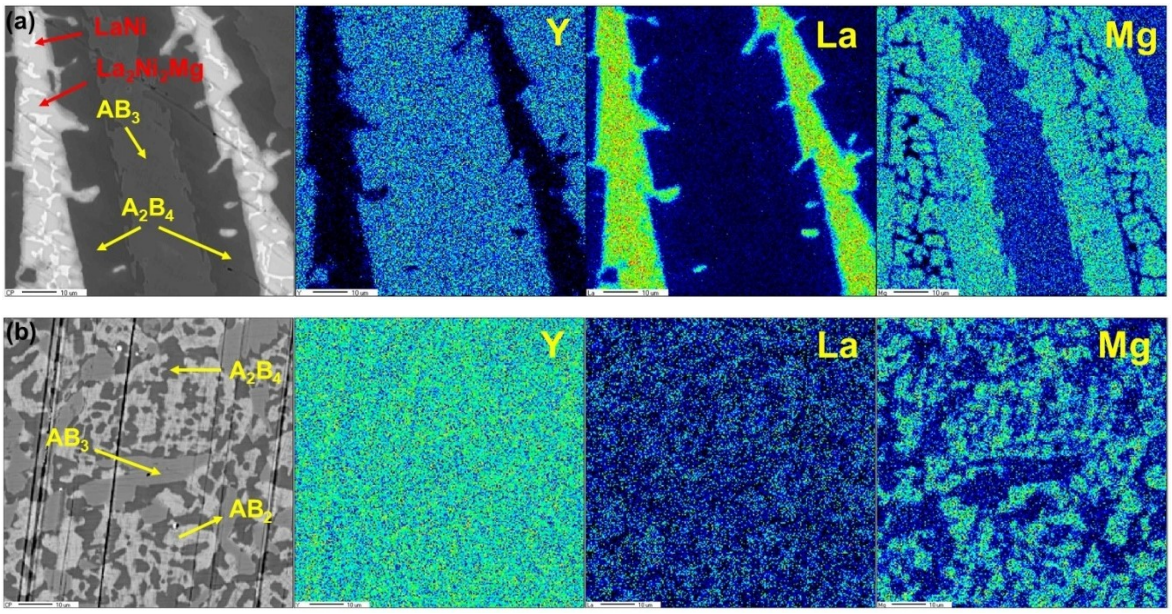


Figure 6.20 EPMA elemental mapping of as-cast (a) and annealed (900 °C + 24 h) samples (b).

For the sample annealed at 700 °C for 8 h, the final composition is very close to the target value, the samples containing in majority $A_2B_4$-type phase ($C15b$) $Y_{0.51}La_{0.16}Mg_{0.32}Ni_2$ (composition measured by EPMA, and small amount of $AB_2$-type ($C15$) $Y_{0.46}La_{0.35}Mg_{0.14}Ni_2$ phase. For sample annealed at 700 °C for 24 h, the Mg loss (ICP analyses, Table 1) leads to a stoichiometric deviation which prompts the formation of $AB_3$ phase. This effect is emphasized for samples annealed at 900 °C, as $AB_3$ phase ($Y_{0.71}La_{0.26}Mg_{0.12}Ni_3$) became the main phase with secondary $A_2B_4$ type ($C15b$) $Y_{0.53}La_{0.16}Mg_{0.26}Ni_2$ phase (900 °C + 24 h).

One can note that the lattice parameters of $A_2B_4$ phase are kept almost unchanged upon annealing, this agrees with its almost constant composition. Using Rietveld analyses, we found that Yttrium occupy simultaneously the 4*a* and 4*c* sites: 4*a* site is occupied by 40% La and 60% Y, whereas 4*c* site is occupied by 60% Mg and 40% Y. Such "mixed" site occupation has been reported in $Gd_yMg_{2-y}Ni_4$ ($0.4 < y < 2$) [215] and $CeMgNi_4$ [216] compounds, where the rare earth atoms occupy both the 4*a* and 4*c* sites with Mg. Also in $Mg_{2-x}RE_xNi_4$ ($x$ = 0.6, 1) compounds [274–276], Mg and RE occupy parallelly the 4*a* site. Even for the $YMgNi_4$

compound ($Y_{0.5}Mg_{0.5}Ni_2$), Y and Mg occupation is ordered: Y is on site 4*a* and Mg on site 4*c* [213,220,283]. Here we prove again, that the $A_2B_4$-type phases exhibit large composition range by adjusting the occupancy ratio on 4*a* and 4*c* sites.

For the $AB_3$ phase, La atoms prefer to occupy the 3*a* site inside the [$AB_5$] subunits while Mg atoms occupy 6*c* site inside the [$A_2B_4$] subunits, which agrees with the occupation of Mg in La-Mg-$Ni_n$ ($n$ = 3 - 4) system[87] and $Y_2MgNi_9$ compound [284].

### 6.2.2.4 Hydrogenation properties

***Reversible capacity***

The hydrogen absorption and desorption capacity versus cycle number of as-cast and annealed samples are shown in Figure 6.21. At room temperature, an initial hydrogen pressure around 6 MPa was given and waited until equilibrium with the final pressure around 4 MPa. The dehydrogenation was performed by heating the hydrogenated samples at 400 ℃ under dynamic vacuum for 1 h. The measured maximum and reversible capacities are summarized in Table 6.14. The gravimetric hydrogen absorption capacities of as-cast and annealed samples decay significantly after the first cycle, then stabilize at around the fourth cycle. It is worth noting that the samples annealed 8 h at 900 ℃ shows dramatically increased reversible capacity than the as-cast sample and a further increased reversible capacity with longer annealing time (24 h). The reversible capacity at $4^{th}$ cycle is as high as 1.63 wt.% for the sample annealed for 24 h at 900 °C. The samples annealed at 700 ℃ for both durations show similar reversible capacity of around 1.26 wt.%, lower than that of as-cast sample.

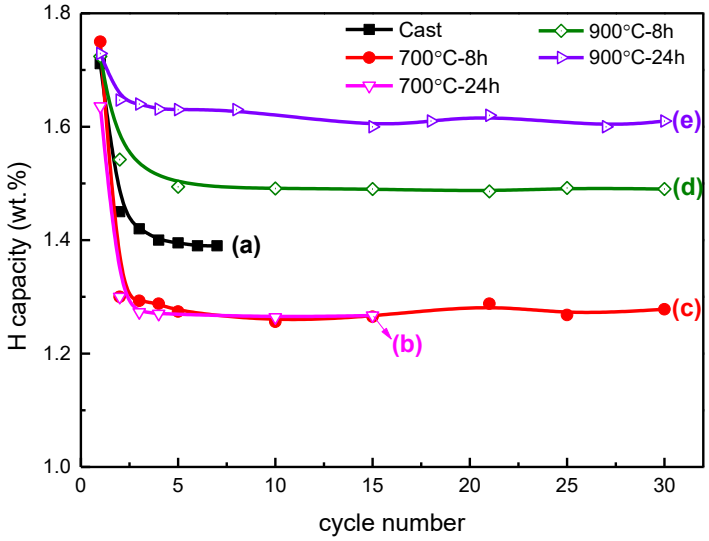


Figure 6.21 The hydrogen absorption capacity as function of cycle number for the as-cast and annealed $Y_{0.5}La_{0.2}Mg_{0.3-z}Ni_2$ compounds (hydrogenation conditions: $PH_2$ = 6 MPa, 25 ℃, dehydrogenation conditions: dynamic vacuum, 400 ℃).

Table 6.14 Cycle behavior for the hydrogen sorption capacity of the as-cast and annealed compounds.

| Sample | Composition | Maximum capacity $C_{1st}$ (wt.%) | Reversible capacity $C_{4th}$ (wt.%) |
|---|---|---|---|
| Cast | $Y_{0.48}La_{0.21}Mg_{0.29}Ni_2$ | 1.71 | 1.39 |
| 700°C-8h | $Y_{0.49}La_{0.19}Mg_{0.31}Ni_2$ | 1.75 | 1.26 |
| 700°C-24h | $Y_{0.48}La_{0.19}Mg_{0.26}Ni_2$ | 1.64 | 1.26 |
| 900°C-8h | $Y_{0.47}La_{0.19}Mg_{0.15}Ni_2$ | 1.72 | 1.49 |
| 900°C-24h | $Y_{0.48}La_{0.19}Mg_{0.10}Ni_2$ | 1.73 | 1.63 |

***Hydrogen-induced disproportionation***

The XRD patterns of dehydrogenated samples after hydrogenation cycling (see Figure 6.21a - e) have been analyzed and the detailed crystallographic data and phase abundance obtained from Rietveld refinement are listed in Table 6.15. As shown in Figure 6.22 and Figure 6.23, after dehydrogenation, the XRD patterns can be indexed with $A_2B_4$, $AB_3$ and (La, Y)$H_2$ phases, indicating a disproportionation reaction of the $AB_2$ phase upon hydrogen absorption and desorption cycles. For the sample annealed for 24 h at 700 °C, the broadening of the diffraction peaks yield large error of the determined phase abundance. For cycled sample, $A_2B_4$ and $AB_3$ phase remain as the major phase in samples annealed at 700 °C and 900 °C respectively. The lattice parameters of $A_2B_4$ phase show significant decrease as compared to the pristine alloy, the Rietveld analyses indicates the depopulation of La in the structure.

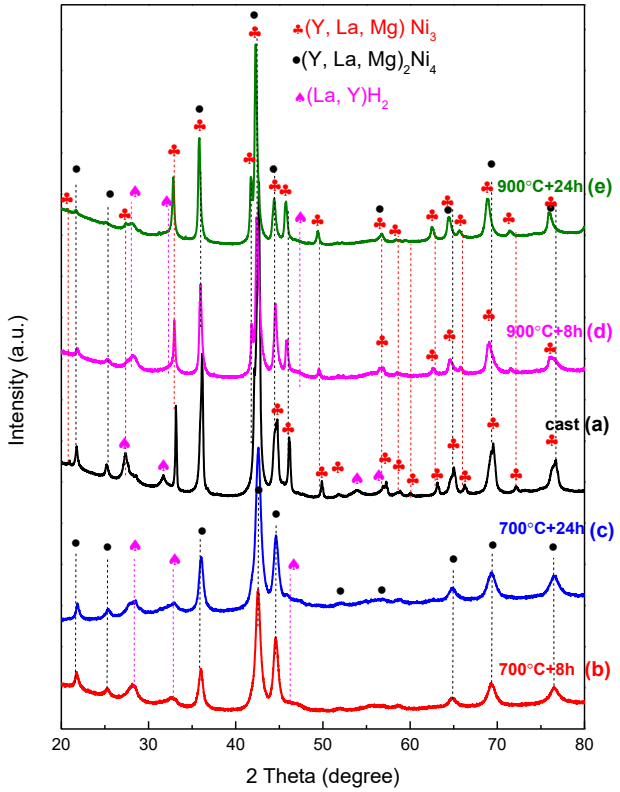


Figure 6.22 X-ray diffraction patterns of the as-cast (a) and annealed samples (b – e) upon hydrogenation and dehydrogenation cycles.

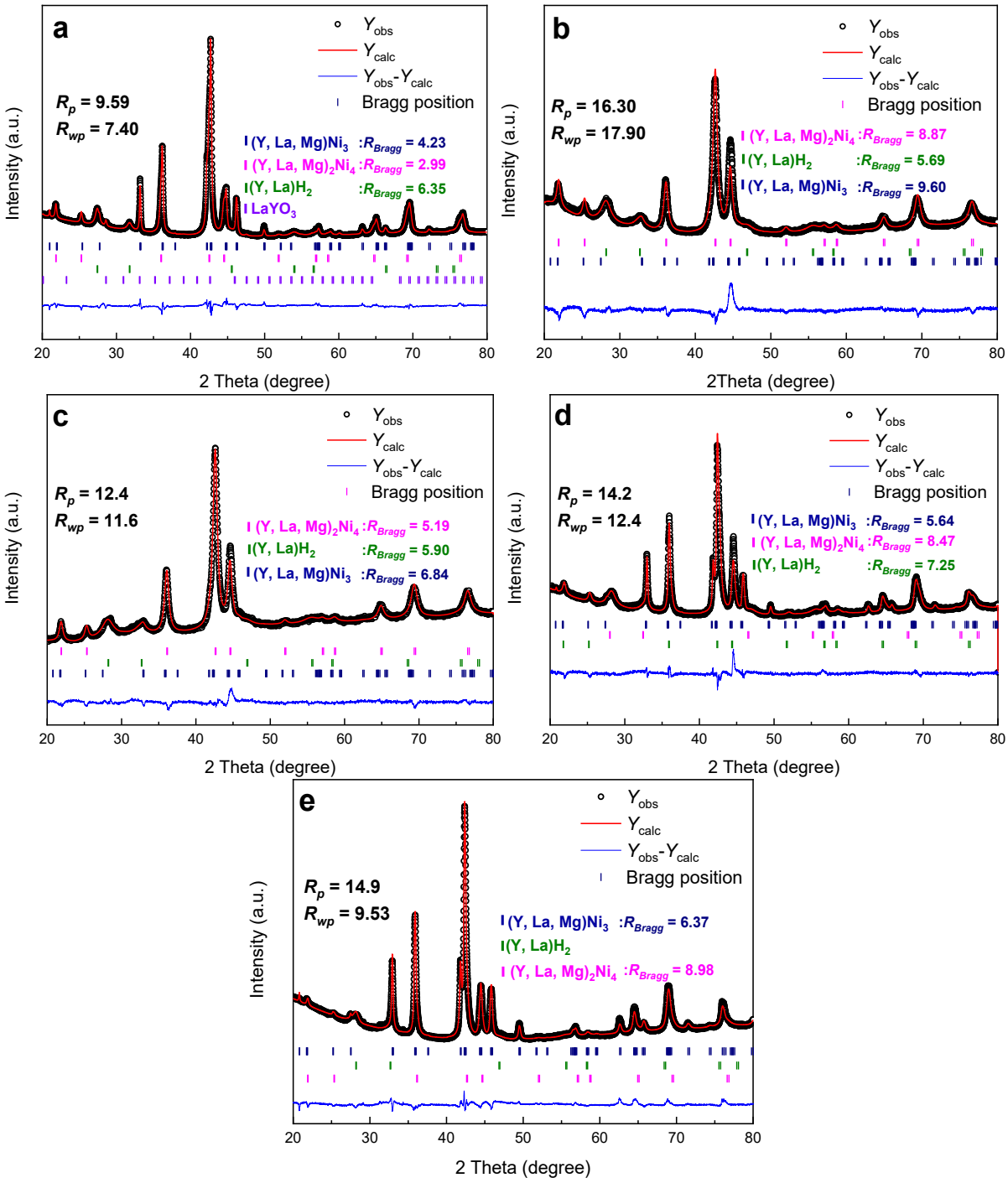


Figure 6.23 Rietveld refinements of the XRD patterns for the $Y_{0.5}La_{0.2}Mg_{0.3-z}Ni_2$ compounds upon hydrogenation and dehydrogenation cycles: a – as-cast, b – annealed at 700 °C for 8 h, c – annealed at 700 °C for 24 h, d – annealed at 900 °C for 8 h, e – annealed at 900 °C for 24 h.

Table 6.15 The refined lattice parameters of $Y_{0.5}La_{0.2}Mg_{0.3-z}Ni_2$ compounds after four hydrogen ab/desorption cycles: as-cast (a), annealed at 700 ℃ for 8 h (b), 24 h (c) and 900 ℃ for 8 h (d), 24 h (e).

| **Sample** | **Phase** | **Abundance (wt.%)** | **Lattice parameters (Å)** | |
|---|---|---|---|---|
| | | | ***a*** | ***c*** |
| Cast (a)<br>$R_p$ = 9.59<br>$R_{wp}$ = 7.40 | (Y, Mg)$_2$Ni$_4$ ($A_2B_4$, $F\bar{4}3m$) | 48 | 7.0512 (2) | |
| | (Y, La, Mg)Ni$_3$ ($AB_3$, $R\bar{3}m$) | 46 | 4.9643 (1) | 24.2563 (1) |
| | (La, Y)H$_2$ ($Fm\bar{3}m$) | 5 | 5.6332 (7) | |
| | LaYO$_3$ ($Ia\bar{3}$) | 1 | 10.818 (2) | |
| 700℃-8h (b)<br>$R_p$ = 16.8<br>$R_{wp}$ = 17.8 | (Y, Mg)$_2$Ni$_4$ ($A_2B_4$, $F\bar{4}3m$) | 80 | 7.0282 (6) | |
| | (Y, La, Mg)Ni$_3$ ($AB_3$, $R\bar{3}m$) | 7 | 5.007 (2) | 24.467 (4) |
| | (La, Y)H$_2$ ($Fm\bar{3}m$) | 13 | 5.484 (1) | |
| 700℃-24h (c)<br>$R_p$ = 11.7<br>$R_{wp}$ = 10.7 | (Y, Mg)$_2$Ni$_4$ ($A_2B_4$, $F\bar{4}3m$) | 79 | 7.0348 (6) | |
| | (Y, La, Mg)Ni$_3$ ($AB_3$, $R\bar{3}m$) | 10 | 5.006 (4) | 24.458 (4) |
| | (La, Y)H$_2$ ($Fm\bar{3}m$) | 11 | 5.484 (2) | |
| 900℃-8h (d)<br>$R_p$ = 16.8<br>$R_{wp}$ = 14.3 | (Y, Mg)$_2$Ni$_4$ ($A_2B_4$, $F\bar{4}3m$) | 45 | 7.0332 (5) | |
| | (Y, La, Mg)Ni$_3$ ($AB_3$, $R\bar{3}m$) | 46 | 5.0053 (3) | 24.412 (1) |
| | (La, Y)H$_2$ ($Fm\bar{3}m$) | 9 | 5.484 (1) | |
| 900℃-24h (e)<br>$R_p$ = 13.6<br>$R_{wp}$ = 9.57 | (Y, Mg)$_2$Ni$_4$ ($A_2B_4$, $F\bar{4}3m$) | 18 | 7.0290 (8) | |
| | (Y, La, Mg)Ni$_3$ ($AB_3$, $R\bar{3}m$) | 78 | 5.0057 (2) | 24.4237 (1) |
| | (La, Y)H$_2$ ($Fm\bar{3}m$) | 4 | 5.482 (3) | |

Consequently, the capacity decay is attributed to the hydrogen-induced disproportionation (HID) occurring for $AB_2$ type (Y, La, Mg)Ni$_2$ and $A_2B_4$ type (Y, La, Mg)$_2$Ni$_4$ phases. Commonly, $AB_2$ compounds for which the atomic radius ratio $r_A/r_B$ lies above 1.37 will be subjected to amorphization upon hydrogenation [201]. In our case, compositions of (Y, La, Mg)Ni$_2$ phases obtained by EPMA is $Y_{0.49}La_{0.35}Mg_{0.13}Ni_2$ (as-cast), $Y_{0.46}La_{0.35}Mg_{0.14}Ni_2$ (700 ℃+8 h) and $Y_{0.54}La_{0.31}Mg_{0.11}Ni_2$ (900 ℃+24 h) respectively, they crystallize in the $C15$ Laves phase structure with all $r_{(Y+La+Mg)}/r_{Ni}$ ratios locating at around 1.45, thus showing poor structural stability. Upon hydrogen absorption and desorption the diffraction peaks of (Y, La, Mg)Ni$_2$ phases cannot be detected, while stable hydride (Y, La)H$_2$ and $AB_3$ phase were formed.

For La-doped $A_2B_4$ phase (take the compound annealed at 700 ℃ with heating time 8 h, for example), the EPMA composition can be described as $(Y_{0.66}La_{0.32})(Y_{0.36}Mg_{0.64})Ni_4$ with the atomic size ratio $r_{(Y+La+Mg)}/r_{Ni}$ reach to 1.40, still higher than the empirical value 1.37. The XRD

shows that the new $A_2B_4$ phase formed after hydrogen absorption and desorption cycles has smaller lattice parameter compare to the initial compound and the Rietveld analyses show stoichiometric site occupation Mg at 4*c* site and Y at 4*a* site, which gives composition of $YMgNi_4$. This indicates that HID reaction $(Y_{0.66}La_{0.32})(Y_{0.36}Mg_{0.64})Ni_4H_x \Rightarrow YMgNi_4$ + (Y, La)$H_2$ occurred. So both the $YMgNi_4$ phase and $AB_3$ -type phase contribute to the reversible capacity.

Therefore, $AB_3$-type $Y_{0.71}La_{0.26}Mg_{0.12}Ni_3$ (78 wt.%) and $A_2B_4$-type $YMgNi_4$ (18 wt.%) phases contribute to the attractive reversible hydrogen absorption capacity of 1.63 wt.% for $Y_{0.48}La_{0.19}Mg_{0.10}Ni_2$ compound (900 °C+24 h). It will be worth to synthesis a double-phases compound ($YMgNi_4$ + $AB_3$) with non-stoichiometric compositions $AB_{3-y}$ for further investigation on their structure evolution and hydrogen sorption properties.

***Pressure Composition Isotherm***

After several cycles of full hydrogen absorption and desorption PCI were measured at 25 °C in $H_2$ pressure ranging from 0.0001 MPa to 10 MPa. Figure 6.24 shows the PCI curves of the as-cast and annealed $Y_{0.5}La_{0.2}Mg_{0.3-z}Ni_2$ compounds. The above Table 6.15 gathers the phase compositions of the samples.

All samples exhibit good reversibility at room temperature. For sample annealed at 900 °C for 8 h, two plateaus are identified, whereas a single sloppy plateau is found for the sample annealed 24 h at 900 °C (see the magenta and green line in Figure 6.24). For the samples annealed 24 h, there is ~ 80% $AB_3$ main phase and ~20% of $A_2B_4$ phases, so we can say that the PCI is dominated by the $AB_3$ phase. The sample annealed 8 h at 900 °C contains the same phase with different abundance, ~ 50% of $AB_3$ and ~ 50% of $A_2B_4$ phase, so the first plateau with equilibrium pressure is around ~0.02 MPa, which is roughly identical to the equilibrium pressures of the sample annealed 24 h contributed to $AB_3$ phase. The second plateau with equilibrium pressure around 0.3 MPa should be a contribution of $A_2B_4$ phase when compared to the PCI curves of samples annealed at 700 °C. This signature of $A_2B_4$ phase is the main contribution of samples annealed at 700 °C (main phase: $A_2B_4$)., The phase composition of the as-cast compound is very similar to that of samples annealed 8 h at 900 °C ($A_2B_4$ phase: 48 wt.%, $AB_3$ phase: 46 wt.%), whereas its PCI shows single plateau. One should notice that the lattice parameter of both phases is quite different compared to other samples: it is larger for $A_2B_4$ phase while it is smaller for $AB_3$ phase. We suppose that the plateau pressure of $AB_3$ phase is raised above 0.02 MPa and is lowered below 0.3 MPa for the $A_2B_4$ phase, so finally the sample gives one plateau with equal contribution of $A_2B_4$ and $AB_3$ phases.

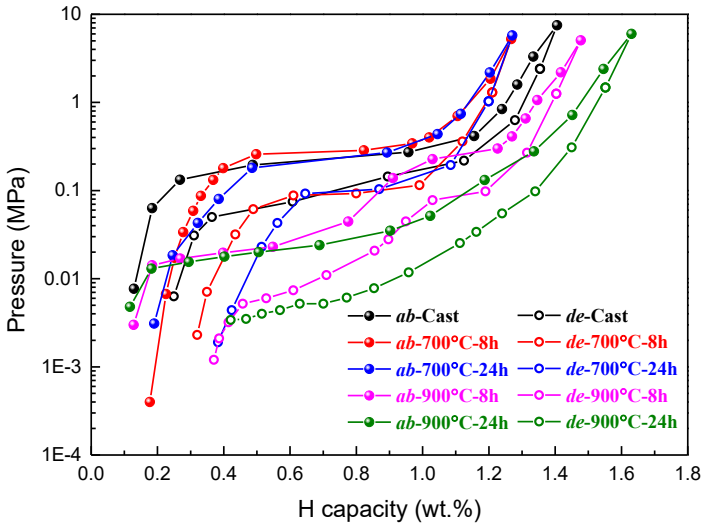


Figure 6.24 *P-C* isotherms measured at 25 °C for the as-cast and annealed $Y_{0.5}La_{0.2}Mg_{0.3-z}Ni_2$ compounds after several hydrogenation and dehydrogenation cycles.

## 6.2.3 Summary

The $Y_{0.7-x}La_xMg_{0.3}Ni_2$ compounds were synthesized and investigated. For the as-cast compounds, $A_2B_4$- and $AB_3$-type phases appear as the main phases. The abundance of $AB_3$ phase increases with increasing La content. $Y_{0.5}La_{0.2}Mg_{0.3}Ni_2$ compound has the maximum reversible hydrogen absorption capacity of 1.44 wt.%. The reversible capacities come from $A_2B_4$- and $AB_3$-type phases. The capacity decay is attributed to the hydrogen induced amorphization or disproportionation of *C*15-type $AB_2$ phase and La-rich, $La_2Ni_2Mg$ and LaNi phases.

The effects of heat treatment and Mg evaporation on phase occurrence, crystal structures and hydrogen sorption properties of $Y_{0.5}La_{0.2}Mg_{0.3-z}Ni_2$ compounds have been investigated. It can be concluded that the annealing temperature of 700 °C could boost the formation of $A_2B_4$ $(Y, La, Mg)_2Ni_4$ phase, the Mg loss during annealing leads to the formation of La-doped $AB_3$ phase.

The substitution of La raised the atomic-size ratio $r_A/r_B$, resulting in a hydrogen induced disproportionation of *C*15*b*-type $A_2B_4$ and *C*15-type $AB_2$ phases upon hydrogen absorption and desorption. New $A_2B_4$ phases with more Mg proportion (close to $YMgNi_4$) prefer to form upon HID. The $Y_{0.48}La_{0.19}Mg_{0.10}Ni_2$ compound shows reversible hydrogen absorption capacity of 1.63 wt.%. $AB_3$-type $Y_{0.71}La_{0.26}Mg_{0.12}Ni_3$ and $A_2B_4$-type $YMgNi_4$ phases contribute to the reversible capacity. The double-phase compounds ($AB_3$ + $YMgNi_4$) with non-stoichiometric compositions ($AB_{3-y}$) then will be investigated.

## 6.3 Hydrogen sorption properties of $AB_{3-y}$ compounds

### 6.3.1 Synthesis of the (Y, La, Mg)$_{0.67+x}$Ni$_2$ compounds

The $Y_{0.27+x}La_{0.25}Mg_{0.15}Ni_2$ compounds ($x$ = 0.03, 0.05, 0.08) were synthesized by induction melting in high purity argon atmosphere (5N) under a pressure of 0.04 MPa in a water-cooled copper crucible. Precursor Y-La-Ni alloys was prepared firstly by induction melting for Y, La and Ni metals (purity ≥ 99.9%, from Trillion Metals Co.,Ltd.), the ingot was turned over and re-melted three time to insure their homogeneity. Then, as-cast $Y_{0.27+x}La_{0.25}Mg_{0.15}Ni_2$ ingots were cracked into powder with sizes below 150 μm. The powder was then mixed with Mg powder (calculated according to the designate compositions) thoroughly and pressed into tablets. The prepared tablets were annealed at 850 ℃ under argon atmosphere for 3 days to obtain the uniformity of microstructure and distribution of compositions.

### 6.3.2 Structural characteristics

The XRD patterns and Rietveld analysis of the three $AB_{3-y}$ compounds are shown in Figure 6.25. The global compositions measured by ICP and crystallographic data from Rietveld refinement are summarized in

Table 6.16. The ICP results indicate that Mg was partially lost during sample preparation: the real compositions and stoichiometric ratios are $AB_{3.04}$, $AB_{2.90}$ and $AB_{2.79}$ respectively. The two phases $AB_3$ (main) and $YMgNi_4$ (secondary) were observed in all compounds. With the increase of stoichiometry ratios ($AB_{2.79}$ to $AB_{3.04}$), the abundance of $AB_3$ phases increased, whereas $YMgNi_4$ phase decreased. The lattice parameters $a$ of $YMgNi_4$ compounds are a bit larger than in literature [213,220] ($a$ = 7.01 Å), and increases slightly with the increasing Y content. This means Y may partially occupy the 4$c$ site or that La substitution for Y occurred in $YMgNi_4$ phases. As for $AB_3$ phases, their lattice parameters $c$ increased with the Y content and decreasing stoichiometric ratios ($AB_{3.04}$ to $AB_{2.79}$).

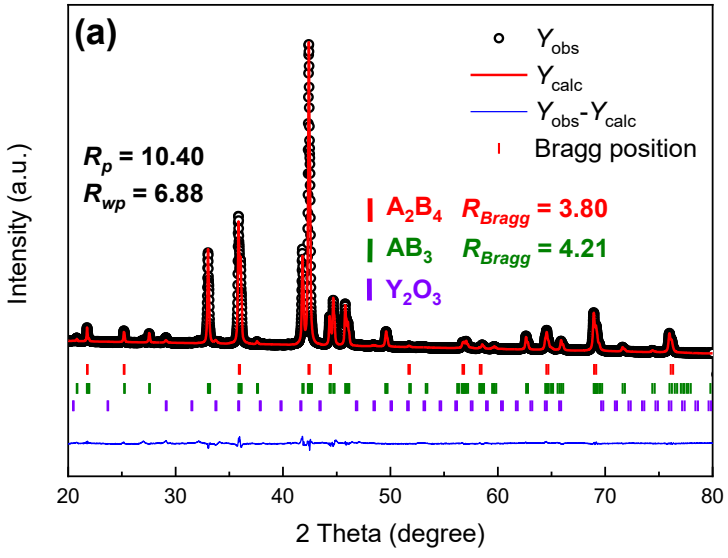

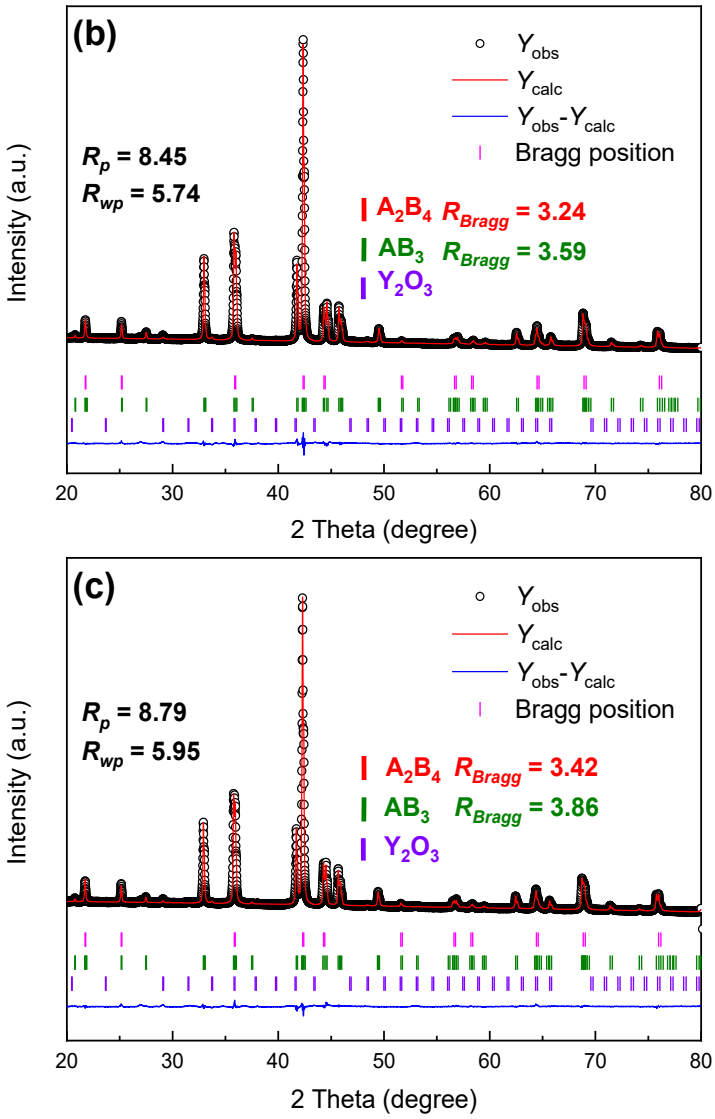


Figure 6.25 Rietveld refinements of the XRD patterns for the nominal $AB_{2.67}$ (a), $AB_{2.78}$ (b) and $AB_{2.86}$ (c) compounds.

Table 6.16 Global compositions measured by ICP and crystallographic data from Rietveld refinement.

| Compositions | | Phase occurrence | | Space group | Lattice parameters (Å) | | Cell volume $V$ (Å$^3$) |
|---|---|---|---|---|---|---|---|
| Designated | ICP | Phase | Abundance (±1%) | | $a$ | $c$ | |
| $x$ = 0.03 | $Y_{0.28}La_{0.23}Mg_{0.14}Ni_2$ | $AB_3$ | 91% | $R\bar{3}m$ | 5.0062 (1) | 24.3216 (1) | 527.89 (1) |
| $AB_{2.86}$ | $AB_{3.04}$ | $YMgNi_4$ | 8% | $F\bar{4}3m$ | 7.0698 (1) | | 353.36 (1) |
| | | $Y_2O_3$ | 1% | $Ia\bar{3}$ | | | |
| $x$ = 0.05 | $Y_{0.30}La_{0.24}Mg_{0.15}Ni_2$ | $AB_3$ | 80% | $R\bar{3}m$ | 5.0016 (1) | 24.3638 (1) | 529.949 (1) |
| $AB_{2.78}$ | $AB_{2.90}$ | $YMgNi_4$ | 19% | $F\bar{4}3m$ | 7.0726 (1) | | 353.789 (1) |
| | | $Y_2O_3$ | 1% | $Ia\bar{3}$ | | | |
| $x$ = 0.08 | $Y_{0.33}La_{0.24}Mg_{0.15}Ni_2$ | $AB_3$ | 77% | $R\bar{3}m$ | 5.0173 (1) | 24.4082 (1) | 532.119 (8) |
| $AB_{2.67}$ | $AB_{2.79}$ | $YMgNi_4$ | 22% | $F\bar{4}3m$ | 7.0797 (1) | | 354.852 (8) |
| | | $Y_2O_3$ | 1% | $Ia\bar{3}$ | | | |

## 6.3.3 Hydrogen sorption properties

### 6.3.3.1 Hydrogen absorption cycles

The kinetic curves measured at 25 ℃ of $AB_{3-y}$ compounds are shown in Figure 6.26. The hydrogen absorption was carried out with the initial hydrogen pressure of around 6 MPa, then the pressure will decrease to around 3.5 MPa and the maximum hydrogen absorption capacities were reached. The hydrogen desorption process was conducted under dynamic vacuum at 400 ℃. All three compounds could reach the equilibrium pressures in 2 min, showing modest kinetic properties. Most notably, they all exhibit perfect structural stability without capacity decay upon four hydrogen absorption and desorption cycles, among which $AB_{3.04}$ has the maximum reversible capacity of 1.69 wt.%. Meanwhile, the hydrogen absorption capacities decrease with the decreasing stoichiometric ratios, *i.e.*, the reduction of $AB_3$ phase abundance.

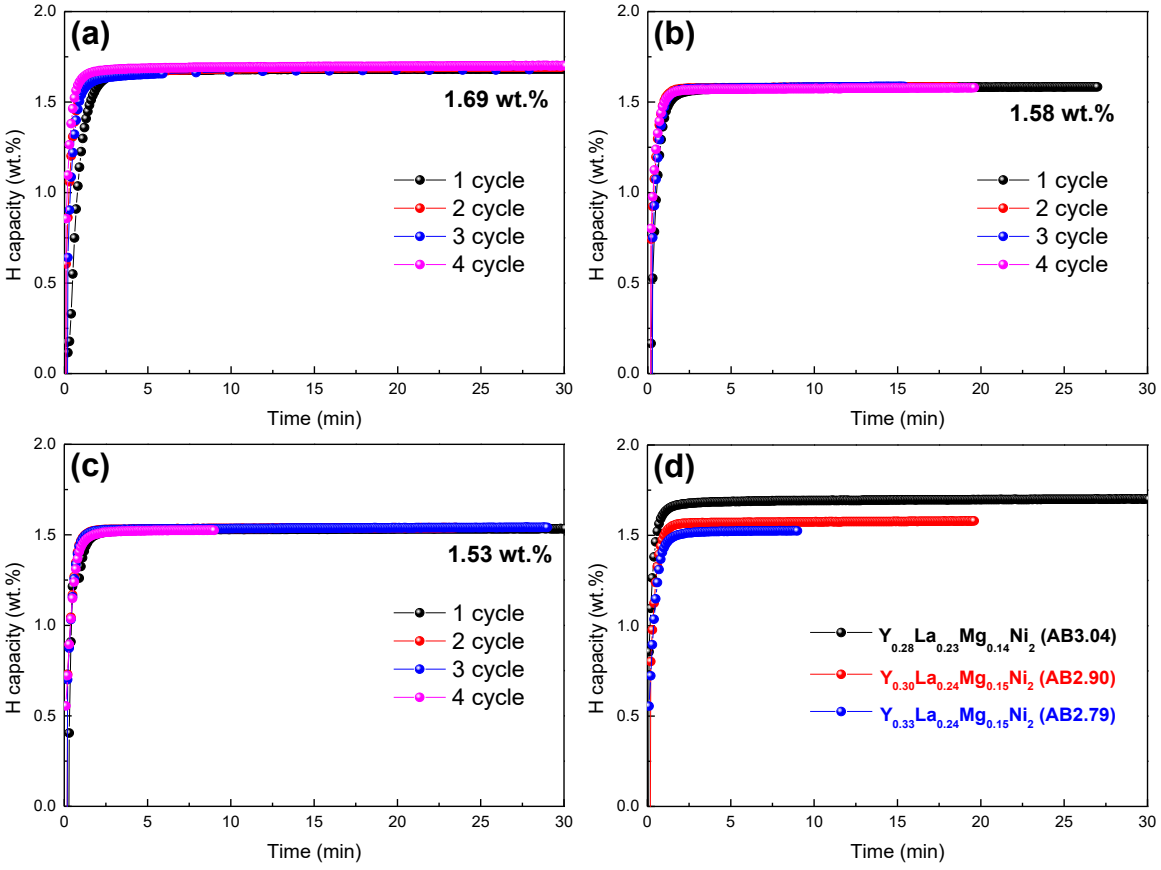


Figure 6.26 Kinetic curves measured at 25 ℃ of $AB_{3.04}$ (a), $AB_{2.90}$ (b) and $AB_{2.79}$ (c) compounds. (d) is the comparison of the fourth cycles of $AB_{3-y}$ compounds.

After the activation by four hydrogen absorption and desorption cycles, the PCI curves of $AB_{3-y}$ compounds were measured at 60 ℃. As shown in Figure 6.27, their hydrogen absorption plateaus are flat, their plateau pressures decrease sensibly with decreasing stoichiometry. This correlation should be related to the lattice parameter of $AB_3$ phase, which increases very slightly with decreasing stoichiometry due to the composition. The sloppy hydrogen desorption curve should be due to a gradient of composition. It is worth noting that the hysteresis of $AB_{3.04}$

compound is smaller than for the other two compounds. This can be attributed to the contribution of high-abundance $AB_3$ phases: $AB_{2.90}$ and $AB_{2.79}$ compounds containing 19 wt.% and 22 wt.% of $YMgNi_4$ phase, and showing similar hydrogen desorption processes. Despite the sloping desorption plateaus and large hysteresis, the hydrogen can be almost entirely released at 60 ℃. The equilibrium pressures of hydrogenation are modest ranging from 0.1 MPa to 0.3 MPa (at 25 ℃ it will be lower), whereas the hydrogen desorption pressures will be relatively low (below 0.01 MPa) at 25 ℃, which limits their practical application.

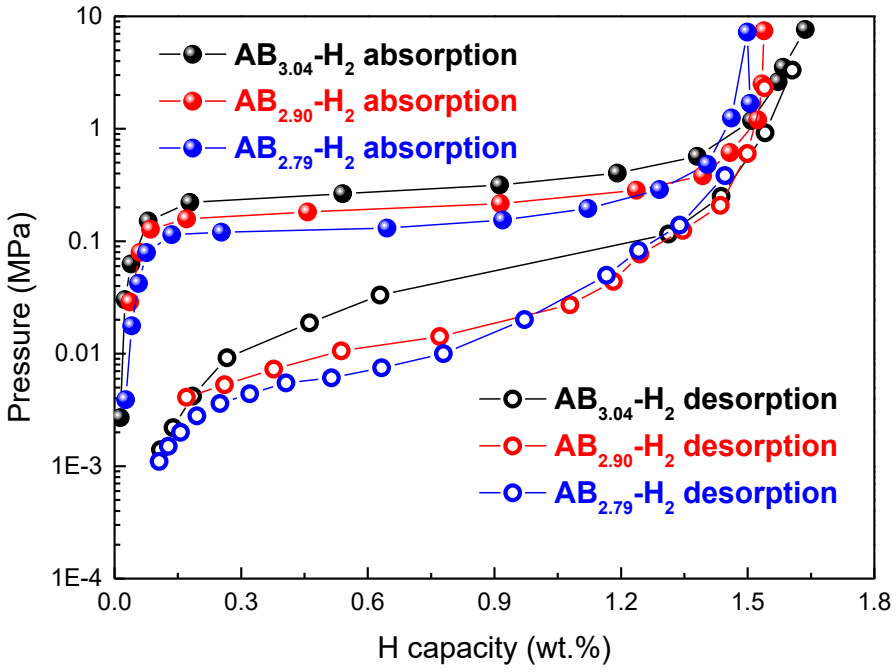


Figure 6.27 PCI curves measured at 60 ℃ of $AB_{3.04}$, $AB_{2.90}$ and $AB_{2.79}$ compounds.

For further optimization, modifying the proportion of Y, La and Mg on *A* side or by additional *B*-side substitution may improve the hydrogen desorption plateaus. Meanwhile, higher capacity and better cycling stability are expected.

## 6.4 Conclusion

In this chapter, the structural and hydrogen sorption characteristics of $Y_{0.7}Mg_{0.3}Ni_{2-y}Al_y$ ($0.05 \leq y \leq 0.25$) and $Y_{0.7-x}La_xMg_{0.3}Ni_2$ ($0.1 \leq x \leq 0.3$) compounds were systematically investigated. The structural stability of $A_2B_4$-type $(Y, Mg)_2Ni_4$ phase could be further enhanced by Al substitution, and the HIA was suppressed. The hydrides of $A_2B_4$ phases in our cases turn from crystalline into microcrystalline structural state upon increasing hydrogen concentration. Then, the microcrystal with hydrogen could revert to $A_2B_4$-type *C*15*b* structure upon hydrogen desorption by heating to more than 400 ℃. Further, all the rearranged $A_2B_4$-type $(Y, Mg)_2Ni_{4-y}Al_y$ or $(Y, La, Mg)_2Ni_4$ phases show a lower occupation ratio of Y at 4*c* site than parent compounds. The doping of La in $A_2B_4$ phase worsen the structural stability and contributes to the occurrence of hydrogen induced disproportionation. Even so, the La doping and heat

treatment generated a mixture of $AB_3$ (main phase) and $YMgNi_4$ phases, which exhibit reversible hydrogen absorption capacity of 1.63 wt.%.

Finally, $Y_{0.43}La_{0.36}Mg_{0.21}Ni_{3.04}$ ($AB_{3.04}$), $Y_{0.44}La_{0.34}Mg_{0.22}Ni_{2.9}$ ($AB_{2.90}$), $Y_{0.46}La_{0.33}Mg_{0.20}Ni_{2.78}$ ($AB_{2.79}$) have been synthesized. They all contain mixture of $AB_3$ (main phase) and $YMgNi_4$ (secondary phase). The maximum reversible hydrogen absorption capacity is around 1.69 wt.% with good cycling stability. With the stoichiometric ratio varying from $AB_{2.78}$ to $AB_{3.04}$, the plateau pressures at 25 ℃ increase from 0.02 MPa to 0.08 MPa. These compounds present interesting hydrogen storage properties for practical application.

# 7 General discussion and conclusions

In this chapter, I synthesize the results obtained with *A*- and *B*-side substitution in $YNi_2$ alloy and give a general discussion. First studies in $AB_2$ compounds (*A* = rare earth, *B* = transition metals) reported that, besides some alloys crystallizing in $MgZn_2$ type *C*14 structure or $MgNi_2$-type *C*36 structure, most of them crystallize in $MgCu_2$-type structure with $Fd\bar{3}m$ space group, which can also be described as *C*15 Laves phase structure [117]. However, recent works show that the latter do not crystallize in the *C*15 Laves structure but either in a tetragonal $La_7Ni_{16}$-type or cubic $TmNi_2$-type structure [119,123]. Atomic size factor and electron concentration are the two main factors affecting not only the formation of the Laves type intermetallic but also their hydrogenation properties. This is in line with the subject of this thesis playing with the atomic radius ratio $r_A/r_B$ of $YNi_2$ by different element substitution. The empirical rule of atomic radius ratio ($r_A/r_B = 1.37$) determining HIA occurrence is discussed when combining either *A* or *B*-side substitution effects.

## 7.1 Structural properties

As overviewed in chapter 2, we are trying to reduce the atomic radii ratio $r_A/r_B$ compared to that of $YNi_2$. Al ($r_{Al} = 1.43$ Å) and Mn ($r_{Mn} = 1.35$ Å) are chosen as *B*-side substituted elements due to their larger atomic radius than Ni ($r_{Ni} = 1.24$ Å).

$YNi_2$ displays a deviation from ideal 1:2 stoichiometry with $Y_{0.95}Ni_2$ composition, crystalizing in the cubic $TmNi_2$-type structure which can be described as a superstructure of *C*15 type structure with 5 % Y vacancies, a doubling of lattice parameter *a*, described in lower symmetric space group $F\bar{4}3m$. Al or Mn for Ni substitution, forming $Y(Ni, Al)_2$ and $Y(Ni, Mn)_2$ phases, stabilize the *C*15-type Laves phase structure with disordered Y vacancies. Indeed, the substitution of Ni by Al and Mn reduces the atomic radius ratio, increases the lattice parameter, and probably brings an electronic effect. As a result, the formation of *C*15-type Laves phase structure with disordered vacancies is favored against the superstructure one. In both cases, even if $YAl_2$ and $YMn_2$ both crystallize in *C*15-structure, a limit of solubility is found in $YNi_{2-x}Al_x$ and $YNi_{2-y}Mn_y$ pseudo-binary compounds with $x \approx 0.11$ and $y \approx 0.40$ respectively.

In the case of Mn substitution, the *C*15 structure forms with a decrease of *A*:*B* ratio from 0.90:2 to 0.825:2 for Mn0.1 and Mn0.3, respectively, by considering Mn located on *B* side only. Neutron Powder Diffraction (NPD) and Density Functional Theory (DFT) calculation studies showed that at low Mn content the *A*-site vacancies stabilize the *C*15 structure, whereas with increasing of Mn content the Y vacancies disappear and Mn substitute partially to Y on *A*-site.

Both Mg ($r_{Mg} = 1.60$ Å) and Sc ($r_{Sc} = 1.64$ Å) are elements with much smaller atomic radius than Y ($r_Y = 1.80$ Å), consequently their substitution for Y drastically reduce the atomic radius ratio. As a result, the HIA was suppressed.

Different from *B*-side substituted elements, Mg and Sc distribute on Y sites showing solid solubility of $x = 0.6$ in $Y_{1-x}Mg_xNi_2$ and $x = 0.9$ in $Y_{0.9-x}Sc_xNi_{1.9}Mn_{0.1}$ compounds. The single *C*15*b*-type $A_2B_4$ phase in Mg-containing compounds and *C*15-type $AB_2$ phase in Sc-containing compounds were obtained [269,285]. From the literature [125,127], the formation of La and Y vacancies in superstructure $LaNi_2$ and $YNi_2$ allows the relaxation of the strains caused by La-La and Y-Y compression, thus the enthalpy of formation is lowered. Mg and Sc, as compared to Y, have much smaller atomic sizes. So, their substitution at Y-site show similar effects to vacancy formation. This helps to release the stress caused by compressed Y atoms and favors structural stability.

The difference between Mg and Sc-substituted $AB_2$ compounds is mainly reflected in their structures. Partial substitution of Mg for Y in $Y_{1-x}Mg_xNi_2$ causes the formation of *C*15*b*-type Laves phase structure with space group $F\bar{4}3m$. When $x < 0.5$, part of the Y atoms occupy Mg sites, when $x > 0.5$, part of Mg atoms occupy the Y sites. For $x = 0.5$, Y and Mg only occupy 4*a* and 4*c* sites, respectively, forming the ordered $YMgNi_4$ compound [213].

Sc substitution for Y in $Y_{0.9-x}Sc_xNi_{1.9}Mn_{0.1}$ is able to maintain the pristine *C*15-type Laves phase structure with space group $Fd\bar{3}m$ for the whole substitution region [286]. With the increase of Sc amount, the vacancies on Y site gradually decrease and disappear for Sc amount $x \geq 0.45$, even when Ni-site vacancies form in $Sc_{0.9}Ni_{1.9}Mn_{0.1}$, which is already reported [270]. To sum up, *A*-side elements Sc and Mg can substitute Y in a large solubility range without the appearance of secondary phases. This is accompanied by a drastic decrease of the atomic radius ratio and the structural stability is enhanced.

By simultaneous substitution on *A*- and *B*-sides, the solubility domains change. In $Y_{0.7}Mg_{0.3}Ni_{2-y}Al_y$ compounds, we can observe that by the incorporation of *A*-side substituted elements (Mg), the limit of solubility of *B*-side elements increases. For example, the solubility of Al in the $Y(Ni_{2-x}Al_x)$ system is $x = 0.11$, while $Y_{0.7}Mg_{0.3}Ni_{1.85}Al_{0.15}$ (*i.e.*, $x = 0.15$) exhibits a single *C*15*b*-type Laves phase structure.

## 7.2 Hydrogenation properties

As discussed in chapter 2, HIA limits the use of $AB_2$ compounds for hydrogen storage application. However, Al and Mn substitutions do not prevent the occurrence of HIA and they show only modest improvement in hydrogen absorption capacity and kinetic properties. This can be interpreted by considering the empirical atomic radius ratio rule, and the solubility limit of Al in $YNi_{2-x}Al_x$ with $x \approx 0.11$. The atomic radius ratio $r_Y/r_{Ni+Al} = 1.44$ is still high for attaining high reversible hydrogen absorption due to amorphization.

It's worth noticing that the experimental maximum anti-site occupation of Mn shown in $Y_{0.825}Ni_{1.7}Mn_{0.3}$ compound yields by NPD the composition $Y_{0.87}Mn_{0.13}Ni_{1.79}Mn_{0.21}$. Its atomic radius ratio is $r_{Y+Mn}/r_{Ni+Mn} = 1.39$, approaching the limit of 1.37. Although HIA may still

occur, the anti-site occupation decreases the atomic radius ratio markedly. It would be expected that for higher Mn contents, the atomic radius ratio may further decrease below 1.37, but unfortunately the *C*15 phase is not stable for Mn content higher than 0.40. Surprisingly, we observed a crystalline phase for $Y_{0.9}Ni_{1.9}Mn_{0.1}$ compound upon both hydrogen absorption or desorption, whereas HIA occurred for $Y_{0.9}Ni_{1.8}Mn_{0.2}$ and $Y_{0.9}Ni_{1.7}Mn_{0.3}$ compounds. This could be explained by the fact that the high-rate Y-site vacancies for $Y_{0.9}Ni_{1.9}Mn_{0.1}$ makes the atomic size ratio as low as $r_{Y+\square}/r_{Ni+Mn} = 1.29$, which make it more stable regarding hydrogenation.

The Mg and Sc substitution for Y brings not only the enhanced structural stability but also large lattice contraction. Therefore, with increasing Sc and Mg content, higher equilibrium pressures for hydrogen absorption are observed which also leads to a limited reversible capacity at ambient condition for moderate pressures (below 100 bar).

These results clearly demonstrate that it is difficult to reconcile the structural stability with hydrogen absorption capacity in $RNi_2$ intermetallic compounds. By *B*-site substitution, the limit of solubility of Al and Mn in *C*15 structure is limited to 0.11 and 0.4, respectively. The atomic radii ratio can be reduced only to a certain extent. The HIA or HID are still present for pseudo-binary compounds. By *A*-site substitution, we reduce the lattice parameter by using Mg and Sc, which leads to an increase of the plateau pressure. To further enhance the structural stability of $YNi_2$ compound by *A*-side elements substitution while limiting the subsequent increase of equilibrium pressure, future research directions were focused on multi-element substitution on *A* and *B* sides.

It is worth noticing that the hydrogen sorption behaviors of $Y_{0.7}Mg_{0.3}Ni_{2-y}Al_y$ compounds are somewhat different from HIA process. The $Y_{0.7}Mg_{0.3}Ni_{2-y}Al_y$ ($0.10 \leq y \leq 0.25$) compounds (EPMA *C*15*b* phase compositions from $Y_{0.71}Mg_{0.32}Ni_{1.91}Al_{0.09}$ to $Y_{0.70}Mg_{0.33}Ni_{1.78}Al_{0.22}$) have the atomic radius ratios $r_{Y+Mg}/r_{Ni+Al}$ ranging from 1.392 to 1.377. The hydrogenation process indicates that with the increase of Al content, the *C*15*b*-type structures become more stable and effective to suppress HIA (see the hydrides of each compound). Even so, after hydrogen absorption at 150 ℃ during PCT measurements, the diffraction peaks of hydrides drastically broaden for all compounds, probably due to the hydrogen solution along the β-hydride branch. Upon hydrogen desorption by heating samples to 600 ℃, only a small quantity of $YH_2$ appeared, confirming that the structural stability resisting to HIA was enhanced.

The most important contribution of *B*-side substituting elements is to optimize hydrogen absorption plateaus. The partial substitution of Ni by Al or Mn in $LaNi_{5-y}Al_y$ [61] and $LaNi_{5-y}Mn_y$ [255] compounds, respectively, leads to a large decrease of the plateau pressures and an increase of the structural stability of the related hydrides. For either ternary $YNi_{2-x}Al_x$ and $Y_xNi_{2-y}Mn_y$ compounds or in quaternary $Y_{0.7}Mg_{0.3}Ni_{2-y}Al_y$ compounds, both Al and Mn substitutions show similar effects. For Mg-substituted compounds with *C*15*b*-type structure, *B*-

side substitutions such as Mn, Fe and Co will be worth studying to optimize the structural stability and hydrogen sorption properties.

The La substitution for Y leads to the formation of various phases, including $A_2B_4$-, $AB_3$-, $AB_2$-type and some La-rich phases. Heat treatments for different temperatures and duration reduced the amount of secondary phases and contributed to La homogenisation. The annealing temperature of 700 °C favored the formation of $A_2B_4$ (Y, La, Mg)$_2$Ni$_4$ phase. However, the substitution of La raised the atomic radius ratio $r_{Y+La+Mg}/r_{Ni}$, making the $C15b$ structure to lose its stability, resulting in the occurrence of HIA and HID. Contrary to the YNi$_{2-x}$Al$_x$ and Y$_x$Ni$_{2-y}$Mn$_y$ systems, the formed stable hydride after HID is (La, Y)H$_2$ rather than YH$_2$. Meanwhile, new $A_2B_4$ phases enriched in Mg (close to YMgNi$_4$) prefer to form after HID. This suggests that La substitution for Y contraries to the atomic-size rule. Increasing the amount of Mg or adding Al or Mn at *B*-side may compensate the negative effects caused by La.

Finally, quaternary Y$_{0.43}$La$_{0.36}$Mg$_{0.21}$Ni$_{3.04}$ ($AB_{3.04}$), Y$_{0.44}$La$_{0.34}$Mg$_{0.22}$Ni$_{2.9}$ ($AB_{2.90}$), Y$_{0.46}$La$_{0.33}$Mg$_{0.20}$Ni$_{2.78}$ ($AB_{2.79}$) compounds have been synthesized. They all contain mixture of $AB_3$ (main phase) and YMgNi$_4$ (secondary phase). The maximum reversible hydrogen absorption capacity is around 1.69 wt.% with a flat plateau and good stable cycling stability. With the stoichiometry ratio varying from $AB_{2.78}$ to $AB_{3.04}$, the equilibrium pressure of hydrogen absorption at 60 °C increase from 0.1 MPa to 0.3 MPa. Those compounds present interesting hydrogen storage properties for practical applications. Further optimization by modifying the proportion of Y, La and Mg or by *B*-side substitution could improve both capacity and cycling stability.

## 7.3 Phase diagram

Some regions of the Y-Ni-Al and Y-Ni-Mn phase diagrams have also been explored in this study. In the case of Y-Ni-Al, there is a reported isotherm section at 800 °C (Figure 7.1) [287]. We have studied non-annealed samples with global composition YNi$_{2-x}$Al$_x$ ($0 \leq x \leq 1$). The formed phases determined by EPMA are shown by empty circles in Figure 7.1. Single-phase compounds reported in the literature for neighboring phase domains are given by dark green stars [126,232–234,239,288]. We observed that the $C15$ phase (blue circles) forms with small amount of Al substitution (up to Y$_{0.95}$Ni$_{1.89}$Al$_{0.11}$). For $AB_3$ phase (violet circles), Al substitution is enlarged up to YNi$_{2.6}$Al$_{0.4}$. This can be interpretated by the fact that Al can substitute Ni either in [YNi$_2$] and [YNi$_5$] slabs. The compositions YNi$_{2.7}$Al$_{0.3}$ and YNi$_{2.6}$Al$_{0.4}$ are close to the reported stoichiometric compound Y$_3$Ni$_8$Al with ordered structure and crystallizing in the S.G $P6_3/mmc$ [239]. However, we observe a solid solution $AB_3$-type compound Y(Ni, Al)$_3$ with no atomic ordering between Ni and Al elements. The YNi, Y$_3$Ni$_6$Al$_2$ and YNiAl compounds (green, wine and black circles respectively) form in stoichiometric ration in agreement with the reported phase diagram. Finally, we fund that the Y$_2$Ni$_2$Al phase

(red circles) forms in a large $YNi_{2-x}Al_x$ region with variable Al and Ni content which was not described so far.

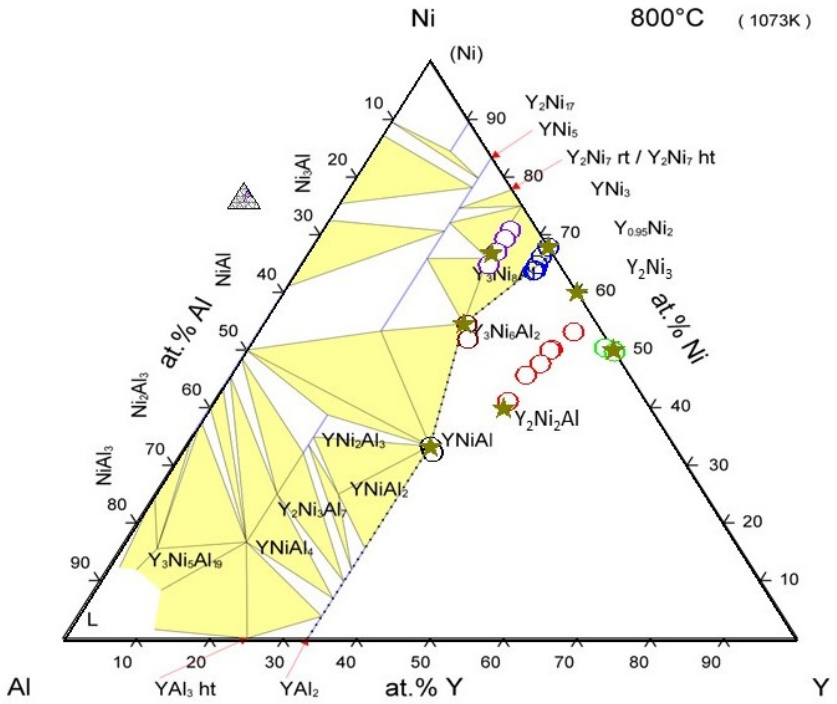


Figure 7.1 The observed phases in this study (blue empty circles), the synthesized samples (red squares) in comparison of published Y-Ni-Al phase diagram at 800 °C [287].

In the case of Y-Ni-Mn system, there is no phase diagram reported. The *AB*-phase YNi is a stoichiometric compound, it does not form solid solution with Mn. In contrast, the $AB_3$ phase admits large quantity of Mn from $YNi_3$ to $YNi_2Mn$. For the $AB_2$ *C*15-phase, we plotted the formation domain superposed on the Y-Ni-Fe phase diagram [289] which chemistry is close to our system (Figure 7.2). The compositional $AB_2$ domain differs between Y-Ni-Mn and Y-Ni-Fe systems. Firstly, the substituent $YNi_{2-x}M_x$ solubility limit is higher for $M$ = Mn ($x$ = 0.4) than for $M$ = Fe ($x$ = 0.1). Secondly, the $YNi_{2-x}M_x$ phase forms with sub-stoichiometry of Y which is not the case of Fe. Thirdly, for pseudo-binary $YNi_{2-x}Mn_x$ compounds a wide homogeneity domain exists for $0.1 \leq x \leq 0.4$ due to additional variation of Y content in relation with anti-site occupancy between Y and Mn atoms. In contrast $YNi_{2-x}Fe_x$ compounds they obey a line compound behavior with constant content of Y.

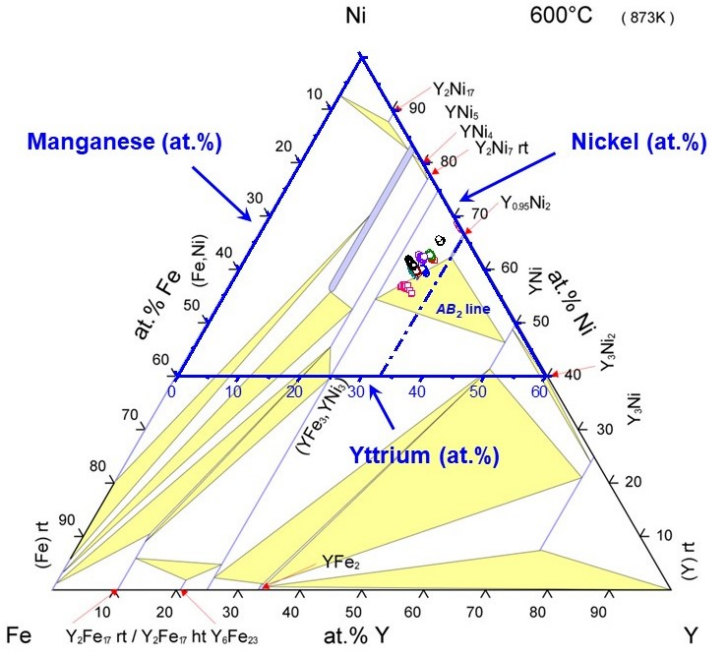


Figure 7.2 the *C*15 phase formation domain in Y-Ni-Mn determined in this study overlaps with reported Y-Ni-Fe phase diagram [289].

## 7.4 Conclusions and outlook

The present work explored chemical substitutions on *A*-, *B*- and combined *A*- and *B*- sites in $YNi_2$ compound. The phase formation, structural properties and hydrogenation properties have been investigated and discussed.

The *B*-side substitution of Ni by Al and Mn is limited by the solubility of these elements in *C*15 structure given by $YNi_{1.89}Al_{0.11}$ and $YNi_{1.6}Mn_{0.4}$. These substitutions improve the structure stability and hydrogen absorption capacity as compared to $YNi_2$ but the HIA is not suppressed, and thus the reversibility remains limited.

The *A*-side substitution of Y by Mg and Sc has wider solubility range. With Mg substitution, the compound $YMgNi_4$ with ordered Y, Mg occupation shows better stability, but moderate capacity. By Sc substitution, the plateau pressures are flatter but the equilibrium pressures dramatically increase which is not suitable for practical applications.

Even with the simultaneous substitution on both sites, no composition was found to provide at the same time good capacity, appropriate plateau pressure and reversibility. We finally conclude that if $YNi_2$ based compounds are interesting for structural and hydrogen storage properties, other systems (like Zr, Ti based compounds [72,79,290–293]) with same *C*15 phase structure could be more attractive for application. Another option is the multi-phase compound, we fund quaternary $Y_{0.43}La_{0.36}Mg_{0.21}Ni_{3.04}$ ($AB_{3.04}$), $Y_{0.44}La_{0.34}Mg_{0.22}Ni_{2.9}$ ($AB_{2.90}$), $Y_{0.46}La_{0.33}Mg_{0.20}Ni_{2.78}$ ($AB_{2.79}$) with mixture of $AB_3$ and $YMgNi_4$, which exhibit reversible hydrogen absorption capacity of 1.69 wt.% with a flat plateau and good stable cycling stability.

# Reference


[1] W.J. Ripple, C. Wolf, T.M. Newsome, M. Galetti, M. Alamgir, E. Crist, M.I. Mahmoud, W.F. Laurance, 15,364 scientist signatories from 184 countries, World Scientists' Warning to Humanity: A Second Notice, BioScience. 67 (2017) 1026-1028. https://doi.org/10.1093/biosci/bix125.

[2] J. Chow, Energy Resources and Global Development, Science. 302 (2003) 1528-1531. https://doi.org/10.1126/science.1091939.

[3] K. Alanne, S. Cao, An overview of the concept and technology of ubiquitous energy, Appl. Energy. 238 (2019) 284-302. https://doi.org/10.1016/j.apenergy.2019.01.100.

[4] World Energy Outlook 2013, Int. Energy Agency. volume 2010 (2012) 3. https://doi.org/doi:10.1023/A:1016045124964.

[5] M. Boudellal, Power-to-Gas: Renewable Hydrogen Economy for the Energy Transition, Walter de Gruyter GmbH & Co KG, 2018.

[6] National Hydrogen Roadmap - Pathways to an economically sustainable hydrogen industry in Australia, (2018).

[7] C. Bailleux, Advanced water alkaline electrolysis: a two-year running of a test plant, Int. J. Hydrog. Energy. 6 (1981) 461-471. https://doi.org/10.1016/0360-3199(81)90078-1.

[8] J.O.M. Bockris, The hydrogen economy: Its history, Int. J. Hydrog. Energy. 38 (2013) 2579-2588. https://doi.org/10.1016/j.ijhydene.2012.12.026.

[9] S. Noor, M.W. Siddiqi, Energy Consumption and Economic Growth in South Asian Countries: A Co-integrated Panel Analysis, Int. J. Energy Power Eng. 4 (2010) 1731-1736.

[10] M. Becherif, H.S. Ramadan, K. Cabaret, F. Picard, N. Simoncini, O. Bethoux, Hydrogen Energy Storage: New Techno-Economic Emergence Solution Analysis, Energy Procedia. 74 (2015) 371-380. https://doi.org/10.1016/j.egypro.2015.07.629.

[11] C.E. Grégoire Padró, F. Lau, eds., Advances in Hydrogen Energy, Springer US, Boston, MA, 2002. https://doi.org/10.1007/b118796.

[12] M.A. DeLuchi, Hydrogen vehicles: an evaluation of fuel storage, performance, safety, environmental impacts, and cost, Int. J. Hydrog. Energy. 14 (1989) 81-130. https://doi.org/10.1016/0360-3199(89)90001-3.

[13] A.X.Y. Mah, W.S. Ho, C.P.C. Bong, M.H. Hassim, P.Y. Liew, U.A. Asli, M.J. Kamaruddin, N.G. Chemmangattuvalappil, Review of hydrogen economy in Malaysia and its way forward, Int. J. Hydrog. Energy. 44 (2019) 5661-5675. https://doi.org/10.1016/j.ijhydene.2019.01.077.

[14] S. Ayalur Chattanathan, S. Adhikari, N. Abdoulmoumine, A review on current status of hydrogen production from bio-oil, Renew. Sustain. Energy Rev. 16 (2012) 2366-2372. https://doi.org/10.1016/j.rser.2012.01.051.

[15] H. Balat, E. Kırtay, Hydrogen from biomass – Present scenario and future prospects, Int. J. Hydrog. Energy. 35 (2010) 7416-7426. https://doi.org/10.1016/j.ijhydene.2010.04.137.

[16] A.G. Bayrakcı, G. Koçar, Utilization of renewable energies in Turkey's agriculture, Renew. Sustain. Energy Rev. 16 (2012) 618-633. https://doi.org/10.1016/j.rser.2011.08.027.

[17] R. Lin, J. Cheng, J.D. Murphy, Unexpectedly low biohydrogen yields in co-fermentation of acid pretreated cassava residue and swine manure, Energy Convers. Manag. 151 (2017) 553-561. https://doi.org/10.1016/j.enconman.2017.09.006.

[18] P.J. de Wild, M.J.F.M. Verhaak, Catalytic production of hydrogen from methanol, Catal. Today. 60 (2000) 3-10. https://doi.org/10.1016/S0920-5861(00)00311-4.

[19] D.R. Palo, R.A. Dagle, J.D. Holladay, Methanol Steam Reforming for Hydrogen Production, Chem. Rev. 107 (2007) 3992-4021. https://doi.org/10.1021/cr050198b.
[20] H.F. Abbas, W.M.A. Wan Daud, Hydrogen production by methane decomposition: A review, Int. J. Hydrog. Energy. 35 (2010) 1160-1190. https://doi.org/10.1016/j.ijhydene.2009.11.036.
[21] N. Shah, D. Panjala, G.P. Huffman, Hydrogen Production by Catalytic Decomposition of Methane, Energy Fuels. 15 (2001) 1528-1534. https://doi.org/10.1021/ef0101964.
[22] T.V. Choudhary, C. Sivadinarayana, C.C. Chusuei, A. Klinghoffer, D.W. Goodman, Hydrogen Production via Catalytic Decomposition of Methane, J. Catal. 199 (2001) 9-18. https://doi.org/10.1006/jcat.2000.3142.
[23] A. Abad, P. Dodds, Production of Hydrogen, in: Ref. Module Earth Syst. Environ. Sci., 2017. https://doi.org/10.1016/B978-0-12-409548-9.10117-4.
[24] A. Hornung, Transformation of Biomass: Theory to Practice, John Wiley & Sons, 2014.
[25] A.M. Abdalla, S. Hossain, O.B. Nisfindy, A.T. Azad, M. Dawood, A.K. Azad, Hydrogen production, storage, transportation and key challenges with applications: A review, Energy Convers. Manag. 165 (2018) 602-627. https://doi.org/10.1016/j.enconman.2018.03.088.
[26] P. Zakkour, G. Cook, CCS Roadmap for Industry: High-purity $CO_2$ sources Sectoral Assessment – Final Report, (2010). https://doi.org/10.13140/RG.2.1.3717.8722.
[27] J.A. Turner, Sustainable Hydrogen Production, Science. 305 (2004) 972-974. https://doi.org/10.1126/science.1103197.
[28] J. Turner, G. Sverdrup, M.K. Mann, P.-C. Maness, B. Kroposki, M. Ghirardi, R.J. Evans, D. Blake, Renewable hydrogen production, Int. J. Energy Res. 32 (2008) 379-407. https://doi.org/10.1002/er.1372.
[29] I. Dincer, Green methods for hydrogen production, Int. J. Hydrog. Energy. 37 (2012) 1954-1971. https://doi.org/10.1016/j.ijhydene.2011.03.173.
[30] D.J. Durbin, C. Malardier-Jugroot, Review of hydrogen storage techniques for on board vehicle applications, Int. J. Hydrog. Energy. 38 (2013) 14595-14617. https://doi.org/10.1016/j.ijhydene.2013.07.058.
[31] T.Q. Hua, R.K. Ahluwalia, J.-K. Peng, M. Kromer, S. Lasher, K. McKenney, K. Law, J. Sinha, Technical assessment of compressed hydrogen storage tank systems for automotive applications, Int. J. Hydrog. Energy. 36 (2011) 3037-3049. https://doi.org/10.1016/j.ijhydene.2010.11.090.
[32] K. R., Ahluwalia, and, Q. T., Hua, and, J.-K., Peng, and, S., Technical assessment of cryo-compressed hydrogen storage tank systems for automotive applications, Int. J. Hydrog. Energy. (2010). https://doi.org/10.1016/j.ijhydene.2010.02.074.
[33] J.O. Abe, A.P.I. Popoola, E. Ajenifuja, O.M. Popoola, Hydrogen energy, economy and storage: Review and recommendation, Int. J. Hydrog. Energy. 44 (2019) 15072-15086. https://doi.org/10.1016/j.ijhydene.2019.04.068.
[34] A. Midilli, M. Ay, I. Dincer, M.A. Rosen, On hydrogen and hydrogen energy strategies: I: current status and needs, Renew. Sustain. Energy Rev. 9 (2005) 255-271. https://doi.org/10.1016/j.rser.2004.05.003.
[35] A.T. Wijayanta, T. Oda, C.W. Purnomo, T. Kashiwagi, M. Aziz, Liquid hydrogen, methylcyclohexane, and ammonia as potential hydrogen storage: Comparison review, Int. J. Hydrog. Energy. 44 (2019) 15026-15044. https://doi.org/10.1016/j.ijhydene.2019.04.112.
[36] K.L. Lim, H. Kazemian, Z. Yaakob, W.R.W. Daud, Solid-state Materials and Methods for Hydrogen Storage: A Critical Review, Chem. Eng. Technol. 33 (2010) 213-226. https://doi.org/10.1002/ceat.200900376.

[37] P.A. Anderson, Storage of hydrogen in zeolites, in: Solid-State Hydrog. Storage, Elsevier, 2008: pp. 223-260. https://doi.org/10.1533/9781845694944.3.223.
[38] R. Chahine, T.K. Bose, Characterization and optimization of adsorbents for hydrogen storage, Hydrog. Energy Prog. 2 (1996) 1259-1264.
[39] M. Hirscher, V.A. Yartys, M. Baricco, J. Bellosta von Colbe, D. Blanchard, R.C. Bowman, D.P. Broom, C.E. Buckley, F. Chang, P. Chen, Y.W. Cho, J.-C. Crivello, F. Cuevas, W.I.F. David, P.E. de Jongh, R.V. Denys, M. Dornheim, M. Felderhoff, Y. Filinchuk, G.E. Froudakis, D.M. Grant, E.MacA. Gray, B.C. Hauback, T. He, T.D. Humphries, T.R. Jensen, S. Kim, Y. Kojima, M. Latroche, H.-W. Li, M.V. Lototskyy, J.W. Makepeace, K.T. Møller, L. Naheed, P. Ngene, D. Noréus, M.M. Nygård, S. Orimo, M. Paskevicius, L. Pasquini, D.B. Ravnsbæk, M. Veronica Sofianos, T.J. Udovic, T. Vegge, G.S. Walker, C.J. Webb, C. Weidenthaler, C. Zlotea, Materials for hydrogen-based energy storage – past, recent progress and future outlook, J. Alloys Compd. 827 (2020) 153548. https://doi.org/10.1016/j.jallcom.2019.153548.
[40] L. Wang, R.T. Yang, New sorbents for hydrogen storage by hydrogen spillover – a review, Energy Environ. Sci. 1 (2008) 268. https://doi.org/10.1039/b807957a.
[41] G.G. Tibbetts, G.P. Meisner, C.H. Olk, Hydrogen storage capacity of carbon nanotubes, filaments, and vapor-grown fibers, Carbon. 39 (2001) 2291-2301. https://doi.org/10.1016/S0008-6223(01)00051-3.
[42] S.J. Yang, H. Jung, T. Kim, C.R. Park, Recent advances in hydrogen storage technologies based on nanoporous carbon materials, Prog. Nat. Sci. Mater. Int. 22 (2012) 631-638. https://doi.org/10.1016/j.pnsc.2012.11.006.
[43] R. Chamoun, U.B. Demirci, P. Miele, Cyclic Dehydrogenation–(Re)Hydrogenation with Hydrogen-Storage Materials: An Overview, Energy Technol. 3 (2015) 100-117. https://doi.org/10.1002/ente.201402136.
[44] B.P. Tarasov, P.V. Fursikov, A.A. Volodin, M.S. Bocharnikov, Y.Y. Shimkus, A.M. Kashin, V.A. Yartys, S. Chidziva, S. Pasupathi, M.V. Lototskyy, Metal hydride hydrogen storage and compression systems for energy storage technologies, Int. J. Hydrog. Energy. (2020) S0360319920326604. https://doi.org/10.1016/j.ijhydene.2020.07.085.
[45] N.A.A. Rusman, M. Dahari, A review on the current progress of metal hydrides material for solid-state hydrogen storage applications, Int. J. Hydrog. Energy. 41 (2016) 12108-12126. https://doi.org/10.1016/j.ijhydene.2016.05.244.
[46] J.H.N. van Vucht, F.A. Kuijpers, H.C. a. M. Bruning, Reversible Room Temperature Absorption Quantities of Hydrogen by Intermetallic, Philips Res Rep. (1970). https://www.osti.gov/biblio/4129528.
[47] J.J. Reilly, R.H. Wiswall, Formation and properties of iron titanium hydride, Inorg. Chem. 13 (1974) 218-222. https://doi.org/10.1021/ic50131a042.
[48] A. Züttel, Materials for hydrogen storage, Mater. Today. 6 (2003) 24-33. https://doi.org/10.1016/S1369-7021(03)00922-2.
[49] H.H. Van Mal, K.H.J. Buschow, A.R. Miedema, Hydrogen absorption in $LaNi_5$ and related compounds: Experimental observations and their explanation, J. Common Met. 35 (1974) 65-76. https://doi.org/10.1016/0022-5088(74)90146-5.
[50] V. Bhosle, E.G. Baburaj, M. Miranova, K. Salama, Dehydrogenation of $TiH_2$, Mater. Sci. Eng. A. 356 (2003) 190-199. https://doi.org/10.1016/S0921-5093(03)00117-5.
[51] E. M. Dematteis, N. Berti, F. Cuevas, M. Latroche, M. Baricco, Substitutional effects in TiFe for hydrogen storage: a comprehensive review, Mater. Adv. 2 (2021) 2524-2560. https://doi.org/10.1039/D1MA00101A.
[52] B. Baranowski, Thermodynamics of metal/hydrogen systems at high pressures, Berichte Bunsenges. Für Phys. Chem. 76 (1972) 714-724. https://doi.org/10.1002/bbpc.19720760805.

[53] W.L. Korst, J.C. Warf, Rare Earth-Hydrogen Systems. I. Structural and Thermodynamic Properties, Inorg. Chem. 5 (1966) 1719-1726. https://doi.org/10.1021/ic50044a018.
[54] M. Dornheim, Thermodynamics of Metal Hydrides: Tailoring Reaction Enthalpies of Hydrogen Storage Materials, Thermodyn. - Interact. Stud. - Solids Liq. Gases. (2011). https://doi.org/10.5772/21662.
[55] B. Sakintuna, F. Lamari-Darkrim, M. Hirscher, Metal hydride materials for solid hydrogen storage: A review, Int. J. Hydrog. Energy. 32 (2007) 1121-1140. https://doi.org/10.1016/j.ijhydene.2006.11.022.
[56] P. Fischer, A. Furrer, G. Busch, L. Schlapbach, Neutron scattering investigations of the $LaNi_5$ hydrogen storage system, Helvetica Phys. Acta. 50 (1977).
[57] Localization of hydrogen (deuterium) in α-$LaNi_5H_x$ ($x$ = 0.1 and 0.4), J. Common Met. 129 (1987) 181-186. https://doi.org/10.1016/0022-5088(87)90046-4.
[58] M. Latroche, J.-M. Joubert, A. Percheron-Guégan, F. Bourée-Vigneron, Neutron diffraction study of the deuterides of the over-stoichiometric compounds $LaNi_{5+x}$, J. Solid State Chem. 177 (2004) 1219-1229. https://doi.org/10.1016/j.jssc.2003.10.029.
[59] J.-M. Joubert, V. Paul-Boncour, F. Cuevas, J. Zhang, M. Latroche, $LaNi_5$ related $AB_5$ compounds: Structure, properties and applications, J. Alloys Compd. 862 (2021) 158163. https://doi.org/10.1016/j.jallcom.2020.158163.
[60] C. Lartigue, A. Percheron-Guegan, J.C. Achard, J.L. Soubeyroux, Hydrogen (deuterium) ordering in the β-$LaNi_5D_{x>5}$ phases: A neutron diffraction study, J. Common Met. 113 (1985) 127-148. https://doi.org/10.1016/0022-5088(85)90155-9.
[61] H. Diaz, A. Percheron-Guegan, J.C. Achard, Thermodynamic and structural properties of $LaNi_{5-y}Al_y$compounds and their related hydrides, Int. J. Hydrog. Energy. 4(5) (1979) 445-454. https://doi.org/10.1016/0360-3199(79)90104-6.
[62] J.J.G. Willems, Metal Hydride Electrodes: Stability of $LaNi_5$-Related Compounds, Z. Für Phys. Chem. 147 (1986) 231-231. https://doi.org/10.1524/zpch.1986.147.1_2.231.
[63] L.O. Valøen, A. Zaluska, L. Zaluski, H. Tanaka, N. Kuriyama, J.O. Ström-Olsen, R. Tunold, Structure and related properties of (La, Ce, Nd, Pr)$Ni_5$ alloys, J. Alloys Compd. 306 (2000) 235-244. https://doi.org/10.1016/S0925-8388(00)00765-9.
[64] R. Singh, M. Lototsky, O. Srivastava, Thermodynamical, structural, hydrogen storage properties and simulation studies of P-C isotherms of (La, Mm)$Ni_{5-y}Fe_y$, Int. J. Hydrog. Energy. 32 (2007) 2971-2976. https://doi.org/10.1016/j.ijhydene.2007.01.017.
[65] D.G. Oliva, M. Fuentes, E.M. Borzone, G.O. Meyer, P.A. Aguirre, Hydrogen storage on $LaNi_{5-x}Sn_x$. Experimental and phenomenological Model-based analysis, Energy Convers. Manag. 173 (2018) 113-122. https://doi.org/10.1016/j.enconman.2018.07.041.
[66] M. Spodaryk, N. Gasilova, A. Züttel, Hydrogen storage and electrochemical properties of $LaNi_{5-x}Cu_x$ hydride-forming alloys, J. Alloys Compd. 775 (2019) 175-180. https://doi.org/10.1016/j.jallcom.2018.10.009.
[67] Z. Zhu, S. Zhu, H. Lu, J. Wu, K. Yan, H. Cheng, J. Liu, Stability of $LaNi_5$-Co alloys cycled in hydrogen - Part 1 evolution in gaseous hydrogen storage performance, Int. J. Hydrog. Energy. 44 (2019) 15159-15172. https://doi.org/10.1016/j.ijhydene.2019.04.111.
[68] D. Chartouni, K. Gross, Phase Transitions in $LaNi_4Co$ during Electrochemical Cycling An In Situ X-Ray Diffraction Study, J. Electrochem. Soc. 148 (2001) A241. https://doi.org/10.1149/1.1350656.
[69] S.B. Gesari, M.E. Pronsato, A. Visintin, A. Juan, Hydrogen Storage in $AB_2$ Laves Phase (A: Zr, Ti; B: Ni, Mn, Cr, V): Binding Energy and Electronic Structure, J. Phys. Chem. C. 114 (2010) 16832-16836. https://doi.org/10.1021/jp106036v.
[70] D.G. Ivey, D.O. Northwood, Storing Hydrogen in $AB_2$ Laves-Type Compounds, Z. Für Phys. Chem. 147 (1986) 191-209. https://doi.org/10.1524/zpch.1986.147.1_2.191.

[71] D.P. Shoemaker, C.B. Shoemaker, Concerning atomic sites and capacities for hydrogen absorption in the $AB_2$ Friauf-Laves phases, J. Common Met. 68 (1979) 43-58. https://doi.org/10.1016/0022-5088(79)90271-6.
[72] D. Shaltiel, I. Jacob, D. Davidov, Hydrogen absorption and desorption properties of $AB_2$ Laves-phase pseudobinary compounds, J. Common Met. 53 (1977) 117-131. https://doi.org/10.1016/0022-5088(77)90162-X.
[73] T. Yamashita, T. Gamo, Y. Moriwaki, M. Fukuda, Hydride Formation of Ti-Mn Binary Alloys, J. Jpn. Inst. Met. 41 (1977) 148-154. https://doi.org/10.2320/jinstmet1952.41.2_148.
[74] V.S. Marinin, K.R. Umerenkova, O.V. Volovchuk, Hydrogen sorption properties of hexagonal laves phase $TiMn_{1.5}$ intermetallic compound, Int. J. Hydrog. Energy. 36 (2011) 1359-1363. https://doi.org/10.1016/j.ijhydene.2010.06.129.
[75] B.K. Singh, A.K. Singh, A.M. Imam, O.N. Srivastava, On the structural characteristics and hydrogenation behaviour of $TiMn_{1.5}$ hydrogen storage material, Int. J. Hydrog. Energy. 26 (2001) 817-821. https://doi.org/10.1016/S0360-3199(01)00012-X.
[76] A.L. Shilov, L.N. Padurets, M.E. Kost, Thermodynamics of hydrides of intermetallic compounds of transition metals, Zh Fiz Khim. 59 (1985) 1857-1875.
[77] T. Zotov, E. Movlaev, S. Mitrokhin, V. Verbetsky, Interaction in (Ti, Sc)$Fe_2$-$H_2$ and (Zr, Sc)$Fe_2$-$H_2$ systems, J. Alloys Compd. 459 (2008) 220-224. https://doi.org/10.1016/j.jallcom.2007.05.027.
[78] S. Mitrokhin, T. Zotov, E. Movlaev, V. Verbetsky, Hydrogen interaction with intermetallic compounds and alloys at high pressure, J. Alloys Compd. 580 (2013) S90-S93. https://doi.org/10.1016/j.jallcom.2013.03.100.
[79] Hydrogen absorption in $Zr(Al_xB_{1-x})_2$ ($B$ = Fe, Co) laves phase compounds, Solid State Commun. 27 (1978) 175-180. https://doi.org/10.1016/0038-1098(78)90826-8.
[80] G. Sandrock, A panoramic overview of hydrogen storage alloys from a gas reaction point of view, J. Alloys Compd. 293-295 (1999) 877-888. https://doi.org/10.1016/S0925-8388(99)00384-9.
[81] K.H.J. Buschow, A.S. Van Der Goot, The crystal structure of rare-earth nickel compounds of the type $R_2Ni_7$, J. Common Met. 22 (1970) 419-428. https://doi.org/10.1016/0022-5088(70)90129-3.
[82] D.T. Cromer, C.E. Olsen, The crystal structure of $PuNi_3$ and $CeNi_3$, Acta Crystallogr. 12 (1959). https://doi.org/10.1107/S0365110X59002006.
[83] T. Kohno, H. Yoshida, F. Kawashima, T. Inaba, I. Sakai, M. Yamamoto, M. Kanda, Hydrogen storage properties of new ternary system alloys: $La_2MgNi_9$, $La_5Mg_2Ni_{23}$, $La_3MgNi_{14}$, J. Alloys Compd. 311 (2000) L5-L7. https://doi.org/10.1016/S0925-8388(00)01119-1.
[84] A.Q. Deng, J.B. Fan, K.N. Qian, Crystal Structure and Electrochemical Properties of $AB_{3.8}$-Type Earth Mg Ni-Based Hydrogen Storage Alloys, Adv. Mater. Res. 156-157 (2010) 108-112. https://doi.org/10.4028/www.scientific.net/AMR.156-157.108.
[85] H. Oesterreicher, J. Clinton, H. Bittner, Hydrides of La-Ni compounds, Mater. Res. Bull. 11 (1976) 1241-1247. https://doi.org/10.1016/0025-5408(76)90028-3.
[86] M. Latroche, A. Percheron-Guégan, Structural and thermodynamic studies of some hydride forming $RM_3$-type compounds ($R$ = lanthanide, $M$ = transition metal), J. Alloys Compd. 356-357 (2003) 461-468. https://doi.org/10.1016/S0925-8388(03)00116-6.
[87] H. Hayakawa, E. Akiba, M. Gotoh, T. Kohno, Crystal Structures of La-Mg-$Ni_x$ ($x$ = 3 - 4) System Hydrogen Storage Alloys, Mater. Trans. 46 (2005) 1393-1401. https://doi.org/10.2320/matertrans.46.1393.

[88] K. Kadir, T. Sakai, I. Uehara, Structural investigation and hydrogen storage capacity of $LaMg_2Ni_9$ and $(La_{0.65}Ca_{0.35})(Mg_{1.32}Ca_{0.68})Ni_9$ of the $AB_2C_9$ type structure, J. Alloys Compd. 302 (2000) 112-117. https://doi.org/10.1016/S0925-8388(00)00581-8.
[89] Y. Liu, The effect of Mn substitution for Ni on the structural and electrochemical properties of $La_{0.7}Mg_{0.3}Ni_{2.55-x}Co_{0.45}Mn_x$ hydrogen storage electrode alloys, Int. J. Hydrog. Energy. 29 (2004) 297-305. https://doi.org/10.1016/S0360-3199(03)00215-5.
[90] B. Liao, Y.Q. Lei, L.X. Chen, G.L. Lu, H.G. Pan, Q.D. Wang, The effect of Al substitution for Ni on the structure and electrochemical properties of $AB_3$-type $La_2Mg(Ni_{1-x}Al_x)_9$ ($x$ = 0 - 0.05) alloys, J. Alloys Compd. 404-406 (2005) 665-668. https://doi.org/10.1016/j.jallcom.2004.10.088.
[91] R. Tang, Y. Liu, C. Zhu, J. Zhu, G. Yu, Effect of Al substitution for Co on the hydrogen storage characteristics of $Ml_{0.8}Mg_{0.2}Ni_{3.2}Co_{0.6-x}Al_x$ ($x$ = 0 - 0.6) alloys, Intermetallics. 14 (2006) 361-366. https://doi.org/10.1016/j.intermet.2005.05.015.
[92] Y.J. Chai, K. Sakaki, K. Asano, H. Enoki, E. Akiba, T. Kohno, Crystal structure and hydrogen storage properties of La-Mg-Ni-Co alloy with superstructure, Scr. Mater. 57 (2007) 545-548. https://doi.org/10.1016/j.scriptamat.2007.05.018.
[93] N. Madern, V. Charbonnier, J. Monnier, J. Zhang, V. Paul-Boncour, M. Latroche, Investigation of H Sorption and Corrosion Properties of $Sm_2Mn_xNi_{7-x}$ ($0 \leq x < 0.5$) Intermetallic Compounds Forming Reversible Hydrides, Energies. 13 (2020) 3470. https://doi.org/10.3390/en13133470.
[94] Yu.V. Verbovyts'kyi, I.Yu. Zavalii, New Metal-Hydride Electrode Materials Based On $R_{1-x}Mg_xNi_{3-4}$ Alloys for Chemical Current Sources, Mater. Sci. 51 (2016) 443-456. https://doi.org/10.1007/s11003-016-9861-0.
[95] V. Charbonnier, N. Madern, J. Monnier, J. Zhang, V. Paul-Boncour, M. Latroche, Thermodynamic and corrosion study of $Sm_{1-x}Mg_xNi_y$ ($y$ = 3.5 or 3.8) compounds forming reversible hydrides, Int. J. Hydrog. Energy. 45 (2020) 11686-11694. https://doi.org/10.1016/j.ijhydene.2020.02.073.
[96] Q. Zhang, Z. Chen, Y. Li, F. Fang, D. Sun, L. Ouyang, M. Zhu, Comparative Investigations on Hydrogen Absorption-Desorption Properties of Sm-Mg-Ni Compounds: The Effect of $[SmNi_5]/[SmMgNi_4]$ Unit Ratio, J. Phys. Chem. C. 119 (2015) 4719-4727. https://doi.org/10.1021/acs.jpcc.5b00279.
[97] J.J. Reilly, R.H. Wiswall, Formation and properties of iron titanium hydride, Inorg. Chem. 13 (1974) 218-222. https://doi.org/10.1021/ic50131a042.
[98] F. Laves, H.J. Wallbaum, Zur Kristallchemie von Titan-Legierungen, Naturwissenschaften. 27 (1939) 674-675. https://doi.org/10.1007/BF01494992.
[99] P.A. Beck, J.B. Darby, O.P. Arora, Occurrence of CsCI-Type Ordered Structures in Certain Binary Systems of Transition Elements, JOM. 8 (1956) 148-149. https://doi.org/10.1007/BF03377661.
[100] T.V. Philip, P.A. Beck, CsCl-type ordered structures in binary alloys of transition elements, JOM. 9 (1957) 1269-1271. https://doi.org/10.1007/BF03398305.
[101] H. Bo, J. Wang, L. Duarte, C. Leinenbach, L. Liu, H. Liu, Z. Jin, Thermodynamic re-assessment of Fe-Ti binary system, Trans. Nonferrous Met. Soc. China. 22 (2012) 2204-2211. https://doi.org/10.1016/S1003-6326(11)61450-7.
[102] M. h. Mintz, S. Vaknin, S. Biderman, Z. Hadari, Hydrides of ternary $TiFe_xM_{1-x}$ (M = Cr, Mn, Co, Ni) intermetallics, J. Appl. Phys. 52 (1981) 463-467. https://doi.org/10.1063/1.329808.
[103] T. Yang, P. Wang, C. Xia, N. Liu, C. Liang, F. Yin, Q. Li, Effect of chromium, manganese and yttrium on microstructure and hydrogen storage properties of TiFe-based alloy, Int. J. Hydrog. Energy. 45 (2020) 12071-12081. https://doi.org/10.1016/j.ijhydene.2020.02.086.

[104] C.-H. Chiang, Z.-H. Chin, T.-P. Perng, Hydrogenation of TiFe by high-energy ball milling, J. Alloys Compd. 307 (2000) 259-265. https://doi.org/10.1016/S0925-8388(00)00827-6.
[105] M. Abe, T. Kuji, Hydrogen absorption of TiFe alloy synthesized by ball milling and post-annealing, J. Alloys Compd. 446-447 (2007) 200-203. https://doi.org/10.1016/j.jallcom.2006.12.063.
[106] H. Emami, K. Edalati, J. Matsuda, E. Akiba, Z. Horita, Hydrogen storage performance of TiFe after processing by ball milling, Acta Mater. 88 (2015) 190-195. https://doi.org/10.1016/j.actamat.2014.12.052.
[107] K. Edalati, J. Matsuda, M. Arita, T. Daio, E. Akiba, Z. Horita, Mechanism of activation of TiFe intermetallics for hydrogen storage by severe plastic deformation using high-pressure torsion, Appl. Phys. Lett. 103 (2013) 143902. https://doi.org/10.1063/1.4823555.
[108] G.K. Sujan, Z. Pan, H. Li, D. Liang, N. Alam, An overview on TiFe intermetallic for solid-state hydrogen storage: microstructure, hydrogenation and fabrication processes, Crit. Rev. Solid State Mater. Sci. 45 (2020) 410-427. https://doi.org/10.1080/10408436.2019.1652143.
[109] H. Buchner, M.A. Gutjahr, K.D. Beccu, H. Saeufferer, Hydrogen in intermetallic phases: the system titanium-nickel-hydrogen, Z Met. 63 (1972) 497-500.
[110] M.H. Mintz, Z. Hadari, M.P. Dariel, Hydrogenation characteristics of $Ti_2NiO_x$ compounds ($0 \leq x < 0.5$), J. Common Met. 63 (1979) 181-191. https://doi.org/10.1016/0022-5088(79)90242-X.
[111] H. Itoh, O. Yoshinari, K. Tanaka, Study of hydrogen storage in $Mg_2Ni$ by thermal desorption spectrometry, J. Alloys Compd. 231 (1995) 483-487. https://doi.org/10.1016/0925-8388(95)01868-9.
[112] A. Reiser, B. Bogdanović, K. Schlichte, The application of Mg-based metal-hydrides as heat energy storage systems, Int. J. Hydrog. Energy. 25 (2000) 425-430. https://doi.org/10.1016/S0360-3199(99)00057-9.
[113] J.J. Reilly, R.H. Wiswall, Reaction of hydrogen with alloys of magnesium and nickel and the formation of $Mg_2NiH_4$, Inorg. Chem. 7 (1968) 2254-2256. https://doi.org/10.1021/ic50069a016.
[114] U. Häussermann, H. Blomqvist, D. Noréus, Bonding and Stability of the Hydrogen Storage Material $Mg_2NiH_4$, Inorg. Chem. 41 (2002) 3684-3692. https://doi.org/10.1021/ic0201046.
[115] F. Liang, J. Lin, Y. Cheng, D. Yin, Y. Wu, L. Wang, Gaseous sorption and electrochemical properties of rare-earth hydrogen storage alloys and their representative applications: A review of recent progress, Sci. China Technol. Sci. 61 (2018) 1309-1318. https://doi.org/10.1007/s11431-018-9316-0.
[116] D. Shaltiel, Hydride properties of $AB_2$ laves phase compounds, J. Common Met. 62 (1978) 407-416. https://doi.org/10.1016/0022-5088(78)90055-3.
[117] F. Laves, Kristallographie der Legierungen, Naturwissenschaften. 27 (1939) 65-73. https://doi.org/10.1007/BF01493214.
[118] D.P. Shoemaker, C.B. Shoemaker, Concerning the relative numbers of atomic coordination types in tetrahedrally close packed metal structures, Acta Crystallogr. B. 42 (1986) 3-11. https://doi.org/10.1107/S0108768186098671.
[119] V. Paul-Boncour, A. Percheron-Guegan, M. Diaf, J.C. Achard, Structural characterization of $RNi_2$ ($R$ = La, Ce) intermetallic compounds and their hydrides, J. Common Met. 131 (1987) 201-208. https://doi.org/10.1016/0022-5088(87)90518-2.
[120] V. Paul-Boncour, A. Percheron-Guégan, M. Escorne, A. Mauger, J.C. Achard, Structural and Electronic Transformation of (La, Ce)$Ni_2$ Compounds upon Hydrogenation, Z. Für Phys. Chem. 163 (1989) 263-274. https://doi.org/10.1524/zpch.1989.163.Part_1.0263.

[121] A.F. Deutz, R.B. Helmholdt, A.C. Moleman, D.B. De Mooij, K.H.J. Buschow, Superstructure in the intermetallic compound $TmNi_2$, J. Common Met. 153 (1989) 259-266. https://doi.org/10.1016/0022-5088(89)90120-3.
[122] A. Percheron-Guégan, V. Paul-Boncour, M. Latroche, J.C. Achard, F. Bourée-Vigneron, Structure of $Y_{0.95}Ni_2$ and its hydride, J. Common Met. 172-174 (1991) 198-205. https://doi.org/10.1016/0022-5088(91)90448-D.
[123] M. Latroche, V. Paul-Boncour, A. Percheron-Guégan, Structural instability in $R_{1-x}Ni_2$ compounds and their hydrides ($R$ = Y, Rare Earth), Z. Für Phys. Chem. 179 (1993) 261-268. https://doi.org/10.1524/zpch.1993.179.Part_1_2.261.
[124] V. Paul-Boncour, A. Lindbaum, M. Latroche, S. Heathman, Homogeneity range and order–disorder transitions in $R_{1-x}Ni_2$ Laves phase compounds, Intermetallics. 14 (2006) 483-490. https://doi.org/10.1016/j.intermet.2005.08.003.
[125] V. Paul-Boncour, A. Lindbaum, *Ab* initio calculations on the formation of $La_{1-x}Ni_2$ compounds, J. Phys. Condens. Matter. 14 (2002) 3921. https://doi.org/10.1088/0953-8984/14/15/306.
[126] M. Latroche, V. Paul-Boncour, A. Percheron-Guégan, J.C. Achard, Structure determination of $Y_{0.95}Ni_2$ by X-ray powder diffraction, J. Common Met. 161 (1990) L27-L31. https://doi.org/10.1016/0022-5088(90)90334-G.
[127] A. Lindbaum, J. Hafner, E. Gratz, *Ab initio* studies of the formation of a $Y_{1-x}Ni_2$ superstructure with ordered Y vacancies, J. Phys. Condens. Matter. 11 (1999) 1177-1187. https://doi.org/10.1088/0953-8984/11/5/006.
[128] J.H. Zhu, P.K. Liaw, C.T. Liu, Effect of electron concentration on the phase stability of $NbCr_2$-based Laves phase alloys, Mater. Sci. Eng. A. 239-240 (1997) 260-264. https://doi.org/10.1016/S0921-5093(97)00590-X.
[129] K. Terakura, H. Akai, eds., Interatomic Potential and Structural Stability: Proceedings of the 15th Taniguchi Symposium, Kashikojima, Japan, October 19-23, 1992, Springer Berlin Heidelberg, Berlin, Heidelberg, 1993. https://doi.org/10.1007/978-3-642-84968-8.
[130] Y. Ohta, D.G. Pettifor, Size versus electronic factors in transition metal Laves phase stability, J. Phys. Condens. Matter. 2 (1990) 8189-8194. https://doi.org/10.1088/0953-8984/2/41/006.
[131] J.H. Zhu, C.T. Liu, L.M. Pike, P.K. Liaw, A thermodynamic interpretation of the size-ratio limits for Laves phase formation, Metall. Mater. Trans. A. 30 (1999) 1449-1452. https://doi.org/10.1007/s11661-999-0292-5.
[132] J.H. Zhu, C.T. Liu, L.M. Pike, P.K. Liaw, Enthalpies of formation of binary Laves phases, Intermetallics. 10 (2002) 579-595. https://doi.org/10.1016/S0966-9795(02)00030-4.
[133] K.A. Gschneidner, Jr., V.K. Pecharsky, Binary rare earth Laves phases - an overview, Z. Für Krist. - Cryst. Mater. 221 (2006) 375-381. https://doi.org/10.1524/zkri.2006.221.5-7.375.
[134] K.H.J. Buschow, Intermetallic compounds of rare-earth and 3*d* transition metals, Rep. Prog. Phys. 40 (1977) 1179-1256. https://doi.org/10.1088/0034-4885/40/10/002.
[135] D.E. Soto-Parra, F. Alvarado-Hernandez, O. Ayala, R.A. Ochoa-Gamboa, H. Flores-Zúñiga, D. Rios-Jara, The effect of Fe addition on the transformation temperatures, lattice parameter and magnetization saturation $Ni_{52.5-x}Mn_{23}Ga_{24.5}Fe_x$ ferromagnetic shape memory alloy, J. Alloys Compd. 464 (2008) 288-291. https://doi.org/10.1016/j.jallcom.2007.09.093.
[136] Y. Zhang, T.T. Zuo, Z. Tang, M.C. Gao, K.A. Dahmen, P.K. Liaw, Z.P. Lu, Microstructures and properties of high-entropy alloys, Prog. Mater. Sci. 61 (2014) 1-93. https://doi.org/10.1016/j.pmatsci.2013.10.001.

[137] A. Lindbaum, E. Gratz, S. Heathman, Pressure-induced order-disorder transitions in $RNi_2$ compounds, Phys. Rev. B. 65 (2002) 134114. https://doi.org/10.1103/PhysRevB.65.134114.
[138] B. Kotur, O. Myakush, I. Zavaliy, Hydrogen Sorption Properties of Some $RM_{2-x}M_x$ and $RM_{2-x}Al_x$ ($R$ = Y, Gd, Tb, Er, Ho; $M$ = Mn, Fe, Co, Ni) Laves Phase Ternary Compounds, Croat. Chem. Acta. 82 (2009) 469-476. https://doi.org/10.1002/chin.201004221.
[139] D.G. Westlake, Hydrides of intermetallic compounds: A review of stabilities, stoichiometries and preferred hydrogen sites, J. Common Met. 91 (1983) 1-20. https://doi.org/10.1016/0022-5088(83)90091-7.
[140] A.N. Bogdanova, A.V. Irodova, G. Andre, F. Bouree, The $ZrV_2D_6$ crystal structure, J. Alloys Compd. 356-357 (2003) 50-53. https://doi.org/10.1016/S0925-8388(02)01214-8.
[141] Y. Makihara, Y. Andoh, Y. Hashimoto, H. Fujii, M. Hasuo, T. Okamoto, Magnetic Characteristics of Laves Phase $R$Mn$_2$ Compounds ($R$ = Gd, Tb, Dy, Ho and Er), J. Phys. Soc. Jpn. 52 (1983) 629-636. https://doi.org/10.1143/JPSJ.52.629.
[142] K. Yoshimura, Y. Nakamura, NMR Study of Magnetic State of $R$Mn$_2$ Intermetallic Compounds. I. $R$ = Light Rare Earth, J. Phys. Soc. Jpn. 53 (1984) 3611-3615. https://doi.org/10.1143/JPSJ.53.3611.
[143] Y. Tagawa, J. Sakurai, Y. Komura, H. Wada, M. Shiga, Y. Nakamura, X-Ray Study of Crystal Distortions in $R$Mn$_2$ Compounds ($R$: Y, Pr, Nd, Sm and Gd), J. Phys. Soc. Jpn. 54 (1985) 591-597. https://doi.org/10.1143/JPSJ.54.591.
[144] K. Yoshimura, M. Shiga, Y. Nakamura, NMR Study of Magnetic State of $R$Mn$_2$ Intermetallic Compounds. II. $R$ = Heavy Rare-Earth, J. Phys. Soc. Jpn. 55 (1986) 3585-3595. https://doi.org/10.1143/JPSJ.55.3585.
[145] H. Fujii, M. Saga, T. Okamoto, Magnetic, crystallographic and hydrogen absorption properties of $YMn_2$ and $ZrMn_2$ hydrides, J. Common Met. 130 (1987) 25-31. https://doi.org/10.1016/0022-5088(87)90083-X.
[146] J. Przewoznik, V. Paul-Boncour, M. Latroche, A. Percheron-Guégan, Structural study of $YMn_2$ hydrides, J. Alloys Compd. 225 (1995) 436-439. https://doi.org/10.1016/0925-8388(94)07048-2.
[147] M. Latroche, V. Paul-Boncour, J. Przewoznik, A. Percheron-Guégan, F. Bourée-Vigneron, Neutron diffraction study of $YMn_2D_x$ deuterides ($1 \leq x \leq 3.4$), J. Alloys Compd. 231 (1995) 99-103. https://doi.org/10.1016/0925-8388(95)01845-X.
[148] H. Figiel, J. Przewoznik, V. Paul-Boncour, A. Lindbaum, E. Gratz, M. Latroche, M. Escorne, A. Percheron-Guégan, P. Mietniowski, Hydrogen induced phase transitions in $YMn_2$, J. Alloys Compd. 274 (1998) 29-37. https://doi.org/10.1016/S0925-8388(98)00566-0.
[149] M. Latroche, V. Paul-Boncour, A. Percheron-Guégan, F. Bourée-Vigneron, Temperature dependence study of $YMn_2D_{4.5}$ by means of neutron powder diffraction, J. Alloys Compd. 274 (1998) 59-64. https://doi.org/10.1016/S0925-8388(98)00539-8.
[150] C.-Y. Wang, V. Paul-Boncour, C.-C. Kang, R.-S. Liu, S.M. Filipek, M. Dorogova, I. Marchuk, T. Hirata, A. Percheron-Guegan, H.-S. Sheu, L.-Y. Jang, J.-M. Chen, H.-D. Yang, The novel $YMn_2D_6$ deuteride synthesized under high pressure of gaseous deuterium, Solid State Commun. 130 (2004) 815-820. https://doi.org/10.1016/j.ssc.2004.03.054.
[151] V. Paul-Boncour, S.M. Filipek, M. Dorogova, F. Bourée, G. André, I. Marchuk, A. Percheron-Guégan, R.S. Liu, Neutron diffraction study, magnetic properties and thermal stability of $YMn_2D_6$ synthesized under high deuterium pressure, J. Solid State Chem. 178 (2005) 356-362. https://doi.org/10.1016/j.jssc.2004.05.066.

[152] J. Przewoźnik, V. Paul-Boncour, M. Latroche, A. Percheron-Guégan, X-ray diffraction and extended X-ray absorption fine-structure study of $R$Mn$_2$ hydrides ($R$ = Y, Gd or Dy), J. Alloys Compd. 232 (1996) 107-118. https://doi.org/10.1016/0925-8388(95)01995-2.
[153] J. Przewoźnik, J. Żukrowski, K. Freindl, E. Japa, K. Krop, Magnetic and structural properties of DyMn$_2$H$_x$ ($0 \leq x \leq 4.2$), J. Alloys Compd. 284 (1999) 31-41. https://doi.org/10.1016/S0925-8388(98)00936-0.
[154] J. Żukrowski, H. Figiel, A. Budziak, P. Zachariasz, G. Fischer, E. Dormann, Structural and magnetic transformations in the GdMn$_2$H$_x$, hydrides, J. Magn. Magn. Mater. 238 (2002) 129-139. https://doi.org/10.1016/S0304-8853(01)00825-3.
[155] H. Figiel, A. Budziak, J. Żukrowski, G. Fischer, M.T. Kelemen, E. Dormann, Structural and magnetic properties of TbMn$_2$H$_x$ hydrides, J. Alloys Compd. 335 (2002) 48-58. https://doi.org/10.1016/S0925-8388(01)01820-5.
[156] A. Budziak, P. Zachariasz, L. Kolwicz-Chodak, H. Figiel, A. Pacyna, J. Żukrowski, Structural and magnetic properties of C15 HoMn$_2$ hydrides, J. Alloys Compd. 509 (2011) 1347-1354. https://doi.org/10.1016/j.jallcom.2010.10.060.
[157] V. Paul-Boncour, S.M. Filipek, G. André, F. Bourée, M. Guillot, R. Wierzbicki, I. Marchuk, R.S. Liu, B. Villeroy, A. Percheron-Guégan, H.D. Yang, S.C. Pin, Structural, thermal and magnetic properties of ErMn$_2$D$_6$ synthesized under high deuterium pressure, J. Phys. Condens. Matter. 18 (2006) 6409-6420. https://doi.org/10.1088/0953-8984/18/27/023.
[158] Q.A. Zhang, Z.Q. Dong, S.C. Xie, Crystal structures and hydrogenation-dehydrogenation characteristics of Er(Ni$_{1-x}$Mn$_x$)$_2$, J. Alloys Compd. 626 (2015) 189-193. https://doi.org/10.1016/j.jallcom.2014.11.157.
[159] K. Aoki, K. Mori, H. Onodera, T. Masumoto, Hydrogen-induced amorphization of C15 Laves TbFe$_2$ compound, J. Alloys Compd. 253-254 (1997) 106-109. https://doi.org/10.1016/S0925-8388(96)02909-X.
[160] X.G. Li, A. Chiba, K. Aoki, T. Masumoto, Differential thermal analysis of hydrogen-induced amorphization in $C$15 Laves compounds $R$Fe$_2$, Intermetallics. 5 (1997) 387-391. https://doi.org/10.1016/S0966-9795(97)00009-5.
[161] M. Dilixiati, K. Kanda, K. Ishikawa, K. Aoki, Pressure dependence of hydrogen-induced amorphization in C15 laves phase TbFe$_2$, Mater. Trans. 43 (2002) 1089-1094. https://doi.org/10.2320/matertrans.43.1089.
[162] M. Dilixiati, K. Kanda, K. Ishikawa, K. Aoki, Hydrogen-induced amorphization in $C$15 Laves phases $R$Fe$_2$, J. Alloys Compd. 337 (2002) 128-135. https://doi.org/10.1016/S0925-8388(01)01923-5.
[163] V. Paul-Boncour, L. Guénée, M. Latroche, M. Escorne, A. Percheron-Guégan, C. Reichl, G. Wiesinger, Structural and magnetic study of new YFe$_2$D$_x$ compounds ($0 < x \leq 3.5$), J. Alloys Compd. 253-254 (1997) 272-274. https://doi.org/10.1016/S0925-8388(96)02915-5.
[164] V. Paul-Boncour, L. Guénée, M. Latroche, A. Percheron-Guégan, B. Ouladdiaf, F. Bourée-Vigneron, Elaboration, Structures, and Phase Transitions for YFe$_2$D$_x$Compounds ($x$ =1.3, 1.75, 1.9, 2.6) Studied by Neutron Diffraction, J. Solid State Chem. 142 (1999) 120-129. https://doi.org/10.1006/jssc.1998.7995.
[165] V. Paul-Boncour, A. Percheron-Guégan, The influence of hydrogen on the magnetic properties and electronic structures of intermetallic compounds: YFe$_2$-D$_2$ system as an example, J. Alloys Compd. 293-295 (1999) 237-242. https://doi.org/10.1016/S0925-8388(99)00323-0.
[166] V. Paul-Boncour, S.M. Filipek, A. Percheron-Guégan, I. Marchuk, J. Pielaszek, Structural and magnetic properties of $R$Fe$_2$H$_5$ hydrides ($R$ = Y, Er), J. Alloys Compd. 317-318 (2001) 83-87. https://doi.org/10.1016/S0925-8388(00)01400-6.

[167] V. Paul-Boncour, C. Giorgetti, G. Wiesinger, A. Percheron-Guégan, Influence of deuterium absorption on structural and magnetic properties of $ErFe_2$, J. Alloys Compd. 356-357 (2003) 195-199. https://doi.org/10.1016/S0925-8388(02)01233-1.
[168] E.A. Sherstobitova, A. Gubkin, L.A. Stashkova, N.V. Mushnikov, P.B. Terent'ev, D. Cheptiakov, A.E. Teplykh, J. Park, A.N. Pirogov, Crystal structure of $ErFe_2D_{3.1}$ and $ErFe_2H_{3.1}$ at 450 K, J. Alloys Compd. 508 (2010) 348-353. https://doi.org/10.1016/j.jallcom.2010.04.043.
[169] K. Shashikala, P. Raj, A. Sathyamoorthy, $ErFe_2$-H system: a new plateau and the structure of the new hydride phase, Mater. Res. Bull. 31 (1996) 957-963. https://doi.org/10.1016/S0025-5408(96)00080-3.
[170] V. Paul-Boncour, S.M. Filipek, I. Marchuk, G. Andre, F. Bouree, G. Wiesinger, A. Percheron-Guegan, Structural and magnetic properties of $ErFe_2D_5$ studied by neutron diffraction and Mo¨ssbauer spectroscopy, (2003) 12.
[171] Z. Li, H. Wang, L. Ouyang, J. Liu, M. Zhu, Reversible hydriding in $YFe_{2-x}Al_x$ ($x$ = 0.3, 0.5, 0.7) intermetallic compounds, J. Alloys Compd. 689 (2016) 843-848. https://doi.org/10.1016/j.jallcom.2016.08.003.
[172] H.-J. Ahn, Y.-G. Kim, J.-Y. Lee, Structural changes of the Laves phase $ErFe_2$ during static and cyclic hydrogenation treatments, J. Alloys Compd. 196 (1993) 45-51. https://doi.org/10.1016/0925-8388(93)90568-8.
[173] T. Leblond, V. Paul-Boncour, F. Cuevas, O. Isnard, J.F. Fernández, Study of the multipeak deuterium thermodesorption in $YFe_2D_x$ ($1.3 \leq x \leq 4.2$) by DSC, TD and in situ neutron diffraction, Int. J. Hydrog. Energy. 34 (2009) 2278-2287. https://doi.org/10.1016/j.ijhydene.2008.12.046.
[174] H. Okamoto, Fe-Sc (Iron-Scandium), J. Phase Equilibria Diffus. 33 (2012) 80-80. https://doi.org/10.1007/s11669-011-9967-x.
[175] D. Niarchos, P.J. Viccaro, G.K. Shenoy, B.D. Dunlap, A.T. Aldred, Mössbauer studies of $ScFe_2$, $LaNi_4Fe$ and their hydrides, Hyperfine Interact. 9 (1981) 563-570. https://doi.org/10.1007/BF01020978.
[176] K.N. Semenenko, R.A. Sirotina, A.P. Savchenkova, V.V. Burnasheva, M.V. Lototskii, E.E. Fokina, S.L. Troitskaya, V.N. Fokin, Interactions of $\lambda_3$-$ScFe_2$ and $\lambda_2$-$ScFe_{1.8}$ with hydrogen, J. Common Met. 106 (1985) 349-359. https://doi.org/10.1016/0022-5088(85)90272-3.
[177] V.A. Yartys', V.V. Burnasheva, K.N. Semenenko, N.V. Fadeeva, S.P. Solov'ev, Crystal chemistry of $RT_5H(D)_x$, $RT_2H(D)_x$ and $RT_3H(D)_x$ hydrides based on intermetallic compounds of $CaCu_5$, $MgCu_2$, $MgZn_2$ and $PuNi_3$ structure types, Int. J. Hydrog. Energy. 7 (1982) 957-965. https://doi.org/10.1016/0360-3199(82)90164-1.
[178] K. Ishikawa, M. Yamaguchi, I. Yamamoto, S. Mizusaki, F. Ishikawa, T. Goto, Magnetic properties of $YCo_2$ hydrides, J. Alloys Compd. 356-357 (2003) 227-230. https://doi.org/10.1016/S0925-8388(03)00110-5.
[179] H. Michor, G. Hilscher, O. Myakush, N. Pyk, P. Myronenko, I. Koval'chuck, B. Kotur, Crystal structure and magnetic properties of V-doped $YCo_2$ and $YCo_3$ and their hydrides, J. Alloys Compd. 509 (2011) 5200-5205. https://doi.org/10.1016/j.jallcom.2011.02.052.
[180] K. Kanematsu, T. Sugiyama, M. Sekine, T. Okagaki, K.I. Kobayashi, Formation and magnetic properties of crystalline and amorphous $SmCo_2$ hydrides, J. Common Met. 147 (1989) 9-18. https://doi.org/10.1016/0022-5088(89)90143-4.
[181] K. Aoki, T. Masumoto, Solid state amorphization of intermetallic compounds by hydrogenation, J. Alloys Compd. 194 (1993) 251-261. https://doi.org/10.1016/0925-8388(93)90009-C.
[182] K. Aoki, T. Yamamoto, T. Masumoto, Hydrogen induced amorphization in $RNi_2$ laves phases, Scr. Metall. 21 (1987) 27-31. https://doi.org/10.1016/0036-9748(87)90401-7.

[183] R.H. Van Essen, K.H.J. Buschow, Hydrogen sorption characteristics of Ce-3d and Y-3d intermetallic compounds, J. Common Met. 70 (1980) 189-198. https://doi.org/10.1016/0022-5088(80)90227-1.
[184] H. Shen, V. Paul-Boncour, M. Latroche, F. Cuevas, P. Li, H. Yuan, Z. Li, J. Zhang, L. Jiang, Investigation of the phase occurrence and H sorption properties in the $Y_{33.33}Ni_{66.67-x}Al_x$ ($0 \leq x \leq 33.33$) system, J. Alloys Compd. 888 (2021) 161375. https://doi.org/10.1016/j.jallcom.2021.161375.
[185] O.V. Myakush, Y.V. Verbovyts'kyi, V.V. Berezovets', O.H. Ershova, V.D. Dobrovol's'kyi, B.Y. Kotur, Sorption and desorption of hydrogen in the alloys based on the $ErNi_2$ compound, Mater. Sci. 5 (2007) 682-688. https://doi.org/10.1007/s11003-008-9014-1.
[186] T. Jin, C. Li, J. Huang, K. Tang, L. Chen, Hydrogenation Induced Change in Structures, Magnetic Properties and Specific Heats of Magnetic Regenerative Material ErNi and $ErNi_2$, Mater. Trans. 54 (2013) 363-366. https://doi.org/10.2320/matertrans.M2012276.
[187] V. Paul-Boncour, C. Lartigue, A. Percheron-Guégan, J.C. Achard, J. Pannetier, In situ neutron powder diffraction measurements of the absorption and desorption of hydrogen (deuterium) in (La, Ce)$Ni_2$ compounds: Amorphization and recrystallization, J. Common Met. 143 (1988) 301-313. https://doi.org/10.1016/0022-5088(88)90052-5.
[188] K. Kawahara, X.G. Li, K. Ishikawa, K. Suzuki, K. Aoki, Formation of amorphous and nanocrystalline alloys by hydrogenation of *C*15 laves *R*$Mn_2$, Scr. Mater. 44 (2001) 2019-2022. https://doi.org/10.1016/S1359-6462(01)00827-2.
[189] K. Mori, K. Aoki, T. Masumoto, Differential thermal analysis of hydrogen-induced amorphization in *C*15 Laves compounds *R*$Co_2$, Mater. Sci. Eng. A. 179-180 (1994) 181-185. https://doi.org/10.1016/0921-5093(94)90189-9.
[190] U.-I. Chung, Y.-G. Kim, J.-Y. Lee, General features of hydrogen-induced amorphization in $RM_2$ (*R* = rare earth, *M* = transition element) Laves phases, Philos. Mag. B. 63 (1991) 1119-1130. https://doi.org/10.1080/13642819108207589.
[191] R.L. Cohen, K.W. West, F. Oliver, K.H.J. Buschow, Moessbauer studies of hydrogen absorption in Dy, $DyMn_2$, $DyFe_2$, $DyCo_2$, and $DyNi_2$, Phys Rev B. 21:3 (1980). https://doi.org/10.1103/PhysRevB.21.941.
[192] Y.-G. Kim, J.-Y. Lee, The mechanism of hydrogen-induced amorphization in intermetallic compounds, J. Alloys Compd. 187 (1992) 1-7. https://doi.org/10.1016/0925-8388(92)90514-A.
[193] Jr. Tomoyasu Aihara, K. Aoki, T. Masumoto, Formation and Crystallization of Hydrogen-Induced Amorphous $RNi_2H_x$ (*R* = Sm, Gd, Dy, Ho, Er) Alloys, Mater. Trans. JIM. 33 (1992) 15-22. https://doi.org/10.2320/matertrans1989.33.15.
[194] U.-I. Chung, J.-Y. Lee, A kinetic study on the hydrogen induced amorphization in $ErNi_2$ laves phase, Acta Metall. Mater. 38 (1990) 811-817. https://doi.org/10.1016/0956-7151(90)90034-E.
[195] U. Chung, Y. Kim, J. Lee, Phase separation in amorphous $ErNi_2H_x$ prepared by hydrogenation, J. Appl. Phys. 69 (1991) 1275-1278. https://doi.org/10.1063/1.347313.
[196] K. Mori, K. Aoki, T. Masumoto, Hydrogen-induced amorphization of Er$M_2$ (*M* = Fe, Co, Ni) compounds with *C*15 structure, in: T. Masumoto, A. Inoue, A. Makishima, L. Arnberg, M. Doyama, M.I. Baskes, R. Nieminen, K. Kuribayashi, H. Hashimoto, M.Z. Saghir, A. Sawaoka, R.S. Sokolowski, H.U. Walter, T. Kishi (Eds.), Adv. Mater. 93, Elsevier, 1994: pp. 119-122. https://doi.org/10.1016/B978-0-444-81993-2.50035-4.
[197] Y.-G. Kim, U.-I. Chung, J.-Y. Lee, Features of hydrogen-induced amorphization of the Er(Co, $Mn)_2$ pseudo-binary Laves compound, Acta Metall. Mater. 40 (1992) 1497-1503. https://doi.org/10.1016/0956-7151(92)90093-T.

[198] K. Ishikawa, N. Ogasawara, K. Aoki, Pressure dependence of hydrogen-induced amorphization in *C*14 Laves phase $NdMn_2$, J. Alloys Compd. 404-406 (2005) 599-603. https://doi.org/10.1016/j.jallcom.2004.11.114.
[199] Y.-G. Kim, J.-Y. Lee, Hydrogen-induced transformation to an amorphous state in the Laves phases Ce(Ru, *M*)$_2$ (*M* = Fe, Co, Ni), J. Alloys Compd. 191 (1993) 243-249. https://doi.org/10.1016/0925-8388(93)90072-U.
[200] K. Yong-Gyoo, L. Sung-Man, L. Jai-Young, Hydrogen-induced amorphization of the Laves compound $CeNi_2$ and the structural and thermal characteristics of the amorphous phase, J. Common Met. 169 (1991) 245-256. https://doi.org/10.1016/0022-5088(91)90073-D.
[201] K. Aoki, X.-G. Li, T. Masumoto, Factors controlling hydrogen-induced amorphization of *C*15 Laves compounds, Acta Metall. Mater. 40 (1992) 1717-1726. https://doi.org/10.1016/0956-7151(92)90115-U.
[202] E. Gratz, A. Kottar, A. Lindbaum, M. Mantler, M. Latroche, V. Paul-Boncour, M. Acet, C. Barner, W.B. Holzapfel, V. Pacheco, Temperature- and pressure-induced structural transitions in rare-earth-deficient (*R* = Y, Sm, Gd, Tb) Laves phases, J. Phys. Condens. Matter. 8 (1996) 8351-8361. https://doi.org/10.1088/0953-8984/8/43/026.
[203] O. Myakush, V. Babizhetskyy, P. Myronenko, H. Michor, B. Kotur, E. Bauer, Influence of doping elements (Cu and Fe) on the crystal structure and electrical resistivity of $YNi_3$ and $Y_{0.95}Ni_2$, Chem. Met. Alloys. 4 (2011) 152-159. https://doi.org/10.30970/cma4.0181.
[204] L. Vegard, Die Konstitution der Mischkristalle und die Raumfüllung der Atome, Z. Für Phys. 5 (1921) 17-26. https://doi.org/10.1007/BF01349680.
[205] K. Yoshimura, M. Takigawa, H. Yasuoka, M. Shiga, Y. Nakamura, Spin Fluctuations in $Y(Mn_{1-x}M_x)_2$ Itinerant Electron System - Nuclear Magnetic Resonance and Relaxation, J. Magn. Magn. Mater. 54 (1986) 1075-1076. https://doi.org/10.1016/0304-8853(86)90388-4.
[206] K. Fujiwara, Effect of Hydrogen Absorption on the Magnetic Properties of Pseudo-binary Intermetallics $Y(Mn_{1-x}T_x)_2$ (*T* = Al, Co and Ni), J. Phys. Soc. Jpn. 57 (1988) 2133-2142. https://doi.org/10.1143/JPSJ.57.2133.
[207] V. Paul-Boncour, S.M. Filipek, K. Provost, F. Couturas, A. Morawski, Structural and magnetic phase diagram of $YMn_{2-x}Fe_x(H, D)_y$ compounds ($5 \leq y \leq 6$) synthesized under high H or D gaseous pressure, J. Alloys Compd. 691 (2017) 884-892. https://doi.org/10.1016/j.jallcom.2016.08.258.
[208] B. Kotur, O. Myakush, H. Michor, E. Bauer, Influence of doping elements (Y and Fe) on crystal structure and electrical resistivity of the $RNi_2$ (*R* = Gd, Er) compounds, J. Alloys Compd. 499 (2010) 135-139. https://doi.org/10.1016/j.jallcom.2010.03.187.
[209] S. Zhao, H. Wang, J. Liu, Exploring the Hydrogen-Induced Amorphization and Hydrogen Storage Reversibility of $Y(Sc)_{0.95}Ni_2$ Laves Phase Compounds, Materials. 14 (2021) 276. https://doi.org/10.3390/ma14020276.
[210] V. Paul-Boncour, A. Lindbaum, E. Gratz, E. Leroy, A. Percheron-Guégan, Structural study of the pseudo-binary Y(Ni, Cu)$_2$ system, Intermetallics. 10 (2002) 1011-1017. https://doi.org/10.1016/S0966-9795(02)00120-6.
[211] K. Kadir, D. Noréus, I. Yamashita, Structural determination of $AMgNi_4$ (where *A* = Ca, La, Ce, Pr, Nd and Y) in the $AuBe_5$ type structure, J. Alloys Compd. 345 (2002) 140-143. https://doi.org/10.1016/S0925-8388(02)00323-7.
[212] C. Geibel, U. Klinger, M. Weiden, B. Buschinger, F. Steglich, Magnetic properties of new Ce-*T*-Mg compounds (*T* = Ni, Pd), Phys. B Condens. Matter. 237-238 (1997) 202-204. https://doi.org/10.1016/S0921-4526(97)00098-7.

[213] K. Aono, S. Orimo, H. Fujii, Structural and hydriding properties of $MgYNi_4$: A new intermetallic compound with *C*15*b*-type Laves phase structure, J. Alloys Compd. 309 (2000) L1-L4. https://doi.org/10.1016/S0925-8388(00)01065-3.
[214] J.-L. Bobet, P. Lesportes, J.-G. Roquefere, B. Chevalier, K. Asano, K. Sakaki, E. Akiba, A preliminary study of some "pseudo-$AB_2$" compounds: $RENi_4Mg$ with RE = La, Ce and Gd. Structural and hydrogen sorption properties, Int. J. Hydrog. Energy. 32 (2007) 2422-2428. https://doi.org/10.1016/j.ijhydene.2006.11.031.
[215] J.-G. Roquefere, B. Chevalier, R. Pöttgen, N. Terashita, K. Asano, E. Akiba, J.-L. Bobet, Structural, magnetic, electrochemical and hydrogen absorption properties of $Gd_yMg_{2-y}Ni_{4-x}Al_x$ compounds with 0.4, Intermetallics. 16 (2008) 179-187. https://doi.org/10.1016/j.intermet.2007.09.002.
[216] J.-G. Roquefere, S.F. Matar, J. Huot, J.-L. Bobet, X-ray/neutron diffraction studies and ab initio electronic structure of $CeMgNi_4$ and its hydride, Solid State Sci. 11 (2009) 1971-1978. https://doi.org/10.1016/j.solidstatesciences.2009.07.003.
[217] M.N. Guzik, J. Lang, J. Huot, S. Sartori, Effect of Al presence and synthesis method on phase composition of the hydrogen absorbing La-Mg-Ni-based compounds, Int. J. Hydrog. Energy. 42 (2017) 30135-30144. https://doi.org/10.1016/j.ijhydene.2017.10.062.
[218] M.K. Benabadji, A. Mahmoudi, D. Bouabdallah, F. Saidi, G. Merad, Investigation of electronic and elastic properties of $YNi_{2-x}M_x$ (M: Fe, Co, Cu and Zn): *Ab* initio calculations analyzed with Data mining approach, Adv. Model. Anal. A. 55 (2018) 35-42.
[219] H. Oesterreicher, H. Bittner, Hydride formation in $La_{1-x}Mg_xNi_2$, J. Common Met. 73 (1980) 339-344. https://doi.org/10.1016/0022-5088(80)90327-6.
[220] V.V. Shtender, R.V. Denys, V. Paul-Boncour, A.B. Riabov, I.Yu. Zavaliy, Hydrogenation properties and crystal structure of $YMgT_4$ ($T$ = Co, Ni, Cu) compounds, J. Alloys Compd. 603 (2014) 7-13. https://doi.org/10.1016/j.jallcom.2014.03.030.
[221] M. Eckert, Max von Laue and the discovery of X-ray diffraction in 1912, Ann. Phys. 524 (2012) A83-A85. https://doi.org/10.1002/andp.201200724.
[222] J. Rodríguez-Carvajal, Recent advances in magnetic structure determination by neutron powder diffraction, Phys. B Condens. Matter. 192 (1993) 55-69. https://doi.org/10.1016/0921-4526(93)90108-I.
[223] H.M. Rietveld, A profile refinement method for nuclear and magnetic structures, J. Appl. Crystallogr. 2 (1969) 65-71. https://doi.org/10.1107/S0021889869006558.
[224] T.P. Blach, E.MacA. Gray, Sieverts apparatus and methodology for accurate determination of hydrogen uptake by light-atom hosts, J. Alloys Compd. 446-447 (2007) 692-697. https://doi.org/10.1016/j.jallcom.2006.12.061.
[225] H. Hemmes, A. Driessen, R. Griessen, Thermodynamic properties of hydrogen at pressures up to 1 Mbar and temperatures between 100 and 1000K, J. Phys. C Solid State Phys. 19 (1986) 3571-3585. https://doi.org/10.1088/0022-3719/19/19/013.
[226] G. Kresse, J. Furthmüller, Efficiency of ab-initio total energy calculations for metals and semiconductors using a plane-wave basis set, Comput. Mater. Sci. 6 (1996) 15-50. https://doi.org/10.1016/0927-0256(96)00008-0.
[227] P. Blochl, Projector augmented-wave method, Phys. Rev. B. 50 (1994) 17953-17979. https://doi.org/10.1103/PhysRevB.50.17953.
[228] J.P. Perdew, K. Burke, M. Ernzerhof, Generalized Gradient Approximation Made Simple, Phys. Rev. Lett. 77 (1996) 3865-3868. https://doi.org/10.1103/PhysRevLett.77.3865.
[229] H. MONKHORST, J. PACK, On Special Points for Brillouin Zone Integrations, Phys. Rev. B Condens. Matter. 13 (1976) 5188-5192. https://doi.org/10.1103/PhysRevB.13.5188.

[230] M. Methfessel, A.T. Paxton, High-precision sampling for Brillouin-zone integration in metals, Phys. Rev. B. 40 (1989) 3616-3621. https://doi.org/10.1103/PhysRevB.40.3616.
[231] R. Grau-Crespo, S. Hamad, C.R.A. Catlow, N.H. de Leeuw, Symmetry-adapted configurational modelling of fractional site occupancy in solids, J. Phys. Condens. Matter. 19 (2007) 256201. https://doi.org/10.1088/0953-8984/19/25/256201.
[232] V.A. Yartys, V.V. Pavlenko, Hydrides of $R_3Ni_6(Al, Ga)_2$ ($R$ = Y, Sm, Gd, Tb, Dy, Ho, Er) intermetallic compounds: structure and properties, Z. Für Phys. Chem. 179 (1993) 269-273. https://doi.org/10.1524/zpch.1993.179.Part_1_2.269.
[233] K. Miliyanchuk, L. Havela, Y. Tsaruk, S. Mašková, R. Gladyshevskii, Hydrogen absorption in $R_2T_2M$ compounds with the $W_2CoB_2$-type structure, J. Alloys Compd. 647 (2015) 911-916. https://doi.org/10.1016/j.jallcom.2015.06.120.
[234] I. Jacob, Z. Hadari, J.J. Reilly, Hydrogen absorption in $A$NiAl ($A$ = Zr, Y, U), J. Common Met. 103 (1984) 123-127. https://doi.org/10.1016/0022-5088(84)90366-7.
[235] R.V. Denys, B. Riabov, V.A. Yartys, R.G. Delaplane, M. Sato, Hydrogen storage properties and structure of $La_{1-x}Mg_x$ $(Ni_{1-y}Mn_y)_3$ intermetallics and their hydrides, J. Alloys Compd. 446-447 (2007) 166-172. https://doi.org/10.1016/j.jallcom.2006.12.137.
[236] A.V. Virkar, A. Raman, Crystal structures of $AB_3$ and $A_2B_7$ rare earth-nickel phases, J. Common Met. 18 (1969) 59-66. https://doi.org/10.1016/0022-5088(69)90120-9.
[237] Q. Zhang, B. Zhao, M. Fang, C. Liu, Q. Hu, F. Fang, D. Sun, L. Ouyang, M. Zhu, $(Nd_{1.5}Mg_{0.5})Ni_7$-Based Compounds: Structural and Hydrogen Storage Properties, Inorg Chem. 51(5) (2012) 2976-2983. https://doi.org/10.1021/ic2022962.
[238] V. Paul-Boncour, J.-C. Crivello, N. Madern, J. Zhang, L.V.B. Diop, V. Charbonnier, J. Monnier, M. Latroche, Correlations between stacked structures and weak itinerant magnetic properties of $La_{2-x}Y_xNi_7$ compounds, J. Phys. Condens. Matter. 32 (2020) 415804. https://doi.org/10.1088/1361-648X/ab9d4c.
[239] V.A. Yartys, I.I. Bulik, O.V. Nakonechna, B.P. Tarasov, Reactions of hydrogen with $R_3Ni_8Al$ intermetallics ($R$ = Y, Pr, Nd, Gd, Tb, Dy, Ho, Er) with the $Ce_3Co_8Si$ type of structure, Sov. Mater. Sci. Transl Fiz.-Khimicheskaya Mekhanika Mater. Acad. Sci. Ukr. SSR. 28 (1992) 240-245. https://doi.org/10.1007/BF00726188.
[240] R.V. Denys, A.B. Riabov, V.A. Yartys, M. Sato, R.G. Delaplane, Mg substitution effect on the hydrogenation behaviour, thermodynamic and structural properties of the $La_2Ni_7$-$H(D)_2$ system, J. Solid State Chem. 181 (2008) 812-821. https://doi.org/10.1016/j.jssc.2007.12.041.
[241] J. Liu, S. Han, Y. Li, S. Yang, L. Zhang, Y. Zhao, Effect of Al incorporation on the degradation in discharge capacity and electrochemical kinetics of La-Mg-Ni-based alloys with $A_2B_7$-type super-stacking structure, J. Alloys Compd. 619 (2015) 778-787. https://doi.org/10.1016/j.jallcom.2014.09.041.
[242] W. Xiong, H. Yan, L. Wang, V. Verbetsky, X. Zhao, S. Mitrokhin, B. Li, J. Li, Y. Wang, Characteristics of $A_2B_7$-type LaYNi-based hydrogen storage alloys modified by partially substituting Ni with Mn, Int. J. Hydrog. Energy. 42 (2017) 10131-10141. https://doi.org/10.1016/j.ijhydene.2017.01.080.
[243] D. Shin, W.J. Golumbfskie, E.R. Ryba, Z.-K. Liu, First-principles study of Al-Ni-Y ternary compounds for crystal structure validation, J. Alloys Compd. 462 (2008) 262-266. https://doi.org/10.1016/j.jallcom.2007.08.010.
[244] L.O. Wasylechko, Yu.N. Grin, A.A. Fedorchuk, $CeNi_3$-type ternary phases in the $R$-Ni-Ga systems ($R$ = Y, Pr, Nd, Sm, Gd, Tb, Dy, Ho, Er, Tm, Yb, Lu), J. Alloys Compd. 219 (1995) 222-224. https://doi.org/10.1016/0925-8388(94)05040-6.
[245] V. Romaka, Magnetic and Crystallographic Parameters of $R_2Ni_2Ga$ and $R_2Ni_2Al$ Compounds, Phys Met Met. USSR. 54 (1982) 58-64.

[246] R. Ferro, G. Zanicchi, R. Marazza, Aluminum-Nickel-Yttrium, Ternary Alloys VCH. 8 (1993) 58-62.
[247] J. Huang, B. Yang, H. Chen, H. Wang, Thermodynamic Optimisation of the Ni-Al-Y Ternary System, J. Phase Equilibria Diffus. 36 (2015) 357-365. https://doi.org/10.1007/s11669-015-0390-6.
[248] A.V. Kolomiets, L. Havela, V.A. Yartys, A.V. Andreev, Hydrogen absorption-desorption, crystal structure and magnetism in RENiAl intermetallic compounds and their hydrides, J. Alloys Compd. 253-254 (1997) 343-346. https://doi.org/10.1016/S0925-8388(97)02982-4.
[249] H. Emami, F. Cuevas, M. Latroche, Ti(Ni, Cu) pseudo-binary compounds as efficient negative electrodes for Ni-MH batteries, J. Power Sources. 265 (2014) 182-191. https://doi.org/10.1016/j.jpowsour.2014.04.114.
[250] J. Prigent, J.-M. Joubert, M. Gupta, Modification of the hydrogenation properties of $LaNi_5$ upon Ni substitution by Rh, Ir, Pt or Au, J. Alloys Compd. 511 (2012) 95-100. https://doi.org/10.1016/j.jallcom.2011.08.094.
[251] Y. Pang, Q. Li, A review on kinetic models and corresponding analysis methods for hydrogen storage materials, Int. J. Hydrog. Energy. 41 (2016) 18072-18087. https://doi.org/10.1016/j.ijhydene.2016.08.018.
[252] V.V. Boldyrev, Control of the Reactivity of Solids, Annu. Rev. Mater. Sci. 9 (1979) 455-469. https://doi.org/10.1146/annurev.ms.09.080179.002323.
[253] M. Nakhl, J.L. Bobet, B. Chevalier, B. Darriet, Hydrogen Sorption Properties of Composites Mixtures Mg + YNi Submitted to Mechanical Grinding, J. Metastable Nanocrystalline Mater. 10 (2001) 637-642. https://doi.org/10.4028/www.scientific.net/JMNM.10.637.
[254] K. Miliyanchuk, L. Havela, R. Gladyshevskii, Department of Condensed Matter Physics, Charles University, R. Gladyshevskii, Department of Inorganic Chemistry, Ivan Franko National University of Lviv, Effect of element substitution on hydrogen absorption in compounds with the structure type $W_2CoB_2$, Chem. Met. Alloys. 12 (2019) 16-20. https://doi.org/10.30970/cma12.0386.
[255] C. Lartigue, A. Percheron-Guégan, J.C. Achard, F. Tasset, Thermodynamic and structural properties of $LaNi_{5-x}Mn_x$ compounds and their related hydrides, J. Common Met. 75 (1980) 23-29. https://doi.org/10.1016/0022-5088(80)90365-3.
[256] T. Kodama, H. Anada, H. Kaminaka, The site occupancies for the excess manganese atoms and the third element niobium in the intermetallic compound $ZrMn_2$, J. Alloys Compd. 224 (1995) 70-75. https://doi.org/10.1016/0925-8388(94)01473-6.
[257] A.A. Coelho, J. Evans, I. Evans, A. Kern, S. Parsons, The TOPAS symbolic computation system, Powder Diffr. 26 (2011) S22-S25. https://doi.org/10.1154/1.3661087.
[258] J.L. Wang, C. Marquina, M.R. Ibarra, G.H. Wu, Structure and magnetic properties of $R$Ni$_2$Mn compounds ($R$ = Tb, Dy, Ho, and Er), Phys. Rev. B. 73 (2006) 094436. https://doi.org/10.1103/PhysRevB.73.094436.
[259] C. Colinet, A. Pasturel, K.H.J. Buschow, Short-range order and stability in Gd-Ni and Y-Ni systems, J. Appl. Phys. 62 (1987) 3712-3717. https://doi.org/10.1063/1.339253.
[260] V. Berezovets, R. Denys, I. Zavaliy, Crystal structure and thermodynamic properties of $YNi_{2.67}Mn_{0.33}H_4$ hydride, 49 (2008) 121-127.
[261] V.V. Berezovets', R.V. Denys, O.B. Ryabov, I.Yu. Zavalii, Hydrides of substituted derivatives based on the $YNi_3$ compound, Mater. Sci. 43 (2007) 499-507. https://doi.org/10.1007/s11003-007-0058-4.
[262] M. Latroche, V. Paul-Boncour, A. Percheron-Guegan, J.C. Achard, Deviations from the $C$15 type structure in $R$Ni$_2$ compounds ($R$ = Y, Ce), Eur. J. Solid State Inorg. Chem. 28 (1991) 597-600.

[263] C. Zhong, D. Chao, Y. Chen, W. Wang, D. Zhu, C. Wu, Microstructures and electrochemical properties of $LaNi_{3.8-x}Mn_x$ hydrogen storage alloys, Electrochimica Acta. 58 (2011) 668-673. https://doi.org/10.1016/j.electacta.2011.10.011.
[264] V. Charbonnier, J. Zhang, J. Monnier, L. Goubault, P. Bernard, C. Magén, V. Serin, M. Latroche, Structural and Hydrogen Storage Properties of $Y_2Ni_7$ Deuterides Studied by Neutron Powder Diffraction, J. Phys. Chem. C. 119 (2015) 12218-12225. https://doi.org/10.1021/acs.jpcc.5b03096.
[265] K. Aoki, Differential thermal analysis of hydrogen-induced amorphization in *C*15 Laves compounds $GdM_2$ (*M* = Fe, Co, Ni), Mater. Sci. Eng. A. 133 (1991) 565-568. https://doi.org/10.1016/0921-5093(91)90135-A.
[266] K. Chattopadyhay, K. Aoki, T. Masumoto, The nature of hydrogen induced amorphization of $SmNi_2$ laves compound, Scr. Metall. 21 (1987) 365-369. https://doi.org/10.1016/0036-9748(87)90230-4.
[267] J.F. Smith, D.A. Hansen, The structures of $YNi_3$, $YCo_3$, $ThFe_3$ and $GdFe_3$, Acta Crystallogr. 19 (1965) 1019-1024. https://doi.org/10.1107/S0365110X65004814.
[268] M. Mezbahul-Islam, D. Kevorkov, M. Medraj, Experimental Study of the Mg-Ni-Y System at 673 K Using Diffusion Couples and Key Alloys, Metals. 5 (2015) 1746-1769. https://doi.org/10.3390/met5031746.
[269] T. Sato, T. Mochizuki, K. Ikeda, T. Honda, T. Otomo, H. Sagayama, H. Yang, W. Luo, L. Lombardo, A. Züttel, S. Takagi, T. Kono, S.-I. Orimo, Crystal Structural Investigations for Understanding the Hydrogen Storage Properties of $YMgNi_4$-Based Alloys, ACS Omega. 5 (2020) 31192-31198. https://doi.org/10.1021/acsomega.0c04535.
[270] S. Linsinger, M. Eul, C. Schwickert, R. Decourt, B. Chevalier, U.Ch. Rodewald, J.-L. Bobet, R. Pöttgen, Structure, homogeneity ranges, magnetic, and electrical properties of the ordered Laves phases $RENi_4Mg$ with $MgCu_4Sn$ type structure, Intermetallics. 19 (2011) 1579-1585. https://doi.org/10.1016/j.intermet.2011.06.002.
[271] I. Park, N. Terashita, E. Abe, Hydrogenation-induced microstructure changes of pseudo-binary $(Pr_xMg_{1-x})Ni_2$ Laves compounds, J. Alloys Compd. 580 (2013) S81-S84. https://doi.org/10.1016/j.jallcom.2013.01.108.
[272] C. Stan, E. Andronescu, D. Predoi, J.-L. Bobet, Structural and hydrogen absorption/desorption properties of $YNi_{4-x}Al_xMg$ compounds (with $0 \leq x \leq 1.5$), J. Alloys Compd. 461 (2008) 228-234. https://doi.org/10.1016/j.jallcom.2007.07.064.
[273] K. Young, T. Ouchi, L. Wang, D.F. Wong, The effects of Al substitution on the phase abundance, structure and electrochemical performance of $La_{0.7}Mg_{0.3}Ni_{2.8}Co_{0.5-x}Al_x$ ($x = 0$, 0.1, 0.2) alloys, J. Power Sources. 279 (2015) 172-179. https://doi.org/10.1016/j.jpowsour.2015.01.022.
[274] N. Terashita, E. Akiba, Hydriding Properties of $(Mg_{1-x}M_x)Ni_2$ *C*15-Type Laves Phase Alloys, Mater. Trans. 47 (2006) 1890-1893. https://doi.org/10.2320/matertrans.47.1890.
[275] N. Terashita, K. Sakaki, S. Tsunokake, Y. Nakamura, E. Akiba, Hydrogenation Properties of Ternary Intermetallic Compounds $Mg_{2-x}Pr_xNi_4$, Mater. Trans. 53 (2012) 513-517. https://doi.org/10.2320/matertrans.M2011334.
[276] K. Sakaki, N. Terashita, S. Tsunokake, Y. Nakamura, E. Akiba, Effect of Rare Earth Elements and Alloy Composition on Hydrogenation Properties and Crystal Structures of Hydrides in $Mg_{2-x}RE_xNi_4$, J Phys Chem C. (2012) 8. https://doi.org/10.1021/jp3052856.
[277] W.J. Golumbfskie, S.N. Prins, T.J. Eden, Z.-K. Liu, Predictions of the Al-rich region of the Al-Co-Ni-Y system based upon first-principles and experimental data, Calphad. 33 (2009) 124-135. https://doi.org/10.1016/j.calphad.2008.09.001.
[278] B. Šorgić, Ž. Blažina, A. Drašner, A study of structural and thermodynamic properties of the $YNi_{5-x}Al_x$-hydrogen system, J. Alloys Compd. 265 (1998) 185-189. https://doi.org/10.1016/S0925-8388(97)00296-X.

[279] J.-L. Bobet, S. Pechev, B. Chevalier, B. Darriet, Structural and hydrogen sorption studies of $NdNi_{5-x}Al_x$ and $GdNi_{5-x}Al_x$, J. Alloys Compd. 267 (1998) 136-141. https://doi.org/10.1016/S0925-8388(97)00565-3.
[280] M. Mezbahul-Islam, M. Medraj, A critical thermodynamic assessment of the Mg-Ni, Ni-Y binary and Mg-Ni-Y ternary systems, Calphad. 33 (2009) 478-486. https://doi.org/10.1016/j.calphad.2009.01.001.
[281] W. Liu, C.J. Webb, E.MacA. Gray, Review of hydrogen storage in $AB_3$ alloys targeting stationary fuel cell applications, Int. J. Hydrog. Energy. 41 (2016) 3485-3507. https://doi.org/10.1016/j.ijhydene.2015.12.054.
[282] A. Ślebarski, Investigation of the crystal structure of $YNi_2$, J. Common Met. 141 (1988) L1-L3. https://doi.org/10.1016/0022-5088(88)90223-8.
[283] W. Song, J. Li, T. Zhang, X. Hou, H. Kou, Formation mechanism of tetrahedral $MgYNi_4$ phase, Mater. Lett. 145 (2015) 193-196. https://doi.org/10.1016/j.matlet.2015.01.103.
[284] K. Kadir, T. Sakai, I. Uehara, Structural investigation and hydrogen capacity of $YMg_2Ni_9$ and $(Y_{0.5}Ca_{0.5})(MgCa)Ni_9$: new phases in the $AB_2C_9$ system isostructural with $LaMg_2Ni_9$, J. Alloys Compd. 287 (1999) 264-270. https://doi.org/10.1016/S0925-8388(99)00041-9.
[285] Z. Cao, S. Liu, X. Fang, K. Cheng, Q. Gao, Y. Du, J. Wang, J. Zhang, W. Huang, C. Tang, Experimental investigation and thermodynamic analysis of the Sc-Ni system supplemented with first-principles calculations, Thermochim. Acta. 586 (2014) 30-39. https://doi.org/10.1016/j.tca.2014.04.006.
[286] M. Yoshida, H. Ishibashi, K. Susa, T. Ogura, E. Akiba, Crystal structure, hydrogen absorbing properties and electrode performances of Sc-based Laves phase alloys, J. Alloys Compd. 226 (1995) 161-165. https://doi.org/10.1016/0925-8388(95)01600-7.
[287] R. Riccardo, B. Gabriella, F. Riccardo, The Al-rich region in the Y-Ni-Al system: microstructures and phase equilibria, Intermetallics. 8 (2000) 247.
[288] K. Klepp, E. Parthé, Yttrium-nickel YNi with the FeB structure type, Acta Crystallogr. B. 36 (1980) 3093-3094. https://doi.org/10.1107/S0567740880010874.
[289] V. Raghavan, Phase diagrams of ternary iron alloys, Indian Institute of Metals, 1992.
[290] A. Suzuki, N. Nishimiya, S. Ono, Thermodynamic properties of $Zr(Fe_xMn_{1-x})_2$-$H_2$ systems, J. Common Met. 89 (1983) 263-268. https://doi.org/10.1016/0022-5088(83)90278-3.
[291] F. Pourarian, V.K. Sinha, W.E. Wallace, Hydrogen absorption by zirconium-manganese-iron ($ZrMn_2Mn_yFe_x$), ACS Publ. (1982). https://doi.org/10.1021/j100222a025.
[292] F. Pourarian, W.E. Wallace, Hydrogen sorption characteristics of $Zr_{1-x}Ti_x(Cr_{1-y}Fe_y)_2$ alloys, J. Common Met. 107 (1985) 69-78. https://doi.org/10.1016/0022-5088(85)90242-5.
[293] E. Akiba, H. Iba, Hydrogen absorption by Laves phase related BCC solid solution, Intermetallics. 6 (1998) 461-470. https://doi.org/10.1016/S0966-9795(97)00088-5.